



THE UNIVERSITY *of* EDINBURGH

This thesis has been submitted in fulfilment of the requirements for a postgraduate degree (e.g. PhD, MPhil, DClinPsychol) at the University of Edinburgh. Please note the following terms and conditions of use:

This work is protected by copyright and other intellectual property rights, which are retained by the thesis author, unless otherwise stated.

A copy can be downloaded for personal non-commercial research or study, without prior permission or charge.

This thesis cannot be reproduced or quoted extensively from without first obtaining permission in writing from the author.

The content must not be changed in any way or sold commercially in any format or medium without the formal permission of the author.

When referring to this work, full bibliographic details including the author, title, awarding institution and date of the thesis must be given.

Nucleic acid detection using
oligonucleotide cross-linked
polymer composites

David Ferrier



THE UNIVERSITY
of EDINBURGH

Thesis submitted in fulfillment of
the requirements for the degree of
Doctor of Philosophy
to the University of Edinburgh

2017

Abstract

There has been much interest in recent years about the potential of microRNA as a new source of biomarkers for the diagnosis of disease. The delivery of new diagnostic tools based on this potential has been limited by shortcomings in current microRNA detection techniques. This thesis explores the development of a new method of microRNA detection through the incorporation of conductive particles into oligonucleotide-functionalised polymers to form oligonucleotide cross-linked polymer composites. Such composites could provide a simple, rapid, and low-cost means of microRNA detection that could be easily multiplexed, providing a valuable tool for point-of-care medical diagnostics.

This work presents oligonucleotide-functionalised carbon/polyacrylamide composites which demonstrate a selective swelling response in the presence of analyte oligonucleotide sequences and for which the electrical conductivity decreases with swelling. The composites were synthesised via UV-initiated free-radical polymerisation of carbon/monomer mixtures upon custom electrode devices, consisting of interdigitated platinum electrodes fabricated upon a silicon substrate. The optimal cross-linker density and carbon loading concentration were determined as well as the best means of dispersing the carbon particles within the polymer. Various types of carbon particles, with differing sizes and aspect ratios, were compared and their performances as conductive additives for polymer swelling transduction evaluated. The swelling behaviour of these composites was evaluated by analysing images of composite microdroplets as they swell. The electrical characteristics of the composites were determined by measuring either the two-terminal resistance or the complex impedance of composite microdroplets on the electrode devices. Alternating and direct current measurement techniques were compared to determine the best approach for the transduction of composite swelling. The volumetric

and electrical responses of oligonucleotide-functionalised carbon/polyacrylamide composites were analysed in solutions of analyte oligonucleotide and non-complementary controls.

It has been demonstrated that, using carbon nanopowder composites and a direct current two-terminal resistance measurement, it is possible to differentiate between analyte and control solutions to concentrations as low as 10 nM, with single-base precision, in less than three minutes. However, the inability to detect at concentrations below this value, difficulties in differentiating between different analyte concentrations and thermal instability mean that, in their current form, oligonucleotide cross-linked polymer composites are unsuitable for the detection of circulating microRNA at clinically relevant concentrations. Potential avenues of work to address these challenges are discussed. Also presented are collaborative results for oligonucleotide-responsive polymers functionalised with morpholino nucleic acid analogues, in what is believed to be the first example of such a material. These morpholino-functionalised polymers offer significant advantages, in terms of stability and sensitivity, over their nucleic acid equivalents for bio-responsive polymer applications.

Lay summary

If you were to ask any doctor ‘what is the best way to beat cancer?’ they would likely tell you, ‘catch it early’. However, this is more easily said than done. Many cancers don’t display symptoms until quite late and many of these symptoms are vague and nonspecific. For this reason there is a lot of effort dedicated to finding new biomarkers, molecules in the blood or other bodily fluids that can be used to detect and diagnose disease faster and more easily than conventional methods. One of the most exciting potential new biomarkers is microRNA, which are small strands of RNA found in the blood. Abnormal levels of microRNA have been linked to a wide range of diseases including most forms of cancer. A major reason why microRNA has not yet been exploited for diagnostic tests is that our current methods for detecting it are slow, complicated and expensive.

This research aims to develop a new technique for detecting short DNA and RNA molecules using polymers that include strands of DNA as part of their structure, like parts of the mesh of a net. When the target molecules are present, they will bind to the strands in the polymer, breaking these parts of the net and allowing the polymer to swell more in water than it would otherwise. This swelling can be measured by mixing electrically conductive particles into the polymer, so that it is highly conductive when they are tightly packed and less conductive when they are loosely packed.

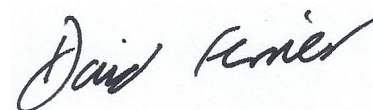
This thesis describes the creation of the first example of these DNA-sensitive polymer/particle mixtures. By experimenting with various parameters, the best recipe for preparing these mixtures was developed as was the best way of measuring their electrical properties as they swell. By measuring the conductivity of these polymers as

they swell, using specially made electrodes, we can detect the presence of the target molecules in under three minutes, without the use of any complicated or expensive techniques. It is hoped that, with some improvements, this approach could form the basis of a simple, fast and low-cost diagnostic tool.

Declaration of authorship

I hereby declare that the research recorded in this thesis and the thesis itself was composed by myself based on work done at the School of Engineering at The University of Edinburgh. This thesis has not entirely or in part been submitted for any other degree or professional qualification.

The morpholino functionalisation described in Section 5.2.1 was performed by Dr. Jaclyn Raeburn as was the experimental measurement of morpholino-functionalised polymers, presented in Figures 5.2, 5.5 and 5.6. The analysis of this data, and the measurement and subsequent analysis for DNA-functionalised polymers presented in the same graphs was performed by myself. The measurements of morpholino-functionalised polymers, and the subsequent data analysis, presented in Figure 5.4 was performed by Geraint Langford. The equivalent measurement and analysis of DNA-functionalised polymers presented in this graph was performed by myself.

A handwritten signature in black ink that reads "David Ferrier". The signature is written in a cursive style with a large initial 'D' and 'F'.

David Ferrier

4th September, 2017

Acknowledgments

Firstly I would like to thank my supervisors Philip Hands and Michael Shaver, without whose advice and guidance this document would not exist. I would like to thank Andrew Bunting, Yifan Li and Ewen Blair for their help and advice in developing microfabrication procedures, as well as Ilka Schmäeser for that any many other things besides. I would like to thank the technical support team, the *sine qua non* of the Scottish Microelectronics Centre, Stewart Ramsay, Richard Blair, Ewan MacDonald and Brian Neilson, as well as Camelia Dunare and Peter Lomax for their help, support and training. I would like to thank Jaclyn Raeburn for her help in NMR measurements, morpholino functionalisation, numerous other things and just generally helping me to pretend to be a chemist. I would also like to thank Gerry Langford for performing some of the morpholino measurements.

I would like to thank Stewart Smith for his help in reviewing this thesis and David Pritchard and Axis-Shield Diagnostics for their support of this project. I would also like to acknowledge the Engineering and Physical Sciences Research Council (EPSRC), Edinburgh Research and Innovation (ERI) and the University of Edinburgh School of Engineering for their financial support. I would like to thank Holger Schulze for his advice regarding DNA hybridisation and thermal cycling and Fabio Nudelman and Kathryn Topham for their help in obtaining SEM images.

Thanks are also due to my friends and fellow denizens of the Scottish Microelectronics Centre, past and present. There are too many to name everyone individually, but honourable mentions must be given to: Anthony Buchoux, Mags Normand, Ewen Blair, Ilka Schmäeser and Karina Jeronimo-Martinez. Also, thanks to all of the members of the Green Materials Laboratory, past and present, but particular mention must be given to Emily Macdonald and Fern Sinclair.

I need to thank Carly Elsworth and Vicki Baumann; better friends I could not ask for. A mention should also be given to all of the members of Combat Ready Krav Maga, for much needed distraction (as well as the odd broken bone). I would also like to acknowledge David Bowie... I do not feel that this requires an explanation.

Finally, and most importantly, I need to thank my family, to whom I owe everything.

Contents

1	Introduction	1
1.1	MicroRNA	2
1.1.1	Formation, structure and function	2
1.1.2	MicroRNA as potential biomarkers	5
1.1.3	Acute leukaemia: a potential application	9
1.2	The challenges of microRNA detection	12
1.3	Oligonucleotide detection – the state of the art	15
1.3.1	Established oligonucleotide detection techniques	15
1.3.2	Emerging oligonucleotide detection techniques	21
1.4	Oligonucleotide cross-linked polymer composites	26
1.4.1	The swelling of hydrogels	27
1.4.2	Oligonucleotide cross-linked polymers	28
1.4.3	The transduction of hydrogel swelling	31
1.4.4	Conductive polymer composites	34
1.5	Summary and outline	39

2	DNA-functionalised hydrogels: materials and methods	41
2.1	Composite preparation	41
2.1.1	Composite synthesis	41
2.1.2	Oligonucleotide design	43
2.1.3	Oligonucleotide preparation	44
2.1.4	Conductive particle dispersion and polymerisation	45
2.1.5	Nuclear magnetic resonance measurements	47
2.2	Optical measurements	48
2.2.1	End-point measurements	49
2.2.2	Kinetic measurements	51
2.3	Electrode design and fabrication	52
2.3.1	Electrode design	52
2.3.2	Electrode fabrication	53
2.3.3	Silanisation	57
2.4	Electrical measurements	57
2.4.1	Sensor model	60
2.4.2	Cyclic voltammetry	61
3	Composite preparation and characterisation: results and discussion	64
3.1	Composite preparation	64
3.1.1	Conductive particle dispersion and polymerisation	64
3.1.2	Nuclear magnetic resonance measurements	73
3.2	Optical measurements	75
3.2.1	Cross-link density dependency of swelling	75

3.2.2	Differential swelling	77
3.2.3	Kinetic swelling	79
3.2.4	A note on errors	84
3.2.5	Thermal stability	86
3.3	Conclusions	91
4	Electrical measurement of composite swelling: results and discussion	94
4.1	Electrode design and fabrication	94
4.2	Electrical measurements	100
4.2.1	Percolation measurements	101
4.2.2	Swelling measurements	107
4.2.3	Oligonucleotide cross-linked polymer composite swelling	122
4.2.4	Cyclic voltammetry	138
4.3	Conclusions	141
5	Morpholino-functionalised hydrogels	145
5.1	Introduction	145
5.1.1	Nucleic acid analogues	146
5.2	Materials and methods	149
5.2.1	Hydrogel formation	149
5.2.2	Differential swelling	149
5.2.3	Hydrophilicity versus salinity	150
5.2.4	Thermal stability	150
5.3	Results and discussion	151

5.3.1	Differential swelling	151
5.3.2	Hydrophilicity versus salinity	154
5.3.3	Thermal stability	157
5.4	Conclusions	159
6	Summary and conclusions	161
6.1	Summary	161
6.2	Conclusions	164
6.3	Future work	165
6.3.1	Composite synthesis	165
6.3.2	Electrode design	169
6.3.3	Delamination	170
6.3.4	Analyte solutions	172
6.3.5	Thermal stability	173
6.3.6	Morpholino-functionalised polymers	174
6.3.7	Alternative applications	175
6.4	Concluding remarks	176
	Acronyms and abbreviations	177
	List of figures	182
	List of tables	188
	References	189
	Appendix A Tools and chemicals	212

Appendix B	MatLab code	215
Appendix C	Fabrication run sheet	228
Appendix D	Cell constant calculation	230
Appendix E	Morpholino functionalisation	232

Chapter 1

Introduction

A significant challenge in biosensing is the simple, sensitive and specific detection of short nucleic acid sequences. The detection of these oligonucleotide sequences has potential applications ranging from medicine to counter-terrorism [1–4]. Specific sequences can be used to diagnose and monitor disease, identify infectious agents, and determine genetic predispositions to disease. A particular class of oligonucleotide, microRNA (miRNA), has recently emerged as a promising biomarker for many diseases and conditions. The nature of miRNA presents many challenges for their detection and the established techniques for oligonucleotide detection lack the capability to fully exploit the potential of miRNA as a new source of biomarkers.

This introductory chapter will introduce miRNA, its biological role and its potential as a new source of biomarkers. It will also discuss the challenges of miRNA detection and the shortcomings of existing techniques. The central premise of this thesis is that a new method of miRNA detection may be achieved through the transduction of the swelling

of oligonucleotide cross-linked polymers by incorporating a conductive component to create oligonucleotide cross-linked polymer composites (OCPCs). The details of this hypothesis and the ideas behind it will be outlined in this chapter. A brief overview of the structure of this thesis is also presented.

1.1 MicroRNA

1.1.1 Formation, structure and function

MicroRNAs (miRNAs) are short (typically 19-24 nucleotides in length [5]), single-stranded RNA molecules (Figure 1.1). Unlike messenger RNA (mRNA), they are not translated into proteins but rather act as regulators of mRNA translation. They do this by binding to partially or fully complementary regions of the mRNA strands, and either blocking the translation process or causing the breakdown of the mRNA, thereby inhibiting the translation of proteins. A single miRNA can target many different mRNAs (up to as many as 200) and a single mRNA sequence can be the target of many different miRNAs. [2, 6, 7]

The genesis of miRNA begins in the cell nucleus with what are known as primary precursor miRNAs (pri-miRNAs). These are single stranded RNA molecules that can be thousands of nucleotides long, have numerous stem-loop (or hairpin) structures and are transcribed from miRNA coding genes (Figure 1.2). The pri-miRNAs are then broken down enzymatically into one or more precursor miRNAs (pre-miRNAs). These

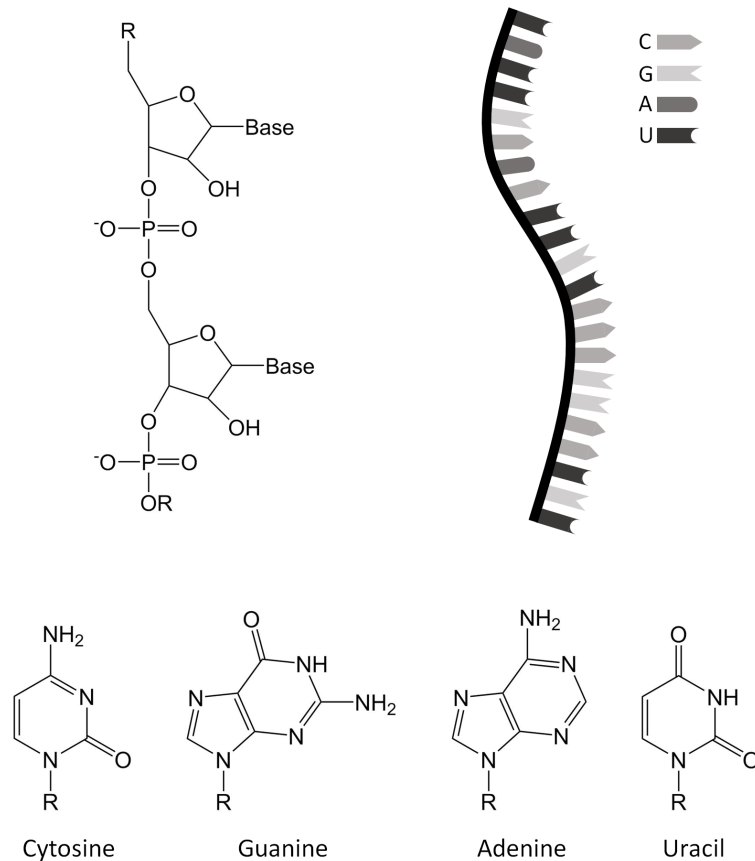


Figure 1.1: Illustration of the structure of miRNA. Like all RNA molecules they are made up of repeating sub-units comprised of one of four bases (cytosine (C), guanine (G), adenine (A) or uracil (U)) joined to a phosphate backbone via a ribose ring (top left). Mature miRNAs are comprised of a chain of approximately 20 of these subunits (top right). In the case of DNA, U is replaced by thymine (T).

pre-miRNAs are typically between 70 and 80 nucleotides in length and have a hairpin configuration. [8,9]

The pre-miRNAs are then transported from the nucleus to the cytoplasm where they are further broken down by enzymes, leaving a double-stranded RNA segment. The double-stranded miRNA complex is then ‘unzipped’ and one or both of the strands incorporated into protein complexes referred to as RNA-induced silencing complexes (RISCs), which comprise the ‘mature’ form of miRNA, *i.e.* that which regulates mRNA transcription. [8,9]

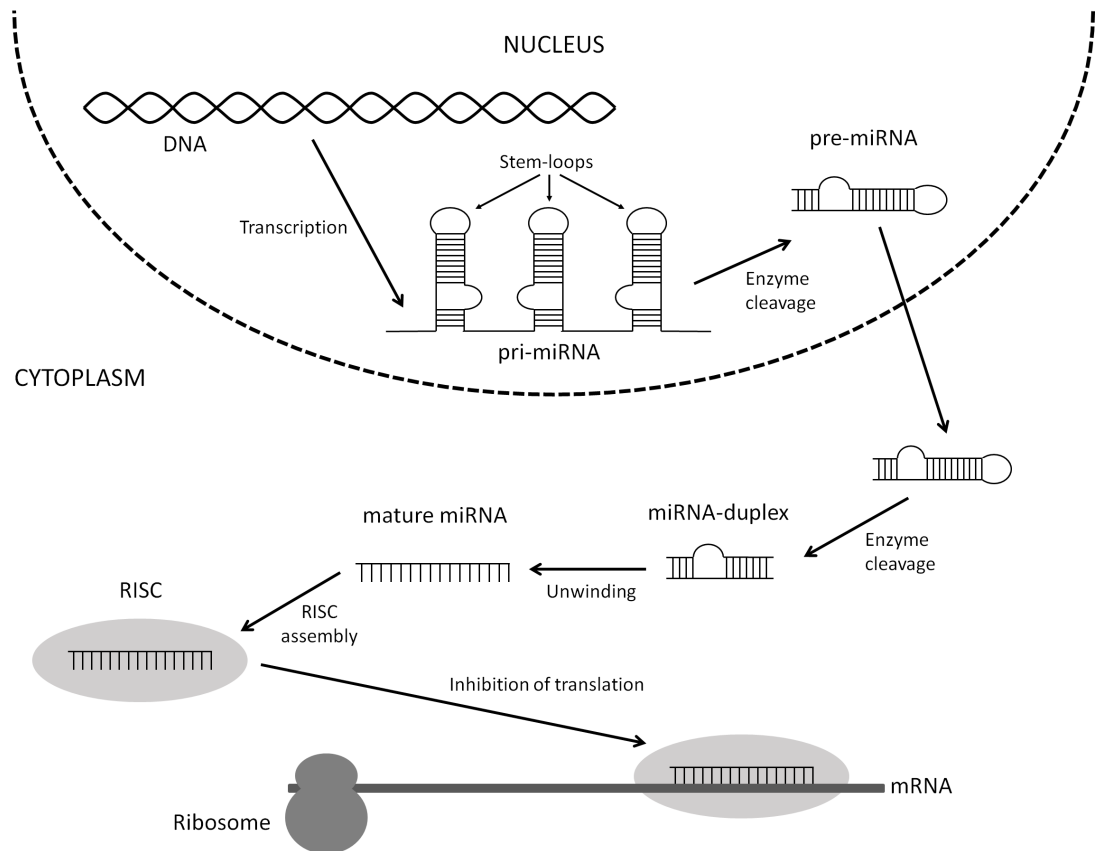


Figure 1.2: Illustration of miRNA genesis and maturation. MiRNA begins its formation in the cell nucleus where they are translated from the relevant genes and go through enzymatic modification before being transported out of the nucleus, into the cytoplasm. Once in the cytoplasm, miRNA goes through further enzymatic modification before combining with proteins to form RNA-induced silencing complexes (RISCs). It is in this form that miRNAs act as gene regulators by blocking translation of mRNA by the ribosomes. Adapted from Arenz *et al.* [9].

Over 2500 miRNAs have been identified in humans to date [10]. It is estimated that 1-4% of all genes in animals code for miRNAs [11, 12] and that over 60% of all genes responsible for encoding proteins are influenced by miRNA [7, 13], making them one of the most significant classes of gene regulators. MiRNAs have been shown to play a role in controlling a wide variety of biological processes, such as; cell proliferation, cell growth, differentiation (the process by which stem cells turn into particular cell types), metabolism and apoptosis (programmed cell death) [2, 7, 14, 15]. MiRNAs are found in

every cell in the human body and also in a wide variety of bodily fluids, a fact that will be discussed in more detail later in this chapter (Section 1.1.2.2).

1.1.2 MicroRNA as potential biomarkers

‘Biomarkers’ is a term given to molecules or proteins of which the measurement and evaluation can be used as an indication as to the existence or state of certain diseases and conditions. Whilst the term can be applied to parameters as well as molecules, it will be used exclusively for the latter throughout this thesis. The search for new biomarkers for the diagnosis of disease and the monitoring of response to treatment is a significant area of research. [16]

1.1.2.1 MicroRNA and disease

Abnormal levels of miRNA expression have been shown to be linked to diseases such as cancer, viral-induced disorders and neurological disorders [7]. To date more than 300 miRNAs have been linked with more than 150 diseases and conditions [17]. The links between miRNA and disease is a rapidly growing field of research, as evidenced by the rate of growth of publications, shown in Figure 1.3.

Approximately half of all human miRNAs discovered to date are located in areas of the genome associated with cancer (so-called ‘fragile regions’) [7] and deregulation of miRNA expression has been shown to contribute to the development of cancer [2], which is unsurprising given their fundamental role in cell proliferation and cell death. It is known that particular miRNAs can both inhibit or stimulate cell growth and

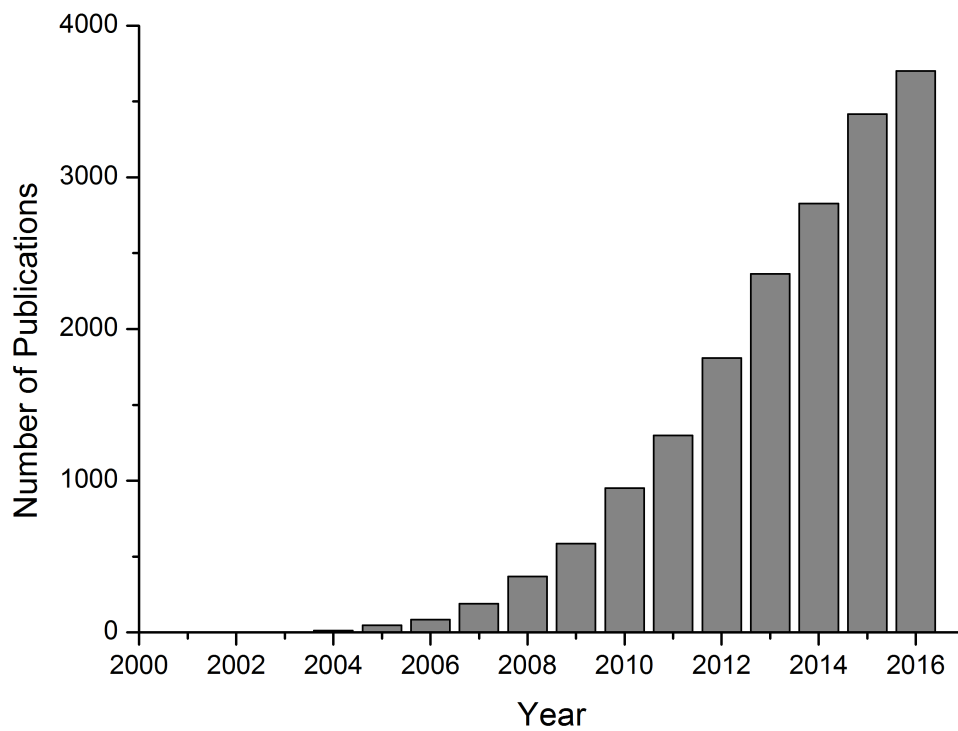


Figure 1.3: Number of publications by year associated with miRNA and disease. This literature search was performed using the terms “(microRNA* AND disease) OR (miRNA* AND disease)” and Thomson Reuters’ Web of Science database. [18]

therefore miRNAs can function as both tumour suppressors and ‘oncogenes’ meaning that, depending on the miRNA in question, a link to cancer could involve either an up-regulation or a down-regulation of miRNA expression. [6, 15, 19]

Abnormal miRNA expression has been shown to be closely associated with most human cancers [7] and miRNAs show promise as potential biomarkers for the diagnosis of many of these [2, 20–24]. It is believed that abnormal miRNA expression occurs early on in tumour formation, meaning miRNA expression profiling could have potential as a technique for early diagnosis [25]. For instance, Chen *et al.* have identified a group of ten serum¹ miRNAs that were able to differentiate samples from patients with non-small

¹The fluid that remains when all of the blood cells and clotting proteins are removed from a sample of blood.

cell lung cancer (NSCLC) from healthy controls more than 30 months prior to a clinical diagnosis, using samples obtained prior to the manifestation of any symptoms. [26]

MiRNA expression profiles are also useful for determining disease progression and prognosis. They have been shown to be of use in differentiating between cancer types and subtypes [2, 6] and to be useful for determining the tissue of origin for cancers of unknown primary origin (an important factor when determining treatment options) [1, 27]. The expression profiles of some miRNAs have been shown to be linked to survival rates for several forms of cancer and some have been linked to re-occurrence rates [2, 22]. The abnormal miRNA expression of cancer patients has been shown to return to normal after surgery, indicating a potential use for monitoring recovery. [2, 28]

In addition to cancer, miRNAs have been shown to be potential biomarkers for a range of other conditions such as neurological disorders and autoimmune diseases [23, 29]. There exist miRNAs that are primarily associated with particular organs, which when present in bodily fluids could be used to monitor the health of these organs. Examples of potential biomarkers in this area include miR-122, which can be used to determine the severity of liver damage, and miR-499, which can be used to determine the extent of damage to the heart. [5]

Additionally, many studies have shown that a range of drugs and other chemical compounds can cause aberrant miRNA expression, raising the prospect of the exploitation of miRNAs for biomarkers in toxicology. [30]

1.1.2.2 Circulating microRNA

The majority of miRNAs are found within cells, but a significant number have been found in the extracellular medium. Given that ordinary RNA is unstable in the extracellular medium, the presence and stability of miRNAs here is perhaps surprising. It is believed that this stability is caused by the miRNAs forming complexes with various proteins (such as the *Argonaute* family). It is also believed that miRNAs are released from cells via one of two mechanisms: they are exuded from cells in exosomes or micro-vesicles (whereupon they are believed to play a role in inter-cell communication), or they are released from a cell when it dies. However, the origin and function of these extracellular miRNAs are still not fully understood. [31,32]

As a result of this unusual stability, miRNAs are present in a wide range of bodily fluids, with at least 600 different miRNAs being present in at least one bodily fluid and at least 60 being present in all bodily fluids (out of 12 bodily fluids tested) [33]. This presents an attractive prospect for biosensing as many bodily fluids – such as blood serum or plasma, saliva and urine, all of which contain significant numbers of miRNAs – are far easier to obtain and process than the relevant cells, which will need to be lysed using reagents, which can prove costly and time consuming. [34]

Within a typical cell the average number of copies of any given miRNA has been estimated to be approximately 500, however these values can vary over several orders of magnitude for different miRNAs, with some being present at more than 10,000 copies per cell [35]. Concentrations of circulating miRNAs are harder to determine; current miRNA detection techniques are either unable to measure absolute quantities of miRNA

(microarrays) or are far better at measuring relative concentrations (quantitative PCR (qPCR), see Section 1.3.1.3). Concentrations of serum miRNAs typically range between ~ 10 fM and ~ 1 pM [36, 37], although this will depend heavily upon the miRNA in question, with concentrations varying over several orders of magnitude between different miRNAs.

The fact that circulating miRNAs are present in different bodily fluids means that miRNA profiling has potential applications in forensic science. Hanson *et al.* have identified a group of 9 miRNAs that can be used as biomarkers to determine the body-fluid origin of an unknown sample from as little as 50 pg of sample RNA, offering both an increase in efficiency and capability compared to current testing techniques [38]. In addition, such miRNA-based forensic techniques would be superior to alternative mRNA-based techniques as miRNA is typically more stable than mRNA. [39–41]

1.1.3 Acute leukaemia: a potential application

As a case study into the potential benefits of a simple, sensitive and specific means of miRNA detection we can consider acute leukaemia. Leukaemia is a cancer of the white blood cells or bone marrow. Overall it is the 12th most common form of cancer in the UK, with approximately 9,500 people being diagnosed in 2014 (roughly 26 per day), and the 11th most common cause of cancer death, with approximately 4,600 people dying from leukaemia in 2014 (roughly 13 per day). The incidence rates for leukaemia in the UK have increased by 43% since the 1970s. [42]

Leukaemia can be subdivided into four main subtypes depending upon the type of cells

affected and the timescale over which the disease manifests. These subtypes are: acute myeloid leukaemia (AML); chronic myeloid leukaemia (CML); acute lymphoblastic leukaemia (ALL) and chronic lymphoblastic leukaemia (CLL). The chronic forms manifest over years whereas the acute forms progress over much shorter time-spans, typically proving fatal within weeks or months of onset. [43,44]

The subtypes are very different in terms of their origins and clinical behaviour but the outward symptoms have a lot in common. They vary from case to case but can include: weakness and fatigue, fever, bruising or bleeding, pain in the bones or joints, headaches and swollen glands. All of these symptoms are vague and non-specific, with each being more likely to be caused by a number of other conditions. The symptoms of most forms of leukaemia could easily be mistaken for those of influenza. [42]

Currently, the diagnosis of all forms of leukaemia involves complex tests carried out by trained and experienced clinical staff [44]. The prognosis and treatment for each of the subtypes can vary significantly so it is imperative that myeloid leukaemia be distinguished from lymphoblastic at diagnosis. Currently there is no single test that can reliably differentiate between the two forms. [45]

The non-specific nature of the symptoms coupled with the technical difficulty in confirming the diagnosis of leukaemia means that the diagnosis can take some time. In the case of acute leukaemia, where the disease can progress over weeks or months, this time may have significant impact upon the chances of survival. It is evident that a simple, fast, low-cost and unambiguous means of diagnosing acute leukaemia would be highly beneficial.

Tanaka *et al.* have shown that the level of miR-92a, and particularly the ratio of miR-92a and miR-638 concentrations, in plasma has great potential as a biomarker for AML and ALL [46]. By analysing the expression of 148 different miRNAs in the plasma of patients suffering from AML and ALL they were able to observe that the relative expression of miR-92a was significantly reduced in sufferers of acute leukaemia. They found that the ratio of miR-92a/miR-638 expression was decreased in all AML and ALL patients compared to healthy controls, with the average expression ratio differing by greater than 10-fold between the two. Clearly there is potential for a simple, fast, low-cost and unambiguous test for acute leukaemia based on a miRNA sensor.

Furthermore, Mi *et al.* have shown that by measuring the expression of as few as two miRNAs it is possible to reliably differentiate between AML and ALL [45]. They conducted a large-scale miRNA expression analysis on miRNAs extracted from cell-lines from acute leukaemia patients and identified 27 miRNAs that exhibited differential expression between AML and ALL. Numerical analysis has shown the four miRNAs that offer the most discriminatory potential between AML and ALL. MiR-128a and miR-128b were significantly over-expressed in ALL samples compared to AML samples and miR-223 and let-7b¹ were significantly under-expressed in ALL samples compared to AML samples. It was found that by measuring the expression of various combinations of these four miRNAs, successful discrimination between AML and ALL patient samples could be achieved with an overall accuracy of at least 97%. These miRNAs could form the basis of a simple, fast and low-cost test for differentiating between subtypes of acute leukaemia.

¹The let-7 family were amongst the first miRNAs ever discovered. As such they were named before a naming convention was established for miRNAs and do not follow the standard format.

1.2 The challenges of microRNA detection

The sensitive, specific and rapid detection of oligonucleotides presents many technical challenges. However, there are several additional challenges particular to the detection of miRNAs. The fact that a single miRNA can be associated with several diseases or conditions renders a degree of potential ambiguity unto any diagnostic tool that relies upon the measurement of the concentration of a particular miRNA. A way to combat this would be to construct arrays of many sensors – each designed to target a different, specific miRNA – and thus measure the concentration of several miRNAs associated with a given disease simultaneously. This multiplex approach to detection will likely be a critical capability of any future miRNA detection technology. These arrays could be small (of the order of tens of sensors) for single diseases or conditions, or large (of the order of hundreds of sensors) for multiple diseases. The use of pattern recognition techniques could further reduce any potential ambiguity.

An additional challenge for miRNA detection is the fact that many miRNAs can be very similar. For instance, the let-7 family of miRNA contains several members; the 5¹ branch of which are shown in Table 1.1. These miRNAs are very similar in sequence, varying between six and only a single nucleotide of difference. Therefore any miRNA sensor will need to have sufficient specificity to be able to detect single-base mismatches. MiRNAs from different families will usually have little similarity. It should be noted that the let-7 family is unusual; few miRNAs have such large families.

The short length of miRNAs makes it difficult for them to be analysed using many

¹5' and 3' (or 5-prime and 3-prime) are the terminologies for the respective ends of nucleotide sequences.

The 5' end is terminated by a phosphate group, on the 5th carbon from the base, whereas the 3' end is terminated by a hydroxyl group, on the 3rd carbon from the base.

miRNA	Nucleotide Sequence	Number of differences
let-7a-5p	UGA GGU AGU AGG UUG UAU AGU U	-
let-7b-5p	UGA GGU AGU AGG UUG UGU GGU U	2
let-7c-5p	UGA GGU AGU AGG UUG UAU GGU U	1
let-7d-5p	AGA GGU AGU AGG UUG CAU AGU U	2
let-7e-5p	UGA GGU AGG AGG UUG UAU AGU U	1
let-7f-5p	UGA GGU AGU AGA UUG UAU AGU U	1
let-7g-5p	UGA GGU AGU AGU UUG UAC AGU U	2
let-7i-5p	UGA GGU AGU AGU UUG UGC UGU U	4

Table 1.1: The 5' branch of the let-7 family. Differences in their nucleotide sequences, when compared to let-7a-5p, are shown in red. Adapted from Driskell *et al.* [49].

conventional oligonucleotide sensing techniques. For instance, the size of miRNAs makes it very difficult to design effective primers (themselves usually *ca.* 20 nucleotides long) for polymerase chain reaction (PCR) amplification. For this reason PCR based methods are often applied to miRNA precursors, from which miRNA expression is inferred. The small size of miRNA also severely limits options when designing capture probes for microarrays, or other approaches for which capture probes are critical. [47, 48]

The melting temperature (T_m) of an oligonucleotide duplex will depend on several factors, but a significant factor will be the ratio between G and C to A and T (or U) bases. The GC content of miRNAs can vary widely, resulting in a broad range for T_m . The melting temperature of a given oligonucleotide is the temperature at which its single-stranded and double-stranded states exist at equal concentration. Above T_m a duplex will mostly be ‘unzipped’ whereas the opposite will be true below T_m . Thus at a given temperature, the efficiency of any hybridisation-based miRNA detection method may vary significantly from one miRNA to the next. The short length of miRNAs is again an issue here as one of the most common methods for compensating for this problem in conventional oligonucleotide detection techniques is to vary the lengths of

capture probes so as to produce a more uniform T_m distribution. This is not an option with short sequences such as miRNA. [48, 50]

MiRNA represents a very small fraction of the total RNA content of a cell (of the order of 0.01%), placing great demands upon the sensitivity required from any detection technique [51]. Also, the expression of miRNAs within cells can vary by several orders of magnitude from miRNA to miRNA [35], and in the case of disease the expression of particular miRNAs can be altered by many times their normal value [52–54]. This means that for a miRNA detection technology to be useful for diagnostic or prognostic purposes it must be highly sensitive and have a large dynamic range.

Depending on the source from which the testing miRNAs are obtained and the method of extracting them from biological samples, any miRNA detection technique may have to be able to differentiate between miRNA and pre- and pri-miRNA, which contain identical nucleotide sequences, or else risk a significant source of interference. [48]

In order to fully exploit the potential offered by miRNA as a new source of biomarkers it will be highly desirable to move any future miRNA detection technology away from large centralised labs and towards point-of-care (PoC) applications. In order for this to occur, a miRNA detection technology that is both simple and low-cost will be necessary. Additionally, it is highly desirable for any technology to return useful results in a timescale of minutes rather than days. Also, in order to be applicable for PoC applications, any miRNA detection technology will need to be able to return useful results from small volumes of sample material, collected in a non-invasive manner. In the words of Yendamuri *et al.* “future directions in early diagnosis likely will be spearheaded

by technological advancements that will enable reproducible measurements of samples with small input material.” [55]

1.3 Oligonucleotide detection – the state of the art

Virtually all oligonucleotide detection techniques exploit the hybridisation mechanism of oligonucleotides. Hybridisation is the process by which an oligonucleotide will bind to its corresponding oligonucleotide strand, via hydrogen bonds between bases, to form a duplex. This mechanism is highly specific and energetically favourable at low temperatures (*i.e.* $\leq 30^{\circ}\text{C}$). Hybridisation is exploited by using synthesised oligonucleotides either as: capture probes (oligonucleotides, complementary to the target, that are bound to the surface of a sensor or substrate); label probes (complementary oligonucleotides, free in solution, that are bound to label molecules such as fluorophores or enzymes); or primers, in the case of PCR-based methods (see Section 1.3.1.3).

1.3.1 Established oligonucleotide detection techniques

Current miRNA detection and quantification techniques can be subdivided into indirect and direct methods. Indirect methods (such as microarrays), require that the target miRNA be modified (usually via labelling) prior to detection. Whilst this greatly increases the sensitivity of many methods, it increases the complexity and the detection time. Also, modification can lead to inaccuracy as the efficiency of the modification reactions can differ from miRNA to miRNA. In contrast, direct detection methods

operate using unmodified target miRNA. Some direct detection methods exist (such as northern blotting) but are generally ill-suited to multiplexing. [56, 57]

Additionally, current miRNA detection techniques can be sub-divided into solution phase and solid phase techniques. In solution phase the hybridisation step takes place in solution (such as with qPCR) whereas in solid phase techniques either the probe or the target strand is immobilised on a solid surface prior to hybridisation (examples include northern blotting and microarrays). Solution phase methods are generally faster (as a result of a greater degree of interaction resulting from more degrees of freedom) whereas solid phase techniques are generally better suited to high-throughput analysis. [48]

Some of the most high-profile established miRNA detection techniques will be outlined in the following sections. This selection is not exhaustive, but represents the most commonly used techniques in the field.

1.3.1.1 Northern blotting

Northern blotting is one of the oldest of the current methods for miRNA detection and expression analysis. It consists of four steps, outlined in Figure 1.4, by which the RNA is extracted from the sample, separated using electrophoresis and identified using labelled probes. The technique was developed in the 1970s and was used in the discovery of the very first miRNAs [48, 58, 59]. The relative strengths and weaknesses of northern blotting are summarised in Table 1.2.

Technique		
Northern blotting	Strengths	Established technique Direct Standardised Quantitative
	Weaknesses	Low sensitivity Slow Labour intensive Not multiplex Requires large input sample Restricted to centralised labs
	LoD TTR	nM – pM >1 day
Microarrays	Strengths	Established technique Multiplex High throughput Simple working principle
	Weaknesses	Low sensitivity Semi-quantitative Slow Low specificity (compared to qPCR) Restricted to centralised labs
	LoD TTR	nM – pM >1 day
qPCR	Strengths	Established technique High sensitivity High specificity Quantitative Multiplex
	Weaknesses	Limited throughput Complex High cost Detailed data analysis required Restricted to centralised labs Only useful for measuring miRNA precursors
	LoD TTR	fM – aM ~1 day

Table 1.2: Strengths and weaknesses of established miRNA detection techniques, along with typical limit of detection (LoD) range and time-to-results (TTR). [35, 50, 58, 60–63]

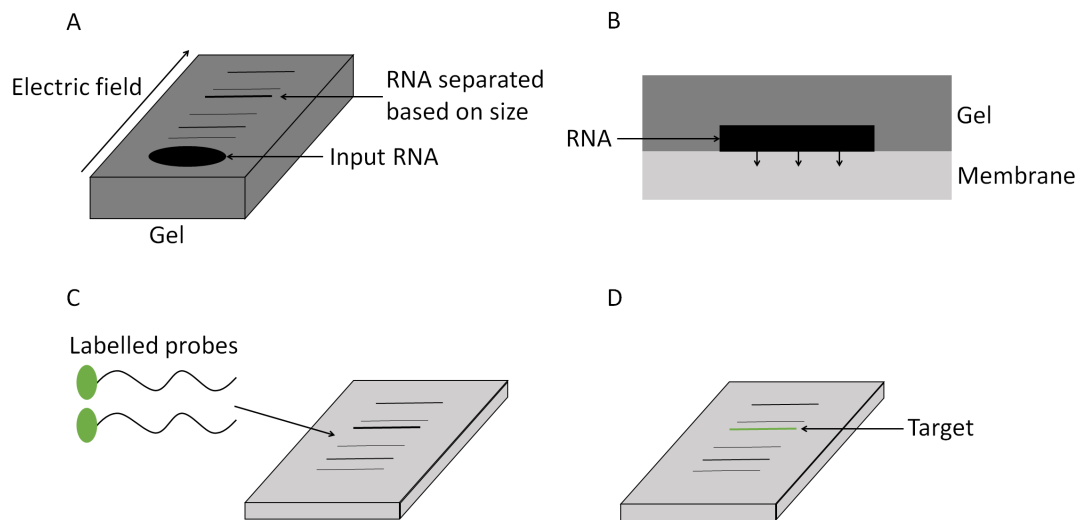


Figure 1.4: Illustration of the steps involved in northern blotting. (A) the unknown RNA sample is separated using gel electrophoresis, (B) the RNA is 'blotted' onto a membrane, (C) labeled nucleotide probes are introduced to the membrane, (D) the membrane is scanned to identify the RNA sequence of interest. Adapted from Conzone *et al.* [59].

1.3.1.2 Microarrays

Perhaps the most common method of analysing large numbers of different miRNAs is that of miRNA microarrays. In a miRNA microarray a complementary DNA (cDNA) capture probe is immobilised in a microdot on a reactive glass surface (Figure 1.5) [58]. The arrays can consist of thousands of such dots, with each dot containing of the order 10^{-12} moles (mol) of a different capture probe [64]. The miRNA to be analysed is then extracted from the relevant source and labelled with fluorescent molecules before being introduced into the array. The capture probes will then hybridise with their respective analyte strands. After rinsing off any un-hybridised oligonucleotides, the array can then be scanned with a laser excitation source and the relative fluorescence intensity of each probe spot will allow the determination of the relative abundance of the target miRNA of that particular probe [59]. The relative strengths and weaknesses of miRNA microarrays are summarised in Table 1.2.

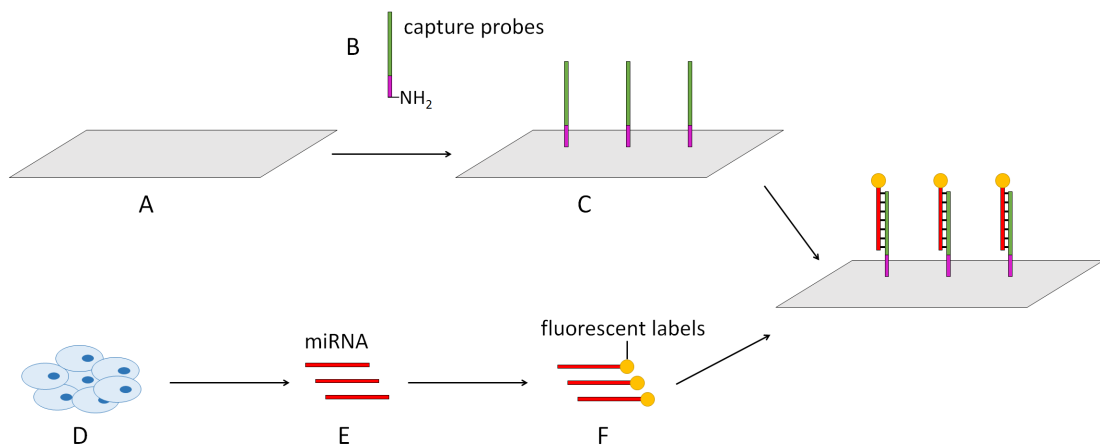


Figure 1.5: The principle behind microarray-based miRNA profiling. It begins with (A) an amine-reactive glass surface, on to which (B) amine-modified oligonucleotide probes are covalently bound to form an element of the array (C). The probes consist of a 'linker' sequence (purple) and a capture sequence (green), the capture sequence is complementary to the target miRNA. MiRNAs are extracted from the sample and labelled with fluorescent molecules (D-F) before being introduced into the array and hybridising with the probes. Each probe site can then be queried with a laser and the relative abundance of each miRNA determined. Adapted from Li *et al.* [58].

1.3.1.3 Quantitative PCR

The polymerase chain reaction (PCR) is a technique for amplifying specific DNA sequences. By combining the initial oligonucleotide sample, carefully designed primers (short oligonucleotide sequences corresponding to the 'beginning' and 'end' of the target sequence), the enzyme *DNA polymerase*, sufficient quantities of the nucleotide building blocks and cycling the temperature, it is possible to exploit DNA's own self-replication mechanism to exponentially amplify the quantity of the target oligonucleotide. [65]

By incorporating fluorescent probes that selectively bind to double-stranded DNA, it is possible to determine the quantity of the target sequence at each repetition of the amplification cycle. Using this data it is possible to infer the starting quantity.

This variation of PCR is known as real-time qPCR¹ [66]. PCR was developed for

¹Not to be confused with reverse transcriptase qPCR (RT-qPCR) a variant for quantifying RNA as opposed to DNA.

DNA amplification but it is applicable to RNA with the incorporation of a reverse transcription step, by which the sample RNA is converted into DNA [47, 67, 68]. The relative strengths and weaknesses of qPCR for the detection and quantification of miRNA are summarised in Table 1.2.

Whilst kits for performing northern blotting [69], microarray analysis [70] and qPCR [71] are commercially available, these are intended for laboratory use and are not suitable for non-specialist users. Additionally, there are some commercially available qPCR tools that are advertised as ‘point-of-care’; such as the Palm PCR [72], Serigene [73] and Freedom4 [74] technologies. However, these technologies, whilst they may reduce the total procedure time, the number of steps involved and the power requirements, do not address the complex data analysis and high reagent costs which limit the application of qPCR to use by specialists in a laboratory setting.

We have seen from the preceding sections that whilst there are several well-established techniques for the detection and quantification of specific miRNAs, there is no single technique that offers a high degree of sensitivity, a capacity for high-throughput testing and a capacity to conduct tests on many different miRNAs simultaneously (multiplex testing). This lack is a significant obstacle to the exploitation of miRNAs as biomarkers for disease and there are currently many avenues of research being pursued in the hopes of overcoming these shortcomings. Some examples of areas of oligonucleotide detection currently being researched will be outlined in the following section.

1.3.2 Emerging oligonucleotide detection techniques

There is much research underway to address the shortcomings of existing miRNA detection techniques, to attempt to meet the challenges discussed in Section 1.2 and to develop simple, sensitive, low-cost and rapid techniques for oligonucleotide detection. The following sections offer a brief introduction to some of the most high profile examples of such emerging techniques. These sections do not represent an exhaustive review, rather an overview of the field. Emphasis is given to techniques that have potential for rapid, PoC oligonucleotide detection.

1.3.2.1 Optical techniques

Optical techniques are amongst the most common forms of transduction in oligonucleotide detection, largely due to their use in the established detection techniques of microarrays and qPCR. Fluorescent probes are widely used in the field of oligonucleotide detection, with perhaps their most notable application being in microarrays. However, some of the limitations of current fluorescence-based approaches (such as quenching, background radiation and auto-fluorescence [60, 63]) have inspired research efforts to develop new probes and labelling techniques, with the aim of achieving improvements in sensitivity, efficiency or other areas of performance.

A notable example of alternative probe design are molecular beacons (MBs). These use capture probes with a hairpin configuration (Figure 1.6) and fluorescence resonant energy transfer (FRET) – also known as Förster resonance energy transfer – such that the fluorescence emission of these probes will vary dramatically in the presence of the

analyte [75]. A particular strength of MBs is that they remove the need to label the analyte oligonucleotides, in effect changing the detection from an indirect to a direct transduction method. [50, 60, 63]

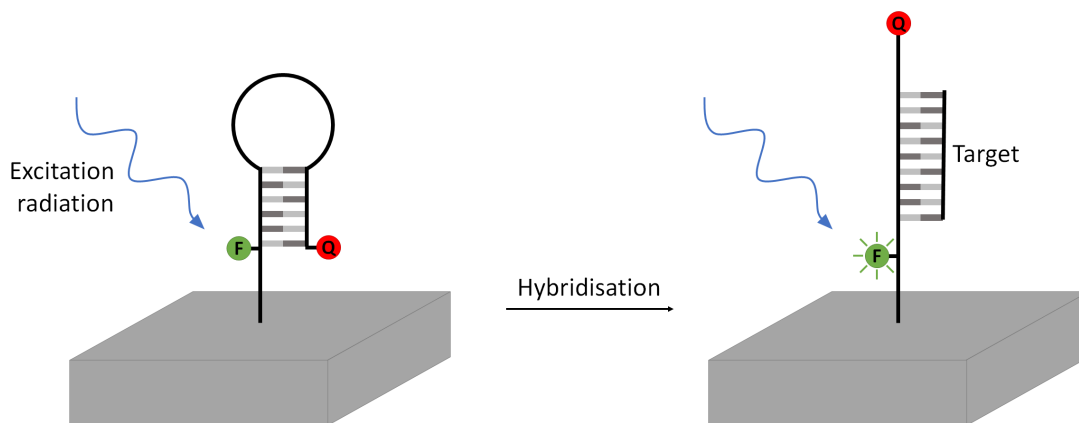


Figure 1.6: Illustration of the form and mechanism of molecular beacons. Initially the beacon is in a hairpin configuration, meaning that the fluorophore and the quenching molecule are in close proximity and that any fluorescence is quenched (left). Upon introduction of the target oligonucleotide the beacon straightens, increasing the separation between the quenching molecule and the fluorophore and thus allowing fluorescence to take place (right). Adapted from Sassolas *et al.* [75].

In order to overcome the issues with fluorescent probes that result from the requirement for excitation light-sources, a variety of non-fluorescent optical probe technologies have been developed. Chemiluminescent (CL) labelling involves labelling the target oligonucleotide with probes that will undergo a chemical reaction that emits light [75]. Bioluminescent (BL) labelling is very similar to CL labelling, only utilising light emitting proteins as the label molecules [8]. Electrochemiluminescent (ECL) labelling – also known as electrogenerated chemiluminescence – is a variation of CL labelling wherein, rather than being initiated by a chemical reactant or catalysed by an enzyme, the light-emitting reaction is initiated by the application of an electric potential [76,77].

Non-fluorescent probes minimise the background radiation and the potential for any interference as they do not require light sources for excitation. However they require

a variety of additional labelling processes which will increase the overall complexity of the system and potentially introduce inefficiencies into the production process.

Other forms of optical oligonucleotide detection, not dependent upon fluorescent or luminescent labels, include approaches such as surface-enhanced Raman spectroscopy, dual polarisation interferometry and surface plasmon resonance based techniques. However, these are less common and are generally more expensive and complex. [48, 62, 75, 78]

A summary of the limits of detection of the various forms of optical oligonucleotide detection discussed here are shown in Table 1.3.

Optical Techniques	Limit of Detection
Fluorescence	200 fM - 10 nM
Chemiluminescence	500 fM - 1 nM
Bioluminescence	1 fM - 20 nM
Electrochemiluminescence	30 fM - 10 nM
SPR	100 fM - 2.5 nM
Overall	1 fM - 20 nM
Electrochemical Techniques	
Enzyme label	100 aM - 100 nM
Ferrocene	370 aM - 2 nM
Intercalators	1 pM - 170 nM
Groove binders	80 pM - 90 pM
Metal nanoparticles	5 pM - 1 nM
Label free	50 pM - 4 nM
Overall	100 aM - 170 nM
MEMS/NEMS-based Techniques	
Bulk acoustic wave (BAW)	74 aM - 50 nM
Surface acoustic wave (SAW)	1 pM - 30 nM
Cantilever	2 aM - 75 nM
GeneFETs	100 fM - 10 μ M
Nanowires	1 aM - 2 nM
Nanopores	1 fM - 1 nM
Overall	1 aM - 10 μM

Table 1.3: Summary of limits of detection of emerging oligonucleotide detection techniques [8, 62, 75, 79, 80]. This selection is not exhaustive.

1.3.2.2 Electrochemical techniques

Electrochemical transduction mechanisms are very attractive for oligonucleotide sensing as they offer a simple, compact and low-cost means of measuring any output signal – when compared with the expensive and bulky equipment required for optical transduction. Additionally, the fact that they have a direct electrical output makes them easy to integrate into any overarching sensor hardware.

Perhaps the simplest way to detect oligonucleotides electrochemically is to bind capture probes to the surface of an electrode and measure (either by amperometric or voltammetric means, or via electrochemical impedance spectroscopy (EIS)) any changes that result to the reduction-oxidation (redox) potential as a result of hybridisation. The binding of an enzyme labelled oligonucleotide to a capture probe at an electrode surface will dramatically alter the redox potential of the electrode [75]. However, the labelling of the target oligonucleotides with enzymes is complex, potentially inefficient and can introduce errors into the final measurement. An common alternative to enzyme labelling is the use of electroactive ferrocene labels. [80]

A common method of detecting oligonucleotide hybridisation via electrochemical means is by the use of electroactive substances, such as intercalators or groove binders, which interact differently with single-stranded DNA as opposed to double-stranded DNA. Such probes will bind to DNA only where hybridisation has occurred, thereby only bringing their redox-active components to the electrode surface when the target oligonucleotides are present [75, 81, 82]. Intercalators and groove binders are attractive for oligonucleotide sensing as they are direct. However, they are disadvantageous in that

they will have poor specificity as they may be unable to distinguish between complete and partial complementarity.

Another method of electrochemical oligonucleotide detection involves the use of metal nanoparticle labelled probes [83–88]. Metal nanoparticles can be used to amplify a signal from the hybridisation of analyte oligonucleotides at the electrode surface by enabling the deposition of metal at the electrodes via techniques such as catalytic deposition or electrochemical reduction. While such techniques can be used for sensitive and specific oligonucleotide detection, the requirement for additional processes and reagents adds complexity.

There are also electrochemical techniques that do not rely on redox-active labels [89–95]. However, while such techniques may be less complex, they are generally less sensitive.

A summary of the limits of detection of the various forms of electrochemical oligonucleotide detection discussed here are shown in Table 1.3.

1.3.2.3 Microelectromechanical systems based techniques

Advances in microfabrication technology have allowed for potential oligonucleotide detection techniques to emerge from the fields of microelectromechanical systems (MEMS) and nanoelectromechanical systems (NEMS). MEMS and NEMS are three-dimensional devices fabricated on the micrometre or nanometre scale respectively¹, leading to the possibility of micro- or nano-scale oligonucleotide sensors. Examples

¹There are considerable areas of overlap between MEMS and NEMS and it is not uncommon to see both fields conflated into ‘MEMS’.

include; bulk acoustic wave (BAW) [96] and surface acoustic wave (SAW) [97] devices, microcantilevers [98], gene field-effect transistors (gene-FETs) [99], nanowire [100] and nanopore [4] sensors. Such sensors offer the benefits of having sensing elements of similar order of magnitude of size as the analyte, which include increased sensitivity and fast response times. Additionally the fact that they are fabricated using techniques from the microelectronics industry gives advantages such as reduced cost due to batch processing, high reliability, direct electrical output, portability and easy incorporation with modern electronics. The principle disadvantage of such systems is the potentially complex fabrication processes.

Technologies such as Ion Torrent [101], which are primarily applied to sequencing rather than oligonucleotide detection and whose use is limited to laboratories, are not discussed here.

A full discussion of MEMS-based oligonucleotide sensors is provided in a review that has been published by the author in [79]. A summary of the limits of detection of the various forms of MEMS-based oligonucleotide detection are shown in Table 1.3.

1.4 Oligonucleotide cross-linked polymer composites

The preceding sections described established and emerging technologies for oligonucleotide detection and outlined the relative strengths and weaknesses of these approaches. The following sections will introduce OCPCs, which are proposed as a potential new form of simple, rapid and low-cost oligonucleotide detection.

1.4.1 The swelling of hydrogels

Hydrogels are hydrophilic macromolecular structures that are insoluble in water. By definition they contain high proportions of aqueous solvent to polymer in their swollen state, containing as much as 90-99% of water by weight [102–106]. Hydrogels are attractive for biosensing applications for many reasons: they can provide three-dimensional environments for bio-molecular interactions; they can undergo significant and abrupt volume changes in response to external stimuli; biological molecules can be incorporated into the structure of hydrogels; the highly porous nature of hydrogels means that analytes can diffuse rapidly into the network; many hydrogels are inert and resistant to bio-fouling; and the mechanical properties of hydrogels can be adjusted by altering parameters such as the cross-link density. [104, 105, 107, 108]

In any given cross-linked polymer, between the randomly arranged molecules there exists a significant proportion of free-space, referred to as the free volume of the polymer. When introduced to a compatible solvent (water, in the case of hydrogels) the much smaller solvent molecules will diffuse into the free volume, causing it to expand and the polymer to swell. Eventually an equilibrium will be reached between the inward force, caused by the tendency of the chains to coil up, and the outward force, caused by tendency of the solvent to diffuse into the network, resulting in the polymer achieving an equilibrium volume. [109]

The swelling of hydrogels can be considered either on the micro- or the macro-scale. According to Ganji *et al.*, on the micro-scale the swelling can be described in terms of the mean molecular weight of polymer chains between cross-links, and the molecular

mesh size, which is the average distance between cross-links [106]. Thus in this model, excluding constants, the swelling of hydrogels are governed solely by terms that are dependent upon the cross-link density.

Considering hydrogel swelling on the macro-scale, a full theoretical model of polymer swelling has been developed by Tanaka *et al.* [110]. Under this model, it has been shown that the rate of swelling depends only upon the final radius of the polymer and the diffusion coefficient. Thus the principle swelling characteristics of hydrogels are dependent upon the cross-link density.

1.4.2 Oligonucleotide cross-linked polymers

Many examples of oligonucleotide-functionalised hydrogels (hydrogels with strands of DNA incorporated into their macromolecular structure) have been reported [111–114]. By synthesising hydrogels where the cross-links are formed from oligonucleotide sequences, it is possible to create hydrogels that will undergo the gel-sol transition (the transition between the gel phase and the solution phase) in the presence of specific oligonucleotide sequences. Such hydrogels have been demonstrated as a means of the controlled release of small molecules [115], quantum dots [116] and proteins [117], and have been proposed as a means of delivery for cancer drugs [115,118].

Oligonucleotide-functionalised hydrogels have also been developed for sensing applications. Liu *et al.* have developed functionalised hydrogel scaffolds for DNA probes for optical sensing techniques [119,120]. Li *et al.* have developed oligonucleotide-functionalised hydrogels for the selective capture of circulating tumor cells [121] and Liu *et al.* have

developed similar hydrogels for the detection and extraction of mercury ions from water [122]. Chan *et al.* have developed oligonucleotide-functionalised hydrogels for the selective capture and concentration of oligonucleotide sequences in gel electrophoresis. [123]

Whilst the aforementioned applications of oligonucleotide-functionalised hydrogels exploit many of the advantageous characteristics of hydrogels described previously, they do not exploit the swelling behaviour. In the work of Stokke *et al.*, selectively swelling hydrogels are created by incorporating oligonucleotide cross-linkers into the structure of a polymer hydrogel [124,125]. To accomplish this, three components (in an aqueous solution) are co-polymerised in a UV-initiated free-radical polymerisation to produce a water-impregnated hydrogel. These three components are: an acrylamide monomer, ‘conventional’ bis(acrylamide) cross-linkers and nucleic acid cross-linkers consisting of two, partially complementary, single-stranded DNA sequences. Each of the nucleic acid sequences is terminated with a chemical modifier, Acrydite (Figure 1.7), which participates in the polymerisation reaction, thereby anchoring the nucleic acids into the hydrogel network. [126,127]

Of the two nucleic acid cross-linkers, one – the sensing strand (Figure 1.8) – is perfectly complementary to the target oligonucleotide, whilst the other – the blocking strand – is partly complementary to the sensing strand and partly a random sequence of nucleotides. Upon the introduction of the target oligonucleotide, it will bind preferentially with the sensing strand, displacing the blocking strand (Figure 1.9). Thus the oligonucleotide cross-links will be broken, reducing the overall cross-link density of the hydrogel and significantly altering its swelling characteristics. It is important to

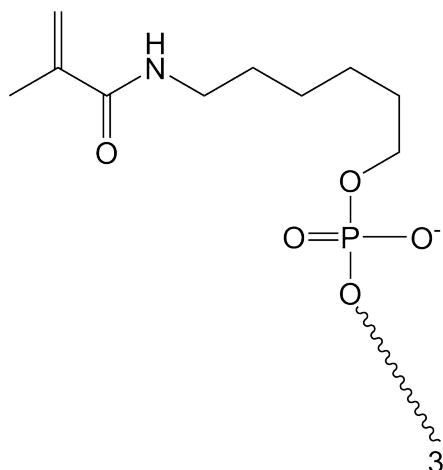


Figure 1.7: Chemical structure of Acrydite. The wavy line represents the oligonucleotide to which it is attached. The C-C double bond allows the group to be integrated into the polymer structure during polymerisation, thereby anchoring the oligonucleotide in place.

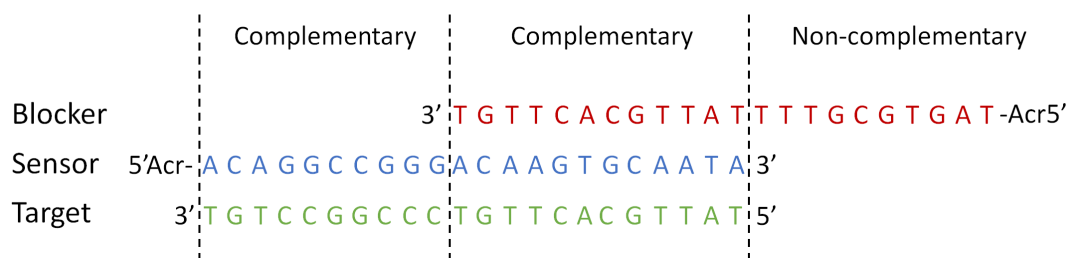


Figure 1.8: An example of oligonucleotide cross-linkers for which the link will break in the presence of a target oligonucleotide and their respective complementarity. The different regions of complementarity are delineated by the vertical dashed lines. 'Acr' represents the Acrydite modification by which the oligonucleotides are incorporated into the polymer structure.

note that the swelling response occurs as a result of the uptake of the supernatant fluid (in this case water). As the target will be in an aqueous medium, the potential for swelling will be significant. This dramatically increases the potential sensitivity of the system to the breaking of a single cross-link. Additionally, this approach is attractive as it is direct and, whilst having the advantages of a solid-phase approach, incorporates the sensing strands into a three-dimensional structure. [104]

The resultant hydrogels can be modified by altering the cross-link to monomer concentration ratios. Increasing the bis(acrylamide) content will produce a more rigid

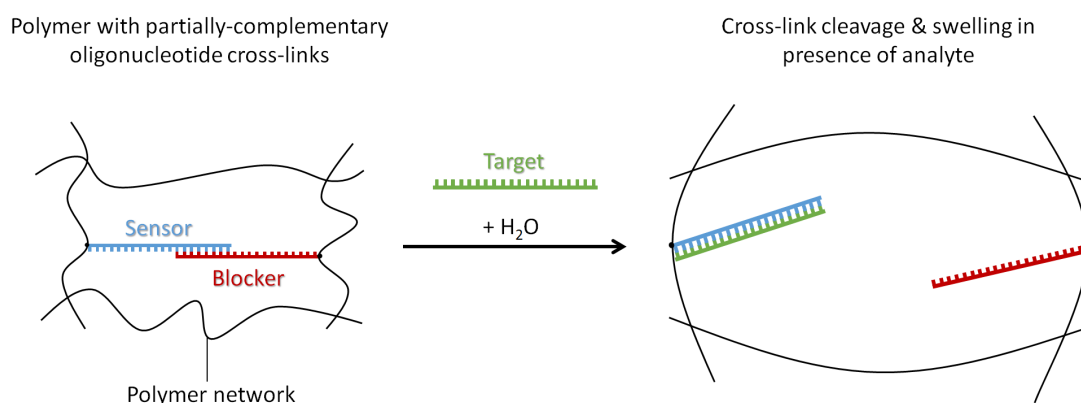


Figure 1.9: Illustration of the swelling response of an oligonucleotide-functionalised hydrogel upon introduction of the target strand. The sensing (blue) and blocking (red) strands form a partially complementary oligonucleotide cross-link (left). Upon the introduction of the target strand (green) the cross-link is broken as the target will hybridise more favourably with the sensing strand (right). This causes the cross-link density to change, thus changing the swelling characteristics of the hydrogel. Adapted from Gao *et al.* [125].

hydrogel with a smaller swelling response. Increasing the oligonucleotide cross-link content will produce a hydrogel with a greater range of swelling responses, but may also decrease the rate of swelling for a given concentration of analyte. [124]

Thus it is possible to synthesise polymers whose swelling behaviour will vary significantly in the presence of a given analyte oligonucleotide. However their utility as a sensing mechanism is wholly dependent upon the transduction of this swelling.

1.4.3 The transduction of hydrogel swelling

There are many existing techniques for transducing and measuring polymer swelling. They can be broadly grouped into several categories which will be outlined in the following sections.

1.4.3.1 Mass sensitive transduction

Perhaps the most obvious way of measuring the swelling of any polymer would be to measure the resultant change in mass. This is relatively simple at large scales (of the order of grams) but becomes more challenging at the smaller scales required of polymer-based sensors. One of the most common methods of achieving small-scale mass measurement is that of BAW devices. These function by detecting the effect of the changing mass of the polymer upon the oscillation of a piezoelectric substrate.

BAW devices have been applied to the transduction of the swelling of pH sensitive hydrogels [128–130] and to the transduction of virus-responsive hydrogels [131]. The advantages of mass sensitive transduction are that it is simple and direct. The disadvantages are that it can be challenging to implement BAW measurement in complex liquid media. [79, 132]

1.4.3.2 Optical transduction

Optical techniques are ubiquitous in the measurement of polymer films and perhaps the most common technique is that of interferometry. Stokke *et al.* have adapted this technique for hydrogel droplets immobilised on the end of an optical fibre, and applied it to glucose [133–135] and DNA [124] responsive hydrogels.

Other optical approaches to the transduction of hydrogel swelling include Bragg diffraction approaches, such as those developed by Asher *et al.* for a range of ion-responsive hydrogels [136], and microlens approaches, such as those developed by Kim *et al.* for antibody cross-linked hydrogels. [137, 138]

Optical techniques for the transduction of hydrogel swelling are advantageous as they can be highly sensitive and they employ techniques and equipment that are widely used. However, disadvantages include the fact that they require optical sources and detectors which can be expensive and bulky. [132]

1.4.3.3 Micromechanical transduction

Advances in the field of microfabrication have led to the development of MEMS devices that can be applied to the transduction of hydrogel swelling. Hydrogels can be synthesised inside microfabricated chambers incorporating piezoresistive pressure sensors, allowing the swelling of the hydrogels to be measured [139–141]. Herber *et al.* have used this approach to create a CO₂ sensors by transducing the swelling of pH sensitive hydrogels. [142]

Another approach to the MEMS-based transduction of polymer swelling involves microcantilevers. Peppas *et al.* have developed microcantilever sensors based on the transduction of the swelling of pH sensitive hydrogels [143, 144] and Zhang *et al.* have developed chromate ion sensors based on a similar approach [145]. More details on cantilever-based sensors can be found in Ferrier *et al.* [79]

The MEMS-based transduction of hydrogel swelling is attractive because of the small size, durability, sensitivity and low power consumption of MEMS devices [79, 132]. However, the potentially complex fabrication processes are disadvantageous.

1.4.4 Conductive polymer composites

Combining two or more materials with differing physical or chemical properties can produce materials that have properties different to their constituent parts. Such materials are referred to as composites. Conductive polymer composites generally consist of a conductive component, such as a conductive metal powder or intrinsically conductive polymer, mixed into a non-conductive polymer matrix. The ability to impart conductive properties to otherwise non-conducting polymers has many uses and applications and consequently conductive polymer composites have attracted much attention over the course of several decades. Conductive polymer composites have been developed for applications ranging from batteries and fuel cells [146] to drug delivery [147], to neuroscience and sensors [148–150].

Metal powders such as nickel, copper and gold can be used to produce conductive polymer composites, but it is also common to use carbon black or other conductive forms of carbon, which, although they possess lower conductivities than metal powders, are attractive due to their ready availability and low cost. [150, 151]

An alternative means of creating electrically conductive composites is to use intrinsically conductive polymers as the conductive component. Conductive polymers such as polypyrrole (PPy), polyaniline (PANI) or poly(3,4-ethylenedioxythiophene) (PEDOT) can be incorporated into non-conductive polymer matrices, either in the form of nanoparticles or fibres [152–156] (similar to conductive powders) or through the *in situ* polymerisation of the conductive polymers within pre-existing hydrogel matrices to

form conductive networks [148,149,157]. However, such intrinsically conductive polymer based composites are outwith the scope of this thesis.

Factors affecting the conductivity of a composite will include the size distribution and morphology of the conductive particles, but the most significant factor will be the concentration of the particles within the polymer matrix. Percolation theory tells us that conductivity within a conductive polymer composite is the result of a three-dimensional network of conductive pathways of interconnecting conductive particles within the polymer matrix, a situation referred to in this context as ‘percolation’ [150]. Modifications of percolation theory, such as general effective medium (GEM) theory (discussed later in this section), describe the conductivity of such composites. If the concentration of the conductive particles is low, they will not be close enough to one another to form conductive pathways, and the resultant conductivity of the composite will be low. Conversely, if the concentration of the conductive particles is high, there will be many conductive pathways and the conductivity of the composite will be high. Somewhere in between these two cases, there will be a point where the conductive particles are at a concentration that allows them to be just close enough to interact and form conductive pathways. At this point the overall conductivity of the composite will change rapidly as it transitions between the low and high conductivity regimes. This critical point is known as the percolation threshold. [150,158–162]

At concentrations away from the percolation threshold the rate of change of conductivity will be relatively small as adding or removing conductive particles will make relatively little difference to the overall conductivity. This behaviour leads to the char-

acteristic sigmoidal shape of so-called percolation curves, an example of which is shown in Figure 1.10.

It should be noted that the conductive particles do not necessarily need to be in direct contact in order to form conductive pathways. Effects such as quantum tunneling mean that conduction can occur when the particles are in close proximity, however this is heavily dependent upon the morphology of the particles. [162]

The effective conductivity of a composite consisting of high conductivity particles in a low conductivity matrix can be described by the GEM equation [164]:

$$\frac{f(\Sigma_l - \Sigma_m)}{\Sigma_l + [f_c/(1 - f_c)]\Sigma_m} + \frac{(1 - f)(\Sigma_h - \Sigma_m)}{\Sigma_h + [f_c/(1 - f_c)]\Sigma_m} = 0 \quad (1.1)$$

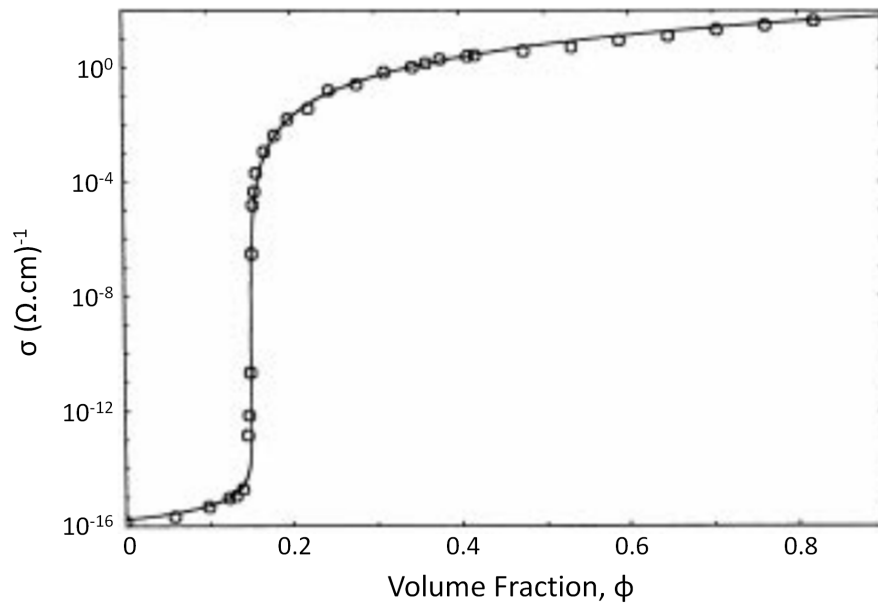


Figure 1.10: Example of a percolation curve for a composite in which the high conductivity component is comprised of graphite micro-particles and the low conductivity component is boron nitride. The experimental data has been fitted to general effective medium theory, the volume fraction, f_c , is 0.85 and the high and low conductivity values, σ_h and σ_l , are $7.39 (\Omega cm)^{-1}$ and $1.38 \times 10^{-16} (\Omega cm)^{-1}$ respectively. [163]

where:

$$\begin{aligned}\Sigma_l &= \sigma_l^{1/t} \\ \Sigma_h &= \sigma_h^{1/t} \\ \Sigma_m &= \sigma_m^{1/t}\end{aligned}\tag{1.2}$$

σ_l is the conductivity of the low conductivity component, σ_h is the conductivity of the high conductivity component and σ_m is the effective conductivity of the resultant composite. The volume fraction of the low conductivity component, f , is sometimes expressed in terms of the volume fraction of the high conductivity component, ϕ , (where $\phi = 1 - f$) and f_c is the critical volume fraction (in effect, the percolation threshold). The value of the exponent t depends on the shape and orientation of the filler particles [165]. The value of t can be determined by fitting experimental data to Equation 1.1.

Equation 1.1 shows that as the volume fraction, f , tends to unity, σ_m will tend to σ_l , and as f tends to zero, σ_m tends to σ_h .

Application of pressure or mechanical deformation will affect the inter-particle separation within a polymer composite, and hence the conductivity [165]. Therefore, if the conductive particles are mixed into a polymer matrix at a sufficient concentration such that they exist in a percolating state when the polymer is in its intrinsic state (Figure 1.11), any swelling from this intrinsic state will result in a reduction in the number of conductive pathways as the relative density of the conductive particles within the polymer matrix decreases and the pathways are broken. This in turn will cause the electrical conductivity of the composite to decrease. If the composite is deposited on appropriate electrodes the changes in conductivity can be easily measured, thus allow-

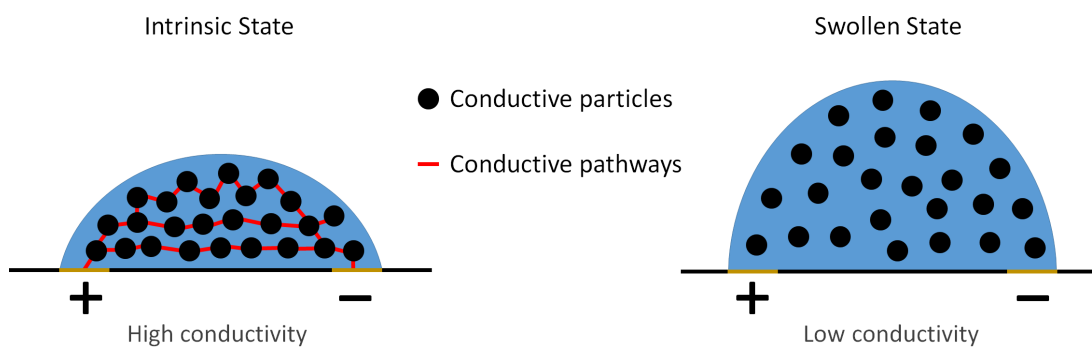


Figure 1.11: Illustration showing the transduction of polymer swelling via changes in the electrical conductivity of conductive polymer composites. As the polymer swells, the conductive pathways formed by the particles are broken, thereby decreasing the electrical conductivity of the composite.

ing for the degree of polymer swelling to be determined. This method of transduction has been applied to electronic nose applications. [166–168]

The investigation of the potential of conductive polymer composites as a transduction mechanism for oligonucleotide cross-linked polymers forms the basis of this thesis. By mixing conductive particles into an oligonucleotide cross-linked polymer (of the type described herein) it is possible to produce an OCPC that will swell selectively in the presence of a given target oligonucleotide, resulting in a significant change in conductivity. Conductive polymer composites were chosen as the transduction method for this work for several reasons: they offer a simple and direct means of transduction; they have the potential to be low-cost and simple to produce; they can potentially be easily deposited upon substrates (*i.e.* via ink-jet printing); and it will be relatively simple to functionalise them for many different targets such that large arrays of many different sensors can be fabricated upon a single device.

1.5 Summary and outline

This chapter has introduced miRNA, its biological origins, structure and function. We have seen that its properties make it an extremely attractive source of potential new biomarkers for disease states, but also present many technical challenges for PoC detection and quantification. There are several existing techniques for miRNA detection but none of these are without their shortcomings and, as such, the full potential of miRNA as a source of biomarkers has yet to be fully exploited. There is a great deal of research being undertaken into new techniques for miRNA detection and quantification, using many different approaches, ranging from fluorescent labelling to MEMS-based devices, each of which have their own strengths and weaknesses.

In this chapter we have seen that hydrogels are attractive materials for biosensing applications. They can swell significantly in aqueous environments and their swelling behaviour is determined largely by their cross-link densities. We have seen that it is possible to synthesise oligonucleotide cross-linked polymers, hydrogels that contain a proportion of oligonucleotide cross-links which will be selectively cleaved in the presence of an analyte oligonucleotide, thereby altering the swelling behaviour of the hydrogel. This chapter also presented a brief overview of existing techniques for the transduction of polymer swelling. We have also seen that it is possible to transduce the swelling of polymers by incorporating conductive particles into the polymer matrix to create conductive composites and by measuring the changes in electrical conductivity that occur with swelling.

As stated previously, the central premise of this thesis is that a new method of miRNA

detection may be achieved through the transduction of the swelling of oligonucleotide cross-linked polymers by incorporating a conductive component to create OCPCs. This technique has the potential to offer simple, rapid and low-cost oligonucleotide detection. Whilst the ultimate aspiration of this work may be miRNA detection, DNA detection is investigated as a first step due to its inherently greater stability [169]. This thesis investigates the creation of OCPCs and their potential application to the detection of short single-stranded DNA sequences.

The structure of this thesis is as follows:

Chapter 2 describes the materials and methods used to create OCPCs and the experiments performed to assess their differential swelling characteristics, electrical properties and their potential as a mechanism for oligonucleotide detection.

Chapter 3 contains the results of the experiments described in Chapter 2 to assess the properties and swelling characteristics of OCPCs, and a discussion of their implications.

Chapter 4 contains the results of the experiments described in Chapter 2 to assess the electrical properties of OCPCs and their potential as a mechanism for oligonucleotide detection.

Chapter 5 introduces nucleic acid analogues, describes the synthesis of morpholino-functionalised polymers and the investigation of their advantageous characteristics as bio-responsive polymers.

Chapter 6 provides a summary of the preceding chapters, a brief discussion of potential avenues for further research and some general concluding remarks.

Chapter 2

DNA-functionalised hydrogels: materials and methods

2.1 Composite preparation

2.1.1 Composite synthesis

Polyacrylamide hydrogels were synthesised via a UV-initiated free radical polymerisation of acrylamide (AAM). These hydrogels were modified by the addition of N, N'-methylene-bisacrylamide (MBA) as a primary cross-linker and Acrydite-functionalised oligonucleotide secondary cross-linkers, so as to produce an interpenetrating network (Figure 2.1). Carbon particles were added to produce a conductive composite. The reaction was initiated using the photo-initiator 1-hydroxycyclohexylphenylketone (HCK). The AAM concentration was 1.41 M, the MBA concentration was varied between 0.4

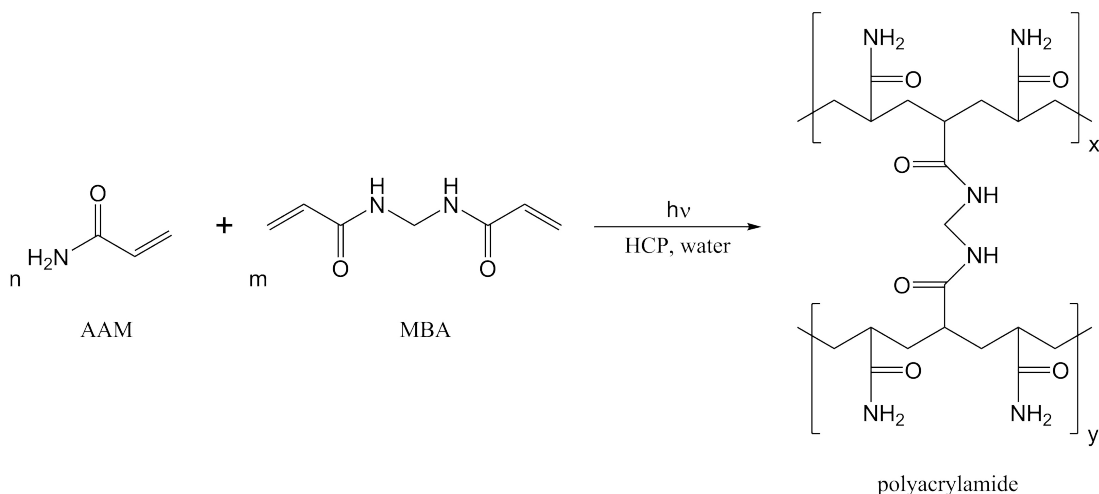


Figure 2.1: The reaction scheme for polyacrylamide synthesis (not including the oligonucleotide cross-linkers).

and 2.0 mol% wrt monomer, the oligonucleotide cross-linker concentration varied between 0 and 0.4 mol% wrt monomer and the HCK concentration was 0.125 mol% wrt monomer. The carbon concentration was varied between 0 and 35 mg/ml. The AAM, HCK and oligonucleotide cross-linker concentrations and the range of MBA concentrations were chosen based on the work of Stokke *et al.* [124, 125]. The range of carbon concentrations was selected based on empirical observations of how much carbon can be added without adversely affecting polymerisation (see Section 3.1.1). Details of all of the chemicals used in this process can be found in Appendix A.

Stock solutions of AAM (2.82 M), MBA (0.2 M) and HCK (0.1 M) were mixed in the appropriate ratios to produce the concentrations described above and then added to the carbon powder (which was dispersed using techniques detailed in Section 2.1.4). The oligonucleotide cross-linkers were added to a concentration of 0.4 mol% wrt monomer by adding 15 μ l of the pre-composite mixture to dried oligonucleotides (prepared as described in Section 2.1.3) and refrigerating the solution at 3°C for 2-3 hours, until the

oligonucleotides are fully dissolved. The carbon is then re-suspended and droplets of this solution are pipetted onto substrates and the polymerisation initiated by exposure to UV radiation.

The AAM and MBA stock solutions were prepared using a 1 mM aqueous phosphate buffer solution (pH 7.4) and the HCK stock solution was prepared using an ethylene glycol solvent [124, 125]. The carbon powder consisted of one of four different particle types: carbon nanopowder (<50 nm), carbon micropowder (2-12 μm), graphite powder (<20 μm) or carbon nanotubes (multiwalled, 10 nm \times 3-6 μm). These particle types were selected so as to provide a variety of particles sizes and aspect ratios. The UV exposure was performed using a Dymax Bluewave 75 UV source with an exposure time of 60 seconds. Full details of the UV source can be found in Appendix A.

2.1.2 Oligonucleotide design

Oligonucleotide cross-linkers consisting of a sensor (S) and blocker (B) strand (Section 1.4.2) as well as analyte and control sequences were designed. The analyte strand (A_0) was designed so as to be a DNA analogue of the microRNA (miRNA) miR-92a (*i.e.* all uracil (U) replaced with thymine (T)), abnormal expression of which in human blood is known to be associated with acute leukaemia [46]. The S strand was designed to be exactly complementary to the analyte sequence (Table 2.1). Using a custom MatLab algorithm, the B strand was designed such that the first 10 bases (from the 5' end) had a random sequence and the remaining 12 bases were perfectly complementary to the final 12 bases of the sensor strand (as shown in Figure 1.8). This 12 base overlap was chosen based on the work of Stokke *et al.* [125]. The S and B strands were both functionalised

Name	Sequence (5' – 3')								
S	Acr-	ACA	GGC	CGG	GAC	AAG	TGC	AAT	A
B	Acr-	TAG	TGC	GTT	TTA	TTG	CAC	TTG	T
A ₀		TAT	TGC	ACT	TGT	CCC	GGC	CTG	T
A ₁		TAT	TGC	CCT	TGT	CCC	GGC	CTG	T
A ₅		TAG	TGC	ACT	TGT	GCG	GCC	CTG	G
R		ACG	TCT	AGA	CGT	AAC	GAA	GGT	C

Table 2.1: Sequences of the sensor (S), blocker (B), analyte (A₀), mismatched (A₁ and A₅) and random (R) oligonucleotides. Mismatched regions, relative to the S strand, are shown in red. 'Acr' denotes the Acrydite modifier.

with the Acrydite functional group (Figure 1.7). Additional oligonucleotide strands were designed; sequences differing from the A₀ sequence by one (A₁) and five (A₅) mismatches and an entirely random sequence (R) to act as a control. The sequences of all of the strands described above are shown in Table 2.1. The MatLab algorithm is provided in Appendix B.

2.1.3 Oligonucleotide preparation

All of the oligonucleotide sequences discussed in the previous section were sourced from Integrated DNA Technologies and were supplied in lyophilised (freeze-dried) form. The S and B strands were supplied functionalised with the Acrydite end-group and all oligonucleotides were used as supplied. Stock solutions of the S and B strands were prepared at 1.69 mM by adding the required volume of 1 mM phosphate buffer to the lyophilised oligonucleotide and leaving at room temperature for 2-3 hours until the oligonucleotides were fully dissolved. These stocks were mixed together in equal volumes to produce an 845 μ M stock of the duplex. This solution was then heated to 95°C and slowly cooled to room temperature over the course of three hours so as to remove any secondary structures and to allow for maximum hybridisation between the

S and B strands [170]. The oligonucleotides were then extracted from solution using a standard precipitation process. The solution was separated into 400 μl aliquots and mixed with 40 μl of 3 M sodium chloride (NaCl) solution and 800 μl of iso-propyl alcohol (IPA). The resultant mixture was centrifuged at 2000 revolutions per minute (rpm) for 30 minutes resulting in a pellet of precipitated oligonucleotide at the bottom of the centrifuge tube. The supernatant was discarded and 400 μl of 70% ethanol was added to the tube to wash away any remaining NaCl; this step was repeated twice. Finally the extracted oligonucleotide was left to dry for a few hours, until all remaining solvent had evaporated, leaving the dried pellet. These pellets were stored at -20°C until required, and used to prepare oligonucleotide cross-linked polymer composites (OCPCs) as described previously.

Whilst it would be desirable to undertake all of the required composite characterisation using oligonucleotide-functionalised hydrogels, matters of supply and expense render this impractical. As such, where the inclusion of oligonucleotide cross-linkers was not critical, tests were performed using non-oligonucleotide cross-linked equivalents. Where this is the case it will be clearly stated.

2.1.4 Conductive particle dispersion and polymerisation

The optimal means of dispersing the carbon particles within the composite was determined by preparing 1 ml samples of composite pre-gel using the following methods.

Firstly, pre-composite solutions were prepared as described previously with a MBA concentration of 0.6 mol% wrt monomer, 0 mol% wrt monomer oligonucleotide cross-

linker and carbon nanopowder concentrations of 10, 15, 20, 25, 30 and 35 mg/ml. The carbon was dispersed by manual agitation of the vial. This method will be referred to as the ‘standard’ method.

Secondly, pre-composite solutions were prepared as for the standard method, but with the addition of a high-power sonication step prior to UV irradiation. The sonication was performed by placing the pre-composite solution in a 1.5 ml Eppendorf tube in close proximity to the tip of a 500 W ultrasonic probe in a custom made sonication bath (Figure 2.2). The ultrasonic probe was set to 60% of maximum amplitude and used in pulsed mode (10 s on, 10 s off) for a total of 10 minutes [171, 172]. Ultrasonic agitation is a standard method of particle dispersion [173]. The pre-composite solution was not sonicated directly as this can cause heating and evaporation of the solution. Full details of the ultrasonic probe can be found in Appendix A.

Thirdly, pre-composite solutions were prepared as for the standard method but replacing the aqueous phosphate buffer medium with a 1:1 by volume mixture of 1

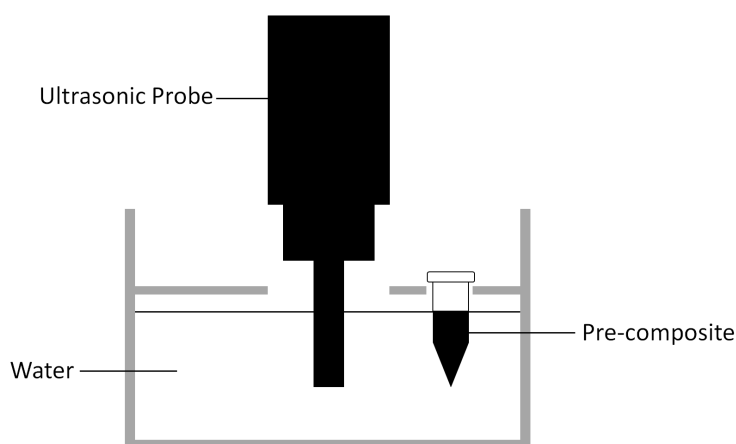


Figure 2.2: Diagram of the set-up used to perform high-powered sonication of the pre-composite solutions.

mM phosphate buffer and dimethylsulfoxide (DMSO). DMSO is used as it has been shown to be a superior solvent for nanoparticle dispersions. [174]

Finally, pre-composite solutions were prepared as for the standard method but with the addition of oligonucleotide cross-linkers at a concentration of 0.4 mol% wrt to monomer, as described previously.

2 μ l droplets of these solutions were then pipetted onto substrates and polymerised as described previously. These substrates were previously silanised as described in Section 2.3.3 so as to improve the adhesion of the composites. After polymerisation the composites were immersed in deionised (DI) water for 1 - 2 hours to allow them to fully saturate. They were then removed from the water, excess water removed from their surface, and imaged using the set-up shown in Figure 2.3. The substrates used were the electrode devices described in Section 2.3. 1 μ l samples of composite were prepared using each of the methods detailed above and imaged under an optical microscope to determine the extent of particle agglomeration.

2.1.5 Nuclear magnetic resonance measurements

2 ml samples of polyacrylamide (0.8 mol% wrt monomer MBA, 0 mol% wrt monomer oligonucleotide cross-linker, 0 mg/ml carbon) were prepared as described in Section 2.1.1. After polymerisation the samples were immersed in 50 ml of DI water for at least 12 hours to allow the hydrogel to saturate and any solvents, un-reacted monomer or other molecules to diffuse out of the polymer network. The saturated hydrogel was then removed from the swelling medium. Dr. Jaclyn Raeburn freeze-dried the

swelling medium, dissolved it in deuterated DMSO and ^1H nuclear magnetic resonance (NMR) spectroscopy was performed on the resultant solution using a BrukerAsance spectrometer operating at 400 MHz. Prior to the spectroscopy, ethanol was added to the solution to act as a standard reference.

The saturated hydrogel was dried in ambient conditions and re-swollen in 50 ml of fresh DI water. This second swelling medium was treated in the same way as the first. Solutions of AAM, MBA and the photo-initiator were prepared and NMR spectra obtained in the same manner, for comparison purposes.

Due to the hydrophilic nature of polyacrylamide, gels ‘dried’ in ambient conditions for *ca.* 12 hours will retain some water. However, in the interests of concision, throughout this thesis gels in such a state will be referred to as ‘dried’.

2.2 Optical measurements

The volume of composite droplets was measured using the set-up shown in Figure 2.3. The composites were placed on the stage, on the substrates upon which they were polymerised, and imaged using the camera. Using a custom MatLab algorithm, the volumes of the polymer droplets were calculated from these images. The fractional volume change, δ_v , of the droplets from their initial volume (*i.e.* the volume at polymerisation) can be calculated by:

$$\delta_v \equiv \frac{V - V_i}{V_i} \quad (2.1)$$

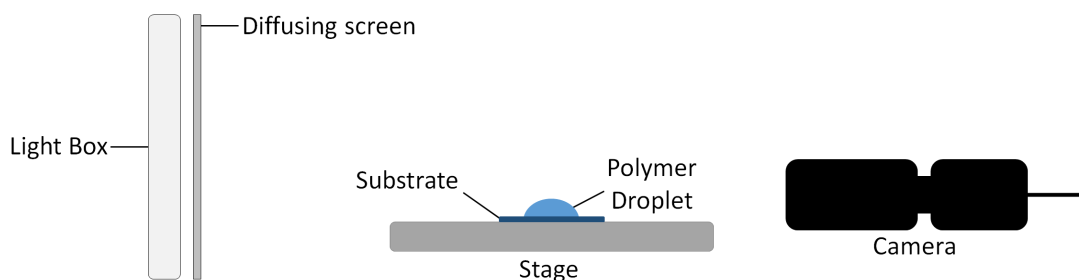


Figure 2.3: Illustration of the polymer droplet imaging set-up. The droplets were deposited on a substrate and placed on a stage in front of a back-light. They were imaged using a Sony XCD-X710 Firewire camera in conjunction with IC Capture image acquisition software.

where V is the measured volume of the polymer and V_i is the initial volume at polymerisation. The MatLab algorithm is provided in Appendix B.

The volume of the composites is measured in two different ways. In ‘end-point’ measurements the samples are swollen in solution, removed, patted dry (both the droplet and the substrate) and imaged. In ‘kinetic’ measurements the samples are immersed in solution on the stage (Figure 2.3), imaged every 10 s as they swell and the volume calculated as a function of time. For these measurements carbon must be added to the composite to act as a contrast agent, allowing a clear definition between the composite and the surrounding solution. The experimental set-up was housed in a temperature controlled environment, held at $(20 \pm 1)^\circ\text{C}$.

2.2.1 End-point measurements

Pre-composite solutions with 0 mg/ml carbon, 0 mol% wrt to monomer oligonucleotide cross-linker and concentrations of MBA varying between 0.4 and 2.0 mol% wrt to monomer were prepared as described in Section 2.1.1 (high-power sonication). 2 μl droplets were pipetted onto substrates and polymerised as described previously. These

samples were then immersed in DI water (held within a water bath at $(23 \pm 1)^\circ\text{C}$) for at least 12 hours to allow them to swell until saturated. After this, they were removed from the DI water, patted dry and imaged as described previously. Five repetitions were performed for each MBA concentration.

A pre-composite solution with 0 mg/ml carbon, 0.6 mol% wrt to monomer MBA and 0.4 mol% wrt to monomer oligonucleotide cross-linker was prepared as described in Section 2.1.1 (standard method). 1 μl droplets of this solution were pipetted onto substrates and polymerised before being immersed in either a 10 μM A_0 solution or a 10 μM R solution. These samples were held at $(23 \pm 1)^\circ\text{C}$, using a water bath, for 12-18 hours to allow them to swell to their equilibrium state, before being removed, patted dry and imaged.

The above procedure was repeated for temperatures ranging from 25 - 50°C . Additionally, the process was repeated with the swelling medium refrigerated at $\sim 3^\circ\text{C}$ for the duration of the experiment. Three repetitions were performed for each temperature.

2 μl droplets of the same pre-composite solution were polymerised on substrates. After polymerisation, the droplets were immersed in 1 μM solutions of either A_0 , A_1 , A_5 or R (Table 2.1). These samples were held at $(23 \pm 1)^\circ\text{C}$ for one hour, before being removed from solution, patted dry and imaged. Five repetitions were performed for each oligonucleotide solution.

2.2.2 Kinetic measurements

Pre-composite solutions with 10 mg/ml carbon nanopowder, 0 mol% wrt to monomer oligonucleotide cross-linker and either 0.6 or 1.0 mol% wrt to monomer MBA were prepared as described previously (high-power sonication) and 2 μ l droplets polymerised on substrates. These samples were then immersed in DI water in a 25 mm beaker on the stage of the camera set-up shown in Figure 2.3 and imaged over time as described previously. Five repetitions were performed for each MBA concentration.

A pre-composite solution with 10 mg/ml carbon nanopowder, 0.6 mol% wrt to monomer MBA and 0.4 mol% wrt to monomer oligonucleotide cross-linker was prepared as described previously (standard method) and 2 μ l droplets polymerised on substrates. Immediately after polymerisation the samples were placed in a 150 mM NaCl, 1 mM phosphate buffer solution for 2 hours to allow any un-fixed carbon (*i.e.* carbon that is not confined to the polymer matrix) to leave the gel. This solution was refrigerated at $\sim 3^{\circ}\text{C}$ for the duration in order to minimise any thermal dehybridisation. The samples were then removed, patted dry and allowed to dry out at $\sim 3^{\circ}\text{C}$ for at least 24 hours.

These samples were then immersed in either an A_0 or R solution on the stage of the optical measurement set-up and imaged over time as described previously. Concentrations of the oligonucleotide solutions were varied between 1 nM and 10 μ M. Five repetitions were performed for each oligonucleotide concentration. All oligonucleotide solutions contained 150 mM NaCl and 1 mM phosphate buffer.

2.3 Electrode design and fabrication

2.3.1 Electrode design

The electrode devices used throughout this thesis consisted of an interdigitated electrode (IDE) array on a silicon (Si) substrate, upon which OCPC droplets can be deposited. The array spanned 1.5×1.46 mm with 30 digits in total, each $10 \mu\text{m}$ in width and separated by $40 \mu\text{m}$. The array dimensions were chosen so as to be smaller than the span of a $2 \mu\text{l}$ composite droplet. The digit width was chosen to be the same as for the off-the-shelf equivalent (discussed later in this section) and the digit separation was chosen as a compromise between providing a large digit spacing (see Section 4.1) and providing a significant number of digits within the given array span.

The substrates consisted of a Si wafer with a surface layer of silicon dioxide (SiO_2). The IDEs were fabricated from platinum (Pt), on top of this SiO_2 layer (Figure 2.4, layer 1). A second layer of parylene was added on top to act as a passivation layer (Figure 2.4, layer 2). Parylene is a common choice for hydrophobic passivation layers. [175,176]

The utility of these electrode devices for measuring the electrical properties of the composites described in Section 2.1, and the adhesion of these composites to the devices, were compared to commercial off-the-shelf electrode devices (G-IDEAU10, Dropsens). These commercial devices had an IDE digit width of $10 \mu\text{m}$, a digit separation of $10 \mu\text{m}$ and the array spanned approximately 6.9×5.3 mm.

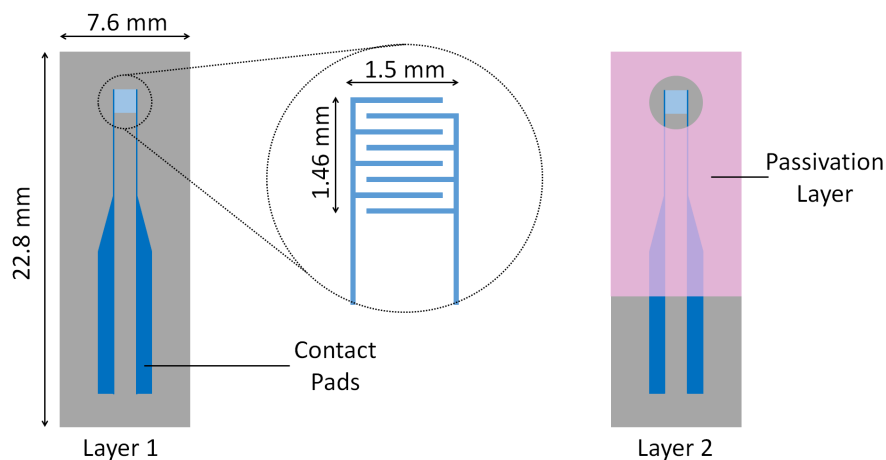


Figure 2.4: Diagrammatic representation of the electrode devices. Left hand side - Layer 1, the blue regions represent Pt and the grey regions SiO_2 . The circled area shows the IDE array, only 8 digits are shown here for clarity. Right hand side - Layer 2, the pink region represents the passivation layer.

2.3.2 Electrode fabrication

The electrode devices were fabricated in a clean-room facility with controlled temperature ($20 \pm 1^\circ\text{C}$) and humidity (40%), and were fabricated on 100 mm diameter Si wafers. These were placed in a wet-oxidation furnace at 1100°C for 40 minutes in order to produce a SiO_2 layer of approximately 500 nm (Figure 2.5 - A). The wafers were then placed in a plasma asher for 30 minutes to remove any traces of moisture from the surface. Full details of all of the materials and tools used in this process are provided in Appendix A.

The electrodes were fabricated using a standard platinum lift-off process [177, 178]. A layer of photoresist (AZ nLOF 2070-3.5) was spin-coated onto the wafers to a thickness of approximately $3.5 \mu\text{m}$ using a spin profile of 700 rpm for 5 s followed by an acceleration of 1000 rpm/s to 3000 rpm for 45 s (Figure 2.5 - B). Prior to

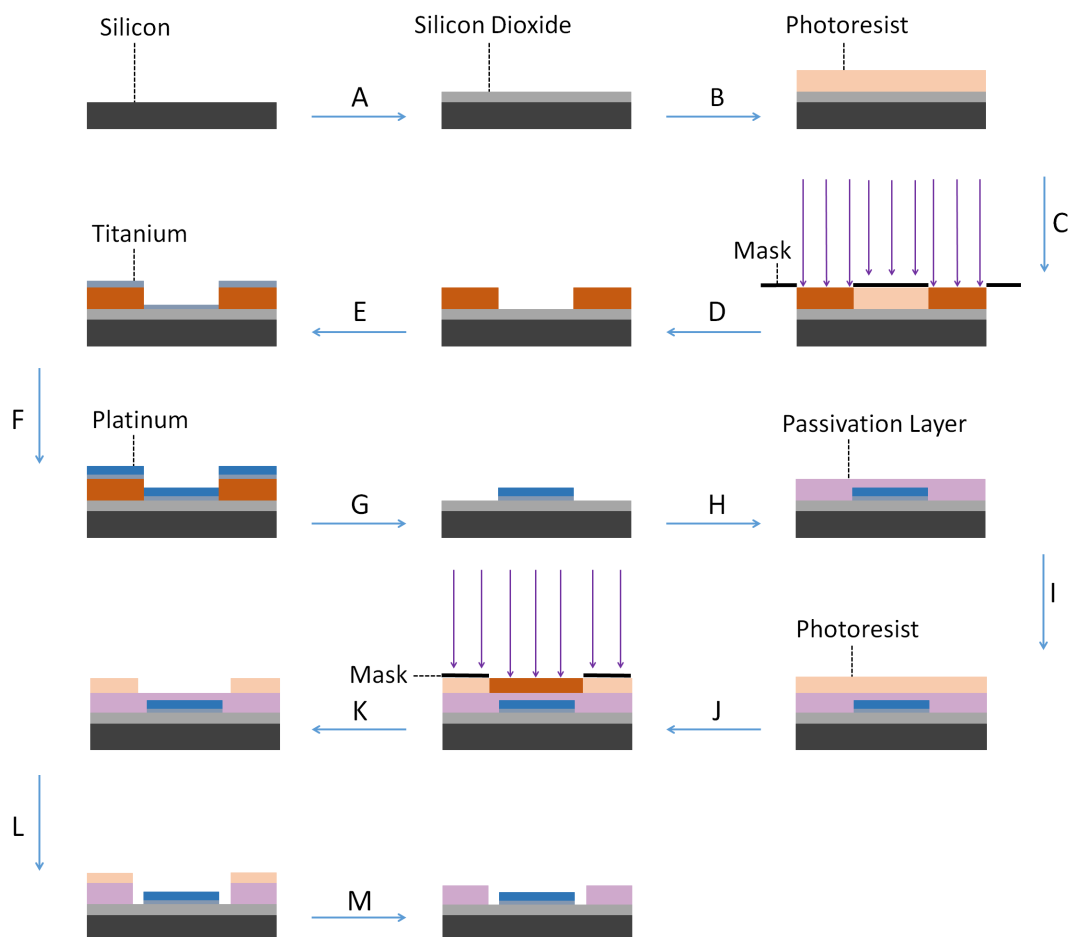


Figure 2.5: The electrode fabrication process: A - an insulating SiO_2 layer is grown upon the silicon wafer; B - a layer of photoresist is deposited; C - the wafer is exposed to UV light through the layer 1 photolithography mask; D - the photoresist is developed; E - Ti is evaporated onto the wafer; F - Pt is evaporated onto the wafer; G - the lift-off process is performed, leaving only the desired pattern; H - a passivation layer is deposited on the wafer; I - a layer of photoresist is deposited; J - the wafer is exposed to UV light through the layer 2 photolithography mask; K - the photoresist is developed; L - the passivation layer is etched away, exposing the IDE and the contact pads; and M - the remaining photoresist is removed.

the deposition of the photoresist the wafers were primed with hexamethyldisilazane (HMDS), by exposure to HMDS vapour in a sealed container for approximately 10 minutes, to improve the adhesion of the photoresist to the surface of the SiO₂ [179]. After the deposition of the photoresist, the wafers were soft-baked on a hotplate at 110°C for 1 minute to remove any remaining solvent.

The photoresist-coated wafers were then exposed to UV radiation (350 - 450 nm, 4 mW/cm²) through the layer 1 photolithography mask (chrome on glass, produced by Compugraphics to the design described in Section 2.3.1) under hard-contact for 30 s (Figure 2.5 - C). After exposure the wafers were transferred to a hotplate for a post-exposure bake at 115°C for 1 minute. The wafers were then placed in developer solution for 2 minutes (Figure 2.5 - D), before being rinsed with DI water and dried using compressed nitrogen.

The metal was then deposited on the wafers via electron-beam evaporation. Titanium (Ti) was deposited to a thickness of 10 nm (Figure 2.5 - E) to act as an adhesion layer and Pt was then deposited on top to a thickness of 50 nm (Figure 2.5 - F). After this the lift-off process was performed by immersing the wafers in a resist stripper solution at 50°C for one hour, after which any remaining unwanted metal was removed by ultrasonic agitation (Figure 2.5 - G). The wafer was then rinsed by immersion in IPA before rinsing with DI water and drying with compressed nitrogen.

After the lift-off step, the thickness, width and separation of the IDE were measured using surface profilometry to ensure that the process performed as expected. If single-layer devices are being prepared, the wafers were then diced into individual devices. If a passivation layer was to be added, this was done by the following process.

Parylene was deposited onto the wafers to a thickness of 1 μm via chemical vapour deposition (CVD) (Figure 2.5 - H). After this, a layer of photoresist (SPR 220) was spin-coated on the wafers using a spin profile of 500 rpm for 5 s followed by an acceleration of 1000 rpm/s to 3000 rpm for 30 s (Figure 2.5 - I). After deposition the wafers were soft-baked at 115°C for 1 minute.

The photoresist-coated wafers were then exposed to UV radiation for 30 s through the layer 2 photolithography mask under hard-contact (Figure 2.5 - J). After exposure the wafers were placed in developer solution for 1 minute (Figure 2.5 - K) before being rinsed with DI water and dried using nitrogen. The thickness of the deposited resist was measured using surface profilometry.

The parylene was then removed from the IDE array and the contact pads using plasma etching (Figure 2.5 - L) (O_2 - 49 standard cubic centimetres per minute (SCCM), 50 mTorr, 100 W, 15 minutes). The remaining photoresist was then removed using an acetone rinse (Figure 2.5 - M) before the wafers were diced into the individual devices.

Prior to use, each electrode device was visually inspected under a microscope to ensure there were no discontinuities in the electrodes or connective tracks and that there were no particulates on the IDE array.

The full run-sheet for the fabrication process can be found in Appendix C.

2.3.3 Silanisation

The electrodes were immersed in a solution of 0.01 M hydrochloric acid (HCl) (37%, Sigma) in DI water for 15 minutes before being removed, rinsed with DI water and dried with compressed nitrogen. The electrodes were then immersed in a solution of 0.02 M 3-(trimethoxysilyl) propyl methacrylate (TPM) (98%, Sigma) in acetone for one hour before being removed, rinsed with DI water and dried with compressed nitrogen. This method was adapted from Tierney *et al.* [124]

2.4 Electrical measurements

The electrical measurement set-up is shown in Figure 2.6. The composite samples were prepared upon the electrode devices as described previously. The electrode devices were connected to either a Keithley 2000 digital multimeter or an AD5933EBZ test board supplied by Analog Devices, which were in turn connected to a computer via a USB connection and controlled using custom LabVIEW algorithms. In the case of direct current (d.c.) measurements the multimeter was used to take 2-terminal resistance measurements with groups of 10 samples separated by 100 ms, with each sample group separated by 10 s. The multimeter was set to auto-range, which means, for the resistances investigated in the tests described herein, the supplied current was 100 μA for low resistances ($<100\text{ k}\Omega$) and 10 μA for high resistances ($>100\text{ k}\Omega$) [180]. In the case of alternating current (a.c.) measurements the AD5933EBZ test board was connected via a 47 k Ω series resistor (Figure 2.6), added to ensure that the resultant impedance was always within the measurement range of the test board. The board was then used to

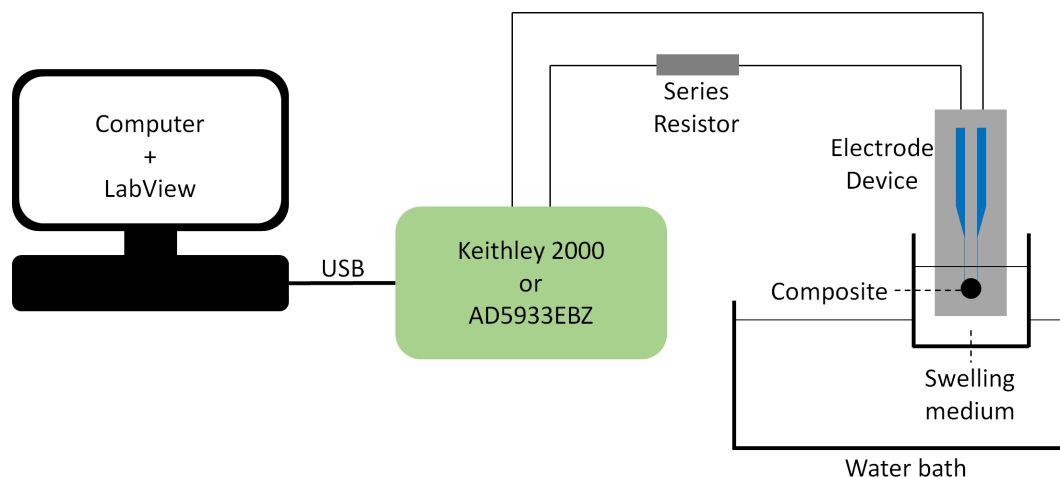


Figure 2.6: Illustration of the electrical measurement set-up. The electrode device under investigation is connected either to the Keithley 2000 multimeter (d.c.) or the AD5933EBZ test board via a series resistor (a.c.). The measurement device is connected via a USB connection to a computer, which is used to operate the measurement device and collect the measurement data.

perform a frequency sweep within the device measurement range of 1 to 100 kHz [181], in increments of 1 kHz. The board measures the magnitude of the complex impedance, $|Z|$, and the phase change, θ , of the resultant signal and was used with a 22 k Ω feedback resistor and was calibrated using a 390 k Ω reference resistor. These values were chosen in accordance with the calculations provided in the AD5933 documentation [182], so as to provide an impedance measurement range of approximately 10 k Ω to 1 M Ω . This range was chosen based on resistance measurements of the composites in various states (see Section 4.2.2.1).

Pre-composite solutions with 0.8 mol% wrt to monomer MBA and 0 mol% wrt to monomer oligonucleotide cross-linker were prepared as described previously (high-power sonication) with carbon nanopowder concentrations ranging from 0 to 20 mg/ml. 2 μ l droplets of these solutions were polymerised upon electrode devices and allowed to dry out in ambient conditions. The d.c. resistance of these composites in their dried state

was measured, as described previously, in air. These tests were repeated using carbon micropowder, carbon nanotubes and graphite particles.

Pre-composite solutions with carbon nanopowder concentrations ranging between 0 and 20 mg/ml, MBA concentrations ranging between 0.6 and 1.0 mol% wrt to monomer and 0 mol% wrt to monomer oligonucleotide cross-linker were prepared as described previously (high-powered sonication). These solutions were used to prepare 2 μ l composite samples which were allowed to dry out in ambient conditions before being immersed in 1.5 ml of either DI water or a 150 mM NaCl, 1 mM phosphate buffer solution. The vessel containing these solutions was held at $(23 \pm 1)^\circ\text{C}$ using a water bath (Figure 2.6). The d.c. resistance or a.c. impedance was measured over time as they swell, as described previously. The d.c. tests were repeated using carbon micropowder and graphite particles at a concentration of 15 mg/ml. Five repetitions were performed for each MBA concentration, solution and carbon particle type.

Samples of pre-composite solution with 20 mg/ml carbon (either nanopowder, micropowder or graphite), 0.6 mol% wrt to monomer MBA and 0.4 mol% wrt to monomer oligonucleotide cross-linker were prepared as described previously (standard method). 2 μ l droplets were deposited upon silanised electrode devices and polymerised *in situ*. The electrodes were then placed under refrigeration at $\sim 3^\circ\text{C}$ for 24 hours to allow the OCPCs to dry out. The samples were then immersed in either an A_0 or R solution and their d.c. resistance measured over time as described previously. The temperature of the swelling medium was held at $(23 \pm 1)^\circ\text{C}$ and the concentrations of the oligonucleotide solutions were varied between 1 nM and 10 μM . All oligonucleotide solutions contained 150 mM NaCl and 1 mM phosphate buffer.

2.4.1 Sensor model

A sensor consisting of a conductive composite upon interdigitated electrodes can be modelled as a resistor (R_p) in parallel with a capacitor (C) as the system will have both resistive and capacitive components. The model is completed by the addition of a parasitic resistance (R_s) and inductance (L) in series (Figure 2.7). These components are to account for the parasitic effects of the electrode devices as well as any contribution of the hardware that is not removed through calibration. Whilst this model was developed from first principles, models that are identical [183] or that differ only in the parasitic terms [184] have been applied elsewhere for different applications of IDEs.

The complex impedance, Z , of each of the components can be expressed as follows:

$$\begin{aligned} Z_{R_p} &= R_p \\ Z_C &= \frac{1}{j\omega C} \\ Z_{R_s} &= R_s \\ Z_L &= j\omega L \end{aligned} \tag{2.2}$$

where ω is the angular frequency and j is $\sqrt{-1}$ [185]. Therefore the total impedance, Z , of the system is given by:

$$Z = \frac{1}{\frac{1}{R_p} + j\omega C} + R_s + j\omega L \tag{2.3}$$

Equation 2.3 equates to:

$$Z = \left[\frac{R_p}{1 + (\omega R_p C)^2} + R_s \right] + j \left[\omega L - \frac{\omega C R_p^2}{1 + (\omega R_p C)^2} \right] \tag{2.4}$$

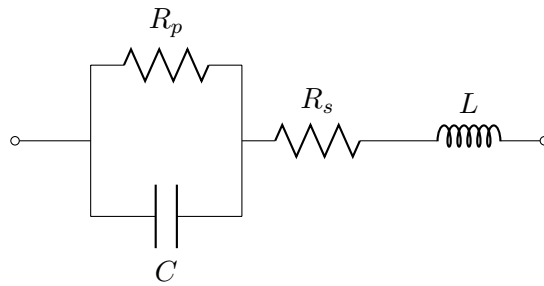


Figure 2.7: The model circuit for the sensor. R_p denotes the resistive component of the sensor and C denotes the capacitive component. R_s and L denote the parasitic resistance and inductance of the system respectively.

Thus the magnitude of the complex impedance, $|Z|$, is given by:

$$|Z| = \left(\left(\frac{R_p}{1 + (\omega R_p C)^2} + R_s \right)^2 + \left(\omega L - \frac{\omega C R_p^2}{1 + (\omega R_p C)^2} \right)^2 \right)^{1/2} \quad (2.5)$$

2.4.2 Cyclic voltammetry

Cyclic voltammetry was performed using a standard three electrode cell set-up (Figure 2.8) [186]. The working electrode (WE) consisted of the parylene coated electrode devices described in Section 2.3 with a crocodile clip shorting both of the contact pads such that the IDE array forms a single electrode. The reference electrode (RE) was a silver/silver chloride (Ag/AgCl) electrode and the counter electrode (CE) was a 7.5×35.0 mm piece of silicon wafer coated with platinum. The CE has a surface area of 2.6 cm^2 , many times that of the WE (approximately 0.005 cm^2).

The potential of the WE relative to the RE was cycled linearly between +1.5 volts (V) and -1.5 V with a scan rate of 0.1 V/s , leading to a cycle time of 60 s. The potential was controlled, and the current through the CE measured, using a potentiostat operated using Nova software (full details can be found in Appendix A). The electrolytic medium

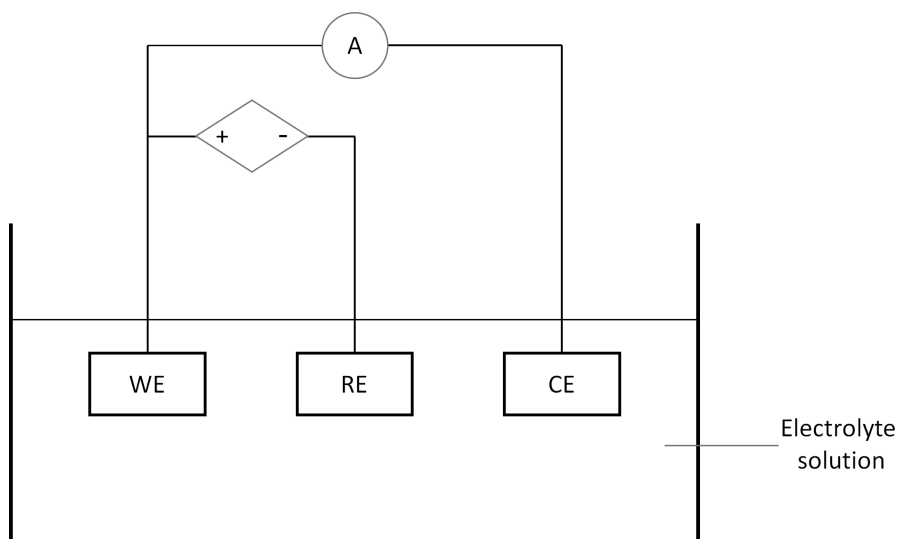


Figure 2.8: Diagram of a standard three electrode cell arrangement with working (WE), reference (RE) and counter (CE) electrodes. A potential is applied between the WE and the RE, and the current is measured between the CE and the WE. Adapted from Villagrasa *et al.* [187].

was an aqueous solution of 150 mM NaCl and 1 mM phosphate buffer. A total of 5 cycles were performed for each test.

The above tests were performed using a WE without the addition of any polymer (blank), one covered with a 2 μl droplet of polyacrylamide (0 mg/ml carbon) and one covered with a 2 μl composite droplet (20 mg/ml carbon nanopowder), prepared as described previously.

This process was repeated with a scan window of +4.0 V to -4.0 V. All other parameters were kept constant, leading to a scan time of 160 s. This scan window represents the maximum voltage range that the electrodes and composites would be expected to be exposed to during the experiments described previously. The narrow scan window is more typical for cyclic voltammetry experiments.

The results for all of the experiments described in this chapter, along with a discussion of their implications, are presented in Chapters 3 and 4.

Chapter 3

Composite preparation and characterisation: results and discussion

3.1 Composite preparation

3.1.1 Conductive particle dispersion and polymerisation

When preparing conductive polymer composites via *in situ* polymerisation, it is important to understand how the incorporation of the conductive component will affect the polymerisation process. It is also necessary to know the upper limit at which conductive particles can be added without adversely affecting the polymerisation process.

Samples of composite were prepared with varying carbon concentrations in order to determine the effects of increasing carbon loading upon the polymerisation. Different methods of dispersing the carbon particles within the composites were compared to determine their relative effectiveness and the effects of carbon particle dispersion upon polymerisation.

Figure 3.1 shows images of composite gels produced with increasing carbon nanopowder density after allowing them to saturate in deionised (DI) water, as described in Section 2.1.4 (standard method). While well-formed composite gels are produced for loading densities up to 20 mg/ml (A-C), beyond this point the resultant composites appear ill-formed and reduced in size (D, E) until, above 30 mg/ml (F), there is no composite formation to speak of. This suggests incomplete polymerisation for carbon loading densities above 20 mg/ml. There are several possible explanations for this phenomenon. Increasing concentrations of carbon may prevent UV radiation from fully penetrating into the centre of the droplets, leading to reduced radical formation deeper in the gel and, therefore, slower polymerisation. Increasing concentrations of carbon particles may also hinder the diffusion of the monomer and growing polymer chains, thereby

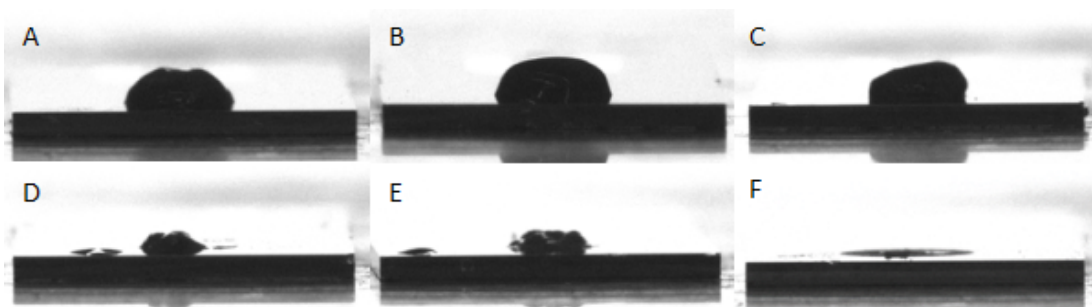


Figure 3.1: Images of composite droplets prepared using the standard method with increasing carbon loading. A - 10 mg/ml, B - 15 mg/ml, C - 20 mg/ml, D - 25 mg/ml, E - 30 mg/ml, and F - 35 mg/ml. The cross-link density was 0.6 mol% wrt monomer N, N' methylene-bisacrylamide (MBA), 0 mol% wrt monomer oligonucleotide cross-linker.

reducing the rate of the polymerisation reaction [188]. Finally, increasing the carbon loading may undermine the stability of the gels by preventing the formation of an interpenetrating network. Short polymer chains, with limited cross-linking, will not retain a three-dimensional structure in solution. It is probable that a combination of these effects leads to the unstable gels evident in Figure 3.1.

Figure 3.2 shows the equivalent images for samples that underwent a high-power sonication step prior to UV exposure. Whilst there is some apparent improvement in composite formation for higher carbon loading, these improvements are minimal. While improved dispersion and de-agglomeration of the carbon particles may mitigate some of the adverse effects described previously, these effects are still apparent.

Figure 3.3 shows the equivalent images for composites produced using a solvent mixture of 1:1 by volume buffer/dimethylsulfoxide (DMSO). While these samples produce excellent composite gels at loading densities of 20 mg/ml and below (A-C), no polymerisation is apparent at higher loading densities (D-F). As DMSO is a superior solvent for non-polar substances, compared to water, it will produce better

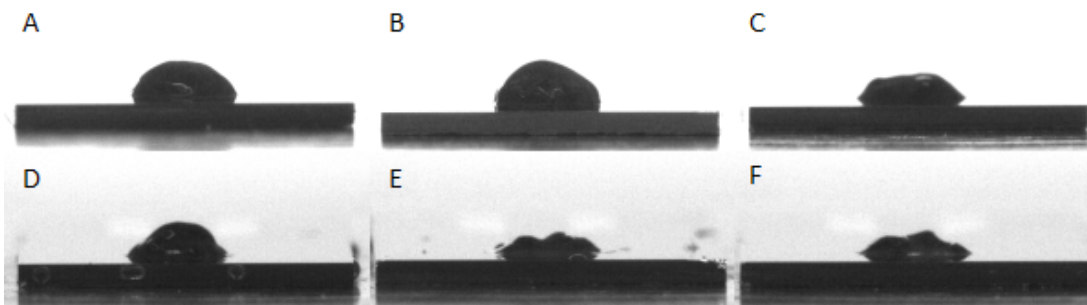


Figure 3.2: Images of composite droplets prepared using high-powered sonication with increasing carbon loading. A - 10 mg/ml, B - 15 mg/ml, C - 20 mg/ml, D - 25 mg/ml, E - 30 mg/ml, and F - 35 mg/ml. The cross-link density was 0.6 mol% wrt monomer MBA, 0 mol% wrt monomer oligonucleotide cross-linker.

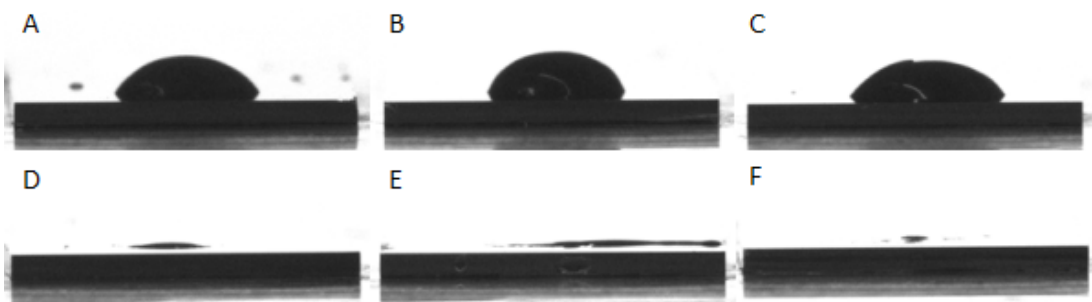


Figure 3.3: Images of composite droplets prepared using 50% DMSO with increasing carbon loading. A - 10 mg/ml, B - 15 mg/ml, C - 20 mg/ml, D - 25 mg/ml, E - 30 mg/ml, and F - 35 mg/ml. The cross-link density was 0.6 mol% wrt monomer MBA, 0 mol% wrt monomer oligonucleotide cross-linker.

carbon particle dispersions [189]. However, Figure 3.3 shows that the adverse effects on polymerisation of carbon concentrations above 20 mg/ml (D-F) are more pronounced with the addition of DMSO. There have been several reports of the rate of free-radical polymerisation being reduced with the addition of solvents [190–193]. A further reduction in the rate of polymerisation as a result of the addition of DMSO would explain the results seen in Figure 3.3 as a slower reaction rate would exacerbate the incomplete polymerisation.

Figure 3.4 shows images of oligonucleotide cross-linked polymer composite (OCPC) droplets with increasing carbon nanopowder loading after saturation in DI water. Unlike the equivalent images for composites without the addition of oligonucleotide cross-links, these composite droplets appear well-formed for carbon loading concentrations up to 35 mg/ml (in that there are no apparent regions where polymerisation has not occurred, unlike in Figures 3.1, 3.2 and 3.3), indicating a more complete and uniform polymerisation. What cannot be seen from these images is that for carbon loading concentrations greater than 25 mg/ml, adhesion to the substrate is impaired – evidenced by the fact that several samples detached from the substrate prior to imaging. This is

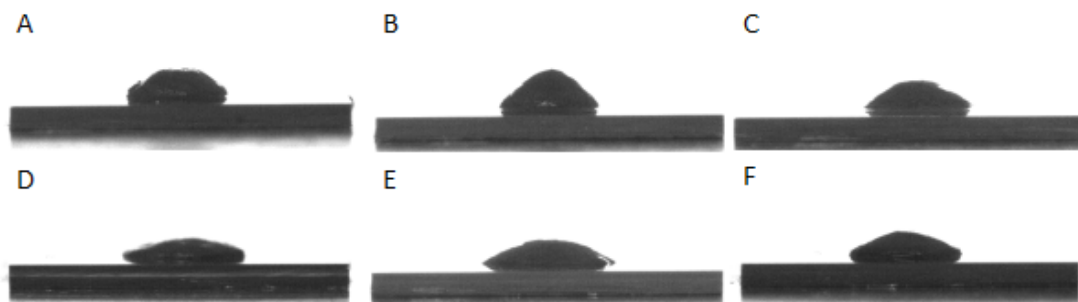


Figure 3.4: Images of composite droplets prepared using the standard method with the addition of oligonucleotide cross-linkers, with increasing carbon loading. A - 10 mg/ml, B - 15 mg/ml, C - 20 mg/ml, D - 25 mg/ml, E - 30 mg/ml, and F - 35 mg/ml. The cross-link density was 0.6 mol% wrt monomer MBA, 0.4 mol% wrt monomer oligonucleotide cross-linker.

hypothesised to be a result of the increased concentration of carbon particles causing a reduction in the area of polyacrylamide bonded to the silanised substrate (Section 2.3.3). The reasons for the superior polymerisation of the oligonucleotide cross-linked droplets will be discussed later in this section.

Under the conditions investigated here, it is unlikely that carbon loading densities of greater than 20 mg/ml can be reliably achieved for polyacrylamide-based composites using UV-initiated free-radical polymerisation.

As has previously been alluded to, the dispersion and agglomeration of the conductive particles are parameters that affect the quality of the polymerisation of these composites. It is highly desirable that the uniformity of the dispersion be maximised and that the extent of particle agglomeration within the composites be minimised.

Figure 3.5 shows microscope images of dried composite droplets produced using the various methods described in Section 2.1.4. For the standard method (Figure 3.5 - A) considerable agglomeration occurs, with agglomerates ranging from the order of 5 μm and below to hundreds of μm in size. This agglomeration is partly reduced by the use of

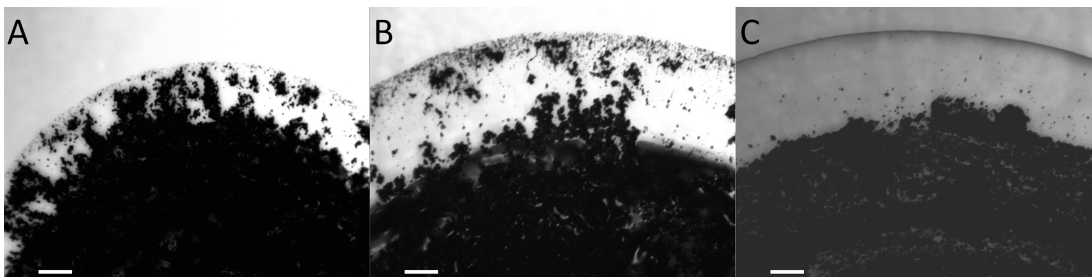


Figure 3.5: Microscope images at $\times 5$ magnification of 10 mg/ml carbon nanopowder composite droplets prepared using various methods of particle dispersion. A - the 'standard' method, B - high-powered sonication, C - 50% DMSO. The cross-link density was 0.6 mol% wrt monomer MBA, 0 mol% wrt monomer oligonucleotide cross-linker. The scale bars represent 100 μm .

high-powered sonication (Figure 3.5 - B), which results in visibly fewer agglomerates, typically of the order of 50 μm or smaller, with some larger examples. The addition of DMSO (Figure 3.5 - C) produces a greater reduction in visible agglomerates, the majority of which are of the order of 10 μm or smaller.

Whilst it is possible to create conductive composites when agglomeration of the conductive particles occurs, it is nonetheless undesirable. Agglomeration will result in poor reproducibility as differences in the size and aspect ratios of the agglomerates may result in differences in the percolation characteristics between samples. Additionally, there is a possibility that, if sufficiently large, agglomerates might short-circuit any electrodes used for the measurement of the conductivity. Finally, agglomeration will render some future droplet dispensing techniques (such as ink-jet printing) unusable. [194,195]

Given the above, it might be thought that the addition of DMSO would be desirable, however DMSO's adverse effects on the gelation process at higher carbon loadings means this is not the case. It may be that alternative concentrations of DMSO or alternative sonication parameters (such as sonication time or intensity) produce

superior carbon particle dispersion. However, as it is known that both DMSO (as well as many other solvents) and high-powered sonication (the most common method of nanoparticle dispersion [196]) adversely affect the hybridisation of DNA [197,198], neither approach was investigated further.

Figure 3.5 shows non-uniform distributions, characterised by a band around the circumference of the droplet where there is little or no carbon. This may be due to the polymerisation occurring faster at the droplet surface, forcing the carbon towards the droplet center. If the agglomerates are larger than the hydrogel mesh size and the mesh forms in an anisotropic manner, there will be a net movement of the agglomerates away from the regions of most rapid polymerisation (Figure 3.6), in this case towards the centre of the droplet.

Figure 3.7 shows a microscope image of a dried OCPC droplet with a carbon nanopowder concentration of 20 mg/ml. Unlike those shown in Figure 3.5, the carbon appears uniformly distributed and appears to occupy space all the way to the edge of

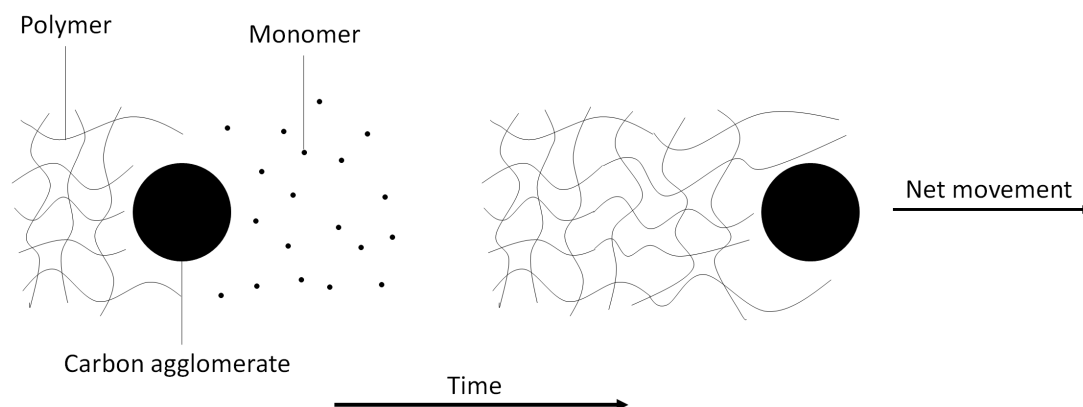


Figure 3.6: Diagrammatic representation of the net inward force on carbon agglomerates during polymerisation. As the polymer mesh size is smaller than the agglomerate size, the polymerisation reaction will result in a net movement of the agglomerates away from the regions where the polymerisation reaction occurs most rapidly.

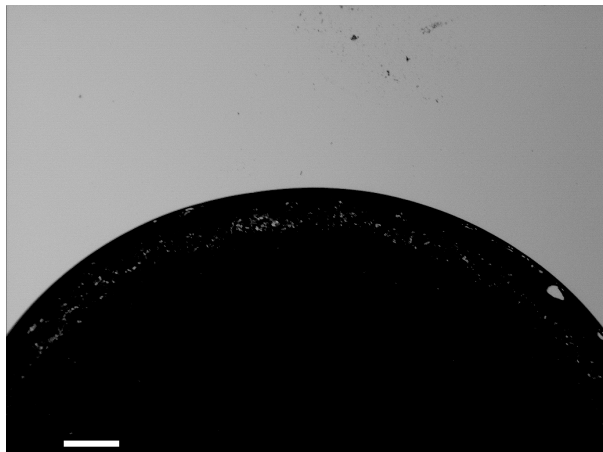


Figure 3.7: Microscope image of a 20 mg/ml droplet prepared using the standard method with the addition of oligonucleotide cross-links. The cross-link density was 0.6 mol% wrt monomer MBA, 0.4 mol% wrt monomer oligonucleotide cross-linker. The image is at $\times 5$ magnification and the scale bar represents 100 μm .

the hydrogel. This tells us that DNA acts as a dispersion agent, leading to more uniform carbon distributions and less agglomeration than can be achieved by either sonication or the use of solvents such as DMSO.

It has been shown that carbon nanoparticles can interact with DNA in solution to form complexes [199–202]. It is hypothesised that these interactions occur within our pre-composite mixtures, breaking up agglomerates and leading to improved dispersion. It is believed that it is this superior dispersion of carbon in the presence of oligonucleotide cross-linkers that leads to the superior polymerisation at higher carbon loading values, as seen in Figure 3.4. Further efforts will be required to fully understand these interactions and their implications for the development of OCPCs.

Figure 3.8 shows a cryo-scanning electron microscope (cryoSEM) image of a polyacrylamide/carbon nanopowder composite prepared using the standard method with 5 mg/ml carbon. A relatively low carbon concentration was used to ensure proper poly-



Figure 3.8: CryoSEM image of polyacrylamide/carbon nanopowder composite. The carbon loading was 5 mg/ml. The cross-link density was 0.6 mol% wrt monomer MBA, 0 mol% wrt monomer oligonucleotide cross-linker.

mer formation. The highly porous nature of such a hydrogel-based composite is clearly evident and the general network structure appears similar to other reported examples of polyacrylamide hydrogels [118, 203], although the pore size can vary widely based on factors such as the monomer and cross-linker concentrations [204, 205]. The pores typically range from approximately 0.2 to 0.5 μm in size, which is of the order that would be expected for hydrogels of this type [106], and smaller than the largest of the carbon agglomerates observed in Figure 3.5. The carbon nanoparticles appear to be approximately 10 to 30 nm in size, which is in agreement with the material specifications [206]. At this concentration, they appear to be well distributed and to display minimal agglomeration. However, as seen previously, at higher concentrations it might be expected that agglomeration of the nanoparticles may begin to occur.

3.1.2 Nuclear magnetic resonance measurements

Nuclear magnetic resonance (NMR) spectroscopy was performed to determine what reaction components remain after polymerisation and to what extent these will leave the hydrogel upon immersion in water. It was performed on the swelling medium rather than the polyacrylamide as hydrogels are not suitable for NMR spectroscopy.

Figure 3.9 shows the NMR spectrum of the polyacrylamide swelling medium, from the first swelling, as described in Section 2.1.5. The x -axis represents the resonant frequency shift, relative to a reference value, and the y -axis represents the intensity of the output. Peak C corresponds to water (the principle constituent of the sample), peaks D and G correspond to the ethanol standard and peak E corresponds to the DMSO solvent [207]. Group B corresponds to un-reacted acrylamide monomer (and MBA cross-linker, although the concentration of the former will significantly exceed that of the latter due to their relative abundances at synthesis), groups A and F correspond to polyacrylamide which has not formed part of the macromolecular structure, and group H corresponds to the photo-initiator. Groups B and H were identified through comparison with the NMR spectra of the solutions of the individual constituents, as described in Section 2.1.5.

The spectrum obtained for the medium of the second swelling shows similar peaks for polyacrylamide and acrylamide. Integration of the area under the peaks gives an indication of the relative concentrations (with respect to the ethanol standard). These calculations (performed by Dr. Raeburn) show that in the second swelling medium, both

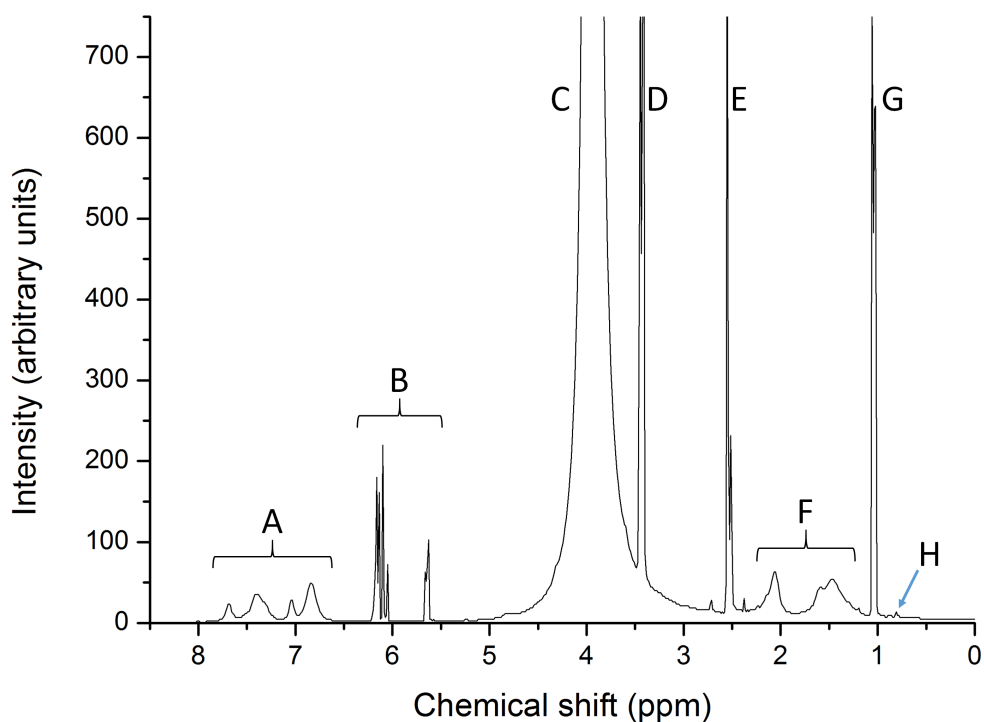


Figure 3.9: NMR spectrum of the swelling medium for polyacrylamide hydrogels.

polyacrylamide and acrylamide are present at lower concentrations, with approximately 20% and 70% reductions respectively.

These results tell us that the polymerisation reaction is incomplete (which is to be expected) as there are quantities of free polymer and un-reacted monomer present in the polyacrylamide hydrogel after polymerisation that will leave the polymer network upon swelling. This will be most prevalent during the first swelling but will occur on subsequent swellings, to diminishing degrees. This is significant as, during swelling, these molecules will be leaving the polymer network as water molecules enter, which adds complexity to the system. Whether this has any observable effect on the hydrogel swelling will be discussed later in this chapter.

3.2 Optical measurements

3.2.1 Cross-link density dependency of swelling

It has been established in Section 1.4.1 that the swelling behaviour of hydrogels is heavily influenced by the cross-link density. When creating OCPCs it is necessary to understand this relationship so as to inform the selection of the concentrations of both the conventional and oligonucleotide cross-linkers. Figure 3.10 shows the fractional volume increase, δ_v , (as defined by Equation 2.1) as a function of the cross-link density for polyacrylamide hydrogels (0 mg/ml carbon, 0 mol% wrt monomer oligonucleotide cross-linker), as described in Section 2.2.1. The swelling behaviour with respect to cross-link density falls into one of two distinct regions. At cross-link densities below 1.0 mol% wrt monomer, δ_v decreases with increasing cross-link density, following what appears to be a broadly linear relationship. The observed volume changes can be significant, with lower cross-link density samples more than doubling in volume.

For cross-link densities greater than or equal to 1.0 mol% wrt monomer, there is little or no observable volume change upon immersion in water, with all data points falling within the error bounds of zero fractional change. It can be concluded that for cross-link densities greater than or equal to 1.0 mol% wrt monomer the equilibrium volume is less than or equal to the synthesis volume and therefore no swelling (relative to the synthesis volume) occurs when the hydrogel is immersed in water.

During polymerisation, a small reduction in the droplet volume as the cross-links form is to be expected [208,209]. Therefore, given how δ_v is defined, negative values are possible

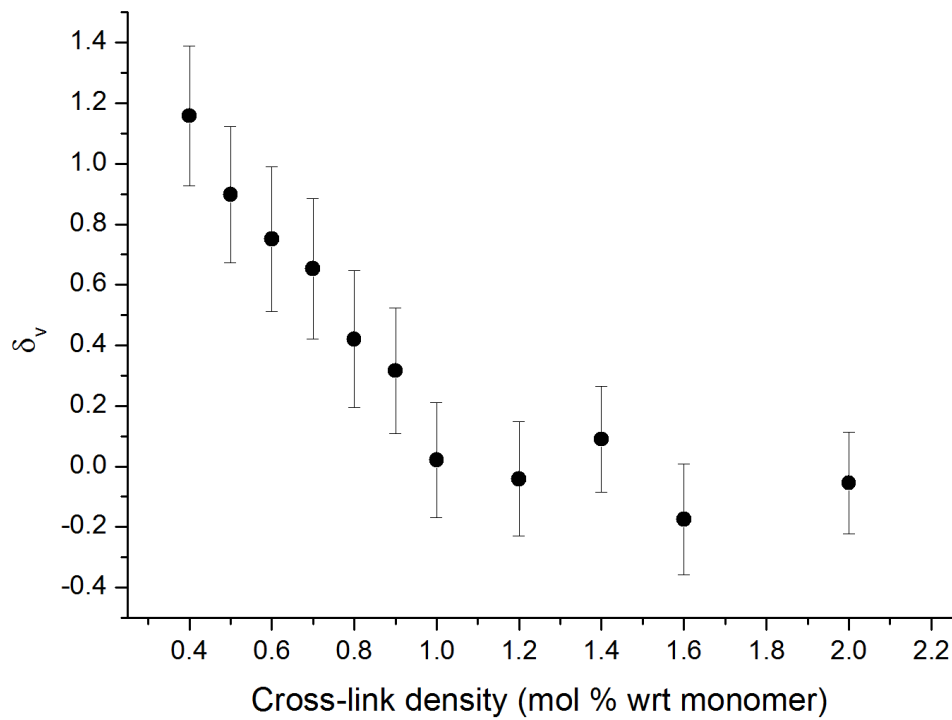


Figure 3.10: Fractional volume increase as a function of cross-link density for polyacrylamide hydrogels. $\delta_v \equiv \frac{V-V_i}{V_i}$, where V is the droplet volume and V_i is the droplet volume at polymerisation.

in these tests. δ_v is defined relative to the volume at polymerisation as this represents the most stable reference point with the lowest experimental uncertainty. The error bars in Figure 3.10 represent the standard error on the mean. The variation between samples will be a result of any variation in the pipetted volume and the measurement error of the volume using the imaging method described in Section 2.2.

To maximise the changes to the swelling behaviour of OCPCs that will result from the selective cleavage of cross-links, it is desirable to have cross-link densities in the region of 1.0 mol% and below, wherein any changes to the cross-link density will produce significant changes to the swelling behaviour. For this reason, the composites produced for this thesis were designed to have a primary cross-link density of 0.6 mol% wrt monomer, with an oligonucleotide cross-linker concentration of 0.4 mol% wrt monomer

to produce a total cross-link density of 1.0 mol% wrt monomer. This is to ensure that any cleavage of the oligonucleotide cross-linkers results in a significant volume change. The ratio of oligonucleotide to conventional cross-linkers was chosen as a compromise between providing sufficient oligonucleotide cross-linkers to allow for large changes in cross-link density and maximising the volume of OCPC that can be produced from a given amount of oligonucleotide, thereby maximising cost-effectiveness.

3.2.2 Differential swelling

Having established the optimal primary and oligonucleotide cross-linker densities, the selective swelling behaviour of OCPCs was established by preparing samples and immersing them in analyte and control solutions and measuring the resultant volume changes. Figure 3.11 shows the average δ_v for OCPCs (0 mg/ml carbon) swollen in oligonucleotide solutions with varying degrees of complementarity for 60 minutes, as described in Section 2.2.1. Differential swelling occurs, with droplets in analyte (A_0) solutions swelling to a δ_v value of approximately 0.7, more than three times the value observed for solutions of a random oligonucleotide sequence (R). This is clear evidence of the selective cleavage of the oligonucleotide cross-linkers in the presence of the analyte molecules. This differential swelling is also evident between analyte solutions and solutions of very similar oligonucleotide sequences. In both A_5 and A_1 solutions (differing from A_0 by 5 and 1 nucleotides respectively) the OCPCs display values of δ_v that are comparable to that of R solutions, indicating that little or no oligonucleotide cross-link cleavage is occurring, beyond those due to thermal effects (see Section 3.2.5).

The error bars in Figure 3.11 represent the standard error on the mean. The variation

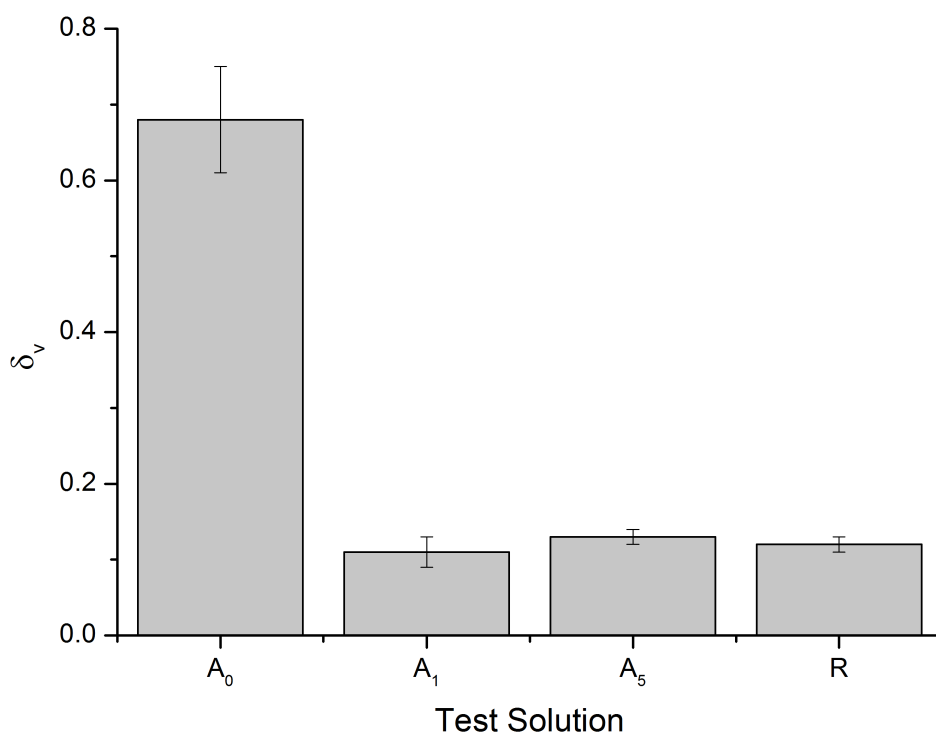


Figure 3.11: Fractional volume increase for OCPCs in various oligonucleotide solutions. The solutions contained $1 \mu\text{M}$ of either a perfectly complementary analyte sequence (A_0), a single-mismatch sequence (A_1), a five-mismatch sequence (A_5) or a random sequence (R). The cross-link density was 0.6 mol% wrt monomer MBA, 0.4 mol% wrt monomer oligonucleotide cross-linker. All solutions contained 150 mM sodium chloride (NaCl) and 1 mM phosphate buffer. $\delta_v \equiv \frac{V - V_i}{V_i}$, where V is the droplet volume and V_i is the droplet volume at polymerisation.

between the samples appears to approximately represent a percentage error and will be the result of the experimental error of the pipetting of the OCPC droplets and the measurement of their swollen volume.

It is clear from these results that OCPCs can demonstrate high specificity, with their differential swelling differentiating between single-base mismatches. This is a highly desirable characteristic for any potential oligonucleotide detection technology.

3.2.3 Kinetic swelling

In order to understand the dynamic swelling behaviour of OCPCs, composite droplets were imaged over time as they swell. This technique was used to investigate the effects of cross-link density upon swelling and the repeatability of that swelling. Additionally, the dependency of the selective swelling behaviour of OCPCs upon analyte concentration was investigated. Figure 3.12 shows δ_v against time for polyacrylamide/carbon nanopowder composites (0 mol% wrt monomer oligonucleotide cross-linkers) as they swell in water from their dried state (as described in Section 2.2.2). It shows results for two different cross-linking densities, and for each there are two sets of data. ‘First swelling’ refers to the first time the sample has been swollen from the dried state after polymerisation. After this, the samples were re-dried and swollen again. This is the ‘second swelling’.

Figure 3.12 shows that the swelling of these composite droplets is highly repeatable, with no discernible differences between the first and second swellings. This is in spite of the differences between the first and second swellings in terms of the quantities of polymer and un-reacted monomer that will leave the polymer matrix, discussed in Section 3.1.2. It appears that these differences have no measurable effect on the total volume of the composite droplet. The difference in final volume between the different cross-link densities is clearly evident, with the 0.6 mol% composites reaching volumes approximately 50% of the volume at polymerisation greater than the 1.0 mol% composites, confirming the predictions discussed in Section 1.4.1. For both cross-link densities, samples with a synthesis volume of 2 μl will reach their equilibrium volume within a time span of approximately one hour.

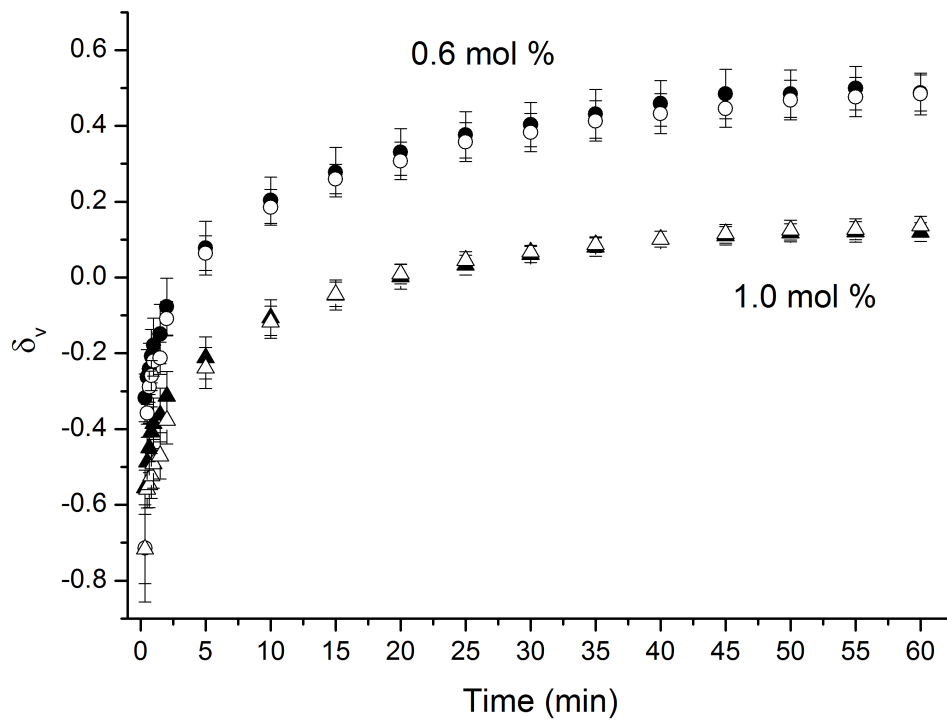


Figure 3.12: Fractional volume increase against time for swelling polyacrylamide hydrogels of different cross-linking densities. ● - cross-link density of 0.6 mol% wrt monomer MBA, first swelling after polymerisation, ○ - second swelling; ▲ - cross-link density of 1.0 mol% wrt monomer MBA, first swelling after polymerisation, △ - second swelling. The carbon loading was 10 mg/ml. $\delta_v \equiv \frac{V - V_i}{V_i}$, where V is the droplet volume and V_i is the droplet volume at polymerisation.

The negative values for δ_v at early times in Figure 3.12 are a result of the fact that these hydrogels have been dried prior to their immersion, meaning that their initial volume will be smaller than their volume at polymerisation, V_i . Hence, the 1.0 mol% samples, which demonstrate no swelling beyond their volume at polymerisation (Figure 3.10), begin at negative values and swell to a δ_v of approximately zero.

Figure 3.13 shows the data for the first swellings for each cross-link density from Figure 3.12 re-expressed as percentages of their peak volume. The composites follow the same swelling profile, swelling to approximately 70% of their maximum volumes within the first five minutes. Thus it can be concluded that the swelling mechanism is the same

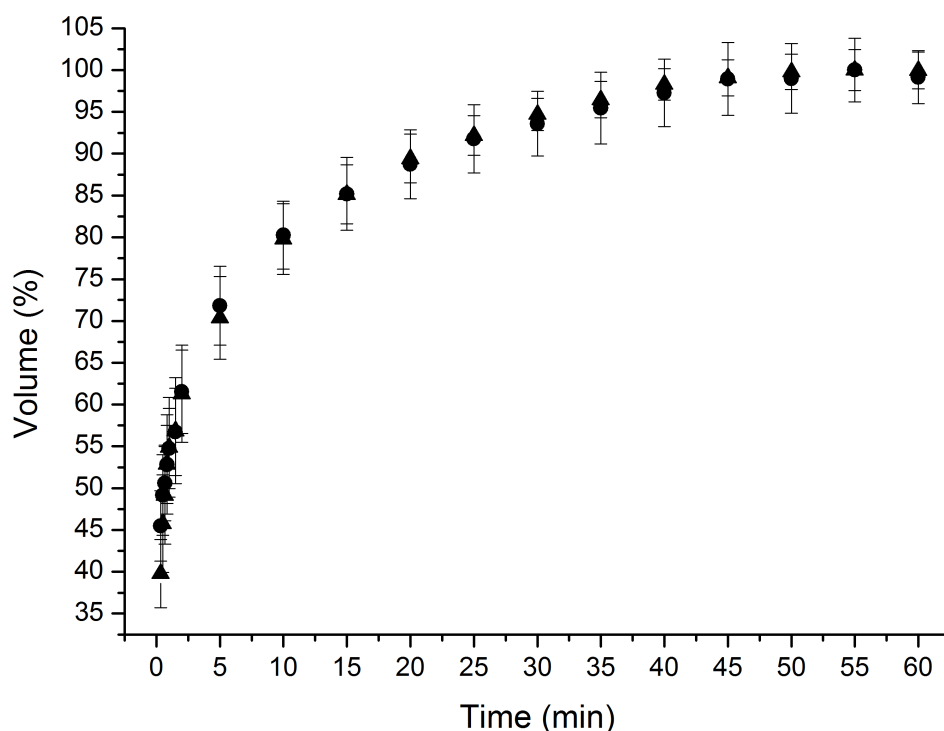


Figure 3.13: Volume against time as a percentage of the maximum volume for swelling polyacrylamide hydrogels of different primary cross-link densities. The primary cross-link densities were 0.6 (●) and 1.0 (▲) mol% wrt monomer MBA, 0 mol% wrt monomer oligonucleotide cross-linkers. The carbon loading was 10 mg/ml.

irrespective of the maximum volume to which hydrogel swells. Additionally, the fact that the majority of the swelling occurs in a relatively short space of time, means that it may not be necessary to use the entirety of the swelling time for detection. A fast swelling response is advantageous if such composites are to form the basis of a sensing technology, as discussed previously it is highly desirable to return results in 10 minutes or less.

Figure 3.14 shows δ_v for OCPC droplets (0.4 mol% wrt monomer oligonucleotide cross-linker) as a function of time as they swell from a dried state in either 10 μM A_0 or R solutions (as described in Section 2.2.2). Samples in A_0 solutions swell to greater volumes than those in R solutions, which is further evidence of the selective cleavage

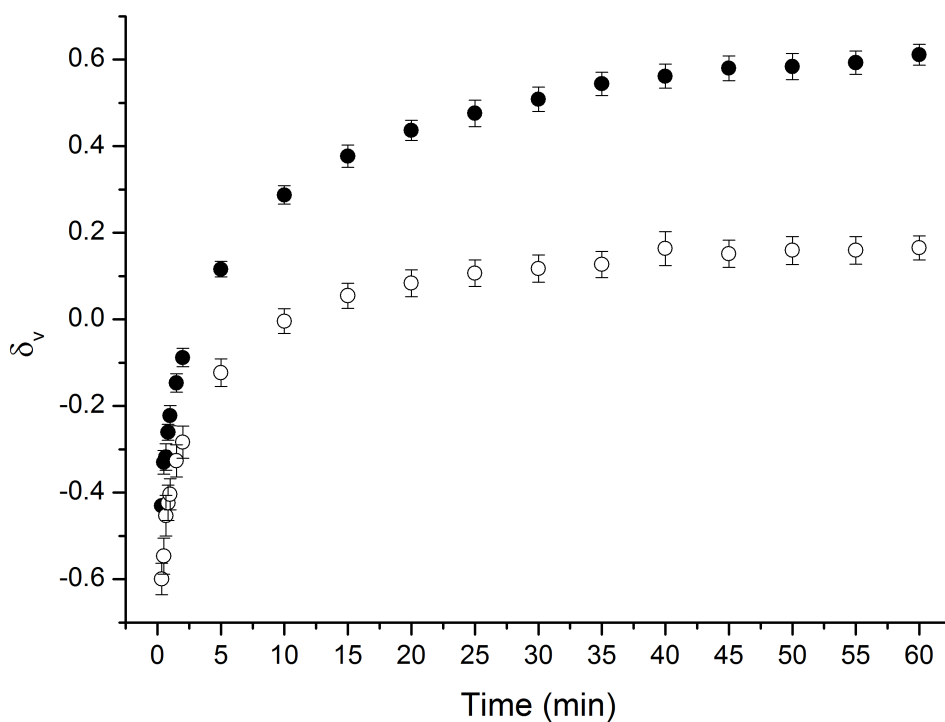


Figure 3.14: Fractional volume increase against time for oligonucleotide-functionalised hydrogels in $10 \mu\text{M}$ A_0 (●) and R (○) solutions (150 mM NaCl, 1 mM phosphate buffer). The cross-link density was 0.6 mol% wrt monomer MBA, 0.4 mol% wrt monomer oligonucleotide cross-linker. The carbon loading was 10 mg/ml. $\delta_v \equiv \frac{V-V_i}{V_i}$, where V is the droplet volume and V_i is the droplet volume at polymerisation.

of oligonucleotide cross-linkers in analyte solutions. Figure 3.14 also shows that the differences in the swelling behaviour between the two solutions are evident within 10 minutes and that the majority of swelling is complete within one hour.

Figure 3.15 shows the same data as for Figure 3.14 but with the addition of results for equivalent tests with reduced analyte concentration. It can be seen that for concentrations ranging from $10 \mu\text{M}$ to 100 nM the OCPCs show near identical swelling behaviour, with any variation being within the bounds of experimental uncertainty. It might have been expected that the rate of swelling would vary with analyte concentration (as has been shown to be the case in experiments of a similar nature,

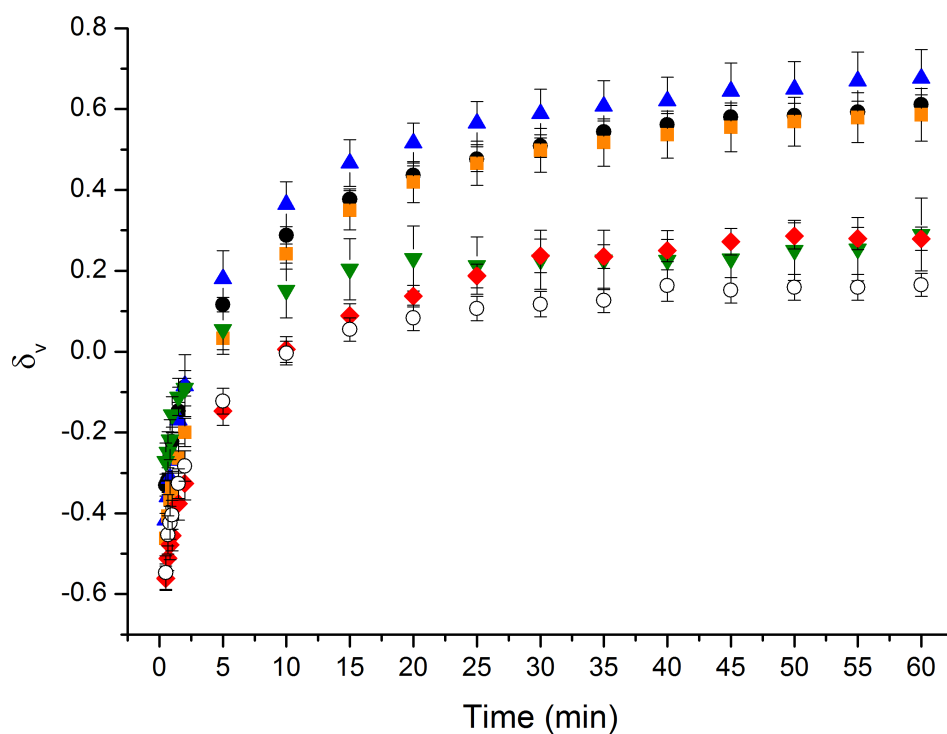


Figure 3.15: Fractional volume increase against time for oligonucleotide-functionalised hydrogels in A_0 solutions of varying concentrations - $10\ \mu\text{M}$ (\bullet), $1\ \mu\text{M}$ (\blacktriangle), $100\ \text{nM}$ (\blacksquare), $10\ \text{nM}$ (\blacktriangledown) and $1\ \text{nM}$ (\blacklozenge), and a $10\ \mu\text{M}$ R solution (\circ). The cross-link density was $0.6\ \text{mol}\%$ wrt monomer MBA, $0.4\ \text{mol}\%$ wrt monomer oligonucleotide cross-linker. All solutions contained $150\ \text{mM}$ NaCl and $1\ \text{mM}$ phosphate buffer. $\delta_v \equiv \frac{V-V_i}{V_i}$, where V is the droplet volume and V_i is the droplet volume at polymerisation.

only swelling from an equilibrated state, rather than a dried state [124]), but this is evidently not the case. There are two processes taking place: 1) the swelling of a hydrogel as water diffuses into the polymer network, and 2) the selective cleavage of cross-links in the presence of analyte molecules. It appears that the second process is significantly faster than the first, such that, for analyte concentrations at or above $100\ \text{nM}$, the swelling is limited by the rate at which the solvent can enter into the hydrogel and not the rate at which cross-links are being cleaved. This corresponds to what has been shown in the models of Tanaka *et al.* in which it is shown that the characteristic swelling time is dependent solely upon the diffusion coefficient and the

final swollen volume [110]. Insofar as these parameters are not affected by the analyte concentration, neither is the rate of swelling of OCPCs.

The swelling behaviour begins to diverge at concentrations of 10 nM, at which point the initial rate of swelling is the same as for higher concentrations, but the rate drops off with time and the droplets tend towards a lower volume. At a concentration of 1 nM the initial rate of swelling is indistinguishable from that of OCPC droplets in R solutions. It appears as if the 1 nM samples may reach a higher volume than those in a random solution, however the uncertainty ranges are such that this cannot be said with certainty. There is no appreciable difference between OCPCs swelling in R solutions of different concentrations.

It can be concluded from the above that the lower limit at which differential swelling can be distinguished, under this experimental configuration, is of the order of 10 nM. It also appears that, for OCPC droplets for the volumes investigated herein, the analyte concentration cannot be inferred from the rate of swelling.

3.2.4 A note on errors

The error bars in Figures 3.12 to 3.15 represent the standard error on the mean. The variation between samples will be the result of the experimental error in the pipetting of the composite droplets and the measurement of their volume. Figure 3.16 A shows the data from Figure 3.14, represented in the manner adopted throughout this thesis, as means along with standard errors on the mean. Figure 3.16 B shows the individual data series that were used to calculate the means. It can be seen that the error bars

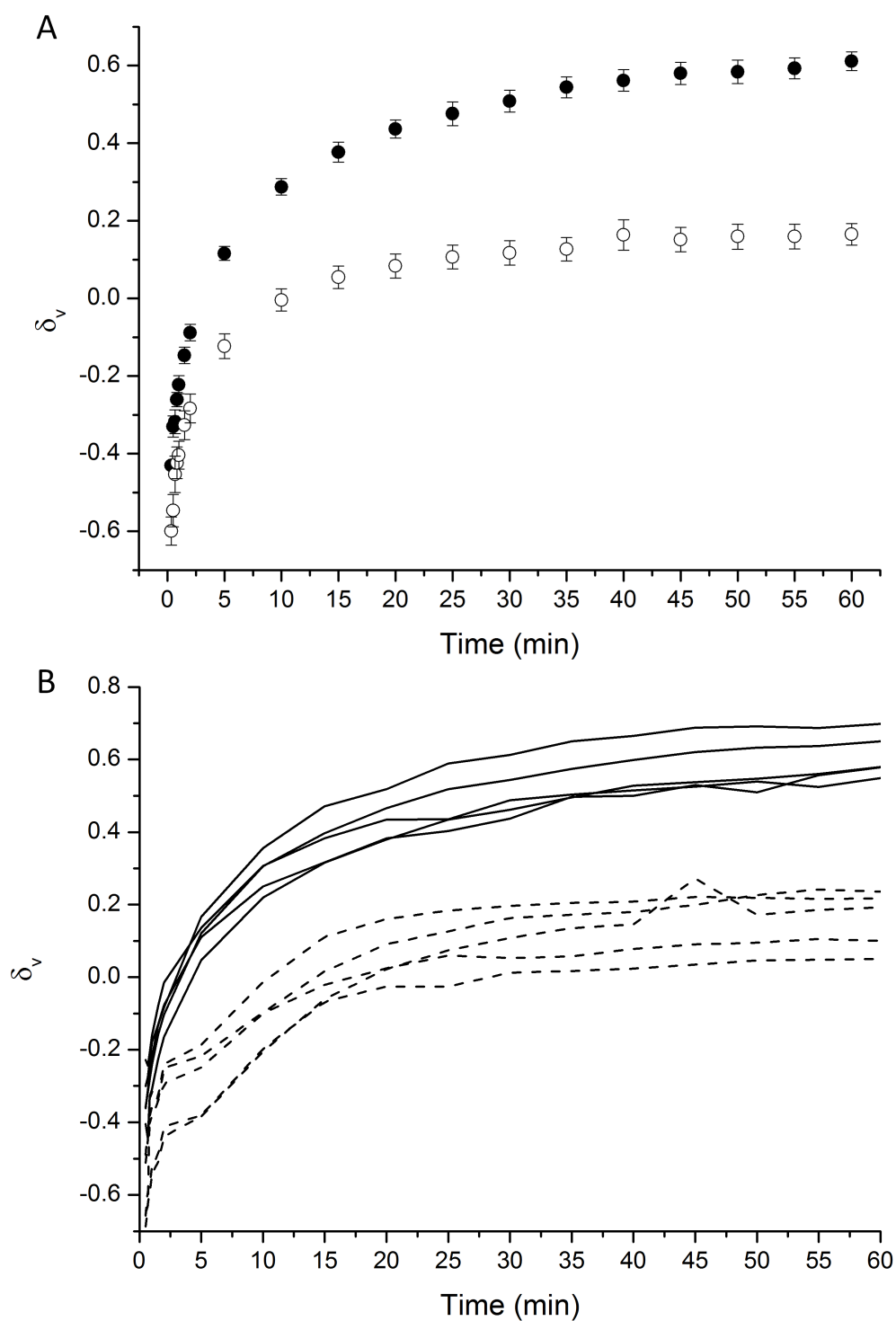


Figure 3.16: Example of the systematic nature of the uncertainty. A - The fractional volume increase for oligonucleotide-functionalised hydrogels in A_0 (\bullet) and R (\circ) solutions (as for Figure 3.14) represented as a mean and a standard error on the mean. B - The individual data series that comprise the averages shown in A (A_0 - solid, R - dashed). $\delta_v \equiv \frac{V - V_i}{V_i}$, where V is the droplet volume and V_i is the droplet volume at polymerisation.

in Figure 3.16 A are primarily a result of systematic errors between data series rather than noise within any individual data series.

The principle sources of uncertainty being systematic is a common feature throughout most of the results presented in this thesis, and this is significant as systematic errors will be simpler to correct for than random noise. However, in the interests of the clarity of the figures, throughout this thesis it was elected to present the data as mean values alongside standard errors on those means.

3.2.5 Thermal stability

For any potential sensor technology it important to understand the effects of temperature upon the response. Thus it is necessary to understand how changing temperature affects the swelling of OCPCs. Figure 3.17 shows δ_v for the final volume as a function of temperature for OCPCs (0.4 mol% wrt monomer oligonucleotide cross-linker) in both 10 μ M A₀ and R solutions (as described in Section 2.2.1). The experimental data is shown alongside a least-squares fit to the sigmoid curve equation:

$$y = D + \frac{A - D}{1 + (x/C)^B} \quad (3.1)$$

where A is the value of the lower plateau region, B is an exponent which determines the slope of the curve, C is the midpoint of the curve and D is the value of the upper plateau region. This equation is commonly referred to as the four-parameter logistic model. [210–212]

There is considerable variation in δ_v , with it ranging between approximately 0.5 and 1.2 for analyte solutions and approximately -0.1 and 1.0 for random solutions. This

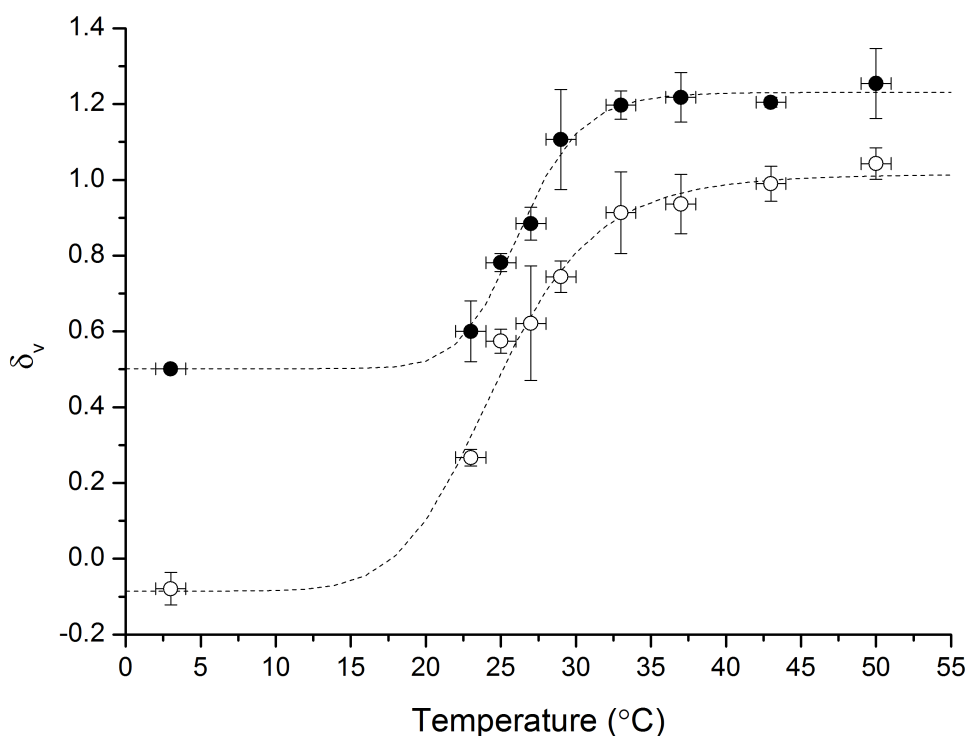


Figure 3.17: Fractional volume increase against temperature for OCPCs in 10 μM A₀ solution (●) and 10 μM R solution (○). The OCPCs contained 0 mg/ml carbon, 0.6 mol% MBA and 0.4 mol% wrt monomer oligonucleotide cross-linker. The oligonucleotide solutions contained 150 mM NaCl and 1 mM phosphate buffer. The dashed lines represent the least-squares fit to the sigmoidal curve equation. $\delta_v \equiv \frac{V - V_i}{V_i}$, where V is the droplet volume and V_i is the droplet volume at polymerisation.

variation is due to thermal dehybridisation of the oligonucleotide cross-linkers. At low temperatures ($<10^\circ\text{C}$) very few of the oligonucleotide cross-links are thermally dehybridised. As the temperature nears the melting temperature (T_m)¹ the number of thermally dehybridised cross-links begins to increase rapidly until, at higher temperatures ($>40^\circ\text{C}$), the majority of the oligonucleotide cross-links are dehybridised and δ_v levels off. This behaviour results in the characteristic sigmoidal patterns for δ_v versus temperature seen in Figure 3.17.

The sigmoidal nature of the analyte curve in Figure 3.17 implies that, even for relatively

¹The temperature at which 50% of the oligonucleotide cross-linkers are dehybridised due to thermal effects.

high analyte concentrations, up to and including room temperature a significant proportion of the oligonucleotide cross-links remain un-cleaved.

Performing least-squares analysis on the data yields a value of C for the A_0 solution of $(26.3 \pm 0.3)^\circ\text{C}$ and $(24.7 \pm 0.5)^\circ\text{C}$ for the R solution, suggesting an average T_m for the system of $(25.5 \pm 0.6)^\circ\text{C}$. Theoretical predictions of the melting temperature for the overlap of the sensor and blocker strands yield a T_m of 32.2°C [213]. Such models deal with oligonucleotides free in solution, rather than anchored in a polymer matrix, and as such the differences between the experimental and theoretical values are most likely a result of the steric effects of the polymer matrix.

The difference between the A_0 and R samples at lower temperatures can be explained by the selective cleavage of oligonucleotide cross-links. When little or no thermal dehybridisation occurs there are few cross-links broken for samples in R solutions, whereas for A_0 solutions a large number of cross-links will be cleaved via the preferential binding of the analyte molecules, leading to larger volumes. However, there is also a smaller difference between the two at higher temperatures, where it would be expected that all of the oligonucleotide cross-links would be thermally dehybridised, where the A_0 samples swell to greater volumes than the R samples. This difference can be explained by the fact that in the A_0 solution the analyte sequences will bind to the sensor strands, thereby increasing the ionic content of the macromolecular structure. The additional charge contributed by the extra oligonucleotides incorporated into the polymer matrix leads to additional repulsion between the strands, and hence additional swelling. Full discussions on how the ionic makeup of hydrogels influences swelling behaviour can be found elsewhere [132, 214]. Whilst the sensor and blocker strands are only partially

complementary, the sensor and analyte strands are fully complementary and thus can be expected to have a much higher T_m . Theoretical predictions for this duplex give a T_m of approximately 72°C [213], thus it is reasonable to expect that the analyte sequence will remain hybridised with the sensor strand within the temperature range investigated here.

The thermal instability shown in Figure 3.17 is particularly significant for OCPCs due to their cross-linking structure (Figure 1.9). If an oligonucleotide cross-link is cleaved as a result of thermal dehybridisation, this will result in increased swelling (as seen in Figure 3.17). This swelling will result in the sensor and blocker strands moving away from each other, making them less likely to re-hybridise. Thus the increased swelling due to thermal dehybridisation will not be fully reversible by simply cooling the sample.

Figure 3.18 shows data for the same experiment carried out using polyacrylamide hydrogels without any oligonucleotide cross-linkers. There is no discernible relationship between δ_v and temperature for hydrogels that are not oligonucleotide-functionalised. This indicates that all of the variation with temperature evident in Figure 3.17 is a result of the oligonucleotide cross-linkers and their thermal dehybridisation. As the samples are removed from solution to be imaged, and the imaging takes place at $(20 \pm 1)^\circ\text{C}$, the samples will be at room temperature when imaged (due to their small volume they will change temperature rapidly). Thus Figure 3.18 does not imply that polyacrylamide does not display any thermal expansion, rather that the effects of whatever thermal expansion does occur are reversible, unlike the effects of thermal dehybridisation, as seen in Figure 3.17.

The horizontal error bars in Figures 3.17 and 3.18 represent the uncertainty of the water

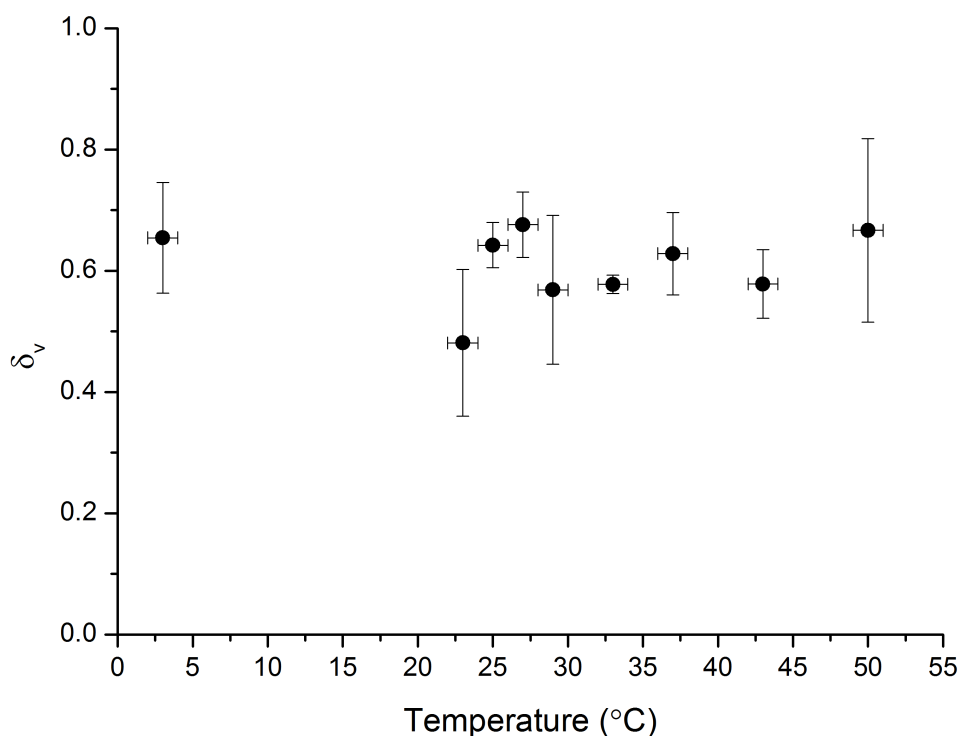


Figure 3.18: Fractional volume change against temperature for non-oligonucleotide-functionalised polyacrylamide hydrogels in 10 μ M R solution (150 mM NaCl, 1 mM phosphate buffer). The cross-link density was 0.6 mol% wrt monomer MBA. $\delta_v \equiv \frac{V-V_i}{V_i}$, where V is the droplet volume and V_i is the droplet volume at polymerisation.

bath used to maintain the solution temperature (Section 2.2.1). The vertical error bars represent the standard error on the mean. As before, the variation between samples will be a result of the error in the pipette dispensing volume and the measurement error on the swollen volume.

Non-specific swelling as a result of variations in temperature is extremely undesirable from the point of view of developing a sensor technology, as increased swelling due to thermal effects constitutes a false positive. Methods by which the effects of this temperature dependence could be mitigated will be discussed in Section 6.3 and the improvements to thermal stability offered by morpholino cross-linked polymers will be discussed in Chapter 5.

It is worth noting that T_m will be dependent upon the guanine (G)/cytosine (C) content (*i.e.* the proportion of nucleotides that are either G or C) of the overlapping section between the sensor and blocker strands. G and C hybridise with 3 hydrogen bonds compared to 2 for adenine (A) and thymine (T), meaning that these pairings are inherently more stable. Therefore sequences with a higher G/C content will form more stable duplexes with a correspondingly higher T_m [215,216]. Thus the thermal stability of OCPCs may vary significantly for different analytes. The G/C content of the overlap in our system (designed as an analogue of miR-92a) is relatively low, at 33%. Other potential analytes may have higher G/C contents and thus more favourable thermal stabilities.

3.3 Conclusions

Conductive composites were synthesised by the incorporation of conductive carbon particles into polyacrylamide hydrogels. Carbon loading densities greater than 20 mg/ml result in poor composite formation, but at carbon loading values of 20 mg/ml or below, highly porous hydrogels containing distributed networks of conductive particles can be created.

Cross-link density influences the swelling behaviour of polyacrylamide hydrogels and the region where changes to the cross-link density will produce significant volume changes has been found to be 1.0 mol% wrt monomer and below. This has informed a selection of cross-linker concentrations of 0.6 mol% wrt monomer of conventional cross-linker and 0.4 mol% wrt monomer of oligonucleotide cross-linker.

Quantities of un-reacted monomer and short-chain polymer are found in the polymer droplet immediately after polymerisation, but these will leave the matrix over the course of successive swellings and do not appear to have a measurable impact upon the volume of the polymer droplets.

Reduced cross-link density leads to increased swelling, resulting in a volume difference of approximately 50% between hydrogels of 0.6 and 1.0 mol% wrt monomer. Additionally, these hydrogels swell to approximately 70% of their maximum volume within 5 minutes and this behaviour is independent of the maximum volume.

OCPCs demonstrate selective swelling in solutions of analyte oligonucleotide molecules when compared to random control oligonucleotides, with single-base specificity. Under this experimental configuration the rate of swelling does not appear to be dependent upon the analyte concentration. Additionally, the limit at which differential swelling can be distinguished is of the order of 10 nM. Whilst this limit is comparable to that reported by Stokke *et al.* [124], it is relatively high compared to techniques such as those outlined in Table 1.3. Methods by which this detection limit may be improved will be discussed in Chapters 5 and 6.

The final swelling volumes of OCPCs vary considerably with temperature due to the non-specific thermal dehybridisation of the oligonucleotide cross-links. In both analyte and random solutions, the temperature at which 50% of oligonucleotide cross-linkers are thermally dehybridised is approximately 25°C, implying that a significant number of oligonucleotide cross-linkers will be broken in a non-specific manner at room temperature. This non-specific swelling due to thermal effects will be detrimental to any potential sensing applications.

As stated in Chapter 1, the central premise of this thesis is that a new method of microRNA (miRNA) detection may be achieved through the transduction of the swelling of oligonucleotide cross-linked polymers by incorporating a conductive component to create OCPCs. With this aim in mind it can be concluded that the strengths of the composites described in this chapter are as follows:

- they demonstrate selective swelling in analyte solutions,
- the volume change as a result of this selective swelling is significant, and
- the selective swelling demonstrates single-bases specificity.

The remaining challenges are as follows:

- the analyte concentration cannot yet be inferred from the response,
- there is a significant degree of thermal instability, and
- the limit of detection is not currently sufficient for the detection of circulating miRNA.

Possible methods by which these challenges could be addressed will be discussed in Chapters 5 and 6. The following chapter presents the results of the investigations of the electrical properties of OCPCs and of their potential as a mechanism for oligonucleotide detection.

Chapter 4

Electrical measurement of composite swelling: results and discussion

4.1 Electrode design and fabrication

In the first instance, off-the-shelf electrode devices (Section 2.3.1) were used to measure the electrical properties of the composites described in Section 2.1. However, when undergoing significant volume changes, the composites frequently detached from the substrate surface. Additionally, when the composites remained in place, large variances and discontinuities of the electrical properties of the composites were observed. An example of such an occurrence is shown in Figure 4.1 where the resistance of two composites, of the same carbon and cross-linker concentrations, are shown against time

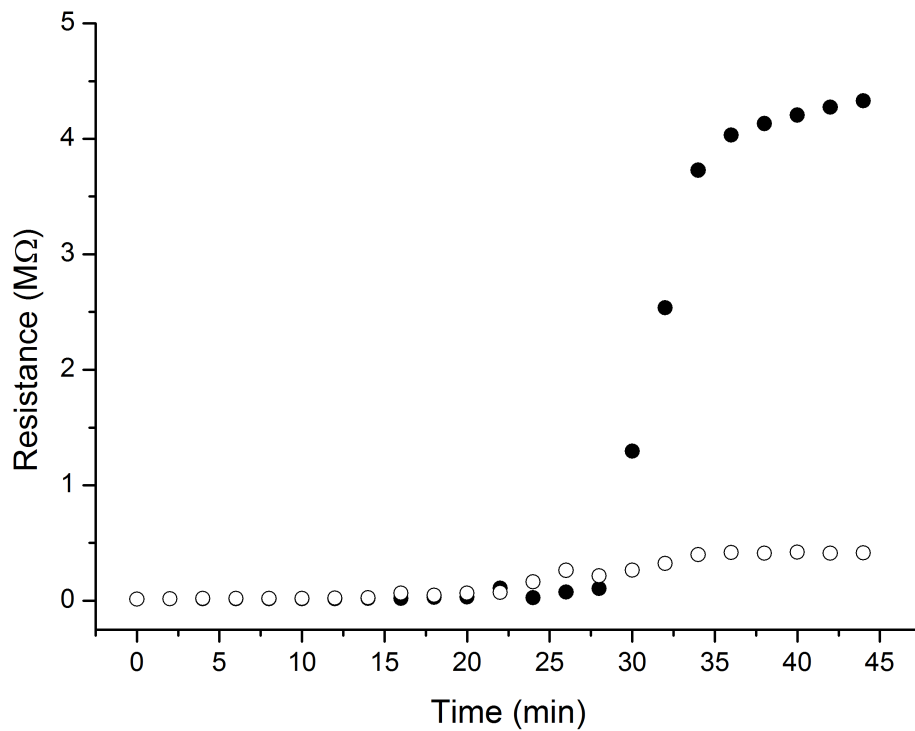


Figure 4.1: An example of anomalous electrical measurements seen with the off-the-shelf electrode devices. The resistance of carbon nanopowder composites are shown against time as the swell in deionised (DI) water. Both samples had identical properties (i.e. cross-link density and carbon loading) but reached radically different resistances. This is believed to be a result of delamination of the second sample (●).

as they swell. The measured values for the resistance differ dramatically, to a degree that cannot be explained by any differences in their volume or carbon dispersion. It is believed that such occurrences are the result of the composite adhering to the silicon dioxide (SiO_2) of the substrate but not the metal of the electrodes, such that, as the composites swell, they push away from the electrode surface, leading to anomalously high resistances (Figure 4.2). Throughout this thesis this phenomenon will be referred to as ‘delamination’. Delamination differs from detachment as the composites remain in place, adhered to the substrate but not the electrodes, and the effects are only apparent through the measurement of the electrical properties.

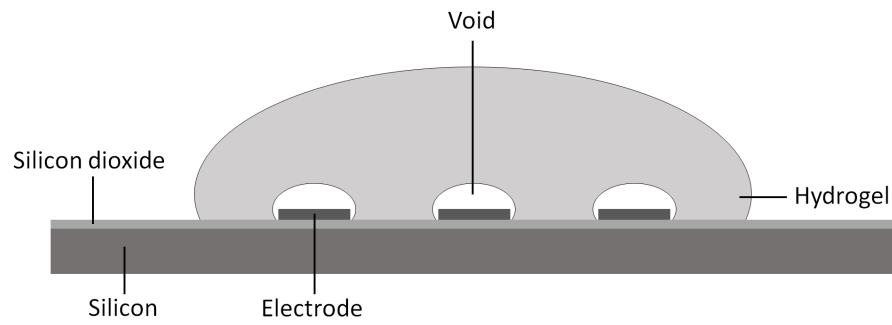


Figure 4.2: Illustration of the mechanism believed to be behind the observed delamination effects. As the hydrogels swell at the electrode surface they adhere more strongly to the substrate than to the metal. This causes differential stress resulting in the hydrogels pushing away from the electrode surfaces, causing void spaces occupied solely by the swelling medium to be formed around the electrodes. For the purposes of clarity, the electrodes and the void spaces are not shown to scale.

The silanisation procedure described in Section 2.3.3 was added to ensure that the composites remained in place on the substrate surface when undergoing significant volume changes. The silane groups of the 3-(trimethoxysilyl) propyl methacrylate (TPM) will covalently bond to the SiO_2 layer of the substrate, establishing a surface coated with pendant methacrylate groups (Figure 4.3). During the free-radical polymerisation, the methacrylate groups will participate in the reaction, covalently bonding the hydrogel to the substrate surface, thereby anchoring it in place.

After the addition of the silanisation step the composites no longer detached from the substrate surface under the experimental conditions described in Chapter 2. However, delamination still occurred.

The off-the-shelf electrode devices were substituted with the custom made alternatives described in Section 2.3 in order to increase the area of substrate relative to electrode beneath the composite and to reduce the span of the interdigitated electrode (IDE) array such that it was smaller than the span of a composite droplet. As such, the digit spacing was increased from $10\ \mu\text{m}$ to $40\ \mu\text{m}$ (whilst keeping the digit width constant),

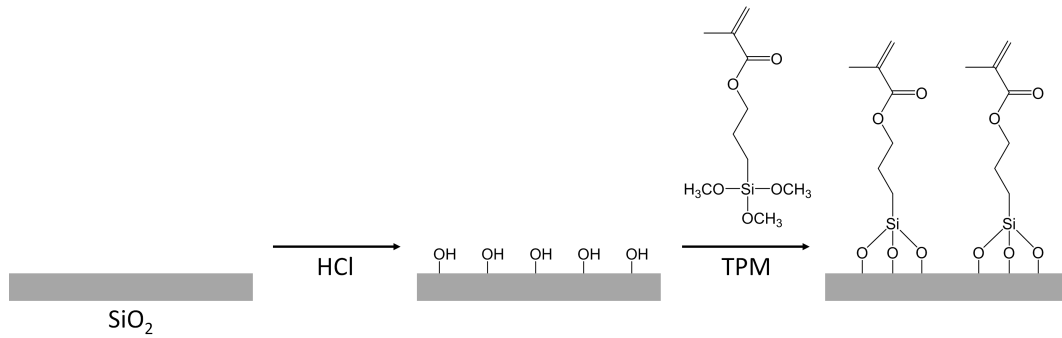


Figure 4.3: The silanisation mechanism. The TPM molecules are covalently bonded to the activated SiO_2 surface of the substrate, resulting in a surface coated with methacrylate groups. Adapted from Schlecht *et al.* [217].

thereby reducing the ratio of metal to substrate from 1:1 to 1:4. Additionally, the dimensions of the IDE array were reduced from approximately 6×5 mm to 1.5×1.46 mm. These dimensions were selected so that the IDE array would be completely covered by a $2 \mu\text{l}$ droplet, thus allowing the composite to be bonded to the substrate around its circumference. This droplet volume was chosen as a compromise between having as small a droplet as possible, so as to maximise the number of tests that can be performed using a given volume of composite and reduce the cost of any end device, and maintaining the ability to reliably deposit the droplets by manual pipetting. Reliable positioning of the droplets on the electrodes is important for ensuring consistency in the tests described in the following sections.

Figure 4.4 shows a photograph of the (single-layer) electrode devices alongside a microscope image of the IDE array. Platinum (Pt) was chosen as the electrode material due to its high conductivity, low reactivity and common usage in microfabrication. The SiO_2 layer is necessary to insulate the IDE array from the conductive silicon (Si) substrate. This Si/ SiO_2 combination was chosen due to its ubiquity in microfabrication

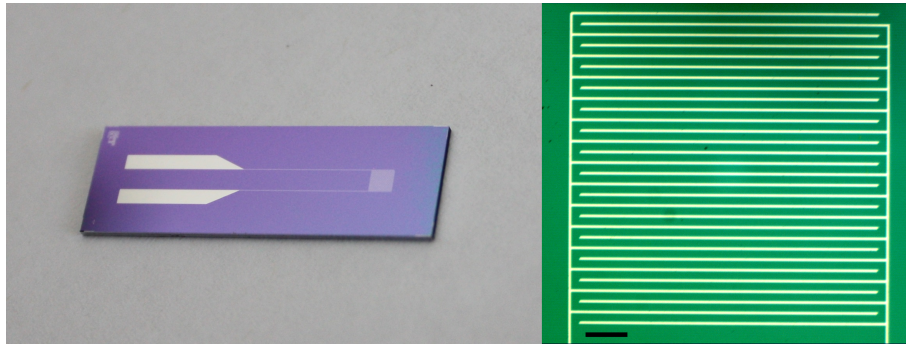


Figure 4.4: Left-hand side: Photograph of a single-layer IDE device. Right-hand side: Microscope image of the interdigitated electrode array at $\times 2.5$ magnification. The scale bar represents $200 \mu\text{m}$.

and the ease of its formation. The titanium (Ti) adhesion layer is necessary as Pt does not adhere well to SiO_2 . [218–223]

For the purposes of this research the passivation layer is not strictly necessary, but can be added to serve the dual purposes of protecting the connecting tracks and aiding the deposition of the composites onto the IDE. The second of these will become increasingly important in future work as the IDEs and the composite droplets decrease in size in order to reduce cost, improve response times and to allow multiple sensors to be fabricated upon a single device. Parylene ($(\text{CH}_2\text{C}_6\text{H}_3\text{ClCH}_2)_n$) is commonly used for passivation and encapsulation as it is chemically inert and hydrophobic, making it an effective electrolyte barrier [175, 176]. Differences in hydrophilicity between the passivation layer and the SiO_2 substrate surface can be exploited to aid the positioning of droplets over IDE arrays as the droplets will naturally favour the more hydrophilic regions. For the purposes of ease of fabrication, unless otherwise stated, the electrode devices used in the tests detailed in Section 2.4 were single-layer devices.

The changes to the IDE parameters described herein were made in order to improve the adhesion of the composites to the substrate to reduce the frequency of delamination.

The use of the custom made electrode devices described herein, in conjunction with the silanisation procedure described previously, significantly reduced the frequency of occurrence of the effects associated with delamination. These effects were completely eliminated from the tests described in Section 2.4 for composites produced without the inclusion of oligonucleotide cross-linkers. However, when performing direct current (d.c.) resistance measurements of oligonucleotide cross-linked polymer composites (OCPCs) (Section 4.2.3) the measured resistances are occasionally observed to increase rapidly to $\sim 3\text{-}4\text{ M}\Omega$ or higher (similar to what is seen in Figure 4.1). It is believed that these anomalous results are a recurrence of the delamination problem.

The fact that, after the taking the steps above, delamination is only observed when the composites are functionalised with oligonucleotide cross-links may be due to the fact that, in such instances, the composites are anionic and thus will be repulsed by any electrodes that are positively charged. Or simply because oligonucleotide functionalised gels are more hydrophilic and hence swell more in water, leading to greater differential stress at the composite/electrode interface. Delamination occurs only in a minority of cases (between 20 and 40% of samples measured), but the probability of occurrence is dramatically increased by actions that are likely to result in more extreme volume changes of the composite droplets or greater differential stress between the composite and the substrate. For instance, drying the composites in desiccators rather than ambient conditions or attempting swelling measurements at low temperatures ($<10^{\circ}\text{C}$) increases the rate of occurrence of delamination to between 90 and 100%. This is presumably because such, more extreme, changes in volume will increase the strain

at the interface between the composite and the electrode substrate, thereby increasing the likelihood of delamination.

Possible methods by which delamination could be reduced or eliminated will be discussed in Section 6.3. All of the tests described in Section 2.4 were carried out in a manner consummate with reducing the likelihood of delamination wherever possible. However, whenever delamination did occur, the experiments were repeated and any anomalous data treated as outliers and discarded.

4.2 Electrical measurements

This section describes the investigations undertaken into the electrical properties of the composites to determine the optimum electrical measurement technique to quantify their swelling response, and to assess the potential of such an electrical measurement of OCPC swelling as a means of oligonucleotide detection. These include measurements undertaken to determine the percolation thresholds of these composites, so as to inform the choice of carbon particle loading, as well as measurements of the resistance (d.c.) and impedance (alternating current (a.c.)) of the composites as they swell in solution, in order to determine which approach is most appropriate. Throughout this section, the composites are swollen both in DI water and in buffered sodium chloride (NaCl) solutions, the latter being used as it will be necessary to stabilise oligonucleotide cross-linkers and as it provides a better representation of biological samples in terms of both salinity and pH [224–227]. Solutions of 150 mM NaCl and a pH of 7.4 are commonly used when solutions representative of human serum or plasma are required [125, 228–231].

The above tests are performed using a variety of different carbon particle types to determine the effects of parameters such as particle size and aspect ratio on the electrical properties of the composites. Also presented in this section are cyclic voltammetry measurements, performed so as to better understand the chemical processes taking place at the electrode surface during electrical measurement.

4.2.1 Percolation measurements

In order to understand the percolation behaviour of composites of polyacrylamide and various types of carbon particle, and to inform the selection of an appropriate carbon loading density, it is necessary to determine the percolation thresholds of these composites. Figure 4.5 shows the conductivity, σ , for polyacrylamide/carbon nanopowder composites (0 mol% wrt monomer oligonucleotide cross-linker), in their dried state, as a function of the carbon loading density. This is plotted alongside the best fit to the general effective medium (GEM) equation (Equation 1.1). The data follows the characteristic sigmoid pattern expected from GEM theory, beginning at low conductivities and transitioning rapidly to higher conductivities at a critical loading density [150, 158, 160, 161]. The high conductivities correspond to the conductivity of the interconnected conductive networks that are formed at these carbon loading densities [164, 232, 233], as measured using the IDE devices described in Section 2.3. The low conductivities should correspond to the conductivity of the dried polyacrylamide, however they are limited by the measurement range of the multimeter. At loading densities of 5 mg/ml and below the resistances of the composites were above the maximum measurement range of the multimeter and, for the purposes of fitting, a value

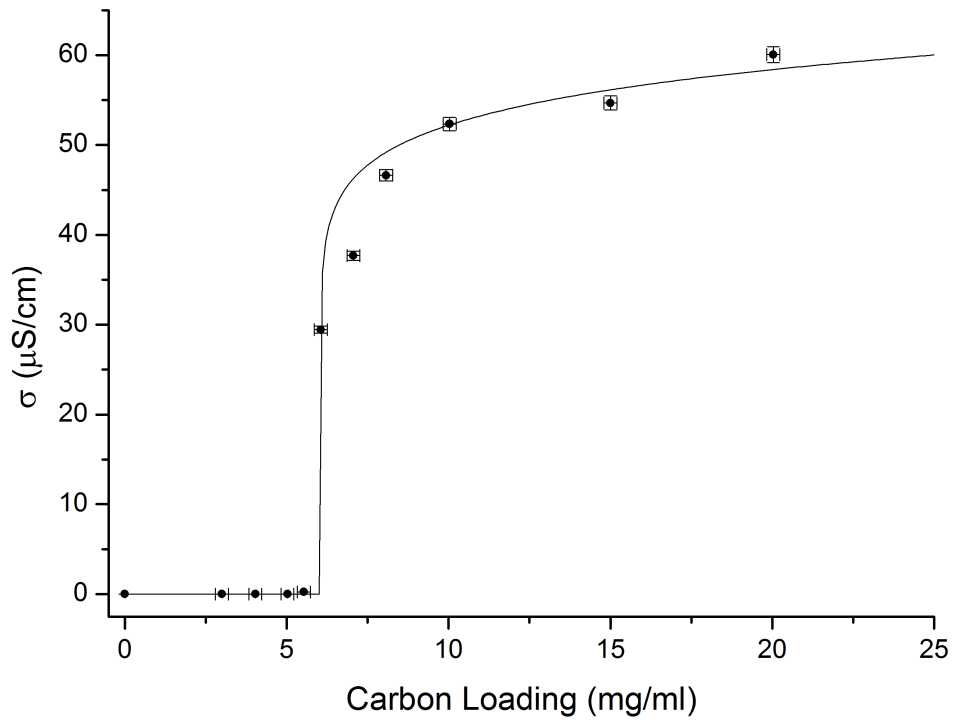


Figure 4.5: Conductivity of polyacrylamide/carbon nanopowder composites as a function of carbon loading (●) shown alongside the best fit to the GEM equation (–). The composites contained 0.8 mol% wrt monomer N, N' methylene-bisacrylamide (MBA) and 0 mol% wrt monomer oligonucleotide cross-linker.

of 120 MΩ was used. This corresponds to the maximum measurable resistance [234].

Whilst this is not ideal, this value represents a very low conductivity (approximately $7 \times 10^{-3} \mu\text{S}/\text{cm}$) and therefore larger resistance values would produce a negligible impact upon the curve fitting.

Simple conversion of resistance to conductivity for samples upon IDEs can be achieved by the calculation:

$$\sigma = \frac{\kappa}{R} \quad (4.1)$$

where κ is the cell constant of the IDE [235] and R is the resistance. A derivation of κ for the IDE devices used in this thesis is presented in Appendix D.

Figure 4.5 shows that polyacrylamide/carbon nanopowder composites have a percolation threshold of approximately 6.0 mg/ml. The fit to the GEM equation has a coefficient of determination (R^2 value) of 0.987, indicating a good fit. However, under percolation and GEM theories, typical values for ϕ_c would be expected to fall between 0.1 and 0.2 [163] (corresponding in this case to carbon loading values between 25 and 120 mg/ml, based on a quoted density range of 0.25 – 0.6 g/cm³ for the carbon particles [206]) and typical values of t between 1.7 and 5.8 [233]. The fit shown in Figure 4.5 yields a ϕ_c value of 0.003 and a t value of 0.09, indicating that these polyacrylamide/-carbon nanopowder composites do not conform to GEM theory in the same way as standard composites.

This behaviour can be understood by considering the structure of hydrogels. One of their defining characteristics is a very high porosity, meaning they contain a significant number of void spaces (as we have seen in Figure 3.8). This can be considered in two ways. Firstly, under percolation theory and GEM theory [164, 233, 236] these voids could be treated as large (~100 nm) particles with very low conductivity. This being the case, our composites can be thought of as being three-phase composites rather than two-phase composites (Figure 4.6), in which case the GEM model discussed in Section 1.4.4 (which describes two-phase mixtures) ceases to apply [237, 238]. Alternatively, the composites can be thought of as two-phase composites in which the effective carbon loading within the polyacrylamide is greatly increased as the result of occupying a lower effective volume of polymer. Either interpretation accounts for the significantly lower than expected values of ϕ_c observed in Figure 4.5. The data presented in Figure

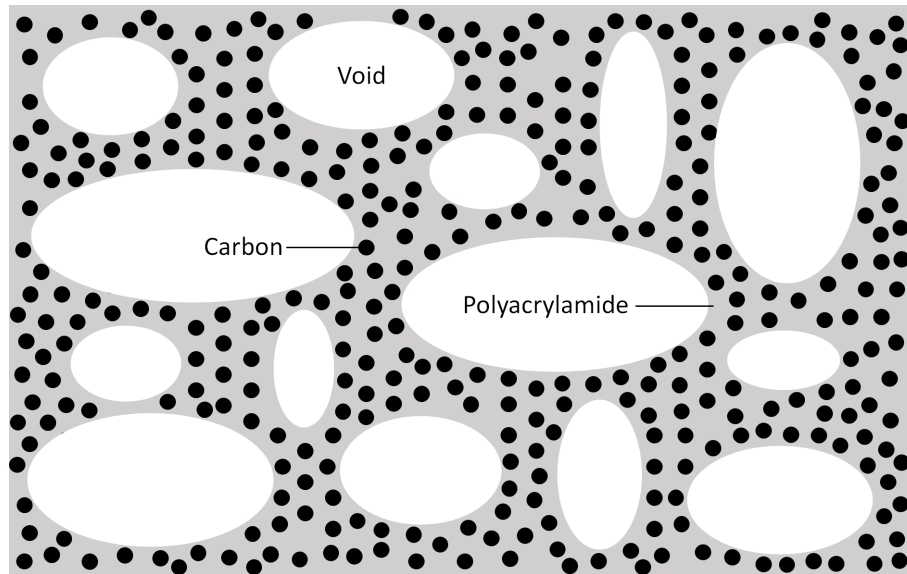


Figure 4.6: Illustration of the three-phase nature of the carbon/polyacrylamide composites. The grey space represents polyacrylamide, the black circles represent carbon nanoparticles and the white areas represent the voids in the hydrogel structure, which can be viewed in terms of percolation theory as particles with very low conductivity. It can be seen that the existences of the voids increases the effective concentration of the carbon nanoparticles.

4.5 is for composites in the dried state. High conductivity regimes were found to be unachievable for composites in the saturated state.

Figure 4.7 shows the fit to the GEM equation for polyacrylamide/carbon nanopowder composites alongside the equivalent model fits for composites prepared using carbon micropowder and graphite. It shows that the critical loading values vary significantly for each of the different particle types. This is to be expected as the percolation threshold is known to vary with parameters such as particle aspect ratio, wetting, aggregation, average size and size distribution [151,233,236,239]. Figure 4.7 shows that carbon micropowder and graphite produce composites with percolation thresholds of approximately 2.2 mg/ml and 1.0 mg/ml respectively. The fits to the GEM equation produce coefficients of determination of 0.958 for carbon micropowder and 0.991 for graphite composites.

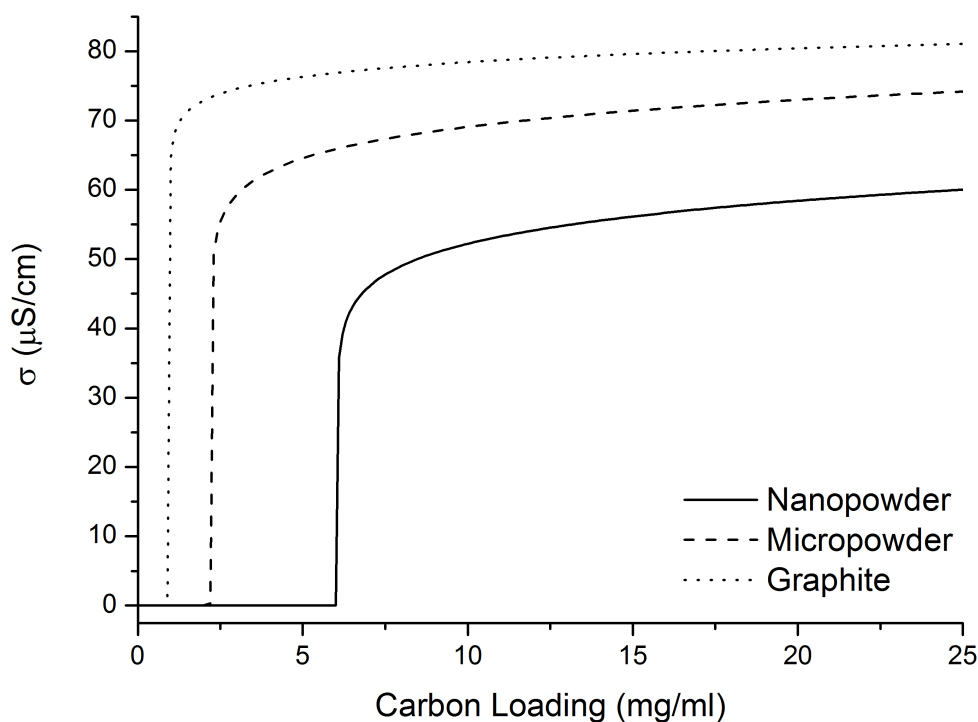


Figure 4.7: Fits to the GEM equation for various carbon particle types: carbon nanopowder, carbon micropowder and graphite. The composites contained 0.8 mol% wrt monomer MBA and 0 mol% wrt monomer oligonucleotide cross-linker.

Percolating composites, in any state, could not be achieved using carbon nanotubes.

Due to their very high aspect ratios they are far more prone to agglomeration than other particles types and thus cannot be easily dispersed in aqueous solutions in their native state [240]. Standard practice in the field is to add a surfactant such as sodium dodecylbenzenesulfonate [240, 241], however it was found that the addition of such a surfactant at the concentrations required for nanotube dispersion caused problems with the free-radical polymerisation of the composite. This can be seen in Figure 4.8, which shows a microscope image of a 10 mg/ml carbon nanotube composite in its dried state. There are large areas where it is clear that the composite has failed to form, leaving areas of the substrate and the electrodes exposed. Proper hydrogel formation relies on a uniform distribution of monomer. It appears from Figure 4.8 as if the addition of

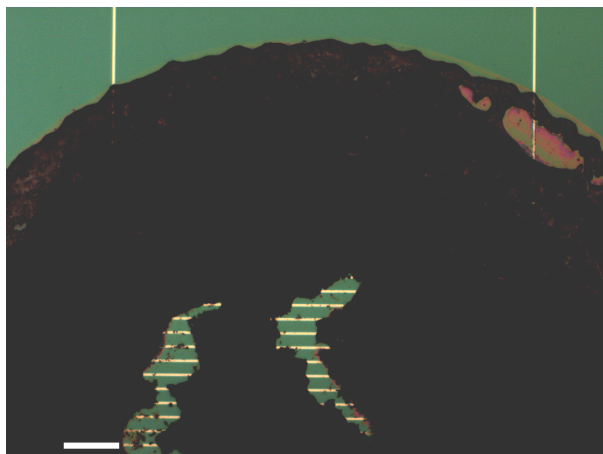


Figure 4.8: Microscope image of a 10 mg/ml composite droplet prepared using carbon nanotubes as the conductive component. The cross-link density was 0.6 mol% wrt monomer MBA, 0 mol% wrt monomer oligonucleotide cross-linker. The image is at $\times 2.5$ magnification and the scale bar represents 200 μm .

the surfactant results in micelle formation, leading to a non-uniform distribution of monomer and therefore non-uniform polymer formation. As a result of these effects, composites could not be formed with carbon nanotube concentrations greater than approximately 2 mg/ml. It is possible that alternative polymerisation mechanisms or surface functionalisation of the nanotubes [242,243] may rectify this problem. However, such investigations are beyond the scope of this thesis. As a result of these issues, carbon nanotubes were not investigated further as a potential conductive component for OCPCs.

Figure 4.7 shows that percolating composites can be prepared from polyacrylamide and either carbon nanopowder, carbon micropowder or graphite. It is known that the percolation threshold of a composite depends on parameters such as the particle aspect ratio, size distribution and surface porosity [150,151,158,236]. Figure 4.7 shows that graphite powder produces composites with a much lower percolation threshold than either carbon micropowder or nanopowder. This is presumably a result of its high

aspect ratio [244,245]. Whilst having a low aspect ratio, the carbon micropowder has a significant size distribution (2 - 12 μm) [246] which may account for it producing composites with a lower percolation threshold than those produced with carbon nanopowder [151,236]. Composites with low percolation thresholds are advantageous for sensing applications [151,236], suggesting that graphite-based composites might be preferable to the alternatives discussed here. However, other factors, such as compatibility with droplet dispersion methods such as ink-jet printing, must be considered [194]. The relative merits of each particle type for creating OCPCs will be discussed in more detail later in this chapter.

4.2.2 Swelling measurements

The objective of adding conductive carbon particles to polyacrylamide hydrogels is to produce composites whose swelling can be quantified by a simple measurement of their electrical conductivity. This section assesses both d.c. and a.c. measurement as methods for quantifying the swelling of such composites.

4.2.2.1 Direct current measurements

Samples of polyacrylamide/carbon nanopowder composite were prepared upon IDE devices and their d.c. resistance measured with time as they swell in solution, as described in Section 2.4. Figure 4.9 shows the d.c. resistance of polyacrylamide/carbon nanopowder composites (0 mol% wrt monomer oligonucleotide cross-linker) as they swell in DI water alongside the optical volume data for equivalent composites, as shown

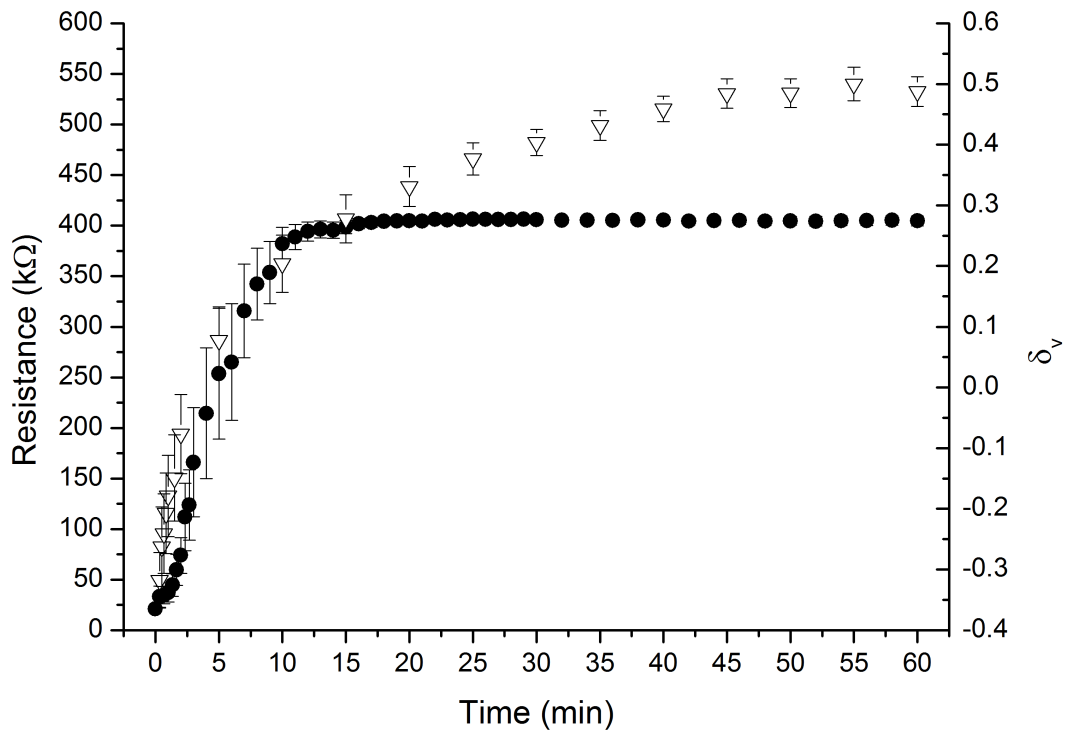


Figure 4.9: The d.c. resistance of polyacrylamide/carbon nanopowder composites with time as they swell in DI water (\bullet , left-hand axis) shown alongside the equivalent optical volume data (∇ , right-hand axis). The carbon concentration was 15 mg/ml and the cross-link density was 0.6 mol% wrt monomer of MBA, 0 mol% wrt monomer oligonucleotide cross-linker. The optical data is that shown in Figure 3.12 (0.6 mol% wrt monomer MBA, 1st swelling). $\delta_v \equiv \frac{V-V_i}{V_i}$, where V is the droplet volume and V_i is the droplet volume at polymerisation.

in Figure 3.12. The resistance rises from a high conductivity state (*ca.* 30 k Ω) to a low conductivity state (*ca.* 400 k Ω) within 10-15 minutes. This transition is consistent with the change from a percolating to a non-percolating state as the composite swells and the relative density of the conductive particles decreases. However, comparing this to the optical measurements it is clear that the plateau in resistance occurs well before the plateau in volume, which occurs after approximately one hour. This suggests that the swelling is continuing well beyond the transition between percolating and non-percolating states and that subsequent swelling does not result in significant changes to the resistance.

The error bars on the resistance data in Figure 4.9 represent the standard error on the mean. The variation between samples is greatest during the transition between high and low conductivity states, where small variations in the carbon concentration will be most significant. Variation in the time of transition will also contribute to this uncertainty. Once the resistance plateaus there is far less variation between samples. This is to be expected as this represents a measurement of the swelling medium within the polymer matrix which would not be expected to display much variability.

Figure 4.10 shows the d.c. resistance of polyacrylamide/carbon nanopowder composites as they swell in DI water (0 mM NaCl) alongside the equivalent data for composites swelling in a 150 mM NaCl, 1 mM phosphate buffer solution. In the buffer solution the resistance of the composites tends to a lower plateau value (*ca.* 350 k Ω compared to *ca.* 400 k Ω), which is to be expected as the presence of salt ions will increase the conductivity of the system [247,248]. However, these differences are small in proportion to the overall resistance range and will be consistent for a given salt concentration, so this will not be an issue for any sensor derived from these composites provided that the salinity of the test solution is known.

Additionally, the transition between high and low conductivity states appears approximately 2 minutes faster in the buffer solution than in DI water. This is most likely a result of the presence of salt ions altering the overall hydrophilicity of the system and thus affecting the rate at which water enters the polymer matrix. The variability between samples is greater in the buffer solutions than in the DI water. Why this is the case is unclear. The swelling medium for each sample is an aliquot of a single prepara-

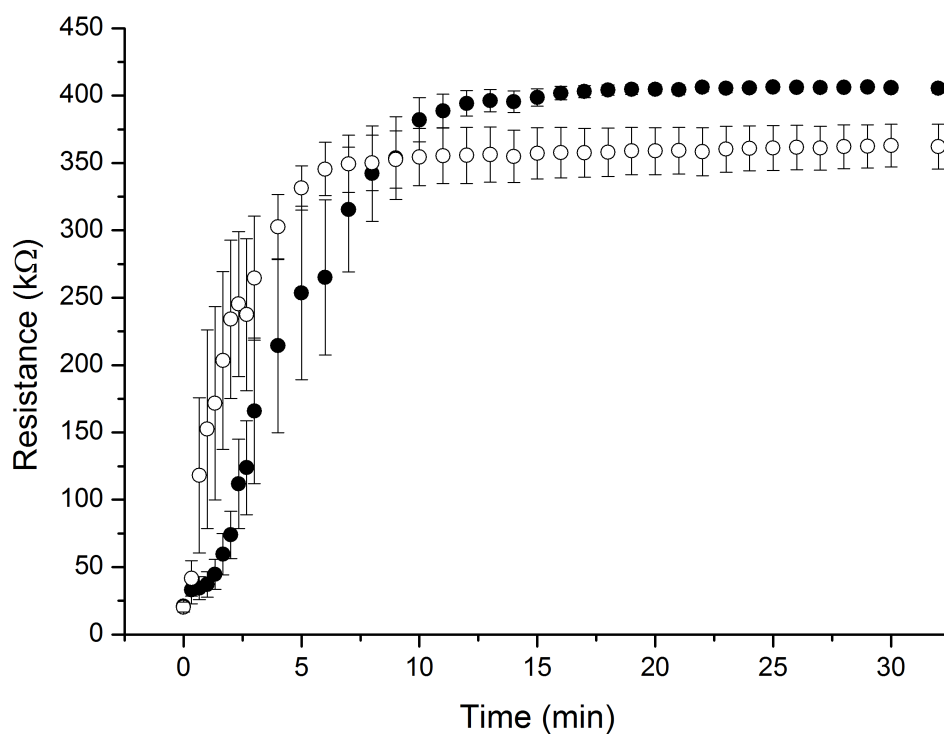


Figure 4.10: The d.c. resistance of polyacrylamide/carbon nanopowder composites with time as they swell in solution. The carbon concentration was 15 mg/ml and the cross-link density was 0.6 mol% wrt monomer of MBA, 0 mol% wrt monomer oligonucleotide cross-linker. The respective swelling media were DI water (0 mM NaCl) (●) and a 150 mM NaCl, 1 mM phosphate buffer solution (○).

tion of the buffer solution, so it would not be expected that there be any variation in salt concentration between samples.

It can be concluded from Figures 4.9 and 4.10 that polyacrylamide/carbon nanopowder composites can be an effective means of measuring the swelling response of hydrogels, with d.c. resistance measurements clearly capturing the change from a high conductivity state to a low conductivity state as the conductive pathways are broken with swelling. These composites are equally effective in DI water and salt solutions. However, it is clear that the full range of swelling is not being captured as the resistance plateaus long before swelling is complete. If unresolved this will place constraints upon the utility of this measurement system for the transduction of polymer swelling.

The above process was repeated using composites prepared using different carbon particle types in order to determine the effects of the differing percolation characteristics discussed in Section 4.2.1 upon the electrical response to swelling. Figure 4.11 shows the d.c. resistance against time for swelling composites in DI water created using: carbon nanopowder (as for Figure 4.10), carbon micropowder and graphite. Whilst each type of composite undergoes a transition between high and low conductivity states, the timescale over which these transitions occur differs for each particle type. Carbon nanopowder demonstrates the most rapid transition, with carbon micropowder beginning approximately one minute later (yet reaching a plateau at approximately the same time) and graphite beginning transition approximately 5 minutes later and reaching a plateau approximately 15 minutes after carbon nanopowder.

As discussed in Section 4.2.1, as a result of factors such as particle aspect ratio and size distribution, composites prepared using carbon nanopowder possess the highest percolation threshold (of the composite types investigated here) and composites produced with graphite possess the lowest. Composites prepared with carbon micropowder have thresholds somewhere in between. For a given conductive particle concentration, composites with lower percolation thresholds will undergo a greater degree of swelling before transitioning between the high and low conductivity states, as the conductive particles will continue to form conductive pathways at lower relative densities. Therefore it is to be expected that graphite composites will display the slowest transition and carbon nanopowder composites the fastest, as seen in Figure 4.11.

Both carbon nanopowder composites and graphite composites reach the same plateau value, whereas carbon micropowder plateaus at a lower resistance. Why this might be

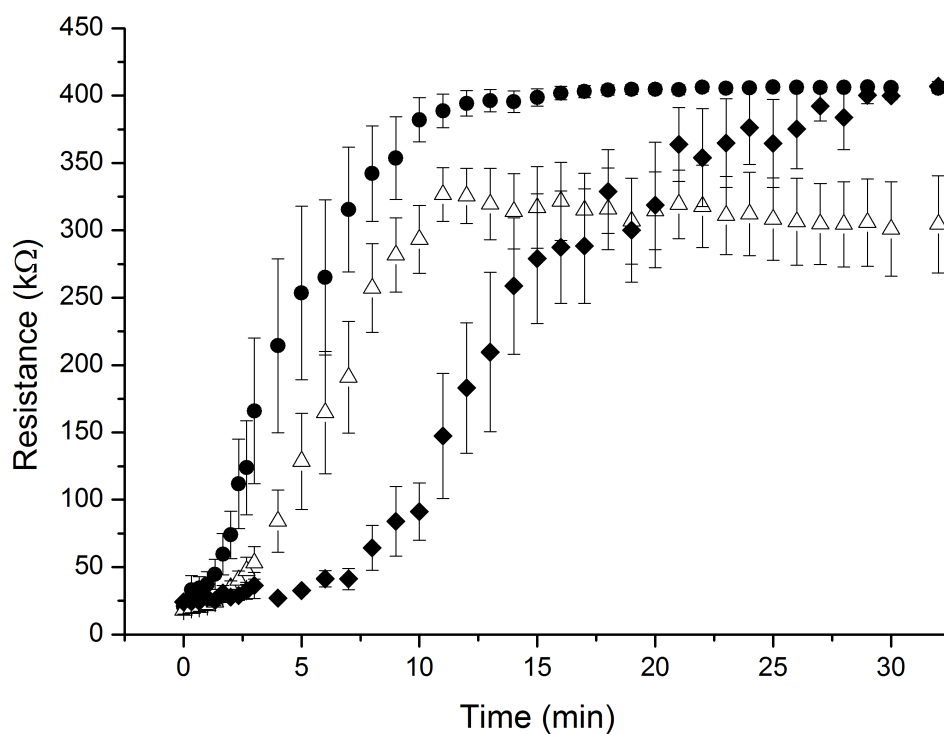


Figure 4.11: The d.c. resistance of composites with different forms of carbon particle additives with time as they swell in DI water (0 mM NaCl). The carbon particles were either nanopowder (●), micropowder (△), or graphite (◆). The carbon was loaded at 15 mg/ml and the cross-link density was 0.6 mol% wrt monomer of MBA, 0 mol% wrt monomer oligonucleotide cross-linker.

the case remains unclear. However it may be that, as a result of their size and aspect ratio (spherical, 2-12 μm), the microparticles are more free to move within the polymer matrix than either the nanoparticles or the graphite particles. Thus it may be that, as the polymer swells, the microparticles begin to drift downwards under the effects of gravity, causing conductive pathways to begin to re-form and the resistance to decrease. This hypothesis is supported by the error bars in Figure 4.11. As the nanopowder and graphite composites reach their plateaus the error bars become very small, indicating very little variation between samples. This is indicative of a state in which the resistance is dominated by the medium within the polymer network, the resistance of which would not be expected to vary between samples. As the micropowder composites reach their

plateau, the error bars remain large, indicating significant variation between samples. This is suggestive of a state in which the resistance is influenced by the formation of conductive pathways, wherein any variation in the particle distribution or network porosity will result in variations in the overall resistance. There also appears to be a slight downward trend after 10 minutes in the micropowder data, perhaps resulting from an increase in the number of conductive pathways as the particles drift downwards over time. However, this difference is smaller than the magnitude of the uncertainty between measurements and therefore this cannot be said with any certainty.

4.2.2.2 Alternating current measurements

The same procedure as for Section 4.2.2.1 was performed, this time measuring the complex impedance, Z , as described in Section 2.4. Figure 4.12 A shows the magnitude of the complex impedance, $|Z|$, for polyacrylamide/carbon nanopowder composites (0 mol% wrt monomer oligonucleotide cross-linker) with time as they swell both DI water and buffer solution. Figure 4.12 B shows the phase, θ , for the same experiments. In the water case $|Z|$ increases from approximately 65 k Ω to approximately 85 k Ω as the composites swell, which is consistent with the breaking of conductive pathways as the carbon particles move away from each other. θ decreases from approximately 5° to approximately -15° which, considering our model of the system (Section 2.4.1), is again consistent with the conductive particles moving away from each other as the polymer swells. When the particles are close enough to interact, the system will be dominated by its resistive components (an ideal resistor has an associated phase change of zero). Whereas, as the particles separate and conductive pathways break,

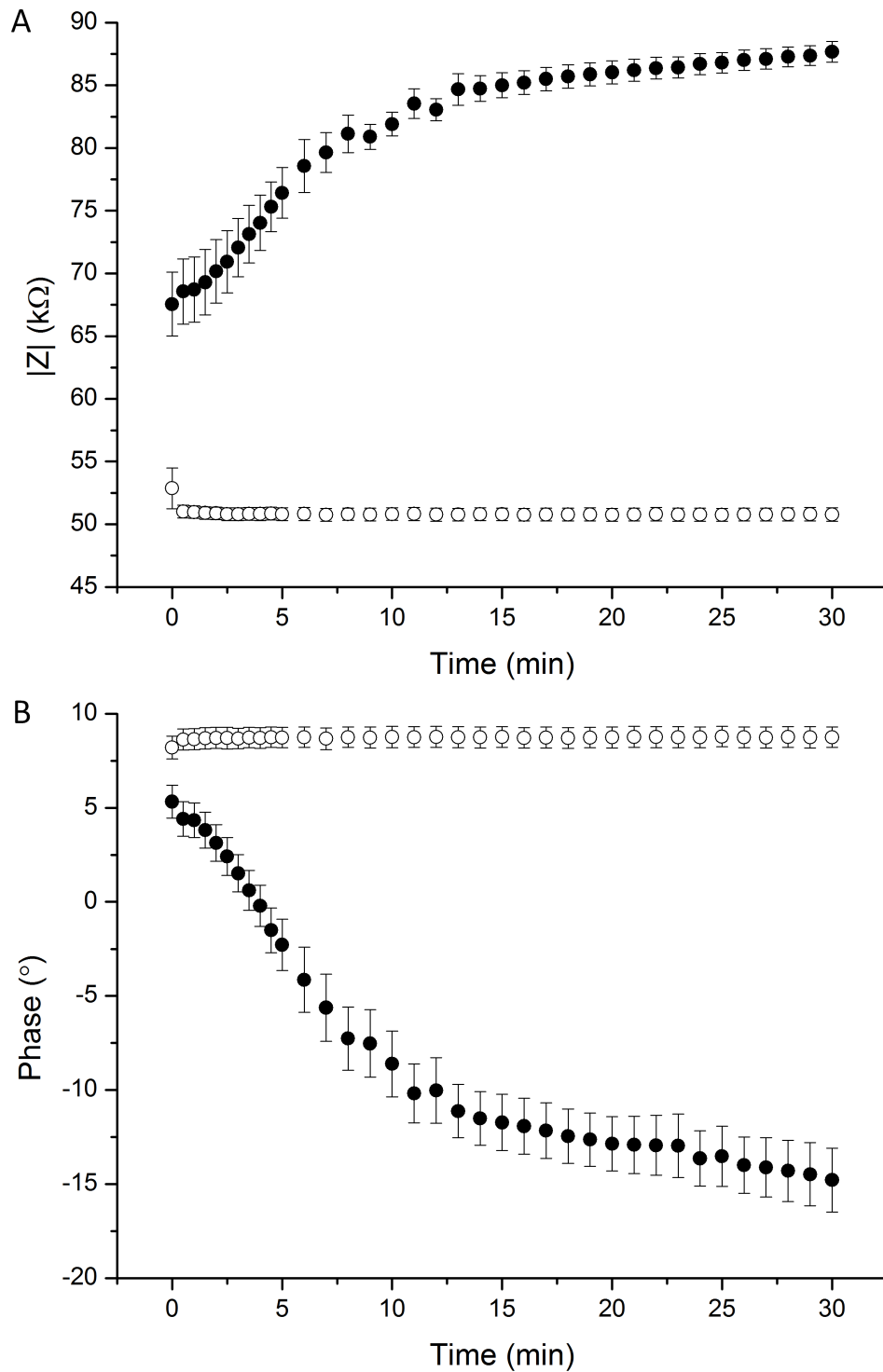


Figure 4.12: The magnitude (A) and phase (B) of the complex impedance against time for swelling polyacrylamide/carbon nanopowder composites, at 10 kHz. The carbon concentration was 10 mg/ml and the cross-link density was 0.8 mol% wrt monomer MBA, 0 mol% wrt monomer oligonucleotide cross-linker. The swelling media were DI water (●) and 150 mM NaCl, 1 mM phosphate buffer solution (○).

the capacitive component will become increasingly significant (an ideal capacitor has an associated phase change of -90°) [185]. As such, it is to be expected that θ would become increasingly negative as the composites swell.

The error bars in Figure 4.12 represent the standard error on the mean. Variation between samples will be a result of small variations in the carbon density and the measurement error of the AD5933EBZ test board.

Figure 4.13 shows the $|Z|$ data from Figure 4.12 A plotted alongside the d.c. resistance data for a similar composite (Figure 4.9). It shows that $|Z|$ undergoes similar behaviour to the resistance, with an initial period of rapid change for the first 10-15 minutes, tending towards a plateau. However, the difference between the high and low conductivity states is far smaller for $|Z|$ than the resistance. This is as would be expected given that the complex impedance will have additional contributions from the capacitive elements (Section 2.4.1), leading to a lower overall impedance.

Figure 4.13 suggests that an a.c. measurement of the complex impedance might also be an effective means of measuring the swelling of polyacrylamide/carbon nanopowder composites. However, in buffer solution the behaviour is radically different (Figure 4.12). There is very little apparent change in either $|Z|$ or θ as the composites swell. $|Z|$ remains fixed at *ca.* 50 k Ω (more conductive than at any point in the 0 mM NaCl case) and θ remains at *ca.* 8° , both indicative of a high conductivity state. The only significant change in both $|Z|$ and θ occurs between the first measurement ($t = 0$) and the second. These changes can be explained by the effects of the solvent entering into the dried composite.

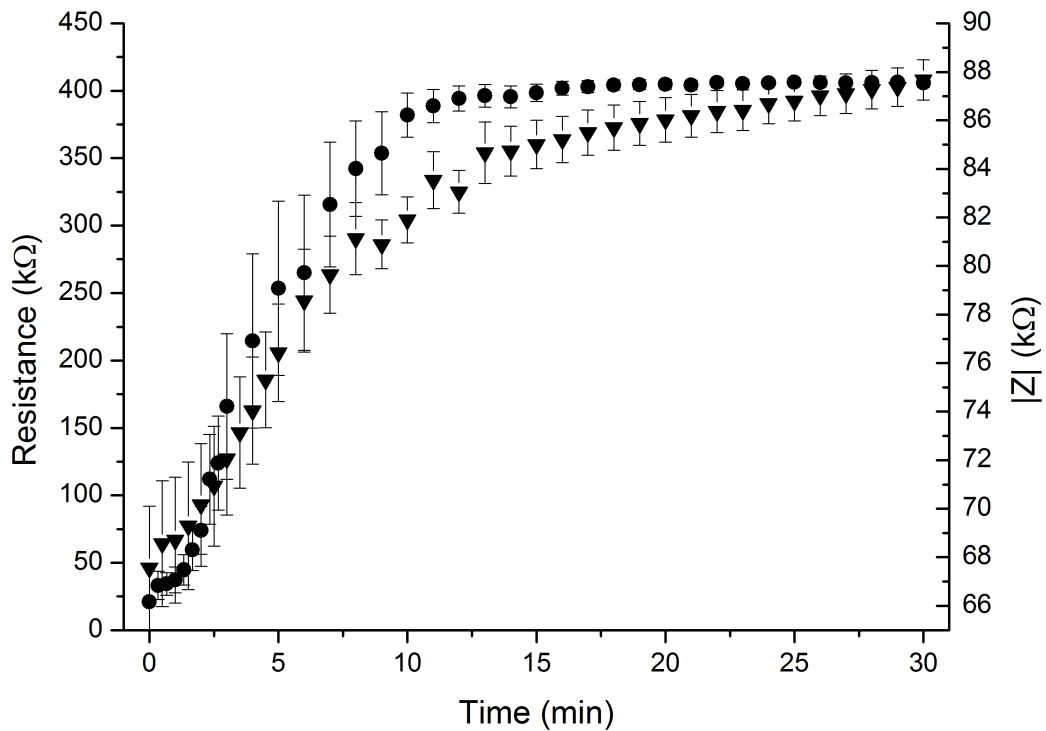


Figure 4.13: The d.c. resistance (●, left axis) of a swelling polyacrylamide/carbon nanopowder composite plotted alongside the magnitude of the complex impedance (▼, right axis) against time at 10 kHz for a similar composite. In both cases the swelling medium was DI water.

It is clear that the presence of salt ions has a significant effect on the measurement of the complex impedance (which should not be unexpected as ionic concentration is known to influence the complex impedance of a solution [249]). This effect is detrimental to the measurement of swelling as it masks any volume dependent impedance changes, such as are seen in the DI water case (Figure 4.12). In Section 4.2.2.3, further evaluation of the model introduced in Section 2.4.1 will be used to reach a better understanding of these effects. The results detailed in this section suggest that, under the experimental parameters described herein, d.c. measurement will be superior to a.c. measurement for the measurement of the swelling of OCPCs. In Section 4.2.3, d.c. measurement will be used to investigate the electrical transduction of the selective swelling of OCPCs in oligonucleotide solutions.

4.2.2.3 Sensor model

We have seen that the presence of salt ions in the swelling medium has a significant detrimental impact upon a.c. measurement as a method of measuring the swelling of polyacrylamide/carbon composites. A greater understanding of these effects can be reached through further examination of the sensor model discussed in Section 2.4.1. Figure 4.14 shows the frequency response of the magnitude of the complex impedance, $|Z|$, for a polyacrylamide/carbon nanoparticle composite (20 mg/ml) in its dried state. This is plotted alongside a best fit to the model (Equation 2.5). The coefficient of determination (R^2 value) is 0.972, indicating a good fit. At lower frequencies (<50 kHz) the data exhibits a downward trend, indicating capacitive behaviour. At higher frequencies (>50 kHz) the data exhibits an upward trend, indicating that Equation 2.5 is dominated by the ωL term and the behaviour is dominated by inductive effects [185]. The error bars in Figure 4.14 represent the measurement error of the AD5933EBZ test board ($\pm 0.5\%$) [181]. A greater degree of insight could be gained by measuring at frequencies below 1kHz, but this is not possible using this experimental set-up.

Figure 4.15 shows the average model fit values for C for polyacrylamide hydrogels, prepared as described in Section 2.4, with and without the addition of carbon nanopowder, in three different conditions: dried, saturated in DI water and saturated in buffer solution. In the no carbon case there is little apparent difference in C between the dried and water saturated cases (1 and 3). Upon the addition of carbon, C for the dried state increases significantly (from *ca.* 0.25 to *ca.* 0.45 nF, for 1 and 2 respectively). This is to be expected as the incorporation of conductive particles will cause the relative

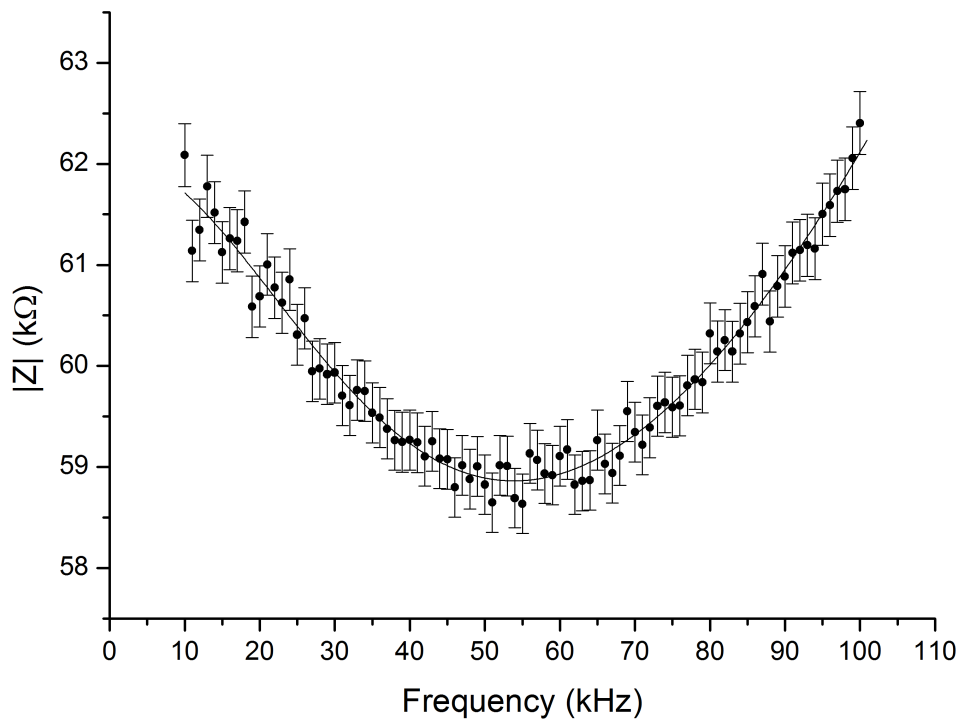


Figure 4.14: The magnitude of the complex impedance against frequency for a polyacrylamide/carbon nanopowder composite (0 mol% wrt monomer oligonucleotide cross-linker) with 20 mg/ml carbon (●) in the dried state, plotted alongside the corresponding model fit (–). The cross-link density was 0.6 mol% wrt monomer MBA, 0 mol% wrt monomer oligonucleotide cross-linker.

dielectric constant, ϵ_r , to increase [233, 250], thereby improving the charge storing capabilities of the system and increasing the capacitance. In the water saturated case the incorporation of carbon appears to have no effect on C (3 and 4). This is because, in the saturated state, the separation between the carbon particles is greater, thus their contribution to the capacitance will be less significant and C will be dominated by the contribution of the water. In the buffer solution saturated case there is a considerable increase in C for both the carbon (6) and no carbon (5) cases relative to the water saturated cases (4 and 3 respectively). For IDEs, C is dependent upon ϵ_r [235, 251, 252]. It is known that ϵ_r is dependent upon the conductivity, σ , of the medium [249, 253, 254] and it therefore follows that C shares this dependency. Therefore the changes in σ

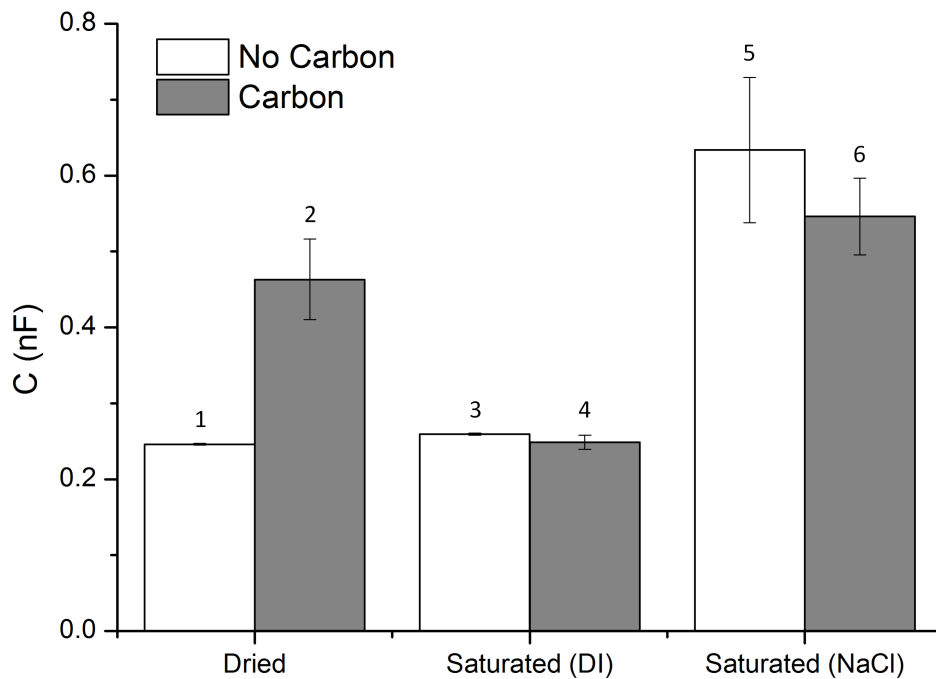


Figure 4.15: The average fitted model parameter for the capacitance, C . Fitted using test data under various conditions: dried, saturated in DI water and saturated in a buffer solution (150 mM NaCl, 1 mM phosphate buffer). In each case the composites contained either 0 mg/ml or 20 mg/ml carbon nanopowder. The cross-link density was 0.6 mol% wrt monomer MBA, 0 mol% wrt monomer oligonucleotide cross-linker.

produced by the inclusion of salt ions result in the differences in C observed in Figure 4.15. These changes mask any effects that might be expected to be seen in the transition from a dried to a saturated state as a result of the addition of carbon.

In the dried and DI water saturated cases without the addition of carbon (1 and 3), the error bars in Figure 4.15 are very small, indicating that there is little variation between samples. Upon the addition of carbon (2 and 4) the error bars increase in size. This is to be expected as uncertainties in the carbon particle distribution will increase variation between the samples. The error in the dried carbon case (2) is larger than for the DI water saturated case (4). This is also to be expected as when the carbon particles are closer together any variations in their distributions will prove

more significant. Additionally, potential variations in the volumes of the dried samples due to variations in the ambient humidity may contribute to the uncertainty. In the buffer solution saturated case polymers both with (6) and without carbon (5) display far higher errors than in the DI water saturated case. This is similar to what is seen in Figure 4.10.

Figure 4.16 shows the average model fit values for R_p for the same hydrogels in the same conditions as in Figure 4.15. In the no carbon case, transitioning between the dried (1) and water saturated (3) states results in a decrease in resistance. This can be explained by the fact that water entering the dried hydrogel will improve ion mobility within the polymer matrix thereby increasing the electrical conductivity [247, 255]. There is a considerable difference in R_p between the carbon (2) and no carbon (1) cases in the dried state, with the carbon case having a resistance of approximately two orders of magnitude lower than the no carbon case. This is to be expected as, in the carbon case, conductive pathways of carbon particles will form throughout the composite, reducing the resistance [150, 166]. In the carbon case, transitioning between the dried (2) and the water saturated (4) states results in an increase of more than an order of magnitude for R_p as these conductive pathways are broken as the composite swells. This corresponds to what we have seen in Section 4.2.2, where the resistance transitioned between *ca.* 10 k Ω and *ca.* 400 k Ω upon swelling. In the buffer solution saturated state there is no observable difference between the carbon (6) and no carbon (5) cases. There is also no observable difference between the carbon cases of the dried (2) and buffer solution saturated (6) states suggesting that, as for C , there will be no detectable change in R_p for composites swelling in NaCl solutions, using this method of electrical measurement.

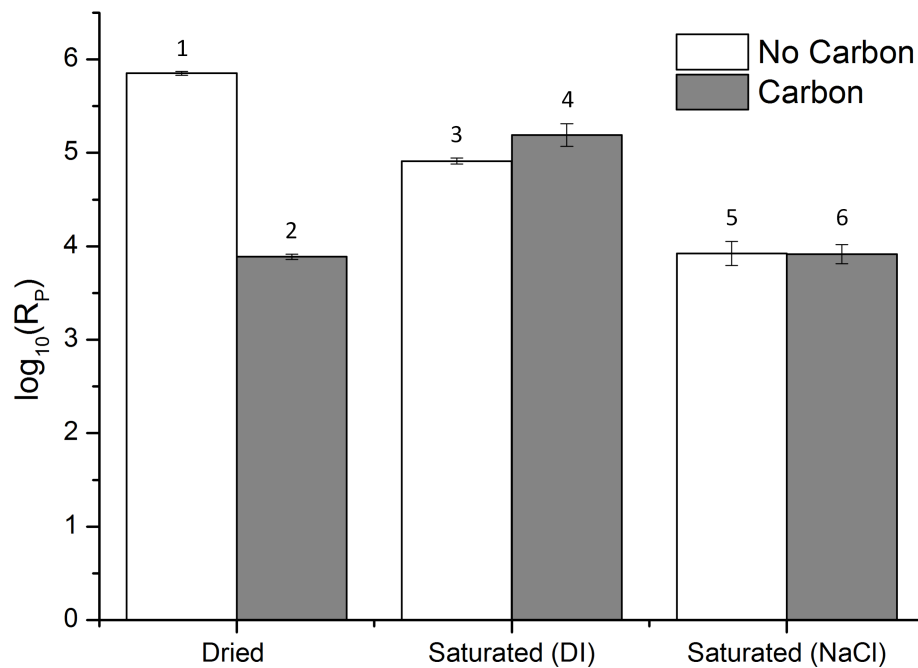


Figure 4.16: The average fitted model parameter for the resistance, R_p . Fitted using test data under various conditions: dried, saturated in DI water and saturated in a buffer solution (150 mM NaCl, 1 mM phosphate buffer). In each case the composites contained either 0 mg/ml or 20 mg/ml carbon nanopowder. The cross-link density was 0.6 mol% wrt monomer MBA, 0 mol% wrt monomer oligonucleotide cross-linker. Shown on a \log_{10} scale.

Figures 4.15 and 4.16 offer further confirmation of what is seen in Section 4.2.2, that composites swelling in NaCl solutions display no changes in Z that can be measured using the method described herein. This is in spite of the increases in volume that occur and a result of the dielectric properties of the swelling medium. This is further evidence that d.c. measurement will be more suitable than a.c. measurement for measuring the swelling response of OCPCs.

The error bars in Figure 4.16 appear smaller than their equivalents in Figure 4.15 but this is predominately an artifact of the logarithmic scale. As in Figure 4.15, the presence of NaCl appears to increase the uncertainty of the measurement.

The model fits described in this section were performed over a frequency range of 10 to 100 kHz, limited by the measurement range of the AD5933EBZ test board. The frequency dependency may diverge beyond this range, necessitating a modification to the model, but in its current form the model predicts that at higher frequencies Z will be increasingly dominated by the parasitic inductance, while at lower frequencies Z will become increasingly dominated by its resistive components ($R_p + R_s$). It is likely that the parasitic inductance could be reduced by redesigning the electrode device or the measurement set-up, but such efforts are beyond the scope of this thesis.

4.2.3 Oligonucleotide cross-linked polymer composite swelling

This section details the application of d.c. resistance measurement to OCPCs swelling in oligonucleotide solutions. OCPCs prepared using different carbon particle types are compared to assess their relative merits as potential means of oligonucleotide detection.

4.2.3.1 Carbon micropowder

Given the favourable percolation characteristics of carbon micropowder discussed in Section 4.2.1, it could reasonably be expected to be a promising candidate for the formation of OCPCs. However, upon the incorporation of oligonucleotide cross-linkers, after polymerisation these composites display d.c. resistances of *ca.* 300-400 k Ω rather than the *ca.* 20 k Ω witnessed without the presence of oligonucleotide cross-links (and for graphite and carbon nanopowder OCPCs, Sections 4.2.3.2 and 4.2.3.3). The resistances observed are in the range of those of the swelling medium within the composite matrix,

indicating that percolation is not taking place, this remains the case even when the composite is in its dried state.

The reasons why the electrical properties are so different with the addition of oligonucleotide cross-linkers become clearer upon inspection of Figure 4.17, which is an image of a $2\ \mu\text{l}$ carbon microparticle OCPC droplet in its dried state. After polymerisation all of the carbon appears to have become concentrated at the centre of the droplet, leaving a clear band of polymer (with no carbon) around the circumference. This is similar to the effect discussed in Section 3.1.1, but occurring to a much greater degree. If the same effect occurs in the z -axis (Figure 4.18) the result will be that the carbon is physically separated from the electrodes, meaning there will be no increase in conductivity.



Figure 4.17: Image of a carbon microparticle OCPC in its dried state. During polymerisation the carbon has migrated into the centre of the droplet, leading to a black carbon rich region surrounded by a clear region of pure polymer. The carbon loading was 20 mg/ml. The cross-link density was 0.6 mol% wrt monomer MBA, 0.4 mol% wrt monomer oligonucleotide cross-linker.

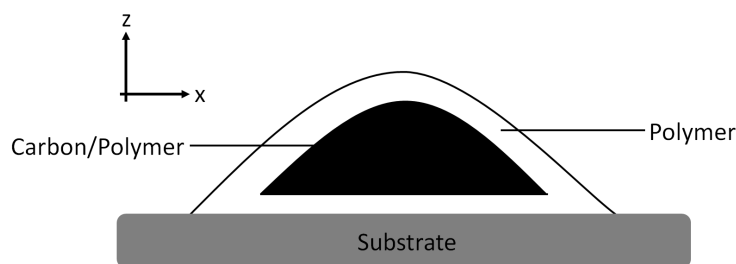


Figure 4.18: Diagrammatic representation of the potential carbon microparticle distribution in the xz -plane. The net inward pressure on the carbon microparticles causes them to group together in the centre of the droplet during polymerisation. In the z -axis this has the effect of forcing the carbon away from the electrodes, leading to low conductivity.

It is hypothesised that this effect is a result of the carbon particle size (2 - 12 μm) being larger than the polymer mesh size (*ca.* 0.5 μm), leading to a more significant ‘squeezing out’ of the carbon during polymerisation – as discussed in Section 3.1.1 (Figure 3.6). If the polymerisation occurs fastest at the droplet surfaces, this will result in a net inward pressure on the carbon particles, leading to the ‘ring’ effect seen in Figure 4.17. The reasons why this effect is much more pronounced with the addition of oligonucleotides than in their absence are unclear. The addition of oligonucleotides to the pre-gel solution will make the solution more viscous, thereby slowing down the polymerisation reaction and potentially accentuating any ‘squeezing out’ effect. Alternatively, it is possible that the addition of oligonucleotides results in increased agglomeration of the carbon microparticles. It is known that oligonucleotide strands can form complexes with carbon nanoparticles [199–202] and it may be possible that a similar effect occurs with carbon microparticles. Again, any agglomeration of the carbon microparticles will accentuate any ‘squeezing out’ effect. The effects evident in Figure 4.17 could be a result of either of these causes or a combination of the two, although a greater understanding of the interactions between carbon microparticles and oligonucleotides would be required to form a proper hypothesis.

Whatever the cause, this effect means that carbon microparticle/polyacrylamide composites are unlikely to be applicable to OCPC applications due to challenges in measuring any changes in conductivity that arise as a result of selective swelling. It is possible that this effect can be mitigated by exploiting alternative methods of polymerisation, other than UV-initiated free-radical polymerisation. Such alternative polymerisation mechanisms will be discussed in Section 6.3.

4.2.3.2 Graphite

Figure 4.19 shows a microscope image of a 2 μl droplet of graphite OCPC in its dried state. The carbon distribution appears uniform and the anomalous effects observed for micropowder OCPCs do not appear to occur, indicating that the process that causes this does not affect the graphite particles in the same way. Quite why this is the case is unclear, but it is most likely due to the much higher aspect ratio of the graphite particles and the way that they interact with the polymer matrix as it forms around them. Significantly, this means that graphite OCPCs are percolating in their dried state.

Figure 4.20 shows the electrical resistance against time for graphite OCPCs swelling in a 1 μM A_0 solution. It shows that, once the samples begin their transition away from the high conductivity state, there is considerable variation in the resistance between samples (as evidenced by the magnitude of the error bars relative to the data values) and that, on average, after initially rising the resistance falls again. This is believed to be a result of the graphite particles moving and re-settling within the polyacrylamide network. Some samples return to their high conductivity state after a period of time and others

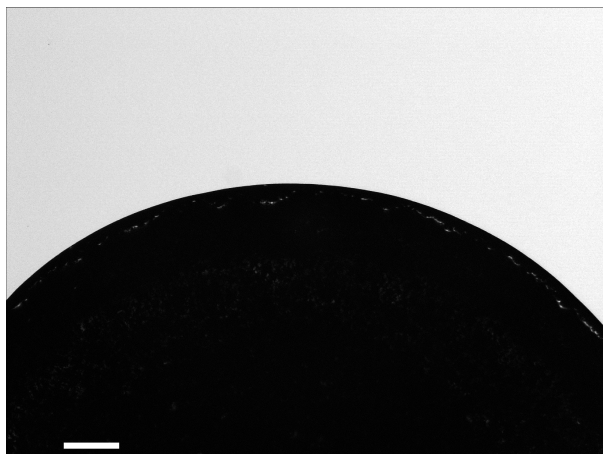


Figure 4.19: Microscope image of a 20 mg/ml graphite OCPC droplet at $\times 5$ magnification. The cross-link density was 0.6 mol% wrt monomer MBA, 0.4 mol% wrt monomer oligonucleotide cross-linker. The scale bar represents 100 μm .

oscillate between the high and low conductivity states, indicating that the conductive pathways are re-forming as the polymer swells. Presumably due to their larger size, it appears that the graphite particles are more free to move within the polymer network than other particle types as the network will form around the particles in a different manner. Also, due to their higher aspect ratio, the orientation of the graphite particles will be of greater significance than for other particle types. The reasons why these inconsistencies are only observed in oligonucleotide-functionalised polymers, and not in the non-oligonucleotide-functionalised case, are unclear. However, it is most likely a result of differences in the formation of the macromolecular structure in the presence of the oligonucleotide cross-linkers.

Due to the unpredictable and inconsistent nature of the resistance changes of graphite OCPCs with swelling, they are deemed unsuitable as a means for the transduction of hydrogel swelling.

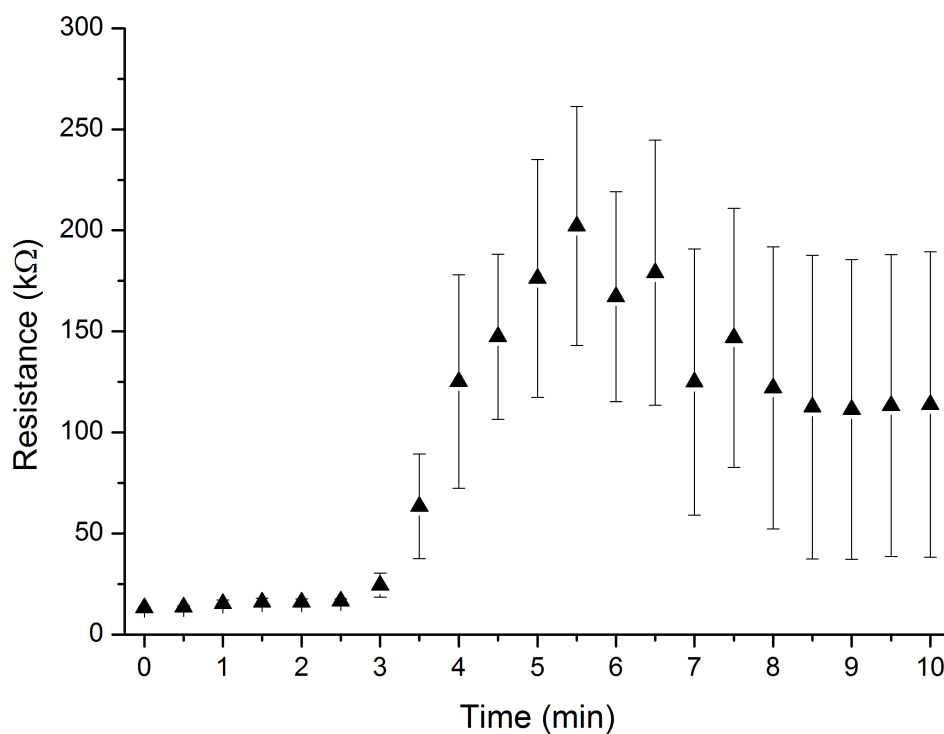


Figure 4.20: The d.c. resistance of graphite OCPCs swelling over time in a $1 \mu\text{M}$ A_0 solution. The carbon loading was 20 mg/ml . The cross-link density was 0.6 mol\% wrt monomer MBA, 0.4 mol\% wrt monomer oligonucleotide cross-linker. The solution was held at 23°C and contained 150 mM NaCl and 1 mM phosphate buffer.

4.2.3.3 Carbon nanopowder

As seen previously, carbon nanopowder OCPCs display uniform carbon distributions and are percolating in their dried state. Figure 4.21 shows the d.c. resistance over time for carbon nanopowder OCPCs swelling in both A_0 and R solutions. In both cases the value of the resistance follows the same trend as for the non-oligonucleotide functionalised composites discussed in Section 4.2.2, beginning at values of *ca.* $10 \text{ k}\Omega$ and rising as the composites swell to values of *ca.* $350\text{-}400 \text{ k}\Omega$. The most significant difference between the oligonucleotide functionalised and non-oligonucleotide functionalised cases is that the OCPCs reach the upper plateau much more quickly (in <3 minutes as opposed to *ca.* 10 minutes). This is believed to be a result of the increased hy-

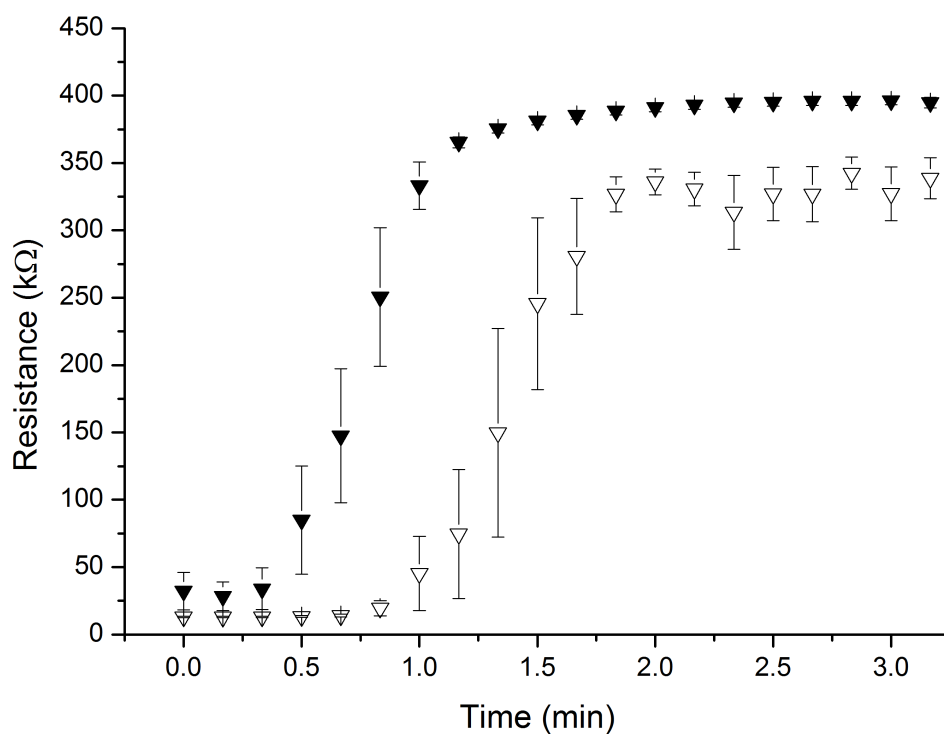


Figure 4.21: The d.c. resistance of carbon nanopowder OCPCs swelling over time in 10 nM A_0 (▼) and R (▽) solutions. The carbon loading was 20 mg/ml. The cross-link density was 0.6 mol% wrt monomer MBA, 0.4 mol% wrt monomer oligonucleotide cross-linker. The solutions were held at 23°C and contained 150 mM NaCl and 1 mM phosphate buffer.

drophilicity imparted to the composites by the inclusion of the anionic DNA. Increased hydrophilicity will cause water to diffuse into the hydrogel more rapidly, leading to faster swelling. Significantly, OCPCs produced using carbon nanopowder display none of the inconsistencies evident for graphite OCPCs (Figure 4.20).

There is a clear difference in the times at which the transitions between the percolating and non-percolating states occur, with OCPCs in A_0 solutions transitioning approximately 40 s before those in R solutions. This is indicative of a difference in the rate of swelling caused by selective cleavage of cross-links, as shown for optical measurements in Figure 3.14 and as predicted by theory (Section 1.4.1). This is clear evidence of dif-

ferential swelling caused by the selective cleavage of cross-links detected via electrical means.

However, as is the case for non-oligonucleotide-functionalised composites, this electrical transduction is only capturing part of the total period of swelling. This is evident from Figure 4.22 which shows the resistance against time for OCPCs in analyte solutions alongside the equivalent optical volume data. The optical data shows that the swelling continues for more than 30 minutes whereas the resistance reaches a peak in under three minutes. This is further evidence of the need to produce composites with either a higher conductive particle loading density or a lower percolation threshold, so as to enable the transduction of a greater range of OCPC swelling. Figure 4.21 also shows that there is a difference in end-point resistance between the A_0 and R solutions. However, it is believed that this difference does not constitute an electrical measurement of the difference in volume of the OCPCs at this point. As we know from Figure 4.22, OCPCs in both solutions will continue to swell beyond the time at which their d.c. resistance plateaus. This indicates, as discussed previously, that such plateaus in resistance are a result of the composites having swollen beyond the point at which all of the conductive pathways are broken and, as such, the principle contribution to the conductivity of the OCPCs in this state is the conductivity of the swelling medium within the hydrogel matrix. Therefore, any differences in the end-point resistance, such as is evident in Figure 4.21, can be concluded to be a result of differences in the conductivity of the swelling medium itself.

It is believed that this difference in end-point resistance between A_0 and R solutions is a result of the differences in complementarity between the analyte and random

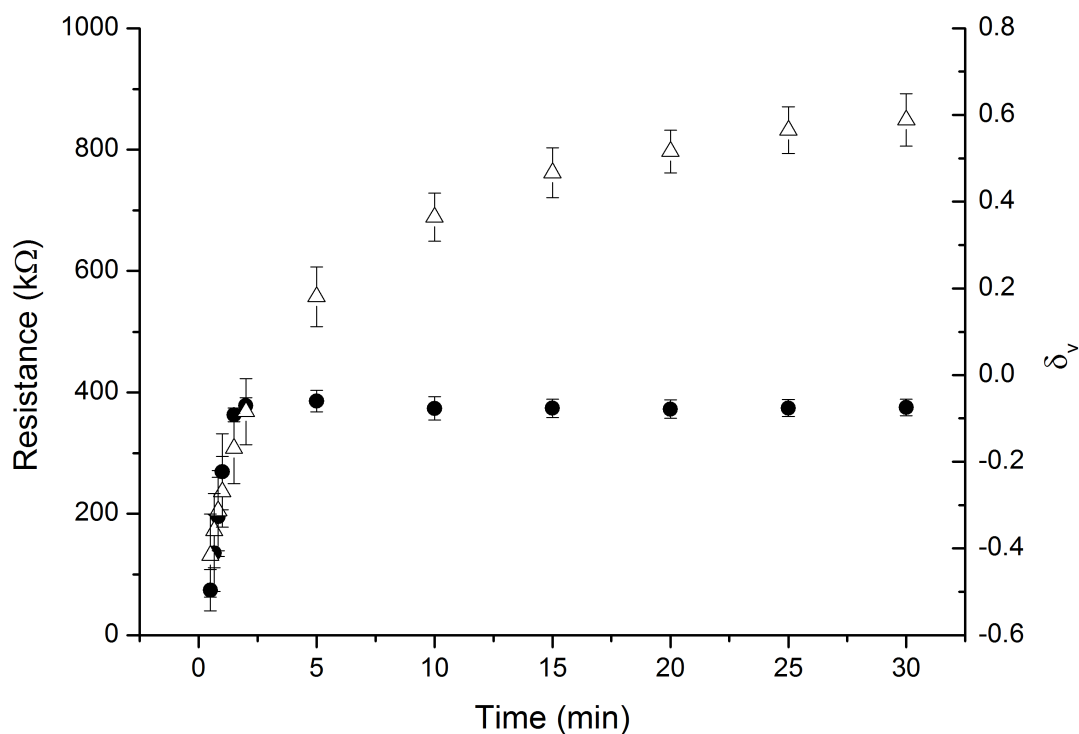


Figure 4.22: The resistance (●, left-hand axis) of OCPCs against time as they swell in an analyte solution, shown alongside the equivalent optical volume measurement (Δ, right-hand axis). The analyte concentration was $1 \mu\text{M}$. The cross-link density was 0.6 mol% wrt monomer MBA, 0.4 mol% wrt monomer oligonucleotide cross-linker. The solutions were held at 23°C and contained 150 mM NaCl and 1 mM phosphate buffer. $\delta_v \equiv \frac{V - V_i}{V_i}$, where V is the droplet volume and V_i is the droplet volume at polymerisation.

oligonucleotide strands. The conductivity of electrolyte solutions depends upon the concentration, mobility and charge of the ionic species [255, 256]. As we know, oligonucleotides are anionic molecules, therefore their presence in solution will increase the ionic concentration, thereby increasing the conductivity. As per design, the analyte oligonucleotides will hybridise with the sensor strands to form part of the polymer structure (Figure 4.23). As a result, these oligonucleotides will be immobilised and no longer free to act as charge carriers, leading to a decrease in conductivity. This will not be the case for the random oligonucleotides, which will remain free in solution and thus free to contribute to the conductivity. Therefore, it is to be expected that

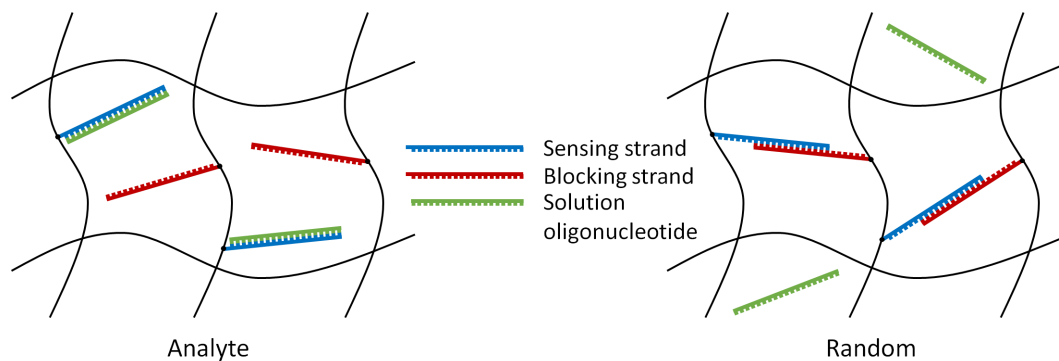


Figure 4.23: Illustration of the differences in ion mobility in OCPCs in analyte and random solutions. In an analyte solution (left) the target molecules will be perfectly complementary to the sensor strands and will thus bind to them and form part of the polymer structure. In random solutions (right) the target molecules will remain free in solution.

the conductivity of R solutions, within the polymer matrix of OCPCs, is greater than that of A_0 solutions, leading to a lower resistance. The influence of DNA molecules on solution conductivity has been demonstrated by Ma *et al.* [255]

We have seen that carbon nanopowder OCPCs can be used to differentiate between analyte and control solutions. To assess their potential as a technology for oligonucleotide detection it is necessary to determine how their electrical response varies with analyte concentration. Figure 4.24 shows the d.c. resistance over time for OCPCs swelling in A_0 solutions of varying oligonucleotide concentration. For concentrations as low as 10 nM there is no observable difference in the rate of change of resistance or the time at which the transition between the high and low conductivity regimes occurs. At 1 nM, the transition occurs approximately 40 s later, at similar times to samples in R solutions (Figure 4.21). This is consistent with what we saw in Section 3.2.3, where for concentrations of 10 nM and above, at early times, there was no discernible difference in volume for OCPCs swelling in A_0 solutions, whereas for concentrations below 10 nM the OCPC volumes were indistinguishable from those of samples in R solutions. The-

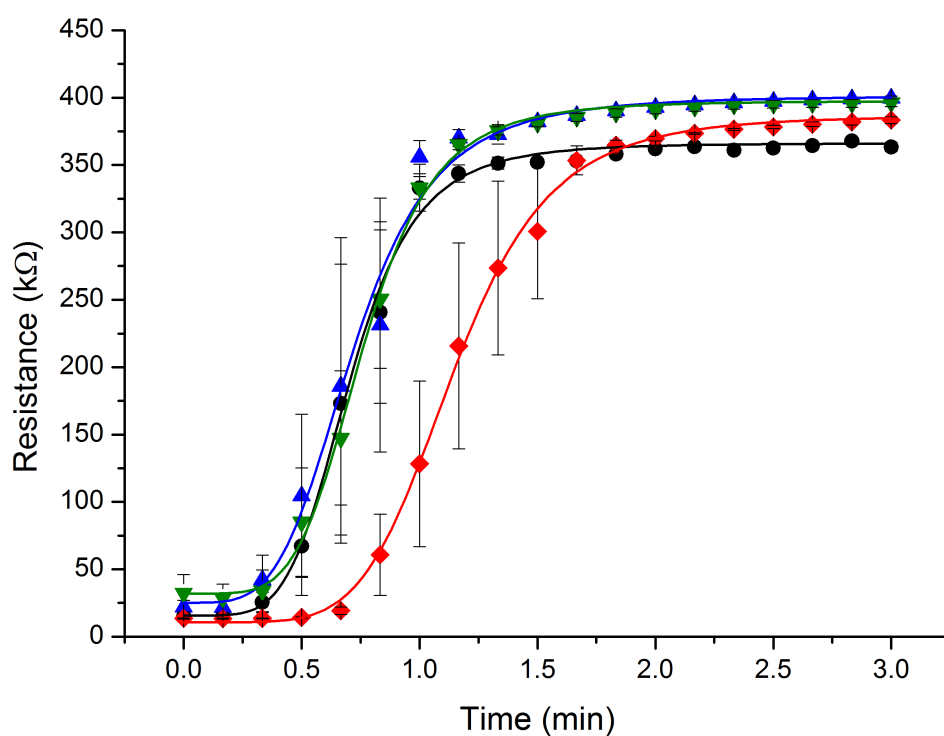


Figure 4.24: The d.c. resistance of carbon nanopowder OCPCs swelling over time in analyte solutions of varying concentration: 10 μM (\bullet), 1 μM (\blacktriangle), 10 nM (\blacktriangledown) and 1 nM (\blacklozenge). The cross-link density was 0.6 mol% wrt monomer MBA, 0.4 mol% wrt monomer oligonucleotide cross-linker. The carbon loading was 20 mg/ml. The solutions were held at 23°C and contained 150 mM NaCl and 1 mM phosphate buffer.

oretical models of hydrogel swelling, as discussed in Section 1.4.1, tell us that the rate of swelling is dependent upon the final swollen volume [110]. Therefore if there is no difference in the final volume of OCPCs in A_0 solutions below 10 nM, when compared to R solutions, it is to be expected that there will be no difference in the time at which the transition between conductivity states occurs. This represents a lower limit of detection for OCPCs.

The error bars in Figure 4.24 represent the standard error on the mean. The principle sources of variation between the samples will be small variations in the carbon

concentration and distribution. Hence the errors are greatest during the transition between conductivity states, where the carbon concentration will be most significant.

Figure 4.24 shows that there is little variation in the end-point resistance in relation to varying A_0 concentration. This compliments the hypothesis that analyte molecules are immobilised in the polymer network and thus do not contribute to the solution conductivity. An exception to this is the end-point resistance in $10 \mu\text{M}$ A_0 solutions, which are lower than for other concentrations. It is possible that at this concentration, there are sufficient numbers of analyte molecules for there to be an excess that remain unbound and thus free to contribute to the solution conductivity.

Figure 4.25 shows the results for the same experiments using R solutions. The results are more variable than for the A_0 case. At all concentrations the transition between the high and low conductivity regimes begins approximately 50 s after immersion. However, there is considerable variation in both the rate of change of resistance and the end-point resistances of the OCPCs with the oligonucleotide concentration in R solutions. These differences are clearly not the result of any differences in volume between the samples as, looking at the equivalent optical volume data for the two most divergent concentrations, $10 \mu\text{M}$ and $1 \mu\text{M}$ (Figure 4.26), there is no appreciable difference in volume between the two over the relevant time-frame.

A significant factor in the variation seen in Figure 4.25 will be the effects of varying oligonucleotide concentration on the conductivity of the swelling medium, discussed previously. This is evident from Figure 4.27, which shows the end-point resistance against the oligonucleotide concentration of the R solutions. For concentrations up to $1 \mu\text{M}$, a higher oligonucleotide concentration leads to a lower resistance, which

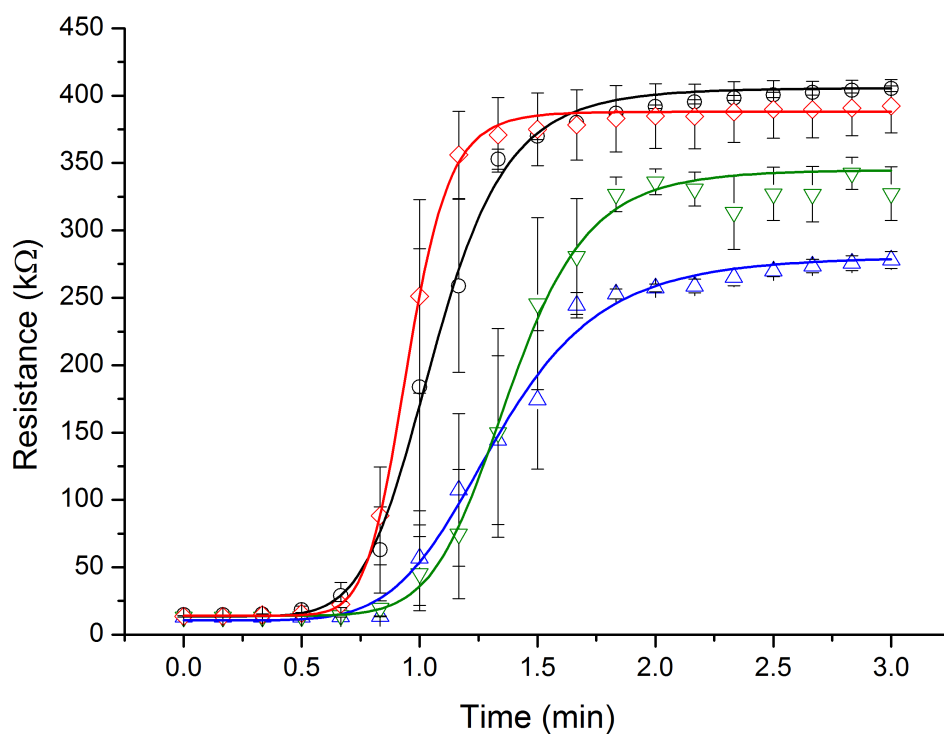


Figure 4.25: The d.c. resistance of carbon nanopowder OCPCs swelling with time in random solutions of varying concentration: 10 μM (\circ), 1 μM (\triangle), 10 nM (∇) and 1 nM (\diamond). The cross-link density was 0.6 mol% wrt monomer MBA, 0.4 mol% wrt monomer oligonucleotide cross-linker. The carbon loading was 20 mg/ml. The solutions were held at 23°C and contained 150 mM NaCl and 1 mM phosphate buffer.

corresponds to what would be expected [255]. However, the end-point resistances of OCPCs in 10 μM solutions are anomalously high, indicating that there are other factors involved. For some concentrations the error bars for the upper plateau in Figures 4.25 and 4.27 are greater than for others, implying greater variation between samples. Why this is the case is unclear. For each concentration, the swelling media are aliquots of a larger volume, meaning that there would be expected to be little variation in oligonucleotide or salt concentration between samples.

The reasons for the anomalous nature of the resistances for OCPCs in 10 μM R solutions remain unclear. Performing similar experiments to those presented in Figure

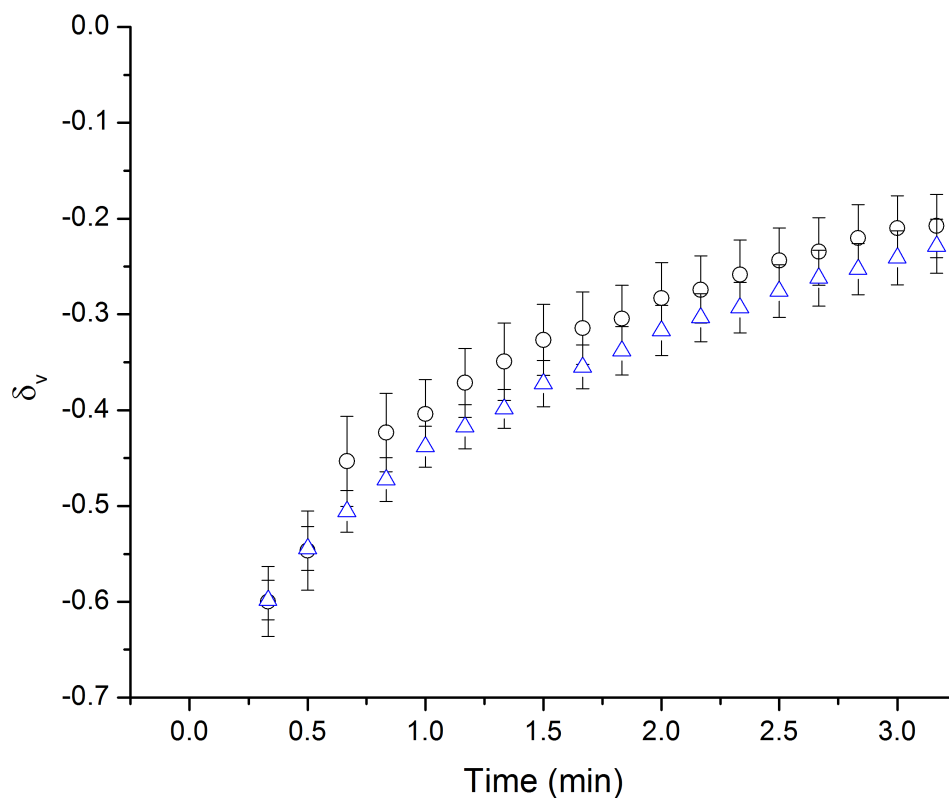


Figure 4.26: Fractional volume increase of OCPCs swelling over time in R solutions of varying concentration. R solution concentrations: 10 μM (\circ) and 1 μM (\triangle). The cross-link density was 0.6 mol% wrt monomer MBA, 0.4 mol% wrt monomer oligonucleotide cross-linker. The carbon loading was 10 mg/ml. The solutions contained 150 mM NaCl, 1 mM phosphate buffer and were held at 23°C.

4.25, without the addition of oligonucleotide cross-linkers, yields final resistances below 350 k Ω , closer to what would be expected from Figure 4.27. This suggests that the anomalous results are the result of interactions between the solution oligonucleotides and the oligonucleotide cross-linkers, rather than the solution oligonucleotides and the carbon particles. It is possible that at 10 μM the hybridisation of short complementary regions (3-4 nucleotides) between the solution oligonucleotides and the oligonucleotide cross-linkers becomes energetically favourable. This will be insufficient to cleave the cross-linkers but sufficient to immobilise the solution oligonucleotides, thereby reducing the conductivity of the solution. However, this does not explain why, at 10 μM , the

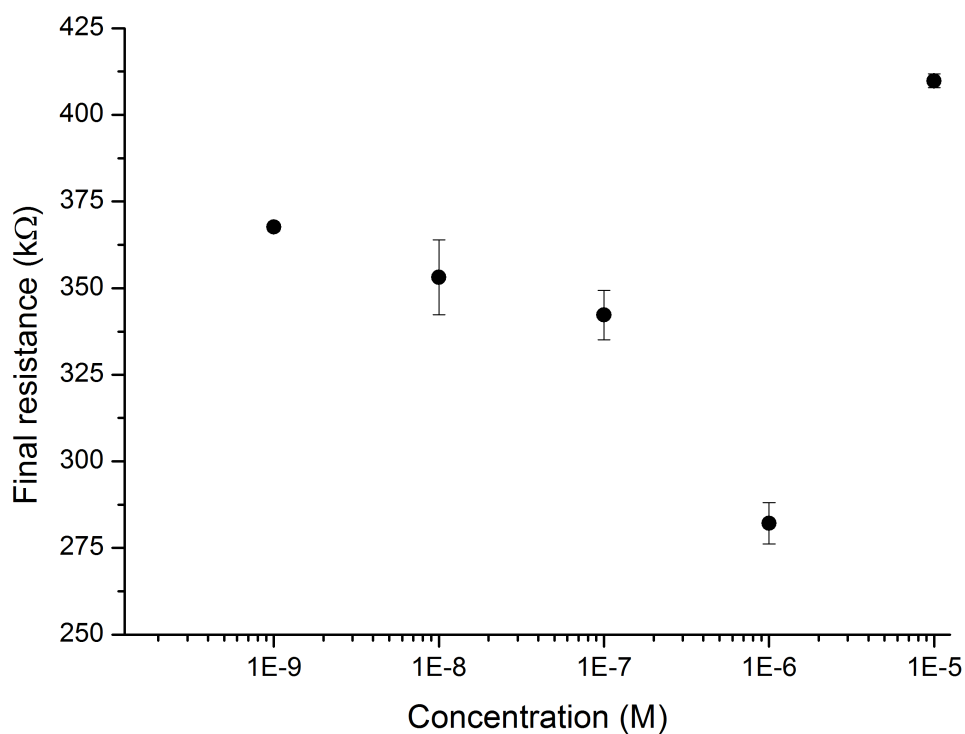


Figure 4.27: The final value of the resistance for OCPCs in R solutions of varying concentration.

final resistances of OCPCs in R solutions are greater than those in A_0 solutions (Figure 4.24).

A greater understanding of some of the results discussed in this section can be reached by considering the relative numbers of oligonucleotide cross-linkers and analyte oligonucleotides for an OCPC droplet in solution. Table 4.1 shows the calculated number of oligonucleotide molecules in the swelling medium, both as an absolute number and as a proportion of the number of oligonucleotide cross-linkers in a $2 \mu\text{l}$ OCPC droplet (prepared using the parameters described in Section 2.1.1). The most noteworthy feature of this data is that (excepting for concentrations of $10 \mu\text{M}$) the analyte molecules are present in far lower numbers than the oligonucleotide cross-linkers, especially given the fact that only a small proportion of the solution

oligonucleotides will diffuse into the OCPC volume within the relevant time-frame. This tells us that the selective swelling documented in this chapter must be the result of the selective cleavage of a very small proportion of the oligonucleotide cross-linkers.

We have seen from Figure 3.17 that, at 23°C, not all of the oligonucleotide cross-linkers will be cleaved, even at relatively high analyte molecule concentrations. However, the differences between partial cross-link cleavage due to the presence of analyte molecules and full cleavage due to thermal dehybridisation are not sufficient to explain the numbers seen in Table 4.1. It may be that only a minority of the cross-links hybridise correctly in the pre-composite solution. It may be that a proportion of the cross-links are cleaved during the polymerisation process. Or it may be that, due to the fact that the oligonucleotide cross-linkers are significantly longer than the conventional MBA cross-linkers, a significant proportion of cross-links form in such a way that their cleavage does not influence the swelling of the OCPC. Whatever the cause, only a minority of the oligonucleotide cross-linkers appear to influence the swelling behaviour of the OCPCs. A second significant point that can be taken from Table 4.1 is that, of the concentrations investigated, only at 10 μM is the number of solution oligonucleotide molecules of the same order of magnitude as the number of oligonucleotide cross-linkers. This supports

Concentration	Number of molecules	Analyte:cross-linkers
10 μM	1.5×10^{-8}	1.3×10^0
1 μM	1.5×10^{-9}	1.3×10^{-1}
100 nM	1.5×10^{-10}	1.3×10^{-2}
10 nM	1.5×10^{-11}	1.3×10^{-3}
1 nM	1.5×10^{-12}	1.3×10^{-4}

Table 4.1: The number of analyte molecules as a proportion of oligonucleotide cross-linkers for varying analyte concentration. The molecule numbers are for a solution volume of 1.5 ml and the ratio is relative to the number of oligonucleotide cross-linkers in a 2 μl OCPC droplet.

the hypothesis that the anomalously low end-point resistance of OCPCs in $10\ \mu\text{M}$ A_0 solutions (Figure 4.24) is the result of excess analyte molecules contributing to the conductivity of the swelling medium.

4.2.4 Cyclic voltammetry

When performing d.c. resistance measurements it is important to ensure that there are no unexpected reactions taking place at the electrode surface, such as reduction-oxidation (redox) reactions of the polymer or of the electrode material itself. Reactions of this kind would affect the resistance measurements and lead to unreliable results.

Figure 4.28 shows cyclic voltammograms for each of the three cases described in Section 2.4.2 (a blank electrode, 0 mg/ml and 20 mg/ml polyacrylamide/carbon nanopowder composite coated electrodes) across the narrow potential window (-1.5 to $+1.5$ V). In the case of a blank working electrode (WE) the voltammogram is dominated by the peaks at the positive and negative extremes of potential, caused by the bulk evolution of oxygen and hydrogen at the WE surface respectively. This is as would be expected for the cyclic voltammogram of a Pt electrode in an electrolyte solution [257,258]. With the addition of 0 mg/ml and 20 mg/ml polyacrylamide/carbon nanopowder composites to the WE surface the current flow appears to decrease. This is to be expected as the presence of the polymer or composite will impede the flow of molecules and ions to and from the electrode surface, thereby reducing the current flow [259, 260]. In the blank case there is an additional peak at approximately -0.9 V, most likely due to the adsorption of hydrogen [257]. This is also suppressed by the addition of polymer or composite.

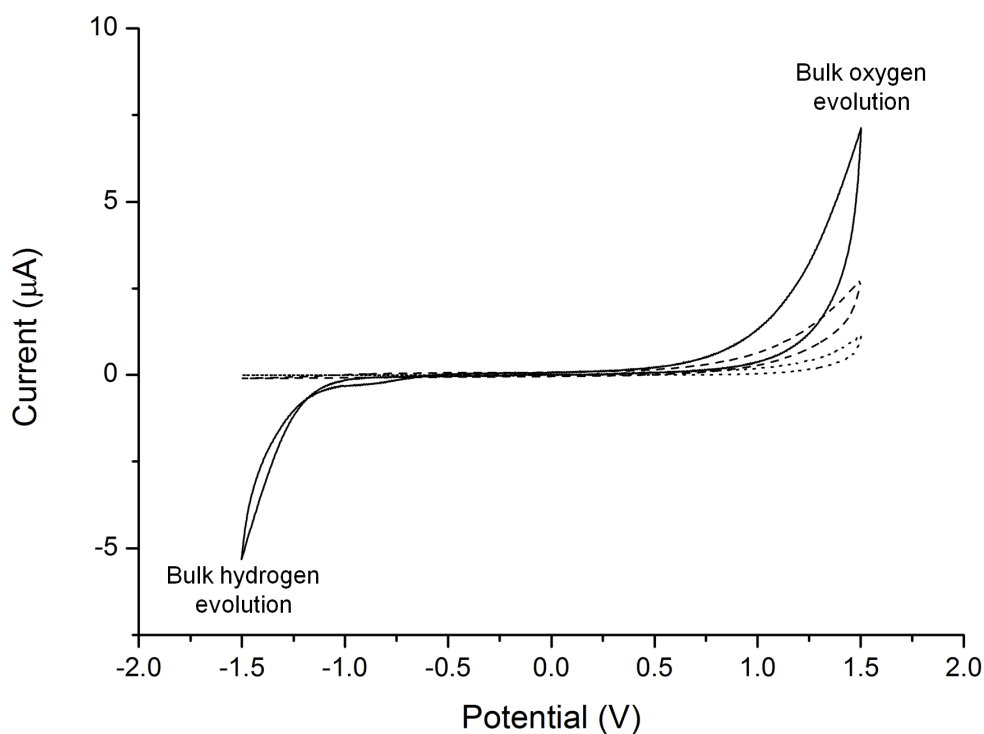


Figure 4.28: Cyclic voltammograms for blank (solid), 0 mg/ml (dashed) and 20 mg/ml polyacrylamide/carbon nanopowder composite (dotted) electrodes in 150 mM NaCl, 1 mM phosphate buffer solution. The potential window ranges from -1.5 to 1.5 V. The scan rate was 0.1 V/s, a single scan is shown for each configuration.

Significantly, there are no observable current peaks in the 0 mg/ml or 20 mg/ml composite configurations that are not evident in the blank configuration (at greater magnitudes), indicating that no unexpected redox reactions take place as a result of the presence of the polymer/composite. Additionally, there are no apparent peaks that can be attributed to reactions of the electrode material. These facts imply that there are no reactions occurring that would adversely affect a d.c. resistance measurement.

Figure 4.29 shows the results of the same experiments over the wide potential window (-4.0 to +4.0 V). The general characteristics of the cyclic voltammograms appear similar to the narrow potential window case. The most significant features are due to the bulk evolution of oxygen and hydrogen at the WE, with both being inhibited in

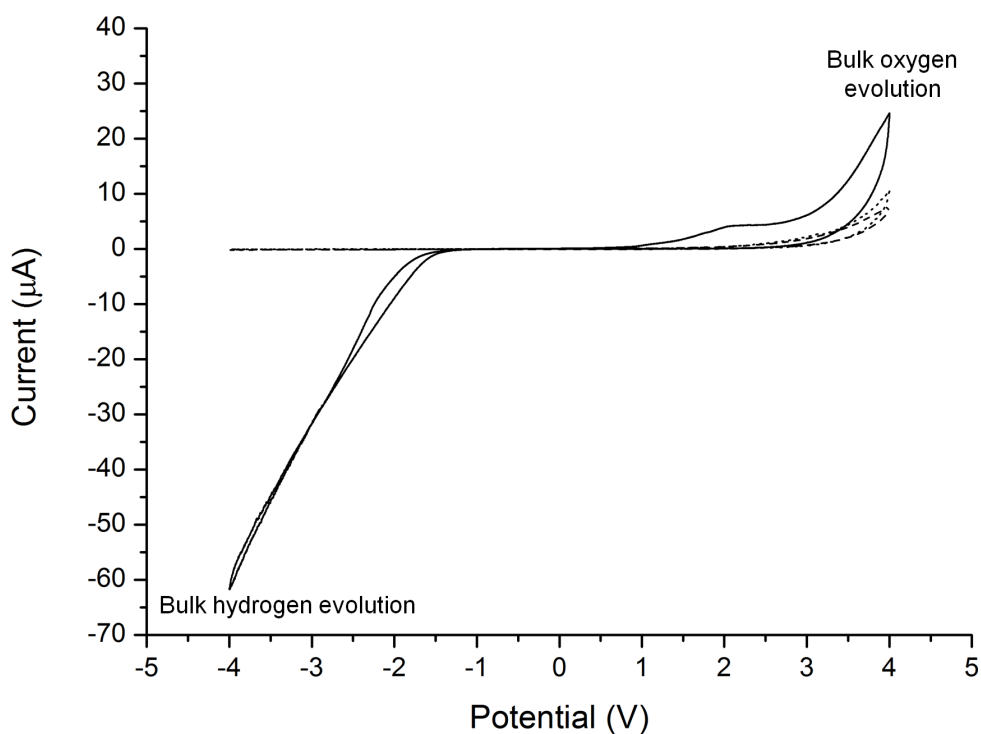


Figure 4.29: Cyclic voltammograms for blank (solid), 0 mg/ml (dashed) and 20 mg/ml polyacrylamide/carbon nanopowder composite (dotted) electrodes in 150 mM NaCl, 1 mM phosphate buffer solution. The potential window ranges from -4.0 to 4.0 V. The scan rate was 0.1 V/s, a single scan is shown for each configuration.

the presence of polyacrylamide or composite. In the blank case there is an apparent peak at approximately +2.0 V, but this is suppressed by the presence of polymer or composite. Once again there are no additional features in the polymer or composite cases, when compared to the blank case, indicating no redox contribution from the polymer or composite.

The wide potential window represents the maximum range a composite would be exposed to during the tests described in Section 2.4 and the preceding sections of this chapter, thus providing a suitable representation of the potentials and currents that an electrode device would be exposed to during a typical d.c. resistance measurement.

Parylene coated electrode devices were used for these measurements to ensure that there was no contribution from any part of the connective tracks that might be immersed in the electrolyte solution.

4.3 Conclusions

Using off-the-shelf electrode devices the composites frequently detached from the substrate surface or delaminated from the electrodes, resulting in highly inconsistent electrical measurements. These issues render these devices unsuitable for the measurement of the electrical properties of OCPCs. Custom electrode devices were designed and fabricated to rectify these shortcomings. These custom electrode devices consist of Pt IDE on a Si/SiO₂ substrate with an optional parylene passivation layer. Composites can be deposited and polymerised *in situ* on the IDE. Pt was chosen for the electrode material due to its high conductivity and low reactivity, Si/SiO₂ was chosen for the substrate due to its ubiquity in microfabrication and microelectronics. The passivation layer was added for the dual purposes of protecting the connecting tracks and facilitating the deposition of the composites onto the IDE.

Using these custom electrode devices, with reduced IDE array size and increased digit spacing, in conjunction with a silanisation procedure to chemically bind the composites to the substrate surface significantly reduces the occurrence of both composite detachment and delamination. These improvements to composite adhesion mean that the custom electrode devices described herein are suitable for the measurement of the electrical properties of polyacrylamide/carbon composites.

The percolation thresholds of composites formed from polyacrylamide and a variety of different forms of carbon particle additives have been determined. These are approximately 6.0 mg/ml for carbon nanopowder composites and 2.2 and 1.0 mg/ml for carbon micropowder and graphite composites respectively. To produce composites that are conductive in their dried state, the carbon particles will need to be loaded at concentrations above these thresholds. We have seen that, whilst the percolation curves presented in this chapter correspond to the general behaviour of GEM theory, the parameter fits to the GEM equation produce values that are outwith the ranges that would be expected from the literature. It is believed that this is a result of the highly porous nature of polyacrylamide. Conductive composites could not be produced using carbon nanotubes using the methodology described in this thesis.

It has been shown that a measurement of the d.c. resistance can be an effective means of measuring the swelling of polyacrylamide/carbon composites electrically. It can successfully be used to detect the transition between high and low conductivity states as the composites swell. However, as yet, it has not been possible to capture the full range of swelling using d.c. resistance measurements due to limitations to the concentrations at which carbon particles can be added to polyacrylamide. Additionally we have seen that the addition of NaCl to the sensing medium reduces the measured resistance, but that the transition between conductivity states is still detectable.

An a.c. measurement of the complex impedance can be used to detect the transition between conductivity states for polyacrylamide/carbon particle composites as a result of swelling in DI water. However, the addition of NaCl to the swelling medium renders his change undetectable (under the conditions investigated). Therefore, it is concluded

that d.c. measurements are a more appropriate means of measuring the conductivity changes of polyacrylamide/carbon particle composites as they swell (for the frequency ranges investigated).

Cyclic voltammetry shows that there are no observable redox contributions from polyacrylamide or polyacrylamide/carbon composites deposited on IDE arrays or from the platinum of the electrodes. This tells us that d.c. resistance measurements will not be subject to undesired reactions of either the polymer or the electrode material, using the parameters described herein.

In the case of carbon micropowder (2-12 μm), unexpected interactions between the carbon particles and the DNA cross-linkers render such OCPCs ineffective as a transduction mechanism. If carbon is to be continued to be used as a conductive additive for OCPCs, further investigations into the interactions between carbon particles and the DNA cross-linkers will be required. Graphite powder is also unsuitable as a conductive component for OCPCs as it results in unstable resistance readings thought to be caused by the particles 'settling' within the hydrogel as it swells.

In the case of carbon nanopowder-based OCPCs, although there is no volume dependent differential end-point in the resistance measurement, analyte solutions can clearly be differentiated from controls in under three minutes via differences in the transition time between the percolating and non-percolating states, caused by differences in the rates of swelling. To increase the volume change measurable using this technique would require either the inclusion of conductive particles to a higher concentration, the use of particles with a lower percolation threshold or the modification of the polymers to produce less non-specific swelling. The lower limit of detection using a d.c. resistance

measurement of OCPCs for oligonucleotide detection is of the order of 10 nM, which corresponds to what we have seen for optical measurements.

As stated in Chapter 1, the central premise of this thesis is that a new method of microRNA (miRNA) detection may be achieved through the transduction of the swelling of oligonucleotide cross-linked polymers by incorporating a conductive component to create OCPCs. With this aim in mind it can be concluded that the strengths of this approach are that it can be used to differentiate between analyte and control solutions in a manner that is:

- simple,
- direct,
- rapid, and
- which provides a direct electrical output.

The remaining challenges are as follows:

- the full range of swelling cannot currently be measured,
- the analyte concentration cannot yet be inferred from the response,
- delamination of the OCPCs from the electrode surface still occurs, and
- this approach has yet to be demonstrated for RNA.

These challenges will be addressed further in Chapter 6.

Chapter 5

Morpholino-functionalised hydrogels

5.1 Introduction

Chapters 1-3 focus solely upon oligonucleotide cross-linked polymer composites (OCPCs) produced using DNA oligonucleotide cross-linkers. However, there are several documented examples of synthetic nucleic acid analogues that possess interesting physical or chemical properties [261–267]. As a means of addressing some of the shortcomings of OCPCs discussed in the previous chapter – namely, the non-specific swelling and the significant degree of thermal instability – the author proposed developing hydrogels incorporating cross-linkers formed from DNA analogues. To achieve this, Dr. Jaclyn Raeburn was recruited to develop a method for functionalising morpholino oligonucleotides with an end-group modifier to allow them to be incorporated into the macromolecular structure of hydrogels in the same manner as DNA oligonucleotides (as discussed in Section 1.4.2).

This chapter introduces the DNA analogue referred to as ‘morpholinos’ and their potential application to bio-responsive polymers. It also details the collaborative efforts to characterise the swelling behaviour of morpholino-functionalised hydrogels and to compare this to their DNA-functionalised equivalents. Section 5.2.1 describes the method by which Dr. Raeburn synthesised morpholino-functionalised hydrogels. Section 5.2.2 details the tests performed to characterise their differential swelling behaviour using the optical measurement method described in Section 1.4.2. The tests for morpholino-functionalised hydrogels were performed by Dr. Raeburn, the equivalent tests for DNA-functionalised hydrogels were performed by the author. Additional kinetic tests were performed by Geraint Langford. Sections 5.2.3 and 5.2.4 detail tests performed to investigate the swelling behaviour of morpholino- and DNA-functionalised hydrogels with respect to varying salt concentration and temperature respectively. The tests for morpholino-functionalised hydrogels were performed by Dr. Raeburn and the equivalent tests for DNA-functionalised hydrogels were performed by the author.

5.1.1 Nucleic acid analogues

The structure of nucleic acids such as DNA or RNA is that of repeating nucleobases attached to a phosphate backbone (Figure 5.1, top). For various applications in medicine and research, synthetic analogues of nucleic acids have been developed. Generally these consist of the same nucleobases attached to backbones utilising different chemistries, producing molecules that will hybridise with natural nucleic acids but which have significantly different physical and chemical properties. There are a variety

of documented examples of such nucleic acid analogues [261–267], but only morpholinos will be investigated as part of this thesis.

5.1.1.1 Morpholinos

Morpholinos are synthetic nucleic acid analogues first described by Summerton in 1985 [268, 269]. The anionic phosphate backbones of DNA and RNA are substituted with a neutral sequence comprised of morpholine rings and phosphorodiamidate linkages (Figure 5.1, bottom). This neutrality means that there is less electrostatic repulsion between morpholinos and conventional nucleotides. Therefore, morpholino/DNA or morpholino/RNA duplexes display increased melting temperatures, and correspondingly greater hybridisation efficiencies and thermal stabilities, when compared to conventional nucleotide duplexes. [268–273]

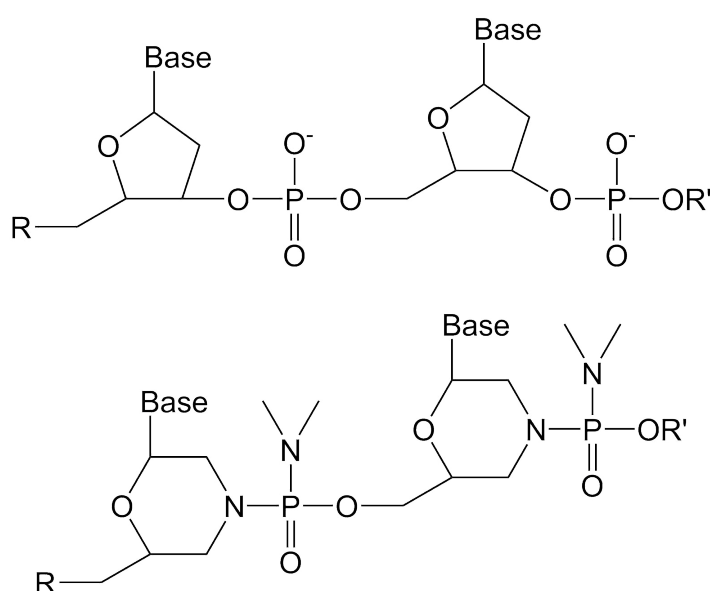


Figure 5.1: The chemical structure of DNA (top) and morpholinos (bottom). These represent a segment of the backbone of a single strand. The bases can be any of the four bases: adenine (A), cytosine (C), guanine (G) or thymine (T). Adapted from Braasch *et al.* [265] and Tercero *et al.* [270].

Additionally, also as a result of the reduced repulsion between strands, duplexes of morpholinos and conventional nucleotides are more sensitive to base mismatches, and thus morpholinos display greater specificity than their conventional counterparts. [271]

Morpholinos are most commonly used as genetic ‘knock-down agents’, tools for the suppression of gene expression within cells, an application for which they were specifically designed. A major advantage of morpholinos for this application is the fact that their non-conventional backbone structure renders them immune to nuclease enzymes (enzymes that break down nucleic acids) making them highly stable in biological environments. [268, 271, 272]

The characteristics of morpholinos described herein – namely greater hybridisation efficiency, stability and specificity – make them a highly attractive alternative to conventional nucleotides for the creation of bio-responsive polymers.

5.1.1.2 Peptide nucleic acids

Peptide nucleic acids (PNAs) are another example of synthetic nucleic acid analogues with a neutral backbone. Consequently, PNA has similarly advantageous physical characteristics when compared to conventional nucleotide duplexes [8, 64, 266, 274, 275] and it is commonly used for probes in biosensing applications [276–280]. Whilst PNA is also a potential alternative to conventional nucleic acids for the creation of bio-responsive polymers, PNAs are approximately one hundred times less soluble in water than morpholinos. Furthermore, morpholinos can be synthesised far more easily and cheaply than PNA [268–272]. For these reasons, morpholinos were selected over PNA as

alternative oligonucleotide cross-linkers for the experiments described in the following sections.

5.2 Materials and methods

5.2.1 Hydrogel formation

Morpholino-functionalised hydrogels were prepared using an adapted version of the method described in Section 2.1.1, wherein the DNA oligonucleotides are replaced with morpholino oligonucleotides (functionalised as described in Appendix E) and the ethanol extraction process is replaced with a lyophilisation (freeze-drying) step. All other factors and parameters remain unchanged, producing hydrogels with 1.41 M acrylamide (AAM), 0.6 mol% wrt monomer N, N' methylene-bisacrylamide (MBA) and 0.4 mol% wrt monomer morpholino cross-linker. The carbon nanopowder concentration was varied between 0 and 10 mg/ml.

5.2.2 Differential swelling

1 μ l samples of morpholino-functionalised hydrogel (0 mg/ml carbon nanopowder) were prepared as described previously. Using the method outlined in Section 2.2.1, these samples were immersed in an A_0 solution (10 μ M, 150 mM sodium chloride (NaCl), 1 mM phosphate buffer) for 12-18 hours until saturated and then removed from solution, patted dry and imaged. The same custom MatLab algorithm was used to determine the

swollen volume. This process was repeated using a R solution of the same concentration and using DNA-functionalised hydrogels, in both A₀ and R solutions, for comparison.

2 μ l samples of morpholino-functionalised hydrogel (10 mg/ml carbon nanopowder) were prepared as described previously. Using the method outlined in Section 2.2.2 these samples were immersed in A₀ solutions (150 mM NaCl, 1 mM phosphate buffer) with concentrations ranging from 10 μ M to 100 pM and imaged whilst swelling. This process was repeated using a R solution of 10 μ M.

5.2.3 Hydrophilicity versus salinity

1 μ l samples of morpholino-functionalised hydrogel (0 mg/ml carbon nanopowder) were prepared as described previously and immersed in 10 μ M A₀ solution (1 mM phosphate buffer) with NaCl concentrations varying between 0 and 200 mM, for 12-18 hours. The samples were then removed, patted dry, imaged, and the volume calculated as before. Three repetitions were performed for each NaCl concentration. The same process was carried out with DNA-functionalised hydrogels for comparison. The temperature of the solutions was maintained at $(23 \pm 1)^\circ\text{C}$, as described in Section 2.4.

5.2.4 Thermal stability

1 μ l samples of morpholino-functionalised hydrogel (0 mg/ml carbon nanopowder) were prepared as described previously, with a NaCl concentration of 50 mM. These samples were then immersed in R solutions (10 μ M, 50 mM NaCl, 1 mM phosphate buffer) at $(23 \pm 1)^\circ\text{C}$ for 12-18 hours to allow them to fully saturate. They were then removed, patted

dry and imaged as before. This process was repeated for solution temperatures ranging between 25°C and 37°C, maintained using a water bath as before. Three repetitions were performed for each temperature. The same process was carried out with DNA-functionalised hydrogels for comparison.

5.3 Results and discussion

5.3.1 Differential swelling

To assess the potential utility of morpholino-functionalised hydrogels for bioresponsive polymer applications it is necessary to determine their swelling characteristics. Figure 5.2 shows the fractional volume change, δ_v , (as defined by Equation 2.1) for morpholino-functionalised hydrogels saturated in 10 μM A_0 or R solution. It is presented alongside the equivalent data for DNA-functionalised hydrogels for comparison. Figure 5.2 shows that morpholino-functionalised hydrogels demonstrate selective swelling, exhibiting volume changes in A_0 solution greater than twice those observed in R solutions. It also shows that, in both A_0 and R solutions, morpholino-functionalised hydrogels swell to smaller volumes than their DNA equivalents. This is likely to be partially a result of the fact that, as they are anchored into the polymer network at the 3' rather than the 5' end, morpholino cross-linkers will be shorter than the equivalent DNA cross-linkers (Figure 5.3). However, the higher hydrophilicity of the DNA cross-linkers relative to morpholinos (which will be discussed in greater detail in Section 5.3.2) will also be a factor.

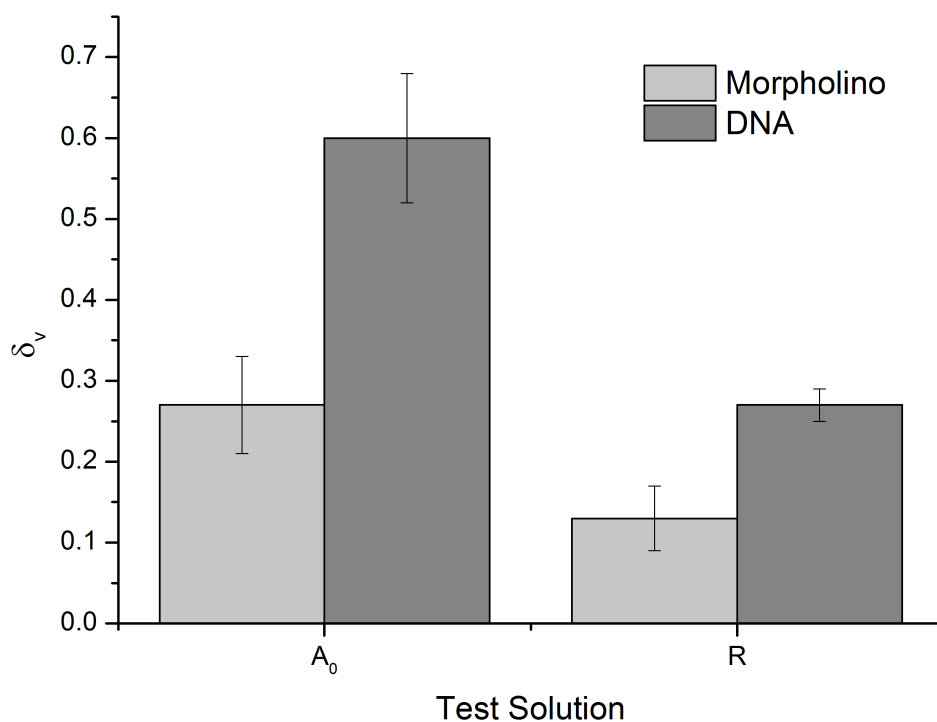


Figure 5.2: Fractional volume increase of morpholino-functionalised hydrogels compared to DNA-functionalised hydrogels. The samples were immersed in either A_0 or R solutions ($10 \mu\text{M}$ oligonucleotide, 150 mM NaCl, 1 mM phosphate buffer) for 12-18 hours at 23°C . The morpholino-functionalised hydrogel data was collected by Dr. Jaclyn Raeburn, the DNA-functionalised hydrogel data was collected by the author.

Figure 5.4 shows δ_v against time for morpholino-functionalised hydrogels in A_0 solutions of $10 \mu\text{M}$ and 100 pM , shown alongside the equivalent data for R solutions of $10 \mu\text{M}$. Differential swelling between the 100 pM A_0 samples and the R samples is evident and the swelling responses of the $10 \mu\text{M}$ and 100 pM A_0 are highly similar, within the margin of error. In Section 3.2.3 we saw that the swelling response of DNA-functionalised hydrogels began to diverge and tend towards the non-specific swelling response at analyte concentrations of 10 nM or below. This suggests an improvement in sensitivity of at least two orders of magnitude for morpholino-functionalised hydrogels compared to their DNA equivalents. It is believed that this improvement in sensitivity is a result of the superior hybridisation efficiency of morpholino/DNA duplexes compared

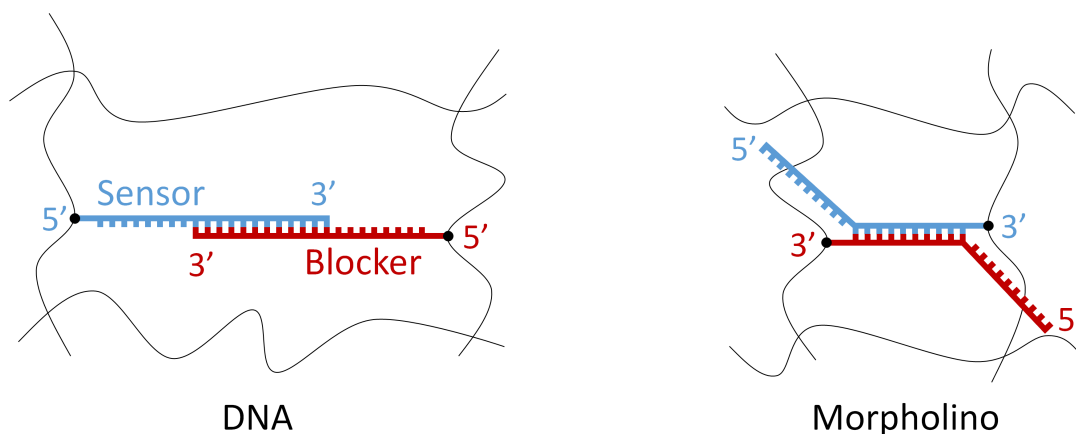


Figure 5.3: Illustration of the difference in cross-linker length between 5' functionalised DNA and 3' functionalised morpholinos.

to DNA/DNA duplexes [268–273]. If the probability of an analyte strand hybridising with a sensor strand is increased, this corresponds to an increase in sensitivity. Thus a greater hybridisation efficiency would result in an increase in sensitivity. The reduced swelling of morpholino-functionalised hydrogels compared to their DNA equivalents should not be taken to imply a corresponding decrease in sensitivity, as it is the minimum concentration at which differential swelling will occur that represents the sensitivity of the system, rather than the magnitude of that swelling.

It is likely that the detection limit for morpholino-functionalised hydrogels is lower than 100 pM but, as a result of a limited supply of morpholinos, this detection limit has yet to be determined.

The error bars in both Figures 5.2 and 5.4 represent the standard error on the mean. The principle sources of variation between samples will be any variation in the volume as the droplet is pipetted and the measurement error of the volume using the imaging method described in Section 2.2.

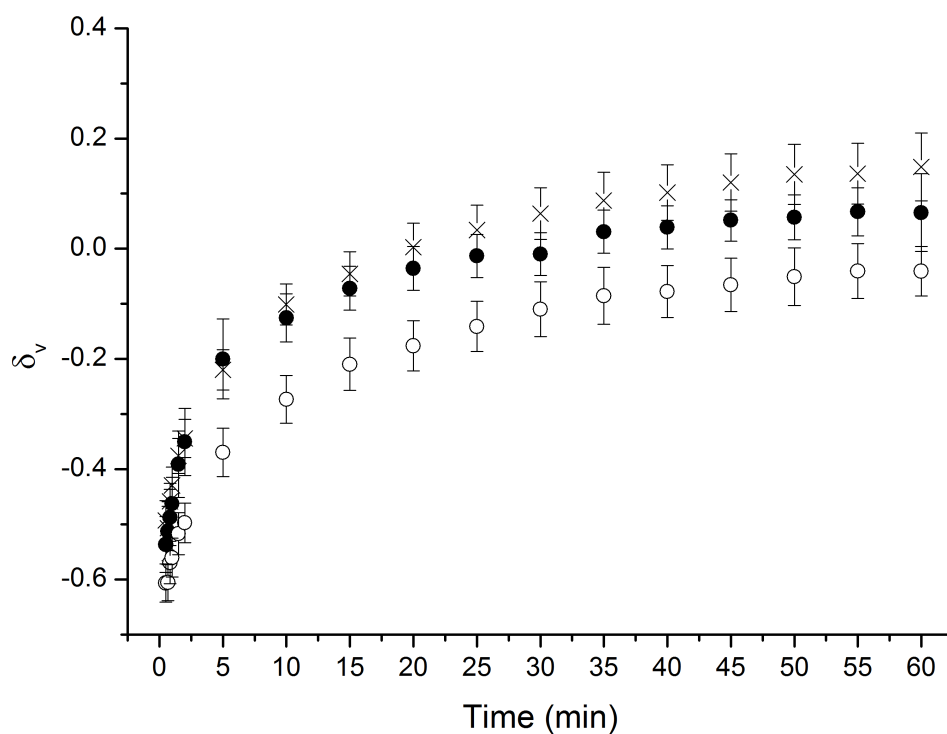


Figure 5.4: The fractional volume increase of morpholino-functionalised hydrogels with time as they swell in 10 μM (\bullet) and 100 pM (X) A_0 solutions and 10 μM (\circ) R solutions. All solutions contained 150 mM NaCl and 1 mM phosphate buffer. The experimental data shown was collected and analysed by Geraint Langford.

In Section 3.2.2 we saw that DNA-functionalised hydrogels demonstrate single-base specificity. Given that morpholino/DNA duplexes are known to demonstrate superior specificity, compared to DNA/DNA duplexes [271], it would be reasonable to assume that morpholino-functionalised hydrogels would also demonstrate single-base specificity.

5.3.2 Hydrophilicity versus salinity

We have seen in the previous section that morpholino-functionalised hydrogels display reduced swelling in analyte solutions, compared to DNA-functionalised hydrogels. It is believed that this is partly a result of the non-ionic structure of morpholinos. To better understand the influence of the ionic composition of the swelling medium on

swelling behaviour, it is necessary to investigate the swelling response of oligonucleotide-functionalised hydrogels as a function of ionic concentration. Figure 5.5 shows δ_v for morpholino- and DNA-functionalised hydrogels against NaCl concentration. It is clear that the swelling of the DNA-functionalised hydrogels has a strong dependence upon the salinity of the analyte solution, with the hydrogels at lower NaCl concentrations having δ_v values many times that for those at higher NaCl concentrations. It is believed that this dependence is due to changes in the underlying hydrophilicity of the hydrogels. The incorporation of anionic cross-links (in the form of DNA) into the hydrogels will significantly increase their hydrophilicity as the anionic chains will show an increased affinity for the polar water molecules. With the addition of NaCl, the Na^+ ions will cluster around the DNA, shielding its charge and reducing the affinity for water molecules. [281, 282]

Figure 5.5 shows that there is very little dependency of δ_v upon the the NaCl concentration for morpholino-functionalised hydrogels, which is to be expected given their neutrality. δ_v is effectively constant across the range of NaCl concentrations tested, with the only exception being in the case with no salt. This slight dependency can be explained by the fact that the analyte oligonucleotide will itself be affected by the presence of salt. With no salt present the DNA will be much more hydrophilic, therefore contributing to the ingress of water molecules into the hydrogel matrix. The vertical error bars represent the standard error on the mean and the principle sources of variation between samples will be those discussed in Section 5.3.1. The fact that they appear significantly smaller than for Figures 5.2 and 5.4 is merely an artifact of

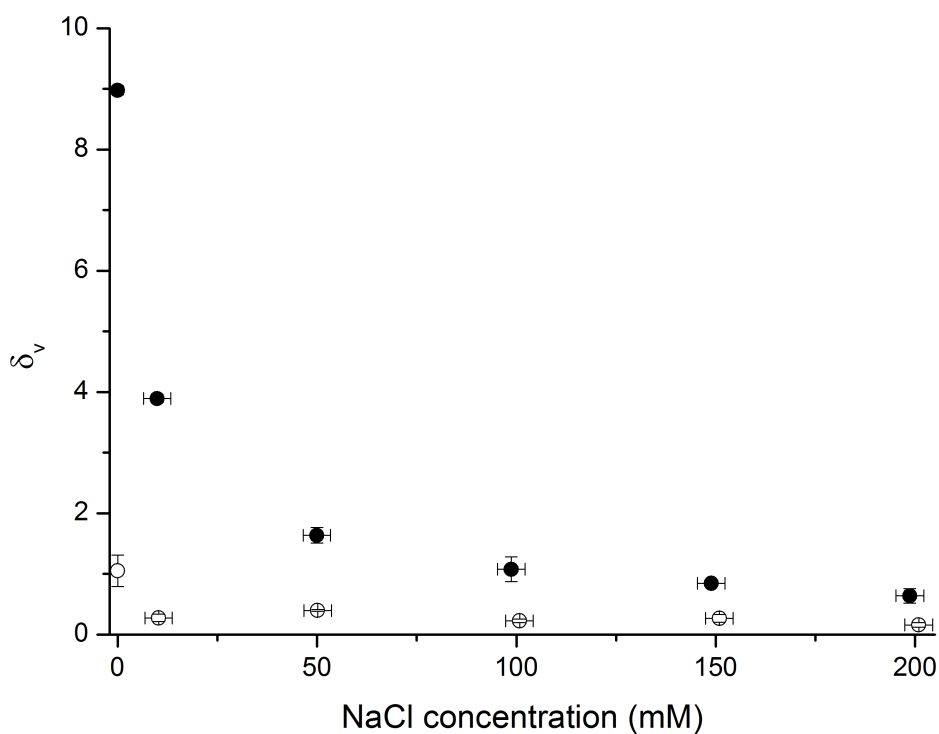


Figure 5.5: Fractional volume increase for morpholino-functionalised hydrogels (\circ) and DNA-functionalised hydrogels (\bullet) saturated in A_0 solution against salt concentration. The samples were immersed in $10 \mu\text{M}$ A_0 solution with varying NaCl concentration at 23°C . The morpholino-functionalised hydrogel data was collected by Dr. Jaclyn Raeburn, the DNA-functionalised hydrogel data was collected by the author.

the much larger scale. The horizontal error bars represent the experimental error in preparing the NaCl solutions.

This independence of swelling volume from salinity in the case of morpholino-functionalised hydrogels offers an advantage over DNA-functionalised hydrogels as the final volume and rate of swelling will be predictable in cases where the ionic concentration of the medium is unknown or variable.

Figure 5.5 presents data for the final volume of the hydrogels. However, it would be reasonable to assume that the rate of swelling for these hydrogels will also show a

dependence upon the salinity, as theory predicts (as discussed in Section 1.4.1) that the rate of swelling is dependent upon the final volume. [110]

A high analyte concentration of 10 μM and a long immersion time were used in these tests to ensure maximum cleavage of the oligonucleotide or morpholino cross-linkers was achieved. This is to ensure that any changes in δ_v were the result of changes to the underlying hydrophilicity of the hydrogel.

5.3.3 Thermal stability

Section 3.2.5 discussed the variation in δ_v as a function of temperature that occurs for DNA-functionalised hydrogels as a result of the thermal dehybridisation of the oligonucleotide cross-linkers. It is well documented that morpholinos have higher melting temperatures (T_m) than their DNA (or RNA) equivalents [268]. It is hypothesised that morpholino-functionalised hydrogels will demonstrate a correspondingly greater thermal stability than DNA-functionalised hydrogels. Figure 5.6 shows δ_v for morpholino- and DNA-functionalised hydrogels as a function of temperature. From room temperature to body temperature the saturated volume of morpholino-functionalised hydrogels shows no appreciable variation other than what might be expected due to experimental error. However, for DNA-functionalised hydrogels there is a large variation in saturated volume with temperature, with values of δ_v ranging from approximately 0.5 at 23°C to approximately 1.2 at 37°C. This is not unexpected. The variation in δ_v is the effect of thermal dehybridisation discussed in Section 3.2.5. For DNA-functionalised hydrogels in R solutions, δ_v will vary between a low value at low temperatures, where few cross-links have been thermally dehybridised, and a maximum value at higher temperatures,

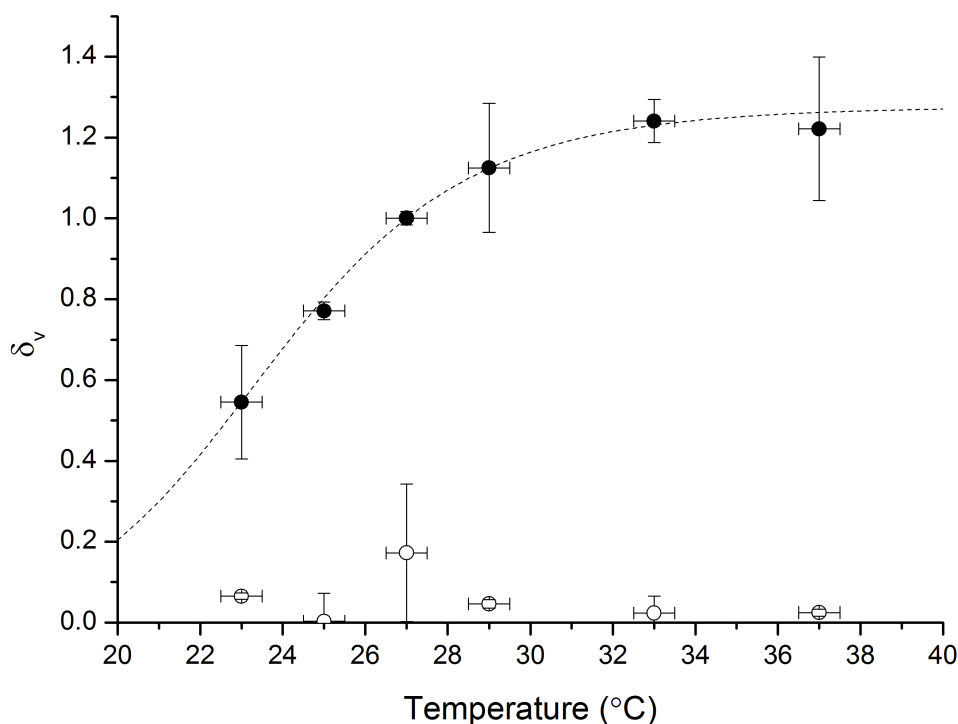


Figure 5.6: Fractional volume increase of functionalised hydrogels saturated in R solution against temperature for morpholino-functionalised hydrogels (○) and DNA-functionalised hydrogels (●). The dashed line represents a best fit to the sigmoid curve equation for the DNA data (as per Section 3.2.5). The samples were immersed in 10 μ M R solution, 50 mM NaCl, 1 mM phosphate buffer at varying temperature. The morpholino-functionalised hydrogel data was collected by Dr. Jaclyn Raeburn, the DNA-functionalised hydrogel data was collected by the author.

where the majority of the oligonucleotide cross-links have been thermally dehybridised.

This behaviour is evident in Figure 5.6.

Figure 5.6 shows that T_m for the morpholino cross-linkers is significantly greater than 37°C and therefore there is no variation in δ_v , as a result of thermal dehybridisation, within the temperature range investigated. Values of T_m of *ca.* 70°C for morpholino/DNA duplexes of similar length (*ca.* 20 bases) have been reported [268]. As before, the vertical error bars in Figure 5.6 represent the standard error on the mean. The horizontal error bars represent the uncertainty on the temperature of the water bath.

This improved thermal stability is significant as, for biosensing applications, swelling

due to thermal dehybridisation constitutes a false positive. If significant thermal dehybridisation can take place within typical testing temperature ranges (20 - 37°C) then the potential for false positives is high. The improvement in thermal stability offered by morpholino-functionalised hydrogels has the potential to greatly reduce, or eliminate, this source of error and eliminate the requirement to implement temperature control of sensors incorporating OCPCs.

Figure 5.6 also suggests that thermal dehybridisation is also a factor in the differences in swelling volume between DNA- and morpholino-functionalised gels discussed in Section 5.3.1.

For these tests a 10 μM R solution was used as the test medium in order to ensure that the ionic content of the solution was consistent with that of previous tests, but that any dehybridisation would be due to thermal effects alone.

As alluded to in Section 5.3.1, the fact that morpholinos are incorporated into the hydrogel structure via a 3' modification rather than a 5' modification (as is the case with the DNA cross-linkers) means that a perfect comparison between morpholino- and DNA-functionalised hydrogels is not currently possible. To achieve this either a 5' modified morpholino or a 3' DNA functionalisation would need to be developed.

5.4 Conclusions

This chapter has introduced synthetic nucleic acid analogues and discussed how an example of such, morpholinos, presents an interesting alternative to DNA oligonucleotide

cross-linkers for OCPCs. A method for functionalising morpholinos with acrylamide moieties and incorporating them into polyacrylamide hydrogels has been presented. To the author's best knowledge, this is the first reported example of a morpholino-functionalised polymer.

This chapter has also presented the characterisation of the selective swelling behaviour of these morpholino-functionalised hydrogels. It has been shown that they demonstrate selective swelling in analyte solutions and that they are sensitive to analyte concentrations at least two orders of magnitude lower than their DNA equivalents. It has also been shown that the swelling response of DNA-functionalised hydrogels is highly dependent upon temperature and the salt concentration of the medium but that morpholino-functionalised hydrogels exhibit greater stability with respect to both variables. These attributes, coupled with the resistance of morpholinos to nucleases, mean that in many respects morpholino-functionalised hydrogels have superior properties and performance when compared to DNA-functionalised hydrogels for bio-responsive polymer applications.

Further work is required to determine the lower limit of detection for morpholino-functionalised hydrogels and to achieve a more direct comparison between morpholino- and DNA functionalised hydrogels via alternative end-group modification techniques.

Chapter 6

Summary and conclusions

6.1 Summary

The simple, sensitive and specific detection of oligonucleotides presents a significant challenge for biosensing. It has potential applications ranging from forensic science to counter-terrorism to, perhaps most notably, the diagnosis of disease [2, 22, 38]. A particular class of oligonucleotides, microRNA (miRNA), has attracted much interest in the biosensing and medical diagnostics communities in recent years, but its potential as a biomarker has been held back by the lack of simple, rapid and low-cost detection techniques.

Polymer hydrogels incorporating oligonucleotide cross-linkers as part of their macromolecular structure have been reported, which undergo selective swelling in the presence of a given analyte oligonucleotide sequence [124, 125]. Conductive polymer composites,

materials in which high conductivity particles are mixed into a low conductivity polymer matrix, are commonly used as a means of transducing polymer swelling [283–286]. The central premise of this thesis is that these two concepts might be combined to create oligonucleotide cross-linked polymer composites (OCPCs) and that such materials might form the basis of a simple, rapid and low-cost means of oligonucleotide detection.

Microdroplet samples of OCPCs were created using carbon particles as the conductive component and DNA-functionalised polyacrylamide as the polymer matrix. The composites were synthesised via a UV-initiated free-radical polymerisation. The physical and electrical properties of these composites were investigated in order to determine the feasibility of their application to oligonucleotide detection. The electrical properties were measured using custom fabricated interdigitated electrode (IDE) devices, the substrate surfaces of which were silanised to improve the adhesion of the composites.

It was found that the swelling of these composites could be measured by performing a simple measurement of the electrical resistance. However, the full range of swelling could not be captured in this manner due to the significant volume changes of the OCPCs and the fact that the amount of carbon that can be added to the hydrogel without adversely affecting its polymerisation is limited to approximately 20–25 mg/ml. It was also found that, in the salt solutions required for stable DNA hybridisation, direct current (d.c.) measurement is superior to alternating current (a.c.) measurement for the transduction of swelling. Composites prepared using carbon nanopowder, carbon micropowder, graphite and carbon nanotubes as the conductive component were investigated. It was found that carbon nanopowder produced the most promising composites for OCPC applications.

Carbon nanoparticle OCPCs were shown to demonstrate selective swelling in analyte solutions with single-base specificity. Analyte solutions can be clearly differentiated from controls, in less than three minutes, via measurement of their electrical resistance by comparing the time taken for the OCPCs to transition between their high and low conductivity states. To the author's best knowledge, this is the first example of oligonucleotide detection using the electrical transduction of conductive composites. However, volume-dependent end-point resistance measurements are not possible using OCPCs in their current incarnation.

The lower concentration limit at which analyte and control solutions could be distinguished by the transition time was found to be of the order of 10 nM. It was also found that the analyte concentration cannot be inferred from the rate of change of OCPC resistance using OCPCs of the volume investigated herein. Additionally, significant thermal dehybridisation can occur in OCPCs and the critical temperature for the OCPCs investigated in this thesis was approximately 25°C. This leads to the potential for significant thermal instability, and non-specific swelling.

The apparent rapid response times and high specificity of OCPCs are extremely attractive attributes for any candidate technology for point-of-care (PoC) diagnostics applications. However, the current detection limit of 10 nM is insufficient for the detection of circulating miRNA in clinical scenarios. This, coupled with the potential for thermal instability means that OCPCs in their current form are unsuitable for miRNA detection applications.

An alternative form of OCPC was proposed in which the DNA cross-linkers are replaced with morpholino cross-linkers. In a collaborative effort, a morpholino-functionalised

hydrogel, believed to be the first ever example of its kind, was synthesised and its swelling behaviour characterised. It was shown that in addition to displaying superior thermal stability and salt-dependent stability, morpholino-functionalised polymers display a sensitivity at least two orders of magnitude superior to their DNA equivalents.

6.2 Conclusions

As was stated in Chapter 1, the central premise of this thesis is that a new method of miRNA detection may be achieved through the transduction of the swelling of oligonucleotide cross-linked polymers by incorporating a conductive component to create OCPCs. Whilst only DNA analytes have so far been investigated, this thesis has shown that analyte solutions can be differentiated from control solutions by an electrical measurement of the selective swelling of OCPCs. The advantages of such an approach are, that it is:

- simple,
- direct,
- rapid (producing results in under three minutes),
- provides a direct electrical output, and
- demonstrates single-bases specificity.

The remaining challenges for this approach are:

- it has yet to be demonstrated for RNA,
- the full range of swelling is not yet measurable,

- the analyte concentration cannot yet be inferred,
- OCPCs show significant thermal instability, and
- at 10 nM, the lower detection limit is relatively high.

This thesis has also shown that morpholino-functionalised hydrogels have the potential to offer considerable improvements to both the thermal stability and sensitivity of OCPCs in the future. Some potential approaches to address the remaining challenges will be discussed in the following section.

6.3 Future work

The research presented in this thesis represents the first steps in the application of conductive composites to oligonucleotide detection. As such there is considerable scope for further work, both in terms of the optimisation of existing methods and additional research. This section will provide a brief overview of some potential avenues for such work.

6.3.1 Composite synthesis

A major obstacle to the successful exploitation of OCPCs for oligonucleotide detection is the difficulty of adding conductive particles at sufficient loading densities to allow the transduction of the full dynamic range of observed swelling. One potential means of improving the dispersion of nanoparticles within the polymer matrix, and hence achieving higher loading densities and lower percolation thresholds, would be to modify

the surfaces of the particles with functional groups that will improve the compatibility of the particles with the polymer. A variety of such functional groups (including amino, hydroxyl and carbonyl groups) have been reported [173, 242, 243]. This approach is similar to the use of dispersion agents and likewise carries the risk of the chemical modifiers interfering with the polymerisation mechanism or oligonucleotide cross-link hybridisation. The challenge will be to find a functionalisation that produces the required improvements to the loading densities, yet which is compatible with the polymerisation process. There is also scope for optimisation of the conductive particles, in terms of the material, particle size, aspect ratio and size distribution, in order to produce optimal percolation characteristics.

An alternative approach would be to employ an alternative polymerisation mechanism which is more compatible with surface functionalisation, dispersion agents or higher loading densities. A common mechanism is redox-initiated polymerisation (as opposed to our UV-initiated polymerisation) such as with the redox pair ammonium persulphate (APS) and tetramethylethylenediamine (TEMED) [112, 127, 287]. The downside with such approaches is that they are not well-suited to the creation of small volumes of polymer as the polymerisation reaction begins upon the mixing of the solutions, thus making it impractical to produce droplets that are aliquots of a larger volume. Technologies such as ink-jet printing could offer a solution to this problem as they are ideally suited to the mixing of small volumes of solution through the sequential deposition of different solutions at a given location. Ink-jet printing will also offer superior repeatability of droplet volume and positioning compared to manual dispensing and allow for the deposition of droplet volumes smaller than any used in this thesis

(*ca.* 1 μl). A reduced droplet volume is attractive as it will reduce the swelling time [110], leading to faster response times, and it will reduce the volume of OCPC required per device, thereby improving cost-effectiveness. Additionally, reducing the droplet volume may allow for the determination of analyte concentration. As discussed in Section 3.2.3, there is currently no dependence of the rate of swelling upon the analyte concentration as the swelling is limited by the rate of the expansion of the polymer matrix, rather than the rate of cleavage of oligonucleotide cross-linkers. If the volume of the OCPC droplets can be reduced sufficiently, it may be possible to reduce the swelling time enough for the concentration dependent cross-linker cleavage to become a limiting factor.

The electrical characteristics of a polymer on IDEs will be dominated by the region closest to the electrode surface [252]. Therefore, it can be assumed that the volume of the OCPC droplets can be reduced without adversely affecting their performance. Some optimisation of the composites, in terms of particle size and distribution, will be required to ensure that they are compatible with ink-jet printing [194, 195]. The synthesis of OCPCs via redox-initiated polymerisation and the ink-jet printing of OCPCs are currently being investigated by Geraint Langford as part of his PhD studies.

At several points throughout this thesis, occurrences have been described that are thought to be the result of interactions between the oligonucleotide cross-linkers and the conductive carbon particles. Whether beneficial (such as improving the dispersion of the carbon nanoparticles) or detrimental (such as in the case of the ‘ring’ effect seen with carbon micropowder – Section 4.2.3.1) these occurrences have been unexpected. In order to further develop and optimise OCPCs using carbon nanoparticles (or any

other conductive nanoparticles) it will be necessary to reach a greater understanding of the interactions between nanoparticles and the oligonucleotide cross-linkers.

To overcome the difficulties of loading conductive particles into hydrogels at high concentrations, it may be desirable to do away with the particles entirely. An alternative means of producing OCPCs would be to synthesise an intrinsically conductive polymer within the matrix of an oligonucleotide-functionalised hydrogel via electroformation. Conductive polymers such as polypyrrole (PPy) and poly(3,4-ethylenedioxythiophene) (PEDOT) can be deposited upon electrodes via electroformation [148, 149, 157]. Typically this will result in a polymer film, however, if a hydrogel saturated with a monomer solution surrounds the electrode then the electroformation will take place within the free-space of the hydrogel matrix, resulting in a continuous network of conductive material within a hydrogel support matrix. Electrical conduction will take place along the conductive polymer backbones and between adjacent tendrils. Such composites have been used for bio-compatible electrode applications [148, 149, 157] but, to the author's best knowledge, never in conjunction with bio-responsive polymers. This approach would be advantageous as it would produce composites that are conductive in their intrinsic state (*i.e.* the state they will swell to in the absence of the analyte) as it is in this state that the electroformation will be performed. Additional swelling beyond this point, caused by the selective cleaving of oligonucleotide cross-linkers by the analyte molecules, would result in the breaking of conductive pathways and a corresponding reduction in conductivity. Such an approach could produce the differential end-point that has so far proven unachievable with conductive-particle based OCPCs.

The principle unknown for this approach would be whether the electroformation can be performed in a manner that does not adversely affect the oligonucleotide cross-linkers.

Additionally, it would be desirable to undertake investigations into the effects of varying parameters such as the oligonucleotide cross-linker density and the lengths of the overlap¹ and toehold² regions of the oligonucleotide cross-linkers. Stokke *et al.* have undertaken some preliminary work in this regard [125], but it needs to be determined how such factors affect the characteristics of OCPCs, particularly with regard to the limit of detection and specificity.

6.3.2 Electrode design

Whilst the custom electrode devices (Section 2.3.1) offer a considerable improvement on their off-the-shelf equivalent, there is potential for the electrode design to be optimised further. The optimal digit width, separation, number and layout for the measurement of the electrical properties of OCPCs could be determined by a combination of numerical modeling and empirical experiments. The optimal configuration would need to take into account both optimal conductivity measurement and optimal adhesion of the composites to the device surface. Reducing the total area of the the IDE array would also be beneficial in terms of reducing the required composite volume, hence improving the cost-effectiveness of any end-device.

It may also be desirable to use alternative materials for both the electrodes and

¹The complementary region between the sensor and blocker strands.

²The region of the sensor strand between the overlap region and the Acrydite modifier. (Section 1.4.2)

the substrate. This could produce improvements in cost-effectiveness and the ease of manufacture for any end-device.

Additionally, it would be desirable to design and fabricate electrode devices that would enable multiple OCPC-based sensors to be prepared on a single device. OCPC arrays could be used to detect multiple biomarkers for a single disease or biomarkers for a range of conditions in a single test. Pattern recognition techniques could be used to process the inputs from a large number of OCPC-based sensors as a method of overcoming the potential ambiguity discussed in Section 1.2 [288]. Alternatively, multiple sensors could be used to provide additional information about a single target. If the limit of detection of OCPCs is dependent upon the oligonucleotide cross-linker density, multiple sensors of different cross-linker density could be used to determine the analyte concentration.

6.3.3 Delamination

If conductive composites are to be developed further as a transduction mechanism for oligonucleotide cross-linked polymers, then the adhesion of the hydrogels to the electrode surface needs to be improved. There are several potential approaches to rectifying this issue. Adapting the silanisation procedure such that the composites are chemically bound to both the substrates and the electrodes may eliminate the problem. This could be achieved by synthesising a molecule with a thiol (-SH) group at one end and a methacrylate group (or equivalent) at the other (Figure 6.1). If incorporated into the silanisation reagent (in addition to the 3-(trimethoxysilyl) propyl methacrylate (TPM)) at appropriate concentrations, the thiol group would bond to the platinum (Pt) to form a self assembled monolayer (SAM) [289]. This would leave the

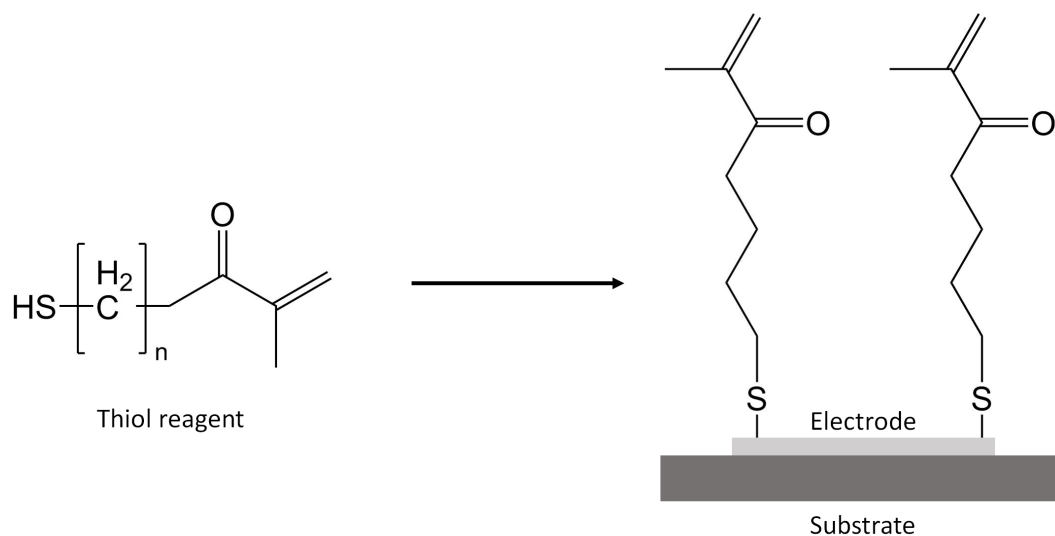


Figure 6.1: Approximate chemical structure of the proposed thiol-based adhesion agent. The thiol group will bond to the platinum of the electrodes and the methacrylate group will form part of the polymer structure of the composite. The exact form of the spacer group, depicted in brackets (left), will be dependent upon the synthesis mechanism, as yet unspecified.

methacrylate groups free to participate in the free-radical polymerisation, in the same manner as those of the TPM. Thus the composite would be chemically bonded to both the electrodes and the substrate. Chemically binding functional groups to noble metals via thiol bonds is a well established procedure. [290–292]

Alternatively, adapting the measurement hardware so as to minimise the voltage applied to the electrodes, and therefore the chances of repulsion between the anionic composite and the electrode (Section 4.1), may also minimise delamination. This would have the twin benefits of potentially reducing the severity of the delamination issue, by reducing the repulsion between the oligonucleotides and the electrodes, and making the approach more readily applicable to PoC applications, where a low power consumption is highly desirable. If, as is suspected, the anionic nature of the OCPCs contributes to delamination, then replacing the DNA with charge neutral alternatives (Chapter 5) may mitigate the problem.

6.3.4 Analyte solutions

As stated in Chapter 1, the eventual aspiration of this work is the detection of miRNA. However, for reasons of practicality and expense, as a first step all of the work described in this thesis is for DNA analytes. RNA is less stable than DNA [169] and this will pose an additional challenge for any oligonucleotide detection technique. The selective response of OCPCs needs to be verified for RNA solutions.

Also, it would be desirable to determine the response of OCPCs in more complex solutions, such as those containing a mixture of analyte and mismatched control oligonucleotides or relevant proteins. The eventual aim would be to demonstrate the response of OCPCs in serum or other relevant bodily fluids.

It would also be desirable to verify the superior nuclease resistance of morpholino-functionalised polymers (Section 5.1.1.1) by comparing the response of such with DNA-functionalised equivalents in analyte and control solutions containing biologically relevant concentrations of suitable enzymes. [293]

Additionally, an integrated microfluidic delivery system could be developed. This would allow for controlled volumes of sample to be delivered to multiple OCPC sensors from a single, small, sample volume in addition to incorporating any necessary sample preparation [294] or amplification [295] processes on a single device.

6.3.5 Thermal stability

While morpholino cross-linked polymers appear to eliminate any thermal instability across relevant temperature ranges (Section 5.3.3), there are other potential methods for improving the thermal stability of OCPCs. The melting temperature (T_m) of the oligonucleotide cross-links could be ‘tuned’ by incorporating locked nucleic acid (LNA) into the sequences. LNAs are synthetic nucleotide analogues first described in 1998 [261, 296, 297]. A LNA nucleotide is identical to a DNA nucleotide except for the addition of an oxygen atom attached to the 2'-carbon of the ribose ring and a methylene bridge connecting this oxygen to the 4'-carbon (Figure 6.2). This bridge effectively makes the backbone more rigid (reducing the number of degrees of freedom) which results in LNA hybridising to DNA and RNA with a much higher affinity and specificity than conventional nucleic acids. The fact that LNA is so structurally similar to DNA and RNA means that it can be synthesised using the same equipment and procedures and LNA sub-units can be interspersed into chains of conventional nucleotides, allowing the fine-tuning of nucleotide properties. [265, 298]

LNA has been used in the field of oligonucleotide detection as a means of improving the sensitivity of detection techniques such as northern blotting [299], microarrays [300] and quantitative PCR (qPCR) [301]. They are also highly useful for normalising the melting temperatures of the various capture probes across a microarray. [298]

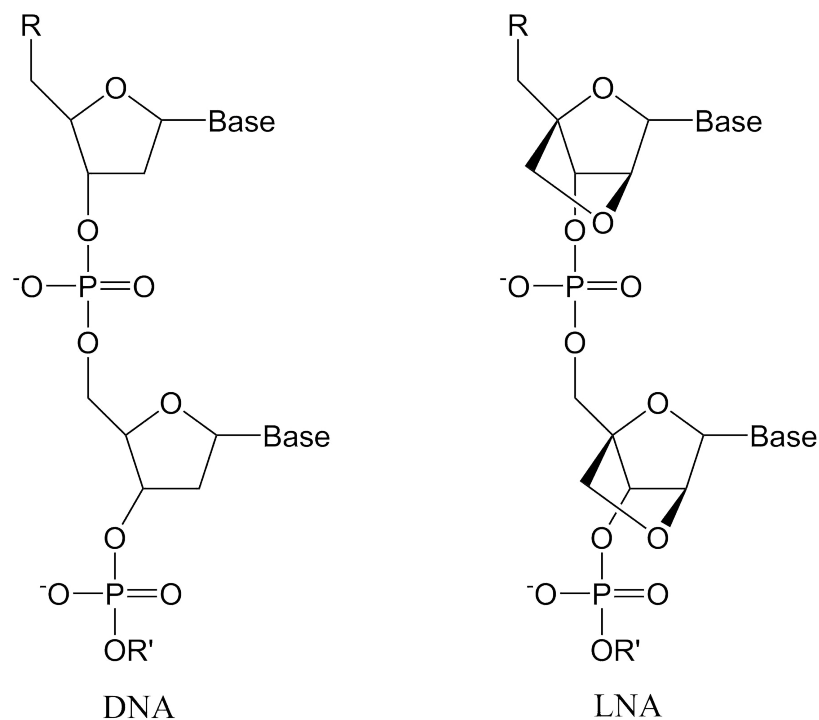


Figure 6.2: Comparison of the structures of DNA (left) and LNA (right). The addition of the oxygen atom and the methylene bridge make the LNA backbone more rigid and increases its hybridisation efficiency. Adapted from Braasch *et al.* [265].

6.3.6 Morpholino-functionalised polymers

As discussed in Section 5.3, morpholino-functionalised hydrogels offer advantages in terms of increased thermal stability and increased sensitivity, when compared to DNA-functionalised hydrogels. Further work needs to be undertaken to determine the limit of detection for morpholino-functionalised hydrogels and to demonstrate their utility for oligonucleotide detection using the electrical measurement of OCPCs, as discussed for their DNA equivalents in Section 4.2.3.

The advantages offered by morpholino-functionalised hydrogels for sensing applications would be transferable to any alternative means of swelling transduction. Additionally, morpholino-functionalised hydrogels have potential for other applications, such as drug

delivery, where oligonucleotide-functionalised hydrogels have been employed [302–304]. Their improved sensitivity, thermal stability and resistance to enzymes may prove advantageous in such applications.

Whilst morpholinos are preferable to peptide nucleic acid (PNA) for OCPC applications (for the reasons discussed in Section 5.1.1.1), PNAs bind more strongly to conventional nucleic acids. It is believed that the superior limit of detection of morpholino-functionalised polymers is a result of improved hybridisation, therefore PNA-functionalised polymers may offer a similar or greater improvement. However, any benefit would need to be weighed against the increased cost.

6.3.7 Alternative applications

OCPCs could be developed as sensors for analytes other than oligonucleotides. Aptamers are synthetic oligonucleotides that can bind to targets such as ions, small molecules and proteins with high affinity through their ability to self-fold into highly specific geometries [305–307]. It has been demonstrated that aptamers and selectively cleavable aptamer cross-links can be incorporated into hydrogels in a similar manner to the oligonucleotide cross-linkers described in this thesis [114, 115, 131, 287, 305, 308] thereby raising the prospect that OCPCs could be adapted and applied to a far broader range of target molecules. The idea of aptamer OCPCs was generated in collaboration with David Pritchard of Axis-Shield Diagnostics, and is currently being pursued by Geraint Langford as part of his PhD studies.

6.4 Concluding remarks

This thesis represents the first attempt to apply simple electrical transduction techniques to oligonucleotide-functionalised polymers for the purposes of oligonucleotide detection. Clear evidence of the simple detection of analyte oligonucleotides using such techniques has been presented, with high specificity and rapid response times. However, limitations to the concentrations at which this can be achieved, to the extent to which conductive particles can be added to the polymers, and to the thermal stability of these polymers mean that, in their current form, these OCPCs are not yet suitable for miRNA detection applications. New avenues of research, such as morpholino-functionalised polymers, the first example of which was developed as part of this work, have the potential to offer significant improvements in the future.

Acronyms and abbreviations

T_m	melting temperature
Ω	ohm
μ	micro-
A	ampere
A	adenine
a	atto-
a.c.	alternating current
AAM	acrylamide
Ag/AgCl	silver/silver chloride
AGM	arithmetic-geometric mean
ALL	acute lymphoblastic leukaemia
AML	acute myeloid leukaemia
APS	ammonium persulphate
BAW	bulk acoustic wave
BL	bioluminescent
C	Celsius
C	cytosine
c	centi-
cdNA	complementary DNA
CE	counter electrode
CL	chemiluminescent

CLL	chronic lymphoblastic leukaemia
CML	chronic myeloid leukaemia
CO₂	carbon dioxide
cryoSEM	cryo-scanning electron microscope
CVD	chemical vapour deposition
d.c.	direct current
DI	deionised
DMSO	dimethylsulfoxide
DNA	deoxyribonucleic acid
ECL	electrochemiluminescent
EIS	electrochemical impedance spectroscopy
F	farad
f	femto-
FET	field-effect transistor
FRET	fluorescence resonant energy transfer
G	guanine
g	grams
GEM	general effective medium
HCK	1-hydroxycyclohexylphenylketone
HCl	hydrochloric acid
HMDS	hexamethyldisilazane
Hz	hertz
IDE	interdigitated electrode
IPA	iso-propyl alcohol
k	kilo-
l	litre
LLC	limited liability company

LNA	locked nucleic acid
LoD	limit of detection
M	mega-
M	molar
m	metre
m	milli-
MALDI-ToF	matrix-assisted laser desorption/ionisation time-of-flight
MB	molecular beacon
MBA	N, N' methylene-bisacrylamide
MEMS	microelectromechanical systems
miRNA	microRNA
mol	moles
mRNA	messenger RNA
n	nano-
Na	sodium
NaCl	sodium chloride
NEMS	nanoelectromechanical systems
NMR	nuclear magnetic resonance
NSA	N-succinimidyl acrylate
NSCLC	non-small cell lung cancer
O₂	oxygen
OCPC	oligonucleotide cross-linked polymer composite
p	pico-
PANI	polyaniline
PCR	polymerase chain reaction
PEDOT	poly(3,4-ethylenedioxythiophene)
PNA	peptide nucleic acid
PoC	point-of-care

PPy	polypyrrole
pre-miRNA	precursor miRNA
pri-miRNA	primary precursor miRNA
Pt	platinum
qPCR	quantitative PCR
RE	reference electrode
redox	reduction-oxidation
RISC	RNA-induced silencing complex
RNA	ribonucleic acid
rpm	revolutions per minute
RT-qPCR	reverse transcriptase qPCR
S	sieverts
s	seconds
SAM	self assembled monolayer
SAW	surface acoustic wave
SCCM	standard cubic centimetres per minute
Si	silicon
SiO₂	silicon dioxide
T	thymine
TEMED	tetramethylethylenediamine
Ti	titanium
Torr	torr
TPM	3-(trimethoxysilyl) propyl methacrylate
TTR	time-to-results
U	uracil
UK	United Kingdom
USB	universal serial bus
UV	ultraviolet

V	volts
W	watt
WE	working electrode
wrt	with respect to

List of figures

1.1	Illustration of the structure of miRNA	3
1.2	Illustration of miRNA genesis and maturation	4
1.3	Number of publications by year associated with miRNA and disease	6
1.4	Illustration of the steps involved in northern blotting	18
1.5	The principle behind microarray-based miRNA profiling	19
1.6	Illustration of the form and mechanism of molecular beacons	22
1.7	Chemical structure of Acrydite	30
1.8	An example of oligonucleotide cross-linkers and their respective complementarity	30
1.9	Illustration of the swelling response of an oligonucleotide-functionalised hydrogel upon introduction of the target strand	31
1.10	Example of a percolation curve for graphite micro-particles in a boron nitride matrix	36
1.11	Illustration showing the transduction of polymer swelling via changes in the electrical conductivity of conductive polymer composites	38

2.1	The reaction scheme for polyacrylamide synthesis	42
2.2	Diagram of the set-up used to perform high-powered sonication of the pre-composite solutions	46
2.3	Illustration of the polymer droplet imaging set-up	49
2.4	Diagrammatic representation of the electrode devices	53
2.5	The electrode fabrication process	54
2.6	Illustration of the electrical measurement set-up	58
2.7	The model circuit for the sensor	61
2.8	Diagram of a standard three electrode cell arrangement	62
3.1	Images of composite droplets prepared using the standard method with increasing carbon loading	65
3.2	Images of composite droplets prepared using high-powered sonication with increasing carbon loading	66
3.3	Images of composite droplets prepared using 50% DMSO with increasing carbon loading	67
3.4	Images of composite droplets prepared using the standard method with the addition of oligonucleotide cross-linkers with increasing carbon loading	68
3.5	Microscope images of 10 mg/ml carbon nanopowder composite droplets prepared using various methods of particle dispersion	69
3.6	Diagrammatic representation of the net inward force on carbon agglomerates during polymerisation	70

3.7	Microscope image of a 20 mg/ml composite droplet prepared using the standard method with the addition of oligonucleotide cross-links	71
3.8	CryoSEM image of polyacrylamide/carbon nanopowder composite	72
3.9	NMR spectrum of the swelling medium for polyacrylamide hydrogels	74
3.10	Fractional volume increase as a function of cross-link density for polyacrylamide hydrogels	76
3.11	Fractional volume increase for OCPCs in various oligonucleotide solutions	78
3.12	Fractional volume increase against time for swelling polyacrylamide hydrogels of different cross-linking densities	80
3.13	Volume against time as a percentage of the maximum volume for swelling polyacrylamide hydrogels of different primary cross-link densities	81
3.14	Fractional volume increase against time for oligonucleotide-functionalised hydrogels in analyte and random solutions	82
3.15	Fractional volume increase against time for oligonucleotide-functionalised hydrogels in analyte and random solutions	83
3.16	Example of the systematic nature of the uncertainty	85
3.17	Fractional volume increase against temperature for OCPCs	87
3.18	Fractional volume change against temperature for non-oligonucleotide-functionalised polyacrylamide hydrogels	90
4.1	An example of anomalous electrical measurements seen with the off-the-shelf electrode devices	95
4.2	Illustration of the mechanism behind the observed delamination effects	96

4.3	The silanisation mechanism	97
4.4	Photograph of a single-layer IDE device	98
4.5	Conductivity of polyacrylamide/carbon nanopowder composites as a function of carbon loading	102
4.6	Illustration of the three-phase nature of the carbon/polyacrylamide composites	104
4.7	Fits to the GEM equation for various carbon particle types	105
4.8	Microscope image of a 10 mg/ml composite droplet prepared using carbon nanotubes as the conductive component	106
4.9	The d.c. resistance of polyacrylamide/carbon nanopowder composites with time as they swell in DI water	108
4.10	The d.c. resistance of polyacrylamide/carbon nanopowder composites with time as they swell	110
4.11	The d.c. resistance of composites with different forms of carbon particle additives with time as they swell	112
4.12	The magnitude of the complex impedance and phase against time for swelling polyacrylamide/carbon nanopowder composites	114
4.13	The d.c. resistance of a swelling polyacrylamide/carbon nanopowder composite plotted alongside the magnitude of the complex impedance against time	116
4.14	The magnitude of the complex impedance against frequency for a polyacrylamide/carbon nanopowder composite at 20 mg/ml, plotted alongside the corresponding model fit	118

4.15	The average fitted model parameter for the capacitance	119
4.16	The average fitted model parameter for the resistance	121
4.17	Image of a carbon microparticle OCPC	123
4.18	Diagrammatic representation of the potential carbon microparticle distribution in the xz-plane	124
4.19	Microscope image of a 20 mg/ml graphite OCPC droplet	126
4.20	The d.c. resistance of graphite OCPCs swelling over time	127
4.21	The d.c. resistance of carbon nanopowder OCPCs swelling over time	128
4.22	The resistance of OCPCs against time as they swell in an analyte solution, shown alongside the equivalent optical volume measurement	130
4.23	Illustration of the differences in ion mobility in OCPCs in analyte and random solutions	131
4.24	The d.c. resistance of carbon nanopowder OCPCs swelling over time in analyte solutions of varying concentration	132
4.25	The d.c. resistance of carbon nanopowder OCPCs swelling with time in random solutions of varying concentration	134
4.26	Fractional volume increase of OCPCs swelling over time in R solutions of varying concentration	135
4.27	The final value of the resistance for OCPCs in random solutions of varying concentration	136
4.28	Cyclic voltammograms for blank, 0 mg/ml and 20 mg/ml polyacrylamide/carbon nanopowder composite coated electrodes for the narrow potential window	139

4.29	Cyclic voltammograms for blank, 0 mg/ml and 20 mg/ml polyacrylamide/carbon nanopowder composite coated electrodes for the wide potential window	140
5.1	The chemical structure of DNA and morpholinos	147
5.2	Fractional volume increase of morpholino-functionalised hydrogels compared to DNA-functionalised hydrogels	152
5.3	Illustration of the difference in cross-linker length between 5' functionalised DNA and 3' functionalised morpholinos	153
5.4	The fractional volume increase of morpholino-functionalised hydrogels with time as they swell in solution	154
5.5	Fractional volume increase of functionalised hydrogels saturated in analyte solution against salt concentration	156
5.6	Fractional volume increase of functionalised hydrogels saturated in random solution against temperature	158
6.1	Approximate chemical structure of the proposed thiol-based adhesion agent	171
6.2	Comparison of the structures of DNA and LNA	174
D.1	Illustration of the electrode array showing the dimension parameters	231
E.1	Functionalisation reaction of morpholino oligonucleotide with N-succinimidyl acrylate (NSA)	233

List of tables

1.1	The 5' branch of the let-7 family	13
1.2	Strengths and weaknesses of established miRNA detection techniques	17
1.3	Summary of limits of detection of emerging oligonucleotide detection techniques	23
2.1	Sequences of the sensor, blocker, analyte and random oligonucleotides	44
4.1	The number of analyte molecules as a proportion of oligonucleotide cross-linkers for varying analyte concentration	137
C.1	Run sheet for electrode fabrication	229

References

- [1] N. Rosenfeld, R. Aharonov, E. Meiri, S. Rosenwald, Y. Spector, *et al.*, “MicroRNAs accurately identify cancer tissue origin,” *Nature Biotechnology*, vol. 26, no. 4, pp. 462–469, 2008.
- [2] N. Kosaka, H. Iguchi, and T. Ochiya, “Circulating microRNA in body fluid: a new potential biomarker for cancer diagnosis and prognosis,” *Cancer Science*, vol. 101, no. 10, pp. 2087–2092, 2010.
- [3] G. Han, S. Zhang, Z. Xing, and X. Zhang, “Absolute and relative quantification of multiplex DNA assays based on an elemental labeling strategy,” *Angewandte Chemie (Int. Ed.)*, vol. 52, no. 5, pp. 1466–1471, 2013.
- [4] L. Wang, Y. Han, S. Zhou, G. Wang, and X. Guan, “Nanopore biosensor for label-free and real-time detection of anthrax lethal factor,” *ACS Applied Materials & Interfaces*, 2014. DOI 10.1021/am500749p.
- [5] A. Etheridge, I. Lee, L. Hood, D. Galas, and K. Wang, “Extracellular microRNA: a new source of biomarkers,” *Mutation Research*, vol. 717, no. 1–2, pp. 85–90, 2011.
- [6] A. Esquela-Kerscher and F. J. Slack, “Oncomirs - microRNAs with a role in cancer,” *Nature Reviews Cancer*, vol. 6, no. 4, pp. 259–269, 2006.
- [7] Y. Ren, H. Deng, W. Shen, and Z. Gao, “A highly sensitive and selective electrochemical biosensor for direct detection of microRNAs in serum,” *Analytical Chemistry*, vol. 85, no. 9, pp. 4784–4789, 2013.
- [8] E. A. Hunt, A. M. Goulding, and S. K. Deo, “Direct detection and quantification of microRNAs,” *Analytical Biochemistry*, vol. 387, no. 1, pp. 1–12, 2009.
- [9] C. Arenz, “MicroRNAs—future drug targets?,” *Angewandte Chemie (Int. Ed.)*, vol. 45, no. 31, pp. 5048–5050, 2006.
- [10] M. Ha and V. N. Kim, “Regulation of microRNA biogenesis,” *Nature Reviews Molecular Cell Biology*, vol. 15, pp. 509–524, 2014.
- [11] D. P. Bartel, “MicroRNAs: genomics, biogenesis, mechanism, and function,” *Cell*, vol. 116, no. 2, pp. 281–297, 2004.

- [12] R. Maqbool and M. U. Hussain, "MicroRNAs and human diseases: diagnostic and therapeutic potential," *Cell and Tissue Research*, vol. 358, no. 1, pp. 1–15, 2014.
- [13] R. C. Friedman, K. K. Farh, C. B. Burge, and D. P. Bartel, "Most mammalian mRNAs are conserved targets of microRNAs," *Genome Research*, vol. 19, no. 1, pp. 92–105, 2009.
- [14] M. Boehm and F. J. Slack, "MicroRNA control of lifespan and metabolism," *Cell Cycle*, vol. 5, no. 8, pp. 837–840, 2006.
- [15] M. Carleton, M. A. Cleary, and P. S. Linsley, "MicroRNAs and cell cycle regulation," *Cell Cycle*, vol. 6, no. 17, pp. 2127–2132, 2007.
- [16] B. Bielekova and R. Martin, "Development of biomarkers in multiple sclerosis," *Brain : a journal of neurology*, vol. 127, no. 7, pp. 1463–1478, 2004.
- [17] Q. Jiang, Y. Wang, Y. Hao, L. Juan, *et al.*, "miR2Disease: a manually curated database for microRNA deregulation in human disease," *Nucleic Acids Research*, vol. 37, pp. 98–104, 2009.
- [18] Thomson Reuters, "Web of science." <http://www.webofknowledge.com>. Accessed October 21, 2016.
- [19] R. Garzon, G. A. Calin, and C. M. Croce, "MicroRNAs in cancer," *Annual Review of Medicine*, vol. 60, pp. 167–179, 2009.
- [20] N. Schöler, C. Langer, H. Döhner, C. Buske, and F. Kuchenbauer, "Serum microRNAs as a novel class of biomarkers: a comprehensive review of the literature," *Trends in Genetics*, vol. 22, no. 3, pp. 165–173, 2010.
- [21] K. A. Cissell and S. K. Deo, "Trends in microRNA detection," *Analytical and Bioanalytical Chemistry*, vol. 394, no. 4, pp. 1109–1116, 2009.
- [22] W. C. Cho, "MicroRNAs: potential biomarkers for cancer diagnosis, prognosis and targets for therapy," *The International Journal of Biochemistry & Cell Biology*, vol. 42, no. 8, pp. 1273–1281, 2010.
- [23] A. Keller, P. Leidinger, J. Lange, A. Borries, *et al.*, "Multiple sclerosis: microRNA expression profiles accurately differentiate patients with relapsing-remitting disease from healthy controls," *PLoS ONE*, vol. 4, no. 10, p. e7440, 2009.
- [24] M. J. Lodes, M. Caraballo, D. Suci, S. Munro, A. Kumar, and B. Anderson, "Detection of cancer with serum miRNAs on an oligonucleotide microarray," *PLoS ONE*, vol. 4, no. 7, p. e6229, 2009.
- [25] Y. Li, L. Liang, and C. Y. Zhang, "Isothermally sensitive detection of serum circulating miRNAs for lung cancer diagnosis," *Analytical Chemistry*, vol. 85, no. 23, pp. 11174–11179, 2013.
- [26] X. Chen, Z. Hu, W. Wang, Y. Ba, *et al.*, "Identification of ten serum microRNAs from a genome-wide serum microRNA expression profile as novel noninvasive biomarkers for nonsmall cell lung cancer diagnosis," *International Journal of Cancer*, vol. 130, no. 7, pp. 1620–1628, 2012.

- [27] J. Lu, G. Getz, E. A. Miska, E. Alvarez-Saavedra, *et al.*, “MicroRNA expression profiles classify human cancers,” *Nature*, vol. 435, no. 7043, pp. 834–838, 2005.
- [28] G. Reid, M. B. Kirschner, and N. van Zandwijk, “Circulating microRNAs: Association with disease and potential use as biomarkers,” *Critical Reviews in Oncology/Hematology*, vol. 80, no. 2, pp. 193–208, 2011.
- [29] P. Kumar, Z. Dezso, C. MacKenzie, J. Oestreicher, *et al.*, “Circulating miRNA biomarkers for Alzheimer’s disease,” *PLoS ONE*, vol. 8, no. 7, p. e69807, 2013.
- [30] B. Siddeek, L. Inoubli, N. Lakhdari, P. B. Rachel, *et al.*, “MicroRNAs as potential biomarkers in diseases and toxicology,” *Mutation Research*, vol. 764–765, pp. 46–57, 2014.
- [31] H. Schwarzenbach, N. Nishida, G. A. Calin, and K. Pantel, “Clinical relevance of circulating cell-free microRNAs in cancer,” *Nature Reviews Clinical Oncology*, vol. 11, no. 3, pp. 145–156, 2014.
- [32] M. Ghildiyal and P. D. Zamore, “Small silencing RNAs: an expanding universe,” *Nature Reviews Genetics*, vol. 10, no. 2, pp. 94–108, 2009.
- [33] J. A. Weber, D. H. Baxter, S. Zhang, D. Y. Huang, *et al.*, “The microRNA spectrum in 12 body fluids,” *Clinical Chemistry*, vol. 56, no. 11, pp. 1733–1741, 2010.
- [34] U. Ghosh, S. Bose, T. Ghosh, T. Bandyopadhyay, and U. Basu, “A monophasic solution for isolation of RNA devoid of polymerase chain reaction-detectable genomic DNA contamination,” *Analytical Biochemistry*, vol. 477, pp. 50–52, 2015.
- [35] C. C. Pritchard, H. H. Cheng, and M. Tewari, “MicroRNA profiling: approaches and considerations,” *Nature Reviews Genetics*, vol. 13, no. 5, pp. 358–369, 2012.
- [36] K. Zen and C. Y. Zhang, “Circulating microRNAs: a novel class of biomarkers to diagnose and monitor human cancers,” *Medicinal Research Reviews*, vol. 32, no. 2, pp. 326–348, 2012.
- [37] S. Campuzano, M. Pedrero, and J. M. Pingarrón, “Electrochemical genosensors for the detection of cancer-related miRNAs,” *Analytical and Bioanalytical Chemistry*, vol. 406, no. 1, pp. 27–33, 2013.
- [38] E. K. Hanson, H. Lubenow, and J. Ballantyne, “Identification of forensically relevant body fluids using a panel of differentially expressed microRNAs,” *Analytical Biochemistry*, vol. 387, no. 2, pp. 303–314, 2009.
- [39] D. Zubakov, A. Boersma, Y. Choi, P. Kuijk, E. Wiemer, and M. Kayser, “MicroRNA markers for forensic body fluid identification obtained from microarray screening and quantitative RT-PCR confirmation,” *International Journal of Legal Medicine*, vol. 124, no. 3, pp. 217–226, 2010.
- [40] C. Courts and B. Madea, “Specific micro-RNA signatures for the detection of saliva and blood in forensic body-fluid identification,” *Journal of Forensic Sciences*, vol. 56, no. 6, pp. 1464–1470, 2011.

- [41] J. Park, S. Park, O. Kwon, H. Lee, *et al.*, “Microarray screening and qRTPCR evaluation of microRNA markers for forensic body fluid identification,” *Electrophoresis*, vol. 35, pp. 3062–3068, 2014.
- [42] Cancer Research UK, “Leukaemia statistics.” <http://www.cancerresearchuk.org/health-professional/cancer-statistics/statistics-by-cancer-type/leukaemia>. Accessed April 25, 2017.
- [43] H. Zhao, D. Wang, W. Du, D. Gu, and R. Yang, “MicroRNA and leukemia: tiny molecule, great function,” *Critical Reviews in Oncology/Hematology*, vol. 74, no. 3, pp. 149–155, 2010.
- [44] Cancer Research UK, “Leukaemia.” <http://www.cancerresearchuk.org/about-cancer/type/leukaemia/>. Accessed October 19, 2016.
- [45] S. Mi, J. Lu, M. Sun, Z. Li, *et al.*, “MicroRNA expression signatures accurately discriminate acute lymphoblastic leukemia from acute myeloid leukemia,” *Proceedings of the National Academy of Sciences of the United States of America*, vol. 104, no. 50, pp. 19971–19976, 2007.
- [46] M. Tanaka, K. Oikawa, M. Takanashi, M. Kudo, *et al.*, “Down-regulation of miR-92 in human plasma is a novel marker for acute leukemia patients,” *PLoS ONE*, vol. 4, no. 5, p. e5532, 2009.
- [47] V. Benes and M. Castoldi, “Expression profiling of microRNA using real-time quantitative PCR, how to use it and what is available,” *Methods*, vol. 50, no. 4, pp. 244–249, 2010.
- [48] M. de Planell-Saguer and M. C. Rodicio, “Analytical aspects of microRNA in diagnostics: a review,” *Analytica Chimica Acta*, vol. 699, no. 2, pp. 134–152, 2011.
- [49] J. D. Driskell, A. D. Seto, L. P. Jones, S. Jokela, *et al.*, “Rapid microRNA (miRNA) detection and classification via surface-enhanced raman spectroscopy (SERS),” *Biosensors & Bioelectronics*, vol. 24, no. 4, pp. 923–928, 2008.
- [50] B. N. Johnson and R. Mutharasan, “Biosensor-based microRNA detection: techniques, design, performance, and challenges,” *The Analyst*, vol. 139, pp. 1576–1588, 2014.
- [51] A. W. Wark, H. J. Lee, and R. M. Corn, “Multiplexed detection methods for profiling microRNA expression in biological samples,” *Angewandte Chemie (Int. Ed.)*, vol. 47, no. 4, pp. 644–652, 2008.
- [52] E. Moussay, K. Wang, J. H. Cho, K. van Moer, *et al.*, “MicroRNA as biomarkers and regulators in b-cell chronic lymphocytic leukemia,” *Proceedings of the National Academy of Sciences of the United States of America*, vol. 108, no. 16, pp. 6573–6578, 2011.
- [53] M. Jung, H. J. Mollenkopf, C. Grimm, I. Wagner, *et al.*, “MicroRNA profiling of clear cell renal cell cancer identifies a robust signature to define renal malignancy,” *Journal of Cellular and Molecular Medicine*, vol. 13, no. 9B, pp. 3918–3928, 2009.

- [54] K. Wang, S. Zhang, B. Marzolf, P. Troisch, *et al.*, “Circulating microRNAs, potential biomarkers for drug-induced liver injury,” *Proceedings of the National Academy of Sciences of the United States of America*, vol. 106, no. 11, pp. 4402–4407, 2009.
- [55] S. Yendamuri and R. Kratzke, “MicroRNA biomarkers in lung cancer: MiRacle or quagMiRe?,” *Translational Research : The Journal of Laboratory and Clinical Medicine*, vol. 157, no. 4, pp. 209–215, 2011.
- [56] D. W. Wegman and S. N. Krylov, “Direct quantitative analysis of multiple miRNAs (DQAMmiR),” *Angewandte Chemie (Int. Ed.)*, vol. 50, no. 44, pp. 10335–10339, 2011.
- [57] B. J. Dodgson, A. Mazouchi, D. W. Wegman, C. C. Gradinaru, and S. N. Krylov, “Detection of a thousand copies of miRNA without enrichment or modification,” *Analytical Chemistry*, vol. 84, no. 13, pp. 5470–5474, 2012.
- [58] W. Li and K. Ruan, “MicroRNA detection by microarray,” *Analytical and Bioanalytical Chemistry*, vol. 394, no. 4, pp. 1117–1124, 2009.
- [59] S. D. Conzone and C. G. Pantano, “Glass slides to DNA microarrays,” *Materials Today*, vol. 7, no. 3, pp. 20–26, 2004.
- [60] G. J. Zhang, J. H. Chua, R. E. Chee, A. Agarwal, and S. M. Wong, “Label-free direct detection of miRNAs with silicon nanowire biosensors,” *Biosensors & Bioelectronics*, vol. 24, no. 8, pp. 2504–2508, 2009.
- [61] C. Y. Hong, X. Chen, T. Liu, J. Li, *et al.*, “Ultrasensitive electrochemical detection of cancer-associated circulating microRNA in serum samples based on DNA concatamers,” *Biosensors & Bioelectronics*, vol. 50, pp. 132–136, 2013.
- [62] H. Šířpová, S. Zhang, A. M. Dudley, D. Galas, *et al.*, “Surface plasmon resonance biosensor for rapid label-free detection of microribonucleic acid at subfemtomole level,” *Analytical Chemistry*, vol. 82, no. 24, pp. 10110–10115, 2010.
- [63] J. Wang, X. Yi, H. Tang, H. Han, *et al.*, “Direct quantification of microRNA at low picomolar level in sera of glioma patients using a competitive hybridization followed by amplified voltammetric detection,” *Analytical Chemistry*, vol. 84, no. 15, pp. 6400–6406, 2012.
- [64] E. Hamidi-Asl, I. Palchetti, E. Hasheminejad, and M. Mascini, “A review on the electrochemical biosensors for determination of microRNAs,” *Talanta*, vol. 115, pp. 74–83, 2013.
- [65] H. A. Erlich, “Polymerase chain reaction,” *Journal of Clinical Immunology*, vol. 9, no. 6, pp. 437–447, 1989.
- [66] H. D. VanGuilder, K. E. Vrana, and W. M. Freeman, “Twenty-five years of quantitative PCR for gene expression analysis,” *BioTechniques*, vol. 44, no. 5, pp. 619–626, 2008.

- [67] T. D. Schmittgen, E. J. Lee, J. Jiang, A. Sarkar, *et al.*, “Real-time PCR quantification of precursor and mature microRNA,” *Methods*, vol. 44, no. 1, pp. 31–38, 2008.
- [68] R. E. Farrell, “RT-PCR: A science and an art form,” in *RNA Methodologies*, ch. 18, pp. 358–448, Academic Press, 4 ed., 2010.
- [69] ThermoFisher Scientific, “Northern blotting.” <https://www.thermofisher.com/uk/en/home/life-science/dna-rna-purification-analysis/nucleic-acid-gel-electrophoresis/northern-blotting.html>. Accessed October 24, 2016.
- [70] ThermoFisher Scientific, “Alexa fluor 488 reactive dye decapack, for microarrays.” <https://www.thermofisher.com/order/catalog/product/A32750?ICID=search-product>. Accessed October 24, 2016.
- [71] ThermoFisher Scientific, “Real-Time PCR & endpoint RT-PCR kits.” <http://www.thermofisher.com/order/catalog/en/US/adirect/lt?cmd=IVGNcatDisplayCategory&catKey=17601>. Accessed October 24, 2016.
- [72] Ahram Biosystems, “Palm PCR.” http://www.ahrambio.com/products_palmPCR-technology_more.html. Accessed October 24, 2016.
- [73] Serigene LLC, “Fully integrated point of care PCR system of accelerated testing.” <http://serigene.com/>. Accessed October 24, 2016.
- [74] M Young (Integrated DNA Technologies), “Developing a qPCR point-of-care diagnostic for ebola.” <http://www.idtdna.com/pages/decoded/decoded-articles/pcr-qpcr/decoded/2016/08/24/developing-a-qpcr-point-of-care-diagnostic-for-ebola>. Accessed October 24, 2016.
- [75] A. Sassolas, B. D. Leca-Bouvier, and L. J. Blum, “DNA biosensors and microarrays,” *Chemical Reviews*, vol. 108, pp. 109–139, 2008.
- [76] K. A. Fährnich, M. Pravda, and G. G. Guilbault, “Recent applications of electrogenerated chemiluminescence in chemical analysis,” *Talanta*, vol. 54, no. 4, pp. 531–559, 2001.
- [77] Y. Cheng, J. Lei, Y. Chen, and H. Ju, “Highly selective detection of microRNA based on distance-dependent electrochemiluminescence resonance energy transfer between CdTe nanocrystals and Au nanoclusters,” *Biosensors & Bioelectronics*, vol. 51, pp. 431–436, 2014.
- [78] T. G. Drummond, M. G. Hill, and J. K. Barton, “Electrochemical DNA sensors,” *Nature Biotechnology*, vol. 21, no. 10, pp. 1192–1199, 2003.
- [79] D. C. Ferrier, M. P. Shaver, and P. J. W. Hands, “Micro- and nano-structure based oligonucleotide sensors,” *Biosensors & Bioelectronics*, vol. 68, pp. 798–810, 2015.
- [80] P. Jolly, M. R. Batistuti, A. Miodek, P. Zhuravski, M. Mulato, L. M. A., and P. Estrela, “Highly selective dual mode electrochemical platform for microRNA detection,” *Scientific Reports*, vol. 6, p. 36719, 2016.

- [81] K. Kerman, M. Kobayashi, and E. Tamiya, "Recent trends in electrochemical DNA biosensor technology," *Measurement Science and Technology*, vol. 15, pp. R1–R11, 2004.
- [82] M. Gebala, G. Hartwich, and W. Schuhmann, "Amplified detection of DNA hybridization using post-labelling with a biotin-modified intercalator," *Faraday Discussions*, vol. 149, pp. 11–22, 2011.
- [83] S. J. Park, T. Taton, and C. A. Mirkin, "Array-based electrical detection of DNA with nanoparticle probes," *Science*, vol. 295, no. 5559, pp. 1503–1506, 2002.
- [84] M. Wang, C. Sun, L. Wang, X. Ji, *et al.*, "Electrochemical detection of DNA immobilized on gold colloid particles modified self-assembled monolayer electrode with silver nanoparticle label," *Journal of Pharmaceutical and Biomedical Analysis*, vol. 33, no. 5, pp. 1117–1125, 2003.
- [85] A. Kawde and J. Wang, "Amplified electrical transduction of DNA hybridization based on polymeric beads loaded with multiple gold nanoparticle tags," *Electroanalysis*, vol. 16, no. 1-2, pp. 101–107, 2004.
- [86] L. Li, H. Cai, T. Lee, J. Barford, and I. Hsing, "Electrochemical detection of PCR amplicons using electroconductive polymer modified electrode and multiple nanoparticle labels," *Electroanalysis*, vol. 16, no. 1-2, pp. 81–87, 2004.
- [87] Y. Cheng, C. Pun, C. Tsai, and P. Chen, "An array-based CMOS biochip for electrical detection of DNA with multilayer self-assembly gold nanoparticles," *Sensors and Actuators B: Chemical*, vol. 109, no. 2, pp. 249–255, 2005.
- [88] S. Moses, S. Brewer, S. Kraemer, R. Fuierer, *et al.*, "Detection of DNA hybridization on indium tin oxide surfaces," *Sensors and Actuators B: Chemical*, vol. 125, no. 2, pp. 574–580, 2007.
- [89] Y. Xu, Y. Jiang, H. Cai, P. He, and Y. Fang, "Electrochemical impedance detection of DNA hybridization based on the formation of M-DNA on polypyrrole/-carbon nanotube modified electrode," *Analytica Chimica Acta*, vol. 516, no. 1-2, pp. 19–27, 2004.
- [90] Y. Fu, R. Yuan, L. Xu, Y. Chai, *et al.*, "Electrochemical impedance behavior of DNA biosensor based on colloidal Ag and bilayer two-dimensional solgel as matrices," *Journal of Biochemical and Biophysical Methods*, vol. 62, no. 2, pp. 163–174, 2005.
- [91] C. Tlili, H. Korri-Youssoufi, L. Ponsonnet, C. Martelet, and N. Jaffrezic-Renault, "Electrochemical impedance probing of DNA hybridisation on oligonucleotide-functionalised polypyrrole," *Talanta*, vol. 68, no. 1, pp. 131–137, 2005.
- [92] Y. Fu, R. Yuan, Y. Chai, L. Zhou, and Y. Zhang, "Coupling of a reagentless electrochemical DNA biosensor with conducting polymer film and nanocomposite as matrices for the detection of the HIV DNA sequences," *Analytical Letters*, vol. 39, no. 3, pp. 467–482, 2006.

- [93] B. Lillis, M. Manning, E. Hurley, H. Berney, *et al.*, “Investigation into the effect that probe immobilisation method type has on the analytical signal of an EIS DNA biosensor,” *Biosensors & Bioelectronics*, vol. 22, no. 7, pp. 1289–1295, 2007.
- [94] H. Peng, C. Soeller, N. Vigar, V. Caprio, and J. Travas-Sejdic, “Label-free detection of DNA hybridization based on a novel functionalized conducting polymer,” *Biosensors & Bioelectronics*, vol. 22, no. 9-10, pp. 1868–1873, 2007.
- [95] H. Peng, C. Soeller, and J. Travas-Sejdic, “Novel conducting polymers for DNA sensing,” *Macromolecules*, vol. 40, no. 4, pp. 909–914, 2007.
- [96] Z. Mo, H. Wang, Y. Liang, F. Liu, and Y. Xue, “Highly reproducible hybridization assay of zeptomole DNA based on adsorption of nanoparticle-bioconjugate,” *The Analyst*, vol. 130, no. 12, pp. 1589–1594, 2005.
- [97] Q. Xu, K. Chang, W. Lu, W. Chen, *et al.*, “Detection of single-nucleotide polymorphisms with novel leaky surface acoustic wave biosensors, DNA ligation and enzymatic signal amplification,” *Biosensors & Bioelectronics*, vol. 33, no. 1, pp. 274–278, 2012.
- [98] B. N. Johnson and R. Mutharasan, “Sample preparation-free, real-time detection of microRNA in human serum using piezoelectric cantilever biosensors at attomole level,” *Analytical chemistry*, vol. 84, no. 23, pp. 10426–10436, 2012.
- [99] P. Estrela, A. G. Stewart, F. Yan, and P. Migliorato, “Field effect detection of biomolecular interactions,” *Electrochimica Acta*, vol. 50, pp. 4995–5000, 2005.
- [100] A. Gao, N. Lu, Y. Wang, P. Dai, T. Li, X. Gao, Y. Wang, and C. Fan, “Enhanced sensing of nucleic acids with silicon nanowire field effect transistor biosensors,” *Nano letters*, vol. 12, no. 10, pp. 5262–5268, 2012.
- [101] ThermoFisher Scientific, “Ion Torrent next-generation sequencing.” <https://www.thermofisher.com/uk/en/home/brands/ion-torrent.html>. Accessed August 17, 2016.
- [102] L. H. Sperling, *Introduction to Physical Polymer Science (4th ed.)*. Wiley-Interscience, 2006.
- [103] H. Elias, *An Introduction to Polymer Science*. VCH, 1997.
- [104] R. Ulijn, N. Bibi, V. Jayawarna, P. Thornton, *et al.*, “Bioresponsive hydrogels,” *Materials Today*, vol. 10, no. 4, pp. 40–48, 2007.
- [105] G. R. Hendrickson and L. A. Lyon, “Bioresponsive hydrogels for sensing applications,” *Soft Matter*, vol. 5, pp. 29–35, 2009.
- [106] F. Ganji, S. Vasheghani-Farahani, and E. Vasheghani-Farahani, “Theoretical description of hydrogel swelling,” *Iranian Polymer Journal*, vol. 19, no. 5, pp. 375–398, 2010.
- [107] T. Miyata, T. Uragami, and K. Nakamae, “Biomolecule-sensitive hydrogels,” *Advanced Drug Delivery Reviews*, vol. 54, no. 1, pp. 79–98, 2002.

- [108] A. Mateescu, Y. Wang, J. Dostalek, and U. Jonas, "Thin hydrogel films for optical biosensor applications," *Membranes (Basel)*, vol. 2, no. 1, pp. 40–69, 2012.
- [109] J. M. G. Cowie, *Polymers: Chemistry & Physics of Modern Materials (2nd ed.)*. Nelson Thornes, 1996.
- [110] T. Tanaka and D. J. Fillmore, "Kinetics of swelling of gels," *Journal of Chemical Physics*, vol. 70, no. 3, pp. 1214–1218, 1979.
- [111] D. C. Lin, B. Yurke, and N. A. Langrana, "Mechanical properties of a reversible, DNA-crosslinked polyacrylamide hydrogel," *Journal of Biomechanical Engineering*, vol. 126, no. 1, pp. 104–110, 2004.
- [112] Y. Murakami and M. Maeda, "Hybrid hydrogels to which Single-Stranded (ss) DNA probe is incorporated can recognize specific ssDNA," *Macromolecules*, vol. 38, pp. 1535–1537, 2005.
- [113] Y. Murakami and M. Maeda, "DNA-responsive hydrogels that can shrink or swell," *Biomacromolecules*, vol. 6, no. 6, pp. 2927–2929, 2005.
- [114] J. Liu, "Oligonucleotide-functionalized hydrogels as stimuli responsive materials and biosensors," *Soft Matter*, vol. 7, pp. 6757–6767, 2011.
- [115] H. Yang, H. Liu, H. Kang, and W. Tan, "Engineering target-responsive hydrogels based on aptamertarget interactions," *Journal of the American Chemical Society*, vol. 130, no. 20, pp. 6320–6321, 2008.
- [116] T. Liedl, H. Dietz, B. Yurke, and F. Simmel, "Controlled trapping and release of quantum dots in a DNA-switchable hydrogel," *Small*, vol. 3, no. 10, pp. 1688–1693, 2007.
- [117] B. Wei, I. Cheng, K. Q. Luo, and Y. Mi, "Capture and release of protein by a reversible DNA-induced sol-gel transition system," *Angewandte Chemie (Int. Ed.)*, vol. 47, no. 2, pp. 331–333, 2007.
- [118] H. Kang, H. Liu, X. Zhang, J. Yan, *et al.*, "Photoresponsive DNA-cross-linked hydrogels for controllable release and cancer therapy," *Langmuir*, vol. 27, no. 1, pp. 399–408, 2011.
- [119] A. Baeissa, N. Dave, B. Smith, and J. Liu, "DNA-functionalized monolithic hydrogels and gold nanoparticles for colorimetric DNA detection," *ACS Applied Materials & Interfaces*, vol. 2, no. 12, pp. 3594–3600, 2010.
- [120] K. Joseph, N. Dave, and J. Liu, "Electrostatically directed visual fluorescence response of DNA-functionalized monolithic hydrogels for highly sensitive Hg²⁺ detection," *ACS Applied Materials & Interfaces*, vol. 3, no. 3, pp. 733–739, 2011.
- [121] S. Li, N. Chen, Z. Zhang, and Y. Wang, "Endonuclease-responsive aptamer-functionalized hydrogel coating for sequential catch and release of cancer cells," *Biomaterials*, vol. 34, no. 2, pp. 460–469, 2013.

- [122] N. Dave, M. Chan, P. Huang, B. Smith, and J. Liu, "Regenerable DNA-functionalized hydrogels for ultrasensitive, instrument-free mercury(II) detection and removal in water," *Journal of the American Chemical Society*, vol. 132, no. 36, pp. 12668–12673, 2010.
- [123] A. Chan and U. J. Krull, "Capillary electrophoresis for capture and concentrating of target nucleic acids by affinity gels modified to contain single-stranded nucleic acid probes," *Analytica Chimica Acta*, vol. 578, no. 1, pp. 31–42, 2006.
- [124] S. Tierney and B. T. Stokke, "Development of an oligonucleotide functionalized hydrogel integrated on a high resolution interferometric readout platform as a label-free macromolecule sensing device," *Biomacromolecules*, vol. 10, no. 6, pp. 1619–1626, 2009.
- [125] M. Gao, K. Gawel, and B. T. Stokke, "Toehold of dsDNA exchange affects the hydrogel swelling kinetics of a polymer-dsDNA hybrid hydrogel," *Soft Matter*, vol. 7, pp. 1741–1746, 2011.
- [126] M. Kenney, S. Ray, and T. Boles, "Mutation typing using electrophoresis and gel-immobilized acrydite probes," *Biotechniques*, vol. 25, pp. 516–521, 1998.
- [127] F. N. Rehman, M. Audeh, E. S. Abrams, P. W. Hammond, *et al.*, "Immobilization of acrylamide-modified oligonucleotides by co-polymerization," *Nucleic Acids Research*, vol. 27, no. 2, pp. 649–655, 1999.
- [128] A. Richter, A. Bund, M. Keller, and K.-F. Arndt, "Characterization of a microgravimetric sensor based on pH sensitive hydrogels," *Sensors and Actuators B: Chemical*, vol. 99, pp. 579–585, 2004.
- [129] P. Asberg, P. Björk, F. Höök, and O. Inganäs, "Hydrogels from a water-soluble zwitterionic polythiophene: dynamics under pH change and biomolecular interactions observed using quartz crystal microbalance with dissipation monitoring," *Langmuir*, vol. 21, no. 16, pp. 7292–7298, 2005.
- [130] A. Sannino, S. Pappada, L. Giotta, L. Valli, and A. Maffezzoli, "Spin coating cellulose derivatives on quartz crystal microbalance plates to obtain hydrogel-based fast sensors and actuators," *Journal of Applied Polymer Science*, vol. 106, no. 5, pp. 3040–3050, 2007.
- [131] R. Wang and Y. Li, "Hydrogel based QCM aptasensor for detection of avian influenza virus," *Biosensors & Bioelectronics*, vol. 42, pp. 148–155, 2013.
- [132] K. Gawel, D. Barriet, M. Sletmoen, and B. T. Stokke, "Responsive hydrogels for label-free signal transduction within biosensors," *Sensors (Basel)*, vol. 10, no. 5, pp. 4381–4409, 2010.
- [133] S. Tierney, D. R. Hjelme, and B. T. Stokke, "Determination of swelling of responsive gels with nanometer resolution. fiber-optic based platform for hydrogels as signal transducers," *Analytical Chemistry*, vol. 80, no. 13, pp. 5086–5093, 2008.
- [134] S. Tierney, S. Volden, and B. T. Stokke, "Glucose sensors based on a responsive gel incorporated as a Fabry-Perot cavity on a fiber-optic readout platform," *Biosensors & Bioelectronics*, vol. 24, no. 7, pp. 2034–2039, 2009.

- [135] S. Tierney, B. M. Falch, D. R. Hjelme, and B. T. Stokke, "Determination of glucose levels using a functionalized hydrogel-optical fiber biosensor: toward continuous monitoring of blood glucose in vivo," *Analytical Chemistry*, vol. 81, no. 9, pp. 3630–3636, 2009.
- [136] J. H. Holtz and S. A. Asher, "Polymerized colloidal crystal hydrogel films as intelligent chemical sensing materials," *Nature*, vol. 389, no. 6653, pp. 829–832, 1997.
- [137] J. Kim, N. Singh, and L. A. Lyon, "Label-free biosensing with hydrogel microlenses," *Angewandte Chemie (Int. Ed.)*, vol. 45, no. 9, pp. 1446–1449, 2006.
- [138] J. Kim, N. Singh, and L. A. Lyon, "Displacement-induced switching rates of bioresponsive hydrogel microlenses," *Chemistry of Materials*, vol. 19, no. 10, pp. 2527–2532, 2007.
- [139] I. S. Han, M. H. Han, J. Kim, S. Lew, *et al.*, "Constant-volume hydrogel osmometer: a new device concept for miniature biosensors," *Biomacromolecules*, vol. 3, no. 6, pp. 1271–1275, 2002.
- [140] S. Herber, J. Eijkel, W. Olthuis, P. Bergveld, and A. van den Berg, "Study of chemically induced pressure generation of hydrogels under isochoric conditions using a microfabricated device," *The Journal of Chemical Physics*, vol. 121, no. 6, pp. 2746–2751, 2004.
- [141] G. Lin, S. Chang, C. H. Kuo, J. Magda, and F. Solzbacher, "Free swelling and confined smart hydrogels for applications in chemomechanical sensors for physiological monitoring," *Sensors and Actuators B: Chemical*, vol. 136, no. 1, pp. 186–195, 2009.
- [142] S. Herber, J. Bomer, W. Olthuis, P. Bergveld, and A. van den Berg, "A miniaturized carbon dioxide gas sensor based on sensing of pH-sensitive hydrogel swelling with a pressure sensor," *Biomedical Microdevices*, vol. 7, no. 3, pp. 197–204, 2005.
- [143] R. Bashir, J. Z. Hilt, O. Elibol, A. Gupta, and N. A. Peppas, "Micromechanical cantilever as an ultrasensitive pH microsensor," *Applied Physics Letters*, vol. 81, no. 16, pp. 3091–3093, 2002.
- [144] J. Z. Hilt, A. K. Gupta, R. Bashir, and N. A. Peppas, "Ultrasensitive biomems sensors based on microcantilevers patterned with environmentally responsive hydrogels," *Biomedical Microdevices*, vol. 5, no. 3, pp. 177–184, 2003.
- [145] Y. Zhang, H. Ji, G. Brown, and T. Thundat, "Detection of CrO₄²⁻ using a hydrogel swelling microcantilever sensor," *Analytical Chemistry*, vol. 75, no. 18, pp. 4773–4777, 2003.
- [146] O. M. Folarin, E. R. Sadiku, and A. Maity, "Polymer-noble metal nanocomposites," *International Journal of the Physical Sciences*, vol. 6, no. 21, pp. 4869–4882, 2011.

- [147] R. C. Barthus, L. M. Lira, and S. I. C. de Torresi, "Conducting polymer-hydrogel blends for electrochemically controlled drug release devices," *Journal of the Brazilian Chemical Society*, vol. 19, no. 4, pp. 630–636, 2008.
- [148] D. Kim, M. Abidian, and D. C. Martin, "Conducting polymers grown in hydrogel scaffolds coated on neural prosthetic devices.," *Journal of Biomedical Materials Research: Part A*, vol. 71, no. 4, pp. 577–585, 2004.
- [149] R. A. Green, S. Baek, and L. A. Poole-Warren, "Conducting polymer-hydrogels for medical electrode applications," *Science and Technology of Advanced Materials*, vol. 11, p. 014107, 2010.
- [150] D. Bloor, K. Donnelly, P. J. Hands, P. Laughlin, and D. Lussey, "A metal-polymer composite with unusual properties," *Journal of Physics D: Applied Physics*, vol. 38, pp. 2851–2860, 2005.
- [151] C. Calberg, S. Blacher, F. Gubbels, F. Brouers, *et al.*, "Electrical and dielectric properties of carbon black filled co-continuous two-phase polymer blends," *Journal of Physics D: Applied Physics*, vol. 32, no. 13, pp. 1517–1525, 1999.
- [152] Z. Wang, C. Roberge, Y. Wan, L. Dao, *et al.*, "A biodegradable electrical bio-conductor made of polypyrrole nanoparticle/poly(D,L-lactide) composite: A preliminary in vitro biostability study," *Journal of Biomedical Materials Research: Part A*, vol. 66, no. 4, pp. 738–746, 2003.
- [153] Z. Wang, C. Roberge, L. Dao, Y. Wan, *et al.*, "In vivo evaluation of a novel electrically conductive polypyrrole/poly(D,L-lactide) composite and polypyrrole-coated poly(D,L-lactide-co-glycolide) membranes," *Journal of Biomedical Materials Research: Part A*, vol. 70A, no. 1, pp. 28–38, 2004.
- [154] G. Shi, M. Rouabhia, Z. Wang, L. Dao, and Z. Zhang, "A novel electrically conductive and biodegradable composite made of polypyrrole nanoparticles and polylactide," *Biomaterials*, vol. 25, no. 13, pp. 2477–2488, 2004.
- [155] N. Ferraz, M. Strømme, B. Fellström, S. Pradhan, *et al.*, "In vitro and in vivo toxicity of rinsed and aged nanocellulose-polypyrrole composites," *Journal of Biomedical Materials Research: Part A*, vol. 100A, no. 8, pp. 2128–2138, 2012.
- [156] E. Zare, M. Lakouraj, and M. Mohseni, "Biodegradable polypyrrole/dextrin conductive nanocomposite: Synthesis, characterization, antioxidant and antibacterial activity," *Synthetic Metals*, vol. 187, pp. 9–16, 2014.
- [157] M. R. Abidian and D. C. Martin, "Multifunctional nanobiomaterials for neural interfaces," *Advanced Functional Materials*, vol. 19, pp. 573–585, 2009.
- [158] E. Sancaktar and N. Dilsiz, "Pressure-dependent conduction behavior of various particles for conductive adhesive applications," *Journal of Adhesion Science and Technology*, vol. 13, no. 6, pp. 679–693, 1999.
- [159] G. M. Nasr, H. M. Osman, M. Abu-Abdeen, and A. I. Aboud, "On the percolative behavior of carbon black-rubber interlinked systems," *Polymer Testing*, vol. 18, no. 7, pp. 483–493, 1999.

- [160] F. Lux, “Models proposed to explain the electrical conductivity of mixtures made of conductive and insulating materials,” *Journal of Materials Science*, vol. 28, no. 2, pp. 285–301, 1993.
- [161] Q. Tang, J. Lin, and J. Wu, “The preparation and electrical conductivity of polyacrylamide/graphite conducting hydrogel,” *Journal of Applied Polymer Science*, vol. 108, no. 3, pp. 1490–1495, 2008.
- [162] Ö. Pekcan and G. A. Evingür, *Carbon Nanotubes – Polymer Nanocomposites*, ch. 10, pp. 197–214. InTech, 2011.
- [163] J. Wu and D. S. McLachlan, “Percolation exponents and thresholds obtained from the nearly ideal continuum percolation system graphite-boron nitride,” *Physical Review B*, vol. 56, no. 3, pp. 1236–1248, 1997.
- [164] D. S. McLachlan, “An equation for the conductivity of binary mixtures with anisotropic grain structures,” *Journal of Physics C: Solid State Physics*, vol. 20, no. 7, pp. 865–877, 1987.
- [165] P. J. W. Hands, *Vapour Sensing Applications and Electrical Conduction Mechanisms of a Novel Metal-Polymer Composite*. PhD thesis, University of Durham, 2003.
- [166] P. Hands, P. Laughlin, and D. Bloor, “Metal-polymer composite sensors for volatile organic compounds: Part 1. flow-through chemi-resistors,” *Sensors and Actuators B: Chemical*, vol. 162, pp. 400–408, 2012.
- [167] M. C. Lonergan, E. J. Severin, B. J. Doleman, S. A. Beaber, *et al.*, “Array-based vapor sensing using chemically sensitive, carbon black-polymer resistors,” *Chemistry of Materials*, vol. 8, no. 9, pp. 2298–2312, 1996.
- [168] B. J. Doleman, M. C. Lonergan, E. J. Severin, T. P. Vaid, and N. S. Lewis, “Quantitative study of the resolving power of arrays of carbon black-polymer composites in various vapor-sensing tasks,” *Analytical Chemistry*, vol. 70, no. 19, pp. 4177–4190, 1998.
- [169] F. Davis and S. P. J. Higson, “Biosensors for DNA and RNA detection and characterization,” in *Biosensors for Medical Applications*, ch. 6, pp. 163–190, Woodhead Publishing, 2012.
- [170] S. N. Syed, H. Schulze, D. Macdonald, J. Crain, A. R. Mount, and T. T. Bachmann, “Cyclic denaturation and renaturation of double-stranded DNA by redox-state switching of DNA intercalators,” *Journal of the American Chemical Society*, vol. 135, no. 14, pp. 5399–5407, 2013.
- [171] A. Khosla and A. L. Gray, “Micropatternable multifunctional nanocomposite polymers for flexible soft NEMS and MEMS applications,” *ECS Transactions*, vol. 45, no. 3, pp. 477–494, 2012.
- [172] V. S. Nguyen, D. Rouxel, and B. Vincent, “Dispersion of nanoparticles: from organic solvents to polymer solutions,” *Ultrasonics Sonochemistry*, vol. 21, pp. 149–153, 2014.

- [173] P. Ma, N. Siddiqui, G. Marom, and J. Kim, "Dispersion and functionalization of carbon nanotubes for polymer-based nanocomposites: A review," *Composites Part A: Applied Science and Manufacturing*, vol. 41, no. 10, pp. 1345–1367, 2010.
- [174] J. Duggan and C. Roberts, "Aggregation and precipitation of gold nanoparticle clusters in carbon dioxide-gas-expanded liquid dimethyl sulfoxide," *Journal of Physical Chemistry C*, vol. 118, no. 26, pp. 14595–14605, 2014.
- [175] A. Kahouli, A. Sylvestre, and J. Laithier, "Performance improvements of the hydrophobic and the dielectric properties of parylene C," *Journal of Applied Physics*, vol. 114, no. 15, p. 154111, 2013.
- [176] T. Trantidou, C. Rao, H. Barrett, P. Camelliti, *et al.*, "Selective hydrophilic modification of parylene C films: a new approach to cell micro-patterning for synthetic biology applications," *Biofabrication*, vol. 6, no. 2, p. 025004, 2014.
- [177] D. W. Widmann, "Metallization for integrated circuits using a lift-off technique," *IEEE Journal of Solid-State Circuits*, vol. 11, no. 4, pp. 466–471, 1976.
- [178] P. Ekkels, X. Rottenberg, R. Puers, and H. Tilmans, "Evaluation of platinum as a structural thin film material for RF-MEMS devices," *Journal of Micromechanics and Microengineering*, vol. 19, no. 6, p. 065010, 2009.
- [179] M. Yamamoto, H. Horibe, A. Sekiguchi, E. Kusano, and S. Tagawa, "Standing-wave effect in photoresist with and without HMDS," *Journal of Photopolymer Science and Technology*, vol. 21, no. 2, pp. 299–304, 2008.
- [180] Keithley, *Data sheet: 2000 - 6 1/2-Digit Multimeter*, 2010.
- [181] Analog Devices, *Data sheet: AD5933*, 2013. Rev E.
- [182] M. Usach, *How to Configure the AD5933/AD5934*. Analog Devices, 2013.
- [183] C. Chung, S. Smith, A. Menachery, P. Bagnaninchi, *et al.*, "Interdigitated electrode modelling for applications in dielectrophoresis," in *2011 IEEE Conference on Microelectronic Test Structures*, pp. 47–79, 2011.
- [184] U. Latif and F. Dickert, "Conductometric sensors for monitoring degradation of automotive engine oil," *Sensors (Basel)*, vol. 11, no. 9, pp. 8611–8625, 2011.
- [185] Agilent Technologies, *Agilent Impedance Measurement Handbook: A guide to measurement technology and techniques*, 4 ed., 2013.
- [186] F. Marken, A. Neudeck, and A. M. Bond, "Cyclic voltammetry," in *Electroanalytical Methods* (F. Scholz, ed.), ch. 2.1, pp. 57–106, Springer-Verlag, 2 ed., 2010.
- [187] J. P. Villagrasa, J. Colomer-Farrarons, and P. L. Miribel, "Bioelectronics for amperometric biosensors," in *State of the Art in Biosensors - General Aspects* (T. Rinken, ed.), ch. 10, pp. 241–274, InTech, 2013.
- [188] A. Rudin and P. Choi, "Free-radical polymerization," in *The Elements of Polymer Science & Engineering*, ch. 8, pp. 341–389, Elsevier, 3 ed., 2013.

- [189] G. Kvakovszky, A. McKim, and J. Moore, "A review of microelectronic manufacturing applications using DMSO-based chemistries," *ECS Transactions*, vol. 11, no. 2, pp. 227–234, 2007.
- [190] B. Sterck, R. Vaneerdeweg, F. Prez, M. Waroquier, and V. Speybroeck, "Solvent effects on free radical polymerization reactions: The influence of water on the propagation rate of acrylamide and methacrylamide," *Macromolecules*, vol. 43, no. 2, pp. 827–836, 2010.
- [191] A. Valdebenito and M. Encinas, "Effect of solvent on the free radical polymerization of N,N-dimethylacrylamide," *Polymer International*, vol. 59, no. 9, pp. 1246–1251, 2010.
- [192] J. Alvarez, M. Encinas, and E. Lissi, "Solvent effects on the rate of polymerization of 2-hydroxyethyl methacrylate photoinitiated with aliphatic azo compounds," *Macromolecular Chemistry and Physics*, vol. 200, no. 10, pp. 2411–2415, 1999.
- [193] G. Burnett, G. Cameron, and S. Joiner, "Solvent effects on the free radical polymerization of styrene," *Journal of the Chemical Society, Faraday Transactions 1: Physical Chemistry in Condensed Phases*, vol. 69, pp. 322–327, 1973.
- [194] A. Kosmala, R. Wright, Q. Zhang, and P. Kirby, "Synthesis of silver nano particles and fabrication of aqueous Ag inks for inkjet printing," *Materials Chemistry and Physics*, vol. 129, no. 3, pp. 1075–1080, 2011.
- [195] P. Calvert, "Inkjet printing for materials and devices," *Chemistry of Materials*, vol. 13, no. 10, pp. 3299–3305, 2001.
- [196] P.-C. Ma, N. Siddiqui, G. Marom, and J.-K. Kim, "Dispersion and functionalization of carbon nanotubes for polymer-based nanocomposites," *Composites: Part A*, vol. 41, pp. 1345–1367, 2010.
- [197] X. Wang and A. Son, "Effects of pretreatment on the denaturation and fragmentation of genomic DNA for DNA hybridization," *Environmental Science Processes & Impacts*, vol. 15, pp. 2204–2212, 2013.
- [198] X. Wang, H. Lim, and A. Son, "Characterization of denaturation and renaturation of DNA for DNA hybridization," *Environmental Health and Toxicology*, vol. 29, p. 2014007, 2014.
- [199] C. Guo, Q. Liu, Q. Ji, H. An, *et al.*, "Carbon nanopowder binds with dna and may induce dna aggregation," in *4th International Conference on Bioinformatics and Biomedical Engineering*, 2010.
- [200] Z. Wang, H. Fang, S. Wang, F. Zhang, and D. Wang, "Simulating molecular interactions of carbon nanoparticles with a double-stranded DNA fragment," *Journal of Chemistry*, vol. 2015, pp. 1–6, 2015.
- [201] H. An, Q. Liu, Q. Ji, and B. Jin, "DNA binding and aggregation by carbon nanoparticles," *Biochemical and Biophysical Research Communications*, vol. 393, no. 4, pp. 571–576, 2010.

- [202] H. An and B. Jin, "Prospects of nanoparticle-DNA binding and its implications in medical biotechnology," *Biotechnology Advances*, vol. 30, pp. 1721–1732, 2012.
- [203] J. Fang, A. Mehlich, N. Koga, J. Huang, *et al.*, "Forced protein unfolding leads to highly elastic and tough protein hydrogels," *Nature Communications*, vol. 4, 2013.
- [204] D. Valade, L. Wong, Y. Jeon, Z. Jia, and M. Monteiro, "Polyacrylamide hydrogel membranes with controlled pore sizes," *Journal of Polymer Chemistry Part A: Polymer Chemistry*, vol. 51, no. 1, pp. 129–138, 2013.
- [205] M. Kremer, E. Pothmann, T. Rossler, J. Baker, *et al.*, "Pore-size distributions of cationic polyacrylamide hydrogels varying in initial monomer concentration and cross-linker/monomer ratio," *Macromolecules*, vol. 27, pp. 2965–2973, 1994.
- [206] Sigma-Aldrich, *Safety Data Sheet: Carbon - 633100*, 5.1 ed., 2013.
- [207] H. E. Gottlieb, V. Kotlyar, and A. Nudelman, "NMR chemical shifts of common laboratory solvents as trace impurities," *Journal of Organic Chemistry*, vol. 62, no. 21, pp. 7512–7515, 1997.
- [208] Y. Jian, Y. He, T. Jiang, C. Li, *et al.*, "Volume shrinkage of UV-curable coating formulation investigated by real-time laser reflection method," *Journal of Coatings Technology and Research*, vol. 10, no. 2, pp. 321–237, 2013.
- [209] P. Contreras, P. Tyagi, and S. Agarwal, "Low volume shrinkage of polymers by photopolymerization of 1,1-bis(ethoxycarbonyl)-2-vinylcyclopropanes," *Polymer Chemistry*, vol. 6, no. 12, pp. 2297–2304, 2015.
- [210] A. Tichopad, M. Dilger, G. Schwarz, and M. W. Pfaffi, "Standardized determination of real-time PCR efficiency from a single reaction set-up," *Nucleic Acids Research*, vol. 31, no. 20, p. e122, 2003.
- [211] S. Zhao and R. Fernald, "Comprehensive algorithm for quantitative real-time polymerase chain reaction," *Journal of Computational Biology*, vol. 12, no. 8, pp. 1047–1064, 2005.
- [212] A. Spiess, C. Feig, and C. Ritz, "Highly accurate sigmoidal fitting of real-time PCR data by introducing a parameter for asymmetry," *BMC Informatics*, vol. 9, no. 1, p. 221, 2008.
- [213] W. A. Kibbe, "OligoCalc: an online oligonucleotide properties calculator.," *Nucleic Acids Research*, vol. 35, pp. W43–46, 2007.
- [214] U. P. Schroder and W. Oppermann, "Properties of polyelectrolyte gels," in *Physical Properties of Polymeric Gels* (J. P. Cohen Addad, ed.), pp. 19–38, John Wiley and Sons, 1996.
- [215] R. D. Blake and S. G. Delcourt, "Thermal stability of DNA," *Nucleic Acids Research*, vol. 26, no. 14, pp. 3323–3332, 1998.

- [216] A. Panjkovich and F. Melo, "Comparison of different melting temperature calculation methods for short DNA sequences," *Bioinformatics*, vol. 21, no. 6, pp. 711–722, 2005.
- [217] C. Schlecht and J. Maurer, "Functionalization of glass substrates: mechanistic insights into the surface reaction of trialkoxysilanes," *RSC Advances*, vol. 1, no. 8, pp. 1446–1448, 2011.
- [218] I. Kondo, T. Yoneyama, O. Takenaka, and A. Kinbara, "Formation of high adhesive and pure Pt layers on TiO₂," *Journal of Vacuum Science and Technology*, vol. 10, no. 6, pp. 3456–3459, 1992.
- [219] S. L. Firebaugh, K. F. Jensen, and M. A. Schmidt, "Investigation of high-temperature degradation of platinum thin films with an in situ resistance measurement apparatus," *Journal of Microelectromechanical Systems*, vol. 7, no. 1, pp. 128–135, 1998.
- [220] C. C. Mardare, E. Joanni, A. I. Mardare, J. R. A. Fernandes, *et al.*, "Effects of adhesion layer (Ti or Zr) and pt deposition temperature on the properties of PZT thin films deposited by RF magnetron sputtering," *Applied Surface Science*, vol. 243, no. 1-4, pp. 113–124, 2005.
- [221] R. M. Tiggelaar, R. G. P. Sanders, A. W. Groenland, and J. G. E. Gardeniers, "Stability of thin platinum films implemented in high-temperature microdevices," *Sensors and Actuators A: Physical*, vol. 152, no. 1, pp. 39–47, 2009.
- [222] A. Ababneh, A. Al-Omari, A. Dagamseh, M. Tantawi, *et al.*, "Electrical and morphological characterization of platinum thin-films with various adhesion layers for high temperature applications," *Microsystems Technology*, vol. 21, pp. 1–7, 2015.
- [223] S. Eränen, "Silicon dioxides," in *Handbook of Silicon Based MEMS Materials and Technologies* (V. Lindroos, M. Tilli, A. Lehto, and T. Motooka, eds.), pp. 137–148, William Andrew, New York, 2010.
- [224] S. Nakano, M. Fujimoto, H. Hara, and N. Sugimoto, "Nucleic acid duplex stability: influence of base composition on cation effects," *Nucleic Acids Research*, vol. 27, no. 14, pp. 2957–2965, 1999.
- [225] R. Owczarzy, Y. You, B. G. Moreira, J. A. Manthey, and other, "Effects of sodium ions on DNA duplex oligomers: improved predictions of melting temperatures," *Biochemistry*, vol. 43, no. 12, pp. 3537–3554, 2004.
- [226] N. Dave and J. Liu, "Fast molecular beacon hybridization in organic solvents with improved target specificity," *Journal of Physical Chemistry B*, vol. 114, no. 47, pp. 15694–15699, 2010.
- [227] H. Tateishi-Karimata and N. Sugimoto, "Structure, stability and behaviour of nucleic acids in ionic liquids," *Nucleic Acids Research*, vol. 42, no. 14, pp. 8831–8844, 2014.

- [228] S. C. Rumsey, N. F. Galeano, A. Yadon, and R. J. Deckelbaum, "Cryopreservation with sucrose maintains normal physical and biological properties of human plasma low density lipoproteins," *Journal of Lipid Research*, vol. 33, pp. 1551–1561, 1992.
- [229] G. V. Richieri and A. M. Kleinfeld, "Unbound free fatty acid levels in human serum," *Journal of Lipid Research*, vol. 36, pp. 229–240, 1995.
- [230] Y. Sun, L. Shen, and B. Dahlbäck, "Gla domainmutated human protein C exhibiting enhanced anticoagulant activity and increased phospholipid binding," *Blood*, vol. 101, no. 6, pp. 2277–2284, 2003.
- [231] H. Deguchi, G. Wolfbauer, M. Cheung, Y. Banerjee, *et al.*, "Inhibition of thrombin generation in human plasma by phospholipid transfer protein," *Thrombosis Journal*, vol. 13, no. 1, pp. 1–9, 2015.
- [232] D. S. McLachlan, "Equations for the conductivity of macroscopic mixtures," *Journal of Physics C: Solid State Physics*, vol. 19, pp. 1339–1354, 1986.
- [233] D. S. McLachlan, "Analytical functions for the dc and ac conductivity of conductor-insulator composites," *Journal of Electroceramics*, vol. 5, no. 2, pp. 93–110, 2000.
- [234] Keithley, *User manual: Model 2000 Multimeter*, 2010. Rev J.
- [235] W. Olthuis, W. Streekstra, and P. Berveld, "Theoretical and experimental determination of cell constants of planar-interdigitated electrolyte conductivity sensors," *Sensors and Actuators B: Chemical*, vol. 24–25, pp. 252–256, 1995.
- [236] W. Zhang, A. Dehghani-Sanij, and R. Blackburn, "Carbon based conductive polymer composites," *Journal of Materials Science*, vol. 42, no. 10, pp. 3408–3418, 2007.
- [237] F. Wu and K. W. Whites, "Computation of static effective permittivity for a multiphase lattice of cylinders," *Electromagnetics*, vol. 21, no. 2, pp. 97–114, 2001.
- [238] A. Moosavi and P. Sarkomaa, "The effective conductivity of three-phase composite materials with circular cylindrical inclusions," *Journal of Physics D: Applied Physics*, vol. 36, pp. 1644–1650, 2003.
- [239] J.-O. You and D. T. Auguste, "Conductive, physiologically responsive hydrogels," *Langmuir*, vol. 26, no. 7, pp. 4607–4612, 2010.
- [240] M. F. Islam, E. Rojas, D. M. Bergey, and A. T. Johnson, "High weight fraction surfactant solubilization of single-wall carbon nanotubes in water," *Nano Letters*, vol. 3, no. 2, pp. 269–273, 2003.
- [241] L. Vaisman, H. Wagner, and G. Marom, "The role of surfactants in dispersion of carbon nanotubes," *Advances in Colloid and Interface Science*, pp. 37–46, 2006.
- [242] M. Moniruzzaman and K. I. Winey, "Polymer nanocomposites containing carbon nanotubes," *Macromolecules*, vol. 39, pp. 5194–5205, 2006.

- [243] M. Melchionna and M. Prato, “Functionalizing carbon nanotubes: an indispensable step towards applications,” *ECS Journal of Solid State Science and Technology*, vol. 2, no. 10, pp. M3040–M3045, 2013.
- [244] M. Pimenta, G. Dresselhaus, M. Dresselhaus, L. Cançado, *et al.*, “Studying disorder in graphite-based systems by Raman spectroscopy,” *Physical Chemistry Chemical Physics*, vol. 9, no. 11, pp. 1276–1290, 2007.
- [245] C. Salzmann, V. Nicolosi, and M. Green, “Edge-carboxylated graphene nanoflakes from nitric acid oxidised arc-discharge material,” *Journal of Materials Chemistry*, vol. 20, no. 2, pp. 314–319, 2010.
- [246] Sigma-Aldrich, *Safety Data Sheet: Carbon - 484164*, 5.2 ed., 2016.
- [247] P. H. Rieger, *Electrochemistry*. Springer, 2 ed., 1994.
- [248] J. O. M. Bockris and A. K. N. Reddy, *Modern Electrochemistry*. Plenum Press, 2 ed., 1998.
- [249] G. J. Shah, S. Sadeghi, H. Ding, S. Chen, and R. M. van Dam, “Impedance-based droplet volume and concentration measurement in digital microfluidics,” in *15th International Conference in Miniaturized Systems for Chemistry and Life Sciences*, pp. 1308–1310, 2011.
- [250] P. Barber, S. Balasubramanian, Y. Anguchamy, S. Gong, *et al.*, “Polymer composite and nanocomposite dielectric materials for pulse power energy storage,” *Materials*, vol. 2, pp. 1697–1733, 2009.
- [251] M. W. den Otter, “Approximate expressions for the capacitance and electrostatic potential of interdigitated electrodes,” *Sensors and Actuators A: Physical*, vol. 96, no. 2–3, pp. 140–144, 2002.
- [252] R. Igreja and C. Dias, “Analytical evaluation of the interdigital electrodes capacitance for a multi-layered structure,” *Sensors and Actuators A: Physical*, vol. 112, no. 2–3, pp. 291–301, 2004.
- [253] R. E. Collin, *Foundations for Microwave Engineering*. McGraw-Hill, 1966.
- [254] J. B. Jarvis, M. D. Janezic, B. F. Riddle, R. T. Johnk, *et al.*, “Measuring the permittivity and permeability of lossy materials: Solids, liquids, metals, building materials, and Negative-Index materials,” tech. rep., National Institute of Standards and Technology, 2005.
- [255] H. Ma, R. Wallbank, R. Chaji, J. Li, *et al.*, “An impedance-based integrated biosensor for suspended DNA characterization,” *Scientific Reports*, vol. 3, p. 2730, 2013.
- [256] Y. Liu, P. Banada, S. Bhattacharya, A. Bhunia, and R. Bashir, “Electrical characterization of DNA molecules in solution using impedance measurements,” *Applied Physics Letters*, vol. 92, no. 14, p. 143902, 2008.
- [257] A. J. Bard and L. R. Faulkner, *Electrochemical Methods: Fundamentals and Applications*. John Wiley & Sons, 2 ed., 2001.

- [258] D. Zhan, J. Velmurugan, and M. Mirkin, “Adsorption/desorption of hydrogen on Pt nanoelectrodes: Evidence of surface diffusion and spillover,” *Journal of the American Chemical Society*, vol. 131, no. 41, pp. 14756–14760, 2009.
- [259] R. W. Murray, “Polymer modification of electrodes,” *Annual Reviews of Materials Science*, vol. 14, pp. 145–169, 1984.
- [260] C. Liebenow and K. Lühder, “Electrochemical characterization of polymer pre-coated lithium electrodes,” *Journal of Applied Electrochemistry*, vol. 26, pp. 689–692, 1996.
- [261] A. Koshkin, S. Singh, P. Nielsen, V. Rajwanshi, *et al.*, “LNA (Locked nucleic acids): Synthesis of the adenine, cytosine, guanine, 5-methylcytosine, thymine and uracil bicyclonucleoside monomers, oligomerisation, and unprecedented nucleic acid recognition,” *Tetrahedron*, vol. 54, no. 14, pp. 3607–3630, 1998.
- [262] S. Karkare and D. Bhatnagar, “Promising nucleic acid analogs and mimics: characteristic features and applications of PNA, LNA, and morpholino,” *Applied Microbiology Biotechnology*, vol. 71, no. 5, pp. 575–586, 2006.
- [263] Q. Wang, L. Chen, Y. Long, H. Tian, and J. Wu, “Molecular beacons of xenonucleic acid for detecting nucleic acid,” *Theranostics*, vol. 3, no. 6, pp. 395–408, 2013.
- [264] A. Taylor, V. Pinheiro, M. Smola, A. Morgunov, *et al.*, “Catalysts from synthetic genetic polymers,” *Nature*, vol. 518, no. 7539, pp. 427–430, 2015.
- [265] D. A. Braasch and D. R. Corey, “Locked nucleic acid (LNA): fine-tuning the recognition of DNA and RNA,” *Chemistry & biology*, vol. 8, no. 1, pp. 1–7, 2001.
- [266] P. E. Nielsen and G. Haaime, “Peptide nucleic acid (PNA). A DNA mimic with a pseudopeptide backbone,” *Chemical Society Reviews*, vol. 26, no. 2, pp. 73–78, 1997.
- [267] M. Schmidt, “Xenobiology: a new form of life as the ultimate biosafety tool,” *Bioessays*, vol. 32, no. 4, pp. 322–331, 2010.
- [268] J. E. Summerton, “Morpholinos and PNAs compared,” *International Journal of Peptide Research and Therapeutics*, vol. 10, pp. 215–236, 2003.
- [269] G. J. Zhang, Z. H. H. Luo, M. J. Huang, G. K. I. Tay, and E. J. A. Lim, “Morpholino-functionalized silicon nanowire biosensor for sequence-specific label-free detection of DNA,” *Biosensors & Bioelectronics*, vol. 25, pp. 2447–2453, 2010.
- [270] N. Tercero, K. Wang, P. Gong, and R. Levicky, “Morpholino monolayers: preparation and label-free DNA analysis by surface hybridization,” *Journal of the American Chemical Society*, vol. 131, no. 13, pp. 4953–4961, 2009.
- [271] J. Summerton, “Morpholino, siRNA, and S-DNA compared: impact of structure and mechanism of action on off-target effects and sequence specificity,” *Current Topics in Medicinal Chemistry*, vol. 7, no. 7, pp. 651–660, 2007.

- [272] J. Heasman, "Morpholino oligos: making sense of antisense?," *Developmental Biology*, vol. 243, no. 2, pp. 209–214, 2002.
- [273] W. Qiao, H. Chiang, H. Xie, and R. Levicky, "Surface vs. solution hybridization: effects of salt, temperature, and probe type," *Chemical Communications*, vol. 51, no. 97, pp. 17245–17248, 2015.
- [274] J. Wang, "DNA biosensors based on peptide nucleic acid (PNA) recognition layers. a review," *Biosensors & Bioelectronics*, vol. 13, no. 7–8, pp. 757–762, 1998.
- [275] H. J. Larsen, T. Bentin, and P. E. Nielsen, "Antisense properties of peptide nucleic acid," *Biochimica et Biophysica Acta*, vol. 1489, no. 1, pp. 159–166, 1999.
- [276] Z. Fang and S. O. Kelley, "Direct electrocatalytic mRNA detection using PNA-nanowire sensors.," *Analytical chemistry*, vol. 81, no. 2, pp. 612–617, 2009.
- [277] G.-J. Zhang, J. H. Chua, R.-E. Chee, A. Agarwal, *et al.*, "Highly sensitive measurements of PNA-DNA hybridization using oxide-etched silicon nanowire biosensors," *Biosensors & Bioelectronics*, vol. 23, pp. 1701–1707, 2008.
- [278] V. G. Joshi, K. Chindera, A. K. Singh, A. P. Sahoo, *et al.*, "Rapid label-free visual assay for the detection and quantification of viral RNA using peptide nucleic acid (PNA) and gold nanoparticles (AuNPs)," *Analytica Chimica Acta*, vol. 795, pp. 1–7, 2013.
- [279] B. Cai, S. Wang, L. Huang, Y. Ning, *et al.*, "Ultrasensitive label-free detection of PNA-DNA hybridization by reduced graphene oxide field-effect transistor biosensor," *ACS Nano*, vol. 8, no. 3, pp. 2632–2638, 2014.
- [280] T. Uno, H. Tabata, and T. Kawai, "Peptide Nucleic Acid-modified Ion-Sensitive Field-Effect Transistor-based biosensor for direct detection of DNA hybridization," *Analytical Chemistry*, vol. 79, pp. 52–59, 2007.
- [281] Z. Tan and S. Chen, "Nucleic acid helix stability: Effects of salt concentration, cation valence and size, and chain length," *Biophysics Journal*, vol. 90, no. 4, pp. 1175–1190, 2006.
- [282] A. Maity, A. Singh, and N. Singh, "Differential stability of DNA based on salt concentration," *European Biophysics Journal*, vol. 46, no. 1, pp. 33–40, 2017.
- [283] B. J. Doleman and N. S. Lewis, "Comparison of odor detection thresholds and odor discriminabilities of a conducting polymer composite electronic nose versus mammalian olfaction," *Sensors and Actuators B: Chemical*, vol. 72, pp. 41–50, 2001.
- [284] F. Zee and J. W. Judy, "Micromachined polymer-based chemical gas sensor array," *Sensors and Actuators B: Chemical*, vol. 72, pp. 120–128, 2001.
- [285] M. C. Burl, B. C. Sisk, T. P. Vaid, and N. S. Lewis, "Classification performance of carbon black-polymer composite vapor detector arrays as a function of array size and detector composition," *Sensors and Actuators B: Chemical*, vol. 87, pp. 130–149, 2002.

- [286] Y. Kim, S. Ha, Y. Yang, Y. Kim, *et al.*, “Portable electronic nose system based on the carbon black/polymer composite sensor array,” *Sensors and Actuators B: Chemical*, vol. 108, no. 1-2, pp. 285–291, 2005.
- [287] I. Khimji, E. Y. Kelly, Y. Helwa, M. Hoang, and J. Liu, “Visual optical biosensors based on DNA-functionalized polyacrylamide hydrogels,” *Methods*, vol. 64, no. 3, pp. 292–298, 2013.
- [288] S. M. Scott, D. James, and Z. Ali, “Data analysis for electronic nose systems,” *Microchimica Acta*, vol. 156, no. 3–4, pp. 183–207, 2007.
- [289] Z. Li, S.-C. Chang, and R. Williams, “Self-Assembly of alkanethiol molecules onto platinum and platinum oxide surfaces,” *Lamgmuir*, vol. 19, no. 17, pp. 6744–6749, 2003.
- [290] J. C. Love, L. A. Estroff, J. K. Kriebel, R. G. Nuzzo, and G. M. Whitesides, “Self-assembled monolayers of thiolates on metals as a form of nanotechnology,” *Chemical Reviews*, vol. 105, no. 4, pp. 1103–1169, 2005.
- [291] C. A. Savran, S. M. Knudsen, A. D. Ellington, and S. R. Manalis, “Micromechanical detection of proteins using aptamer-based receptor molecules,” *Analytical Chemistry*, vol. 76, no. 11, pp. 3194–3198, 2004.
- [292] S.-W. Ryu, C.-H. Kim, J.-W. Han, C.-J. Kim, *et al.*, “Gold nanoparticle embedded silicon nanowire biosensor for applications of label-free DNA detection,” *Biosensors & Bioelectronics*, vol. 25, pp. 2182–2185, 2010.
- [293] E. J. Zöllner, G. Seibert, H. Slor, and R. K. Zahn, “Purification of a nuclease from human serum,” *Cellular and Molecular Life Sciences*, vol. 37, no. 6, pp. 548–550, 1981.
- [294] G. J. Zhang, Z. Luo, M. Huang, J. Ang, T. Kang, and H. Ji, “An integrated chip for rapid, sensitive, and multiplexed detection of cardiac biomarkers from fingerprick blood,” *Biosensors & Bioelectronics*, vol. 28, no. 1, pp. 459–463, 2011.
- [295] Y. Zhang and P. Ozdemir, “Microfluidic DNA amplification – a review,” *Analytica Chimica Acta*, vol. 638, no. 2, pp. 115–125, 2009.
- [296] A. A. Koshkin, V. K. Rajwanshi, and J. Wengel, “Novel convenient syntheses of LNA [2.2.1] bicyclic nucleosides,” *Tetrahedron Letters*, vol. 39, pp. 4381–4384, 1998.
- [297] S. Obika, D. Nanbu, Y. Hari, J. Andoh, *et al.*, “Stability and structural features of the duplexes containing nucleoside analogues with a fixed n-type conformation, 2'-O,4'-C-methyleneribonucleosides,” *Tetrahedron Letters*, vol. 39, pp. 5401–5404, 1998.
- [298] A. J. Qavi, J. T. Kindt, and R. C. Bailey, “Sizing up the future of microRNA analysis,” *Analytical and bioanalytical chemistry*, vol. 398, no. 6, pp. 2535–2549, 2010.

- [299] A. Válczi, C. Hornyik, N. Varga, J. Burgyán, *et al.*, “Sensitive and specific detection of microRNAs by northern blot analysis using LNA-modified oligonucleotide probes,” *Nucleic Acids Research*, vol. 32, no. 22, p. e175, 2004.
- [300] M. Castoldi, S. Schmidt, V. Benes, M. Noerholm, *et al.*, “A sensitive array for microRNA expression profiling (miChip) based on locked nucleic acids (LNA),” *RNA*, vol. 12, pp. 913–920, 2006.
- [301] D. Andreasen, J. U. Fog, W. Biggs, J. Salomon, *et al.*, “Improved microRNA quantification in total RNA from clinical samples,” *Methods (San Diego, Calif.)*, vol. 50, no. 4, pp. S6–S9, 2010.
- [302] M. R. Battig, Y. Huang, N. Chen, and Y. Wang, “Aptamer-functionalized superporous hydrogels for sequestration and release of growth factors regulated via molecular recognition,” *Biomaterials*, vol. 35, no. 27, pp. 8040–8048, 2014.
- [303] Z. Wang, J. Xia, F. Cai, F. Zhang, *et al.*, “Aptamer-functionalized hydrogel as effective anti-cancer drugs delivery agents,” *Colloids and Surfaces B: Biointerfaces*, vol. 134, pp. 40–46, 2015.
- [304] X. Zhang, B. Soontornworajit, Z. Zhang, N. Chen, and Y. Wang, “Enhanced loading and controlled release of antibiotics using nucleic acids as an antibiotic-binding effector in hydrogels,” *Biomacromolecules*, vol. 13, no. 7, pp. 2202–2210, 2012.
- [305] C. Lu, X. Qi, J. Li, and H. Yang, “Aptamer-based hydrogels and their applications,” in *Aptamers Selected by Cell-SELEX for Theranostics* (W. Tan and X. Fang, eds.), ch. 8, pp. 163–195, Springer-Verlag Berlin Heidelberg, 2015.
- [306] A. D. Keefe, S. Pai, and A. Ellington, “Aptamers as therapeutics,” *Nature Reviews Drug Discovery*, vol. 9, pp. 537–550, 2010.
- [307] Y. Cheung, J. Kwok, A. Law, R. Watt, *et al.*, “Structural basis for discriminatory recognition of plasmodium lactate dehydrogenase by a DNA aptamer,” *Proceedings of the National Academy of Sciences*, vol. 110, no. 40, pp. 15967–15972, 2013.
- [308] Z. Zhu, C. Wu, H. Liu, Y. Zou, *et al.*, “An aptamer crosslinked hydrogel as a colorimetric platform for visual detection,” *Angewandte Chemie (Int. Ed.)*, vol. 122, pp. 1070–1074, 2010.
- [309] S. Adlaj, “An eloquent formula for the perimeter of an ellipse,” *Notices of the AMS*, vol. 59, no. 8, pp. 1094–1099, 2012.

Appendix A

Tools and chemicals

Polymerisation chemicals

Monomer:	Acrylamide (AAM)	≥ 99%
Cross-linker:	N, N' methylene-bisacrylamide (MBA)	99%
Photo-initiator:	1-hydroxycyclohexylphenylketone (HCK)	99%
Buffer:	Phosphate buffer, aqueous, pH 7.4	1.0 M
Initiator solvent:	Ethylene glycol	≥ 99%
Additional solvent:	Dimethylsulfoxide (DMSO)	≥ 99.5%

All of the above chemicals were supplied by Sigma Aldrich and used as supplied. The MBA and the phosphate buffer were stored at 2-4°C, all other chemicals were stored at room temperature.

Conductive particles

Carbon nanopowder:	<50 nm
Carbon micropowder:	99.95%, glassy, spherical powder, 2–12 μm
Graphite:	99.99%, <45 μm
Carbon nanotubes:	≥ 98% carbon basis, O.D. × I.D. × L: 10 ± 1 nm × 4.5 ± 0.5 nm × 3~6 μm

All carbon particles were supplied by Sigma Aldrich and used as supplied. All were stored at room temperature.

Microfabrication tools

Furnace:	HITEC 8" Oxide Furnace
Parylene coater	Labcoater 2 Parylene Deposition System (PDS 2010), Specialty Coating Systems Inc. (SCS)
Asher:	Electrotech O ₂ Plasma Asher
Mask aligner:	Karl Suss MA / BA 8
Spin coater:	Polos 150
E-beam evaporation:	Helios Series cluster tool by Advanced Neotech Systems Inc. (ANS), custom designed for MicroEmissive Displays plc
Dry etcher:	JLS RIE80
Dicing:	DISCO DAD-640 wafer dicing saw

Metrology

Reflectometry:	Nanospec 300 Film Analyser, Nanometrics
Profilometry:	Veeco DekTak 8000 Surface Profiler

Microfabrication chemicals

Photoresists:	AZ NLoF 2070-3.5 (platinum lift-off), AZ SPR 220-4.5 (parylene patterning), Microchem
Adhesion promoter:	HMDS - 1,1,1,3,3,3 hexamethyldisilazane, Aldrich, 97% purity
Photoresist developers:	AZ726 (NLoF), AZ MF26A (SPR220), Microchem
Photoresist stripper:	NMR 1165 (lift-off), Dow

DI water

All deionised (DI) water was obtained from an ELGA DI water system. This system consists of a Filtromat activated carbon filter, an ELGA Purelab Prima 120 reverse osmosis unit, C260 and C270 deionising cylinders, a 0.2 micron filter and an ultraviolet disinfection unit. Water quality is continuously monitored by conductivity meters.

Imaging

Optical microscope: Reicher-Jung Polyvar MET
Scanning Electron Microscope: Hitachi S-4700

Pipettes

0.1 - 2 μ l: VWR Standard Line Pipettor, single channel, 2 μ l
2 - 20 μ l: Gilson Pipetman Classic P20
20 - 200 μ l: Gilson Pipetman Classic P200
100 - 1000 μ l: Gilson Pipetman Classic P1000

Other tools

UV source: Dymax Bluewave 75, 280 - 450 nm, intensity: $>19 \text{ W/cm}^2$
(UVB: 1.5 W/cm^2)
Sonicator: Fisher Scientific, 500 W, 20 kHz, 12.7 mm probe tip
Potentiostat: Metrohm Autolab PGSTAT12 potentiostat/galvanostat, operated by Nova software (version 1.11)
Balance: Fisherbrand Analytical Series, 210 g, 0.1 mg

Appendix B

MatLab code

Droplet volume calculation

```
function V = gel_vol_1(I,LHS,RHS,horizon ,top ,width , chip_size)
%-----
%Function to calculate droplet volume from an image given a
%pre-defined 'region of interest '
%-----
%AUTHOR: David Ferrier
%DATE: 26/11/15
%-----
%Inputs:
%I          - image data
%LHS        - left hand extent of region of interest
%RHS        - right hand extent of region of interest
%width      - width of chip (in pixels)
%horizon    - lower extent of region of interest
%top        - upper extent of region of interest
%chip_size  - width of chip in mm
%-----
%Output:
%V          - Droplet volume (in uL)
%-----
I = double(255-I);      %Invert image (light to dark)
%-----
%Crop image to region of interest
```

```

J = I(top:horizon ,LHS:RHS);
[row , col] = size(J);
%-----
%-----
%Define threshold for droplet edge detection based on image
%edges
left_edge = J(:,1);
right_edge = J(:,col);
left_max = max(left_edge);
right_max = max(right_edge);
edge_max = max(left_max , right_max);
thresh = edge_max + 10;
%-----
%Find edges of droplet for every row
lhs = zeros(row,1); %Left hand side
for ind = 1:row
    for dni = 1:col
        if J(ind , dni)>thresh
            lhs(ind,1) = dni;
            break
        end
    end
end
end

rhs = zeros(row,1); %Right hand side
for ind = 1:row
    for dni = col:-1:1
        if J(ind , dni)>thresh
            rhs(ind,1) = dni;
            break
        end
    end
end
end
%-----
%-----
%Calculate volume by assuming droplet is composed of a series
%of perfect circles stacked on top of each other
Vpix = 0;
for ind = 1:row
    if rhs(ind,1)==col || lhs(ind,1)==1;
        continue
    end
    d = rhs(ind,1) - lhs(ind,1); %diameter of circle
    a = pi*(d/2)^2; %number of pixels in layer
    Vpix = Vpix + a;
end
end

```

```
%-----  
  
%-----  
%Convert from pixels to real scale  
pixel_d = chip_size/width; %mm  
pixel_d = pixel_d/1000; %m  
pixel_v = pixel_d^3; %m3  
  
V = Vpix*pixel_v; %m3  
  
V = V*1e9; %uL  
%-----  
%-----
```

Oligonucleotide design

```

function oligo_design
%-----
%Function to take desired target DNA/RNA strand and generate
%appropriate Sensor and Blocker strands as well as a number
%of mismatched target strands.
%-----
%Author: David Ferrier
%Date 18/12/13
%-----

%-----
% Target oligo
t = 'UAUUGCACUUGUCCCGGCCUGU';    % mir-92a, Acute Leukemia
%-----

%-----
% Output oligos to be DNA or RNA? D for DNA, R for RNA
DorR = 'D';
%-----

len = length(t);

%-----
% Design sensor and blocker oligos
output = oligo_gen(t,DorR);

S = char(output(1,:));    % sensor oligo
B = char(output(2,:));    % blocker oligo
%-----

%-----
% Create Random sequence of same length as target
r = oligo_rand(len);
R = oligo_convert(r,DorR);
R = ['5-',R,'-3'];
R = char(R);
%-----

T = ['5-',t,'-3'];

%-----
% Output oligos to terminal
fprintf('\n-----\n')
formatspec1 = 'Target length: %1.0d nucleotides ';
fprintf(formatspec1,len)

```

```

fprintf('\n-----\n')
fprintf('T: ')
fprintf(T)
fprintf('\nS: ')
fprintf(S)
fprintf('\nB: ')
fprintf(B)
fprintf('\nR: ')
fprintf(R)
fprintf('\n-----\n')
%-----

%-----
% Design mismatched targets
%-----
N = 5;           % Number of mismatched targets
start = 1;      % Initial number of mismatches
increment = 1;  % Increment of mismatches between
                % successive targets

%-----
% Get oligos
output = mismatchgen(t,N,start ,increment ,DorR);
%-----

%-----
% Print output to terminal
for ind = 1:N
    lab = ['A' num2str(ind)];
    fprintf(lab)
    fprintf(': ')
    fprintf(char(output(ind,:)))
    fprintf('\n')
end

fprintf('\n-----\n')
%-----
end
%-----
%-----
%Subroutines
function output = oligo_gen(input ,DorR)
%Function to generate Sensor and Blocker strands
%-----
%Inputs:
%input - target sequence in symbolic form (1,n)
%DorR - outputs DNA or RNA? 'D' for DNA, 'R' for RNA
%-----

```



```
%Output:
%output - array containing sensor and blocker sequences in
%          symbolic form (2,n)
%-----

%-----
%define constants
toe = 10;          % length of toehold region
s_buff = 0;       % length of buffer (NT between toehold and
                  % anchor)
b_buff = 10;      % length of buffer (NT between blocking
                  % region and anchor)
%-----

%-----
%Get target in numerical sequence
T = oligo_backconvert(input);
T = fliplr(T); %Flip so target reads from 3' to 5'
%-----

%-----
%Create Sensor
%-----
%random buffer region
S1 = oligo_rand(s_buff);
%-----
%sensing region (complimentary to target)
S2 = oligo_comp(T);
%-----
S = [S1 S2];
%-----

%-----
%Create Blocker
%-----
%Active region (complimentary to Sensor)
B1 = T(1,toe+1:end);
%-----
%Random buffer region
B2 = oligo_rand(b_buff);
%-----
B = horzcat(B1,B2);
%-----
%flip blocker so all oligo strands read from 5-3
B = fliplr(B);
%-----
%Convert to symbols
```

```
sensor = oligo_convert(S,DorR);
blocker = oligo_convert(B,DorR);

sensor = ['5-' sensor '-3'];
blocker = ['5-' blocker '-3'];

output = zeros(2,length(sensor));

output(1,:) = sensor;
output(2,:) = blocker;
%-----
end
%-----
%-----

function output = oligo_rand(N)
%function to return random string of NTs of length N
%-----
%Input:
%N - length of sequence in nucleotides
%-----
%Output:
%output - oligonucleotide in numeric form
%-----
output = zeros(1,N);
for ind = 1:N
    r = randi([1,4]);
    output(1,ind) = r;
end

end
%-----
%-----

function output = oligo_convert(input,DorR)
%subroutine to convert numerical sequence (1,2,3,4) into
%symbolic sequence (C,G,A,T)
%-----
%Inputs:
%input - NT sequence in numeric form
%DorR - outputs DNA or RNA? 'D' for DNA, 'R' for RNA
%-----
%Output:
%output - NT sequence in symbolic form
%-----
%-----
```

```

%C = 1
%G = 2
%A = 3
%T(U) = 4
%-----
L = length(input);
output = zeros(1,L);
for ind = 1:L
    if input(1,ind)==1
        x = 'C';
    elseif input(1,ind)==2
        x = 'G';
    elseif input(1,ind)==3
        x = 'A';
    elseif input(1,ind)==4
        if DorR == 'D'
            x = 'T';
        elseif DorR == 'R'
            x = 'U';
        end
    end
    output(1,ind) = x;
end
end
%-----
%-----

function output = oligo_backconvert(input)
%subroutine to take oligo string in (C,G,T,A format and
%convert to numerical format)
%-----
%Inputs:
%input - NT sequence in symbolic form
%-----
%Output:
%output - NT sequence in numeric form
%-----

%-----
%C = 1
%G = 2
%A = 3
%T(U) = 4
%-----
L = length(input);
output = zeros(1,L);
for ind = 1:L

```

```

    if input(ind)=='C'
        x = 1;
    elseif input(ind)=='G'
        x = 2;
    elseif input(ind)=='A'
        x = 3;
    elseif input(ind)=='T'
        x = 4;
    elseif input(ind)=='U'
        x = 4;
    end

    output(1,ind) = x;
end
end
%-----
%-----

function output = oligo_comp(input)
%subroutine to return oligo strand that is exactly
%complementary to input sequence
%-----
%Inputs:
%input - initial sequence (1,n)
%-----
%Output:
%output - complementary sequence (1,n)
%-----

L = length(input);
output = zeros(1,L);
for ind = 1:L
    if input(ind)==1
        output(1,ind) = 2;
    elseif input(ind)==2
        output(1,ind) = 1;
    elseif input(ind)==3
        output(1,ind) = 4;
    elseif input(ind)==4
        output(1,ind) = 3;
    end
end
end
end
%-----
%-----

function output = mismatchgen(input,N,start,increment,DorR)

```

```

%function to generate N mismatched target sequences with
%varying numbers of mismatches
%-----
%Inputs:
%input      - initial sequence in symbolic form (1,length)
%N          - number of mismatched sequences to be generated
%start      - initial number of mismatches
%increment  - increase in number of mismatches between
%            sequences
%DorR       - outputs DNA or RNA? 'D' for DNA, 'R' for RNA
%-----
%Output:
%output     - array containing mismatched sequences in
%            symbolic form (N,length)
%-----

output = zeros(1,length(input)+4);
I = oligo_backconvert(input);
n = start;
for ind = 1:N
    x = mismatch(I,n);
    X = oligo_convert(x,DorR);
    X = ['5-' X '-3']; %ok<AGROW>
    output(ind,:) = X;
    n = n + increment;
    clear X
end
end
%-----
%-----

function output = mismatch(input,N)
%subroutine to return oligo sequence with N random mismatches
%when compared to input oligo
%-----
%Inputs:
%input      - initial sequence in symbolic form (1,length)
%N          - number of desired mismatches
%-----
%Output:
%output     - mismatched sequence (1,length)
%-----
L = length(input);
output = input;
%-----
%Get out clause in case specified number of mismatches is
%greater than oligo strand length

```

```

if N>L
    print('WARNING: N > L. Procedure terminated.')
    return
end
%-----
ind = 0;
ref = [];
while ind<N
    r = randi([1,L]); %randomly select NT to edit
    %Search all previous edited nucleotides, if this one has
    %been changed already skip until a new one is selected
    len = length(ref);
    fu = 0;
    for dni = 1:len
        if ref(1,dni)==r
            fu = 1;
        end
    end
    end

    if fu==1
        continue
    end

    ref = [ref r]; %#ok<AGROW> %store which NT is
                    %being edited for future reference
    p = randi([1,3]); %randomly select replacement from
                    %pool of alternative bases

    x = input(1,r);
    %-----
    %based on current identity of NT, define possible
    %alternatives
    if x==1
        pool = [2,3,4];
    elseif x==2
        pool = [1,3,4];
    elseif x==3
        pool = [1,2,4];
    elseif x==4
        pool = [1,2,3];
    end
    %-----
    output(1,r) = pool(p);
    ind = ind + 1;
end
end
%-----
%-----

```

Cell constant calculation

```

function k = kappa_calc(L,W,S,N)
%function to calculate the cell constant for a given IDE
%array.
%-----
%AUTHOR: David Ferrier
%DATE: 21/05/2015
%-----
%Inputs:
%L      - digit length , in um
%W      - digit width , in um
%S      - digit seperation , in um
%N      - number of digits
%-----
%Output:
%k      - cell constant
%-----

tol = 1e-6; %define tolerance (for AGM calculation)

%-----
%Convert to cm
L = L/10000;
W = W/10000;
S = S/10000;
%-----

mod = cos((pi/2)*(S/(S+W))); %modulus of IDE array

K1 = elliptic_calc(mod,tol); %complete elliptic integral
K2 = elliptic_calc(sqrt(1-mod^2),tol);

k = (1/((N-1)*L))*(2*K1/K2);

end
%-----
%-----
%Subroutines
function output = elliptic_calc(input,tol)
%function to calculate complete elliptic integral
%-----
%Inputs:
%input    - integration variable
%tol      - tolerance (for AGM calculation)
%-----
%Output:

```

```
%output      - integral
%-----
a = 1;
b = sqrt(1-input^2);

output = (pi/2)*agm_calc(a,b,tol);

end
%-----
%-----

function agm = agm_calc(a,b,tol)
%function to calculate the arithmetic-geometric mean of two
%numbers
%-----
%Inputs:
%a      - first number
%b      - second number
%tol    - tolerance
%-----
%Output:
%agm    - arithmetic-geometric mean
%-----

a_var = a;
g_var = b;
fu = 0;
while fu==0
    delta = abs(g_var - a_var);
    a_var_2 = (a_var + g_var)/2;
    g_var_2 = sqrt(a_var*g_var);
    if(delta<tol)
        fu = 1;
    end
    a_var = a_var_2;
    g_var = g_var_2;
end

agm = (a_var + g_var)/2;

end
%-----
%-----
```


Appendix C

Fabrication run sheet

This appendix contains the run sheet used for the fabrication of the electrodes used throughout this thesis (as described in Section 2.3). The single layer devices are produced by following the steps below, excluding steps 18-30.

Step	Description	Equipment	Parameters	Notes
1	Thermal Oxidation	F1	WETOX14, $t = 40$ min	
2	Measure T_{OX}	Nanospec	Prog 1, oxide on silicon	
3	Dehydration ash	ET barrel asher	Std conditions, 30 min	May be omitted if wafers primed shortly after being unloaded from furnace
4	Wafer prime	Wet deck	HMDS, room temperature, 10 min	
5	Photoresist coat	Polos 150	AZ NLOf, 5s at 700 rpm, 60s at 3000rpm	
6	Soft bake	EMS hotplate	110°C, 1 min	
7	Align & expose	KS MA8	Mask 1, hard contact, 30s	
8	Post exposure bake	EMS hotplate	115°C, 1 min	
9	Develop	Wet deck	AZ726, 120s	
10	Rinse	Wet deck	DI water, dry	
11	Inspection	Microscope	Check for obvious defects and CD markers	
12	Metal deposition	ANS	100 Å Ti / 500 Å Pt	
13	Lift-off	Ultrasonic bath	1165, 1 hr at 50°C	
14	IPA rinse	Ultrasonic bath	Multiple times	Perform at least three times, or until solution appears free of particulates
15	Rinse	Wet deck	DI water, dry	

16	Inspect	Microscope	Check for obvious defects	
17	Measure	DekTak	CD and metal thickness	If doing single layer devices, go straight to step 31
18	Parylene coat	Parylene tool	1 μm	
19	Wafer prime	Wet deck	HMDS, room temperature, 10 mins	
20	Photoresist coat	Polos 150	SPR220-4.5; 5s at 500 rpm, 30s at 3000 rpm	
21	Softbake	EMS hotplate	115°C, 1 min	
22	Exposure	KS MA8	Align to layer 1, Mask 2, hard contact, 30s	
23	Develop	Wet deck	MF26A, 1 min	
24	Rinse	Wet deck	DI water, dry	
25	Inspect	Microscope	Check for obvious defects	
26	Measure	DekTak	Resist thickness; expecting $\sim 1\mu\text{m}$	
27	Parylene etch	JLS RIE 80	Prog 12, 15 min	
28	Inspect	Microscope	Check for obvious defects	
29	Resist strip	Wet deck	Acetone	
30	Rinse	Wet deck	IPA Rinse, DI Rinse, dry	
31	Photoresist coat	Polos 150	SPR350; 5s at 500 rpm, 30s at 3000 rpm	
32	Softbake	EMS hotplate	90°C, 1 min	
33	Dice	Disco saw	22.9 mm x 7.7 mm	
34	Protective layer removal	Wet deck	Acetone rinse, IPA rinse, DI rinse, dry	

Table C.1: Run sheet for electrode fabrication. For single layer devices, steps 18-30 were omitted.

Appendix D

Cell constant calculation

According to Olthuis *et al.*, for planar interdigitated electrode (IDE) the cell constant, κ , can be expressed as:

$$\kappa = R\sigma \quad (\text{D.1})$$

where R is the resistance of the medium, and σ its conductivity [235]. For an IDE array κ is given by:

$$\kappa = \frac{1}{(N-1)L} \frac{2K(k)}{K[\sqrt{1-k^2}]} \quad (\text{D.2})$$

where N is the number of digits, L is the length of the digits and $K(k)$ is the complete elliptic integral of the first kind:

$$K(k) = \int_0^1 \frac{dt}{\sqrt{(1-t^2)(1-k^2t^2)}} \quad (\text{D.3})$$

which can be approximated in terms of the arithmetic-geometric mean (AGM) as follows [309]:

$$K(k) = \frac{\pi/2}{AGM(1, \sqrt{1-k^2})} \quad (\text{D.4})$$

The argument k is the modulus of the IDE array and can be approximated, for values of $N > 2$, by:

$$k = \cos\left(\frac{\pi}{2} \frac{s}{s+w}\right) \quad (\text{D.5})$$

where s is the separation between electrode digits and w is the digit width (Figure D.1).

Therefore, for IDE where s is 40 μm , w is 10 μm , L is 1400 μm and N is 30; κ is approximately equal to 0.8 cm^{-1} . A MatLab algorithm for calculating κ can be found in Appendix B.

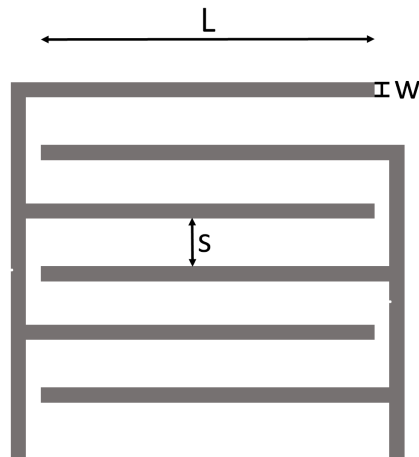


Figure D.1: Illustration of the electrode array showing the parameters s , w and L (only 6 digits are shown for clarity).

Appendix E

Morpholino functionalisation

In order that morpholino oligonucleotides can be incorporated into the structure of polymer hydrogels in the same manner as DNA oligonucleotides, it is necessary to functionalise the chain end with an acrylamide-based moiety, similar to the Acrydite functionality for DNA (Section 1.4.2). To achieve this, morpholino oligonucleotides were purchased from Gene Tools LLC with a primary amine group attached to the 3' end via an ethyl linker (Figure E.1), thereby rendering them active for chemical modification. The base-sequences of the morpholino oligonucleotides were chosen to be exactly analogous to the sensor and blocker sequences described in Section 2.1.2. The morpholinos were supplied in their lyophilised form and the sensor and blocker sequences were each dissolved in DI water to a concentration of 1 mM. To these solutions an aqueous solution of N-succinimidyl acrylate (NSA) was added to 2 molar equivalents and the resultant mixture was left to stir in a round bottomed flask at room temperature for 20 hours. The ensuing reaction results in an amide bond

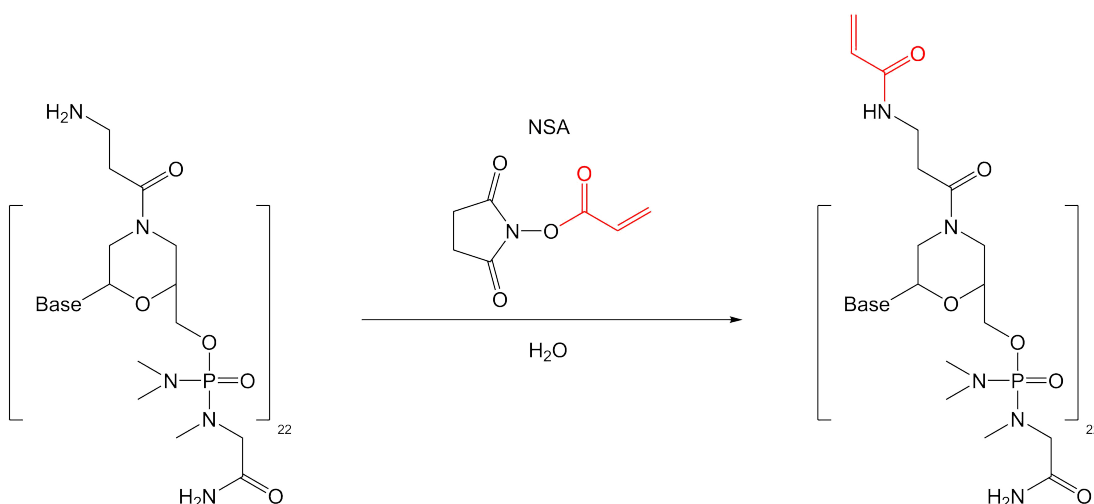


Figure E.1: Functionalisation reaction of morpholino oligonucleotide with NSA. The bases can be any of the four standard oligonucleotide bases: adenine (A), cytosine (C), guanine (G) or thymine (T). The functional acrylamide moiety is shown in red.

formation between the amine of the morpholino and the carbonyl of the NSA, yielding a morpholino oligonucleotide with an acrylamide moiety (Figure E.1). The formation of the product was confirmed using MALDI-ToF mass spectroscopy.

The product was extracted from solution via lyophilisation, after which the product was washed with hot (*ca.* 50°C) ethyl acetate to remove any residual succinimide. Once lyophilised the sensor and blocker strands can be re-suspended, mixed and then lyophilised into smaller aliquots for use in gel preparation (similar to the process used for DNA cross-linkers - Section 2.1.3). The NSA and ethyl acetate were sourced from Sigma Aldrich and used as supplied. This procedure was developed and performed by Dr Jaclyn Raeburn. The MALDI-ToF mass spectroscopy was performed using an Ultraflex II MALDI-ToF/ToF mass spectrometer (Bruker Daltronics) and the data was processed using FlexAnalysis software.